Modal analysis of an ultrafast frequency comb : from classical to quantum spectral correlations

Valérian Thiel

▶ **To cite this version:**

Valérian Thiel. Modal analysis of an ultrafast frequency comb : from classical to quantum spectral correlations. Quantum Physics [quant-ph]. Université Pierre et Marie Curie - Paris VI, 2015. English. NNT : 2015PA066661 . tel-01367423

HAL Id: tel-01367423

https://theses.hal.science/tel-01367423

Submitted on 7 Jul 2017

HAL is a multi-disciplinary open access archive for the deposit and dissemination of scientific research documents, whether they are published or not. The documents may come from teaching and research institutions in France or abroad, or from public or private research centers.

L'archive ouverte pluridisciplinaire **HAL**, est destinée au dépôt et à la diffusion de documents scientifiques de niveau recherche, publiés ou non, émanant des établissements d'enseignement et de recherche français ou étrangers, des laboratoires publics ou privés.

Thèse de doctorat de
l'Université Pierre et Marie Curie

présentée par

Valérian THIEL

pour obtenir le grade de Docteur de l'Université Pierre et Marie Curie
sur le sujet:

Analyse modale d'un peigne de fréquences femtoseconde :
Correlations spectrales classiques et quantiques

Modal analysis of an ultrafast frequency comb:
From classical to quantum spectral correlations

Laboratoire Kastler Brossel
Physique quantique et applications

Membres du jury :	
M. Marco BARBIERI	Rapporteur
M. Yanne CHEMBO	Membre du jury
M. Scott DIDDAMS	Rapporteur
M. Claude FABRE	Membre invité
M. Sébastien PAYAN	Membre du jury
M. Nicolas TREPS	Directeur de thèse

For my mother

who has always put knowledge
and education in front of everything

Contents

Acknowledgements xi

Introduction 1

I Measuring with ultra-fast frequency combs 7

1 The modes and states of a beam of light 9
1.1 The classical electromagnetic field . . . 10
1.1.1 Description of the real electromagnetic field . . . 10
1.1.2 Fourier space formalism . . . 11
1.2 Modal description . . . 13
1.2.1 Temporal and spectral modes . . . 13
1.2.2 Spatial modes . . . 14
1.2.3 Spatio-temporal modes . . . 16
1.2.4 Basis change . . . 17
1.2.5 Power and energy . . . 17
1.3 The quadratures of the classical field . . . 19
1.3.1 Quadrature amplitudes . . . 19
1.3.2 Quadrature fluctuations . . . 20
1.4 Quantization of the field . . . 21
1.4.1 Bosonic operators . . . 21
1.4.2 Modal decomposition . . . 21
1.4.3 Quadrature operators . . . 23
1.4.4 Relation to the classical field . . . 24
1.5 Quantum states . . . 25
1.5.1 Density operator . . . 25
1.5.2 Wigner function . . . 26
1.6 Gaussian states . . . 27
1.6.1 Definition and quantum covariance matrix . . . 27
1.6.2 Examples of Gaussian states . . . 27

2 Femtosecond ultrafast optics **31**
2.1 Description of pulses of light . . . 32
2.1.1 Optical frequency combs . . . 32
2.1.2 Energy and peak power . . . 35
2.1.3 Moments of the field . . . 36
2.1.4 Gaussian pulses . . . 37
2.2 The influence of dispersion . . . 38
2.2.1 Spectral and temporal phases . . . 39
2.2.2 Effects on the pulse shape . . . 39
2.3 Representations of the pulse . . . 44
2.3.1 Time-frequency distributions . . . 44
2.3.2 Some examples . . . 46
2.3.3 Experimental realizations . . . 47
2.4 Generation of pulses of light . . . 48
2.4.1 Steady-state laser cavity . . . 48
2.4.2 Mode-locked lasers . . . 50

3 Revealing the multimode structure **55**
3.1 General experimental scheme . . . 56
3.1.1 Laser source . . . 57
3.1.2 Interferometric photodetection . . . 59
3.1.3 Pulse shaping . . . 62
3.2 Signal measurement . . . 68
3.2.1 Modulations of the field . . . 68
3.2.2 Data acquisition . . . 70
3.3 Mode-dependent detection . . . 73
3.3.1 Quantum derivation . . . 73
3.3.2 Spectrally-resolved homodyne detection . . . 75
3.3.3 Temporally-resolved homodyne detection . . . 78
3.3.4 Addendum: single diode homodyne detection . . . 82

II Quantum metrology **83**

4 Parameter estimation at the quantum limit **85**
4.1 Projective measurements . . . 86
4.1.1 Displacements of the field in specific modes . . . 86
4.1.2 Sensitivity . . . 88
4.1.3 The Cramér-Rao bound . . . 89
4.2 Spectral and temporal displacements . . . 89

4.2.1 Temporal displacements . . . 90
4.2.2 Spectral displacements . . . 92
4.2.3 Conjugated parameters . . . 94
4.2.4 Application to range-finding . . . 96
4.3 Space-time coupling: a source of contamination . . . 102
4.3.1 Transverse displacements . . . 102
4.3.2 Homodyne contamination . . . 104

5 Measuring the multimode field 107
5.1 Experimental details . . . 108
5.1.1 Measurement strategy . . . 109
5.1.2 Phase modulation at high frequencies . . . 110
5.1.3 Spatial filtering . . . 114
5.2 Interferometer calibration . . . 115
5.2.1 Calibration of displacement . . . 116
5.2.2 Sensitivity measurement . . . 120
5.3 Multipixel detection . . . 122
5.3.1 Design and construction . . . 122
5.3.2 Gain calibration . . . 125
5.3.3 Space-wavelength mapping . . . 127
5.3.4 Clearance . . . 128
5.4 Spectrally-resolved multimode parameter estimation . . . 128
5.4.1 A glimpse at the multimode structure . . . 129
5.4.2 Signal extraction . . . 132
5.4.3 Heterodyne measurements: the need for a stable reference . . . 134
5.4.4 Space-time positioning . . . 136
5.4.5 Dispersion . . . 141
5.4.6 Quantum spectrometer . . . 144

III Noise analysis of an ultra-fast frequency comb 149

6 Optical cavities 151
6.1 Fabry-Perot cavities . . . 152
6.1.1 Input-output relations . . . 152
6.1.2 Characteristic quantities . . . 154
6.1.3 Spatial mode . . . 155
6.1.4 Noise filtering . . . 156
6.1.5 Quadrature conversion . . . 156
6.2 Synchronous cavities . . . 157

6.2.1 Resonance condition . . . 158
6.2.2 The cavity's comb . . . 158
6.2.3 Simulations . . . 160
6.3 Experimental realization . . . 162
6.3.1 Motivations . . . 162
6.3.2 Design and construction . . . 162
6.3.3 Cavity lock . . . 163
6.3.4 Environnemental pressure dependency . . . 163
6.3.5 Noise properties . . . 165

7 Experimental study of correlations in spectral noise 169
7.1 The modal structure of noise . . . 170
7.1.1 Introduction and motivations . . . 170
7.1.2 The noise modes . . . 170
7.2 Measuring spectral correlations in the noise . . . 171
7.2.1 Classical covariance matrix . . . 171
7.2.2 Retrieving the fluctuations . . . 173
7.2.3 Experimental scheme . . . 175
7.3 Experimental results . . . 177
7.3.1 Amplitude and phase spectral noise . . . 177
7.3.2 The noise modes . . . 179
7.3.3 Collective parameters projection . . . 180
7.3.4 Phase-amplitude correlations . . . 181
7.3.5 Real-time laser dynamics analysis . . . 183

IV Going further with quantum frequency combs 187

8 Multimode squeezed states 189
8.1 Generating quantum states . . . 190
8.1.1 Creation of squeezed states . . . 190
8.1.2 Parametric down conversion with an optical frequency comb . . . 191
8.1.3 Objectives and perspectives . . . 192
8.2 Single-pass squeezing . . . 193
8.2.1 Parametric down conversion . . . 193
8.2.2 Eigenmodes of the parametric down conversion . . . 194
8.2.3 Expected efficiency . . . 198
8.3 Second harmonic generation . . . 198
8.3.1 Efficiency . . . 199
8.3.2 The influence of temporal chirp . . . 202

8.4 An ultra-fast squeezer . . . 203
8.4.1 Pump generation . . . 203
8.4.2 Synchronously pumped optical parametric amplifier . . . 204
8.5 Perspectives . . . 205
8.5.1 Quantum enhanced metrology . . . 205
8.5.2 Entanglement . . . 207

Conclusion and outlooks **209**

Appendix A Medium dispersion **213**
A.1 Sellmeyer equation . . . 213
A.2 Wave-vector dispersion . . . 214
A.3 Application to delay and dispersion estimation . . . 214

Appendix B Projective measurements by pulse shaping **217**
B.1 Pulse shaping the time-of-flight mode . . . 218
B.2 Locking on the time-of-flight mode . . . 219
B.3 Dispersion measurement . . . 221

Appendix C Experimental construction of the detection modes **225**

Appendix D Conjugated variable of space-time position **227**
D.1 Detection mode for a global displacement . . . 227
D.2 Detection mode for a spectral displacement . . . 228
D.3 Conjugated parameter . . . 230

Acknowledgements

This dissertation is the conclusion of three years of work, work that could never have happened without all the people that contributed to it. And in term of people that I had the privilege to work with, I believe it will prove hard in the future to replicate such a remarkable work environnement.

Before all, I would like to thank my jury, for reviewing my thesis on such short notice, and for bringing very interesting insight to the work. I can only imagine how daunting it must be to review such a long document, and you have my sincere gratitude for that.

In my opinion, what is probably the most important aspect of research in general is team work. Being part of a united group increases productivity and has the advantage of looking forward to going to work every day. Working in the quantum optics group of LKB was for me a perfect realization of this statement.

Therefore, I would like to thanks everybody in the LKB for being nice colleagues and co-workers, for sharing their different ways of working around a cup of coffee, or simply for discussing a broad variety of subjects among highly educated people. Moreover, the presence of people from all over the world allowed interesting insights into the world in general, making it suddenly a much smaller place, and making you feel more like a citizen of the world rather than of a single nation. Thanks also to the engineers and administrative people without who our work would be impossible. In particular, thanks to Thierry, Romain, Laetitia and Michel for flawlessly taking care of virtually every investment. A gigantic "thank you" to Monique, without who this place wouldn't run as good as it is today. I wish all the best to her successor, Nora, who is already proving to be as exceptionally efficient at her job ! Another very sincere and loving acknowledgement to the electronics workshop, with Brigitte and Jean-Pierre, for their incredible work. The research that is presented in this thesis would most certainly have been very different without their knowledge and service. Walking into the electronics workshop for soldering work or just chatting was always a pleasure, and that is once again thanks to the people that work here. Thanks also to the IT department, Serge, Corinne, Jeremie and Mathilde for their great job at taking care of our computers and networks, globally making working in the lab easier. Thanks to Annick and Bintou, who were always nice and smiling every morning, and for keeping my desk from collapsing under the weight of the mess I negligently made (sorry about that).

I would like to thank also the other research groups at the LKB and other labs. Notably, I am thankful to the optomechanics group of LKB in general for allowing me to start learning optics and quantum optics during my studies. Thanks in particular to Tristan

for his teaching and counsel, thanks to Antoine for being always nice and cheerful, making today a very good director for the lab. My sincere thanks go to Alexandros, for introducing me to the work and for giving a glimpse of what research should be. You taught me a lot of what I know today, and I am deeply grateful for that. Moreover, the intense pleasure that was procured by the process of cavity alignement will forever be etched in my mind. Thanks also to my friends from SYRTE, who showed me that metrology could-sometimes-be fun, with who my relationships were as fruitful as they were joyful and learning experiences, and for sharing a rather interesting conference in Prague.

A special thanks to our former interns, who allowed me to express my teaching personality (which I hope I did well) that I love showing. Thanks to Adrien and Martin for being so eager to learn, and for participating to the fun in the lab; Francesco, also for the fun he's brought, for bringing more of that italian theoretician dimension to the team; Catx, for all the nice time we've shared and all the interesting discussion we've had, for bringing the sun with her every day (which I think you took away with you: bring it back !) and for being such a friendly, always smiling, very interesting person.

Finally and most importantly, there are all those colleagues that I today call friends, thanks to all the wonderful time we had outside of work. I wish to acknowledge from the bottom of my heart: all of my colleagues from my Master at ENS, Baptiste, Marion, Hugo, Thomas, Raphael, Rémi, Camille and so forth, for being such nice friends that made hard years of learning much more fun that I originally expected; Roman for sharing his last PhD year with me, walking me through the experiment, teaching me the delicate nature of metrology, the magic of crazy glue, and for, globally, giving me the German experience (what is regularly refereed to in the group as the Schmeissner®experience, something that no Man can forget); Renné, also for introducing me to the lab and the way things worked; Hanna, for not pushing charges against me; Pierre, for the same reason (although I know he would have enjoyed it) and for having spent some good time with us in Munich; Vanessa, for putting up with my appetite for German profanities and my unreasonable behavior in general; Valentin, for all the interesting discussion on theoretical physics with a russian accent we've had (but mostly for everything that wasn't science related, such as the poster sessions at the DPG); Ale, for the amount of man-love that we still share today around a beer, buratta and 80's movies; Guilia, for being Giulia: words are not sufficient to describe how amazing this woman is; the same goes for Pu, for all the great time we shared together, all the cooking, dancing and singing; all the people from Cai Labs, J-F for being a great captain, for all the great time we've had sailing around the Greek islands, and Guillaume for the fun we've had in the lab. All of you people greatly contributed to making me a better person, and I will never forget all the time we've had together.

Another huge acknowledgement goes to the Unit, Clément and Jon, my brothers from

other mothers, for having turned the lab into some kind of underground disco room, where the amount of hard work and productivity was always directly proportional to the fun we've had. It was always a genuine pleasure coming to work early in the morning and to go back home late at night. As hard as the work was, it was definitely worth it. So thanks from the bottom of my heart to Clément, without who I wouldn't be here, for being such a great friend, for making life in the lab better, for bringing the spirit of party with him everyday, for throwing amazing parties and dinners, for renting LED-blasters, for cooking Tiramisu, for buying italian salamee, for all the "*Game over, man*" situations, for sharing interesting rocket, airplane designs and delta-v optimization on Kerbal Space Program®, for his ability to make lemonade with a strong, single crushing gesture, for being my Linux Guru when I needed one, for his impressive mastery of the German side at Company of Heroes... Concerning Jon, words are also lacking to describe how incredibly lucky I was to accomplish my PhD with you. You taught me most of what I know about optics today, and I feel like I've learned more in these three years that I have during all my studies, and that is thanks to you. Your impressive knowledge of a broad variety of subject made working with you a precious experience, one I will also never forget. It is worth stressing that I believe that none of the work presented in this dissertation would have been possible without you, and it has truly been a privilege working with you. And again, the amount of work that we accomplished together is only matched by the amount of fun we've had together. It has been a lot of hard work, but it has also been a LOT of beers at the pub nextdoor, a lot of Lebanese sandwiches at 2AM, where I really enjoyed all the discussion that we've had about science, life and death. I shall never forget these days, I cherish the memory of California with you, Mission Peak (which was just a bit more challenging than expected), San Francisco, the rat parade, the Farmer's Market... Thanks to both of you brothers, we've had the time of our lives during these years. In the name of the parameter estimation experiment, we would also like to thank Jameson, 1664, Chouffe, Leffe, Glenfiddich, the bathroom next to the lab, the people at Epsilon and Inevitable, the B-52 and madeleine shooters, black magic, voodoo magic, blood magic, Dante, my friend Jack, our mastah Vlad, El Scorpio, John Matrix, Bennett, Ash, Toni, Gunther, the Throne of Blood, the Centercom and its Tegam slave, the Warclub of Affliction, the Finger of Death, the Tooth of Sorrow, the Holy Horn, the Swing of Redemption and the Four Riders of the Apocalypse: the experiment would never have ended without them.

Last, but not least, my most sincere thanks go to our bosses, Nicolas and Claude. Working under your direction has truly been a pleasure for multiple reasons. First, because you both are among the most brilliant person I had the chance to meet, such that learning from you has always been very rewarding. Then, because you have very kind personalities, and appreciate all the small things in life that make it worth living. I will always remember the pic-nics, group meeting / buffets, dinners and so on that we shared.

It really helped make the group something unique, which created bonds not unlike a family. So thank you again, it has been a privilege working in the shadow of geniuses ! In term of latest addition to the team of brilliant people, Vale is there too, strengthening the italian, feminine presence in the group. Thanks you so much for your cheesecake (which should be put somewhere on your professional resume), and also for the short time we've spend together: you're gonna do really fine in this group, and I foresee great things happening for you (which you definitely deserve).

All of this would also never have been possible without the support of my family. Thanks to my sisters and parents who supported me (quite literally at first) in my endeavor, who made me push always harder to reach the top. Also, I cannot be thankful enough to Tiphaine, whose love and attention allowed her to put up with my frequent mis-behavior, for taking so good care of me, and for always being there when I needed it.

Introduction

The ability to perform precise measurements is a fundamental aspect of all quantitative science. To determine the value of a parameter in a physical system, an experimentalist uses a probe to interact with the system. By measuring the way the probe has been altered by its interaction with the system, it is possible to deduce the value of the parameter. Any probe can however be intrusive in the sense that it affects the physical system on its interaction, thus altering the response of the system to its presence. From a classical physics point of view, the usage of a beam of light as a probe is adapted to a non-intrusive measurement since it can be attenuated to a point where its interaction with matter is negligible.

For instance, light has been used extensively to the purpose of estimating distances. More than 2000 years ago, Eratosthenes estimated the circumference of the Earth using geometric consideration of the shadow cast by the Sun. If the same measurement were made today using current data, the retrieved value would be accurate to less than 1%.

Accuracy is a fundamental concept in experimental science. It defines how different the value of a parameter will be when an experiment is repeated several times. The finite accuracy is a direct consequence of other physical phenomena that limit the knowledge of a variable, which may be described as the noise in a measurement. Without noise, any measurement would be always perfect.

The discovery in the end of the 18^{th} century of the wave-like nature of light gave birth to the field of interferometry, allowing to measure distances with a precision limited only by the wavelength of light. In 1894, Michelson measured the length of a platinium-iridium standard by interferometry and defined it in terms of an emissive wavelength of cadmium. He advocated the use of wavelengths as a natural standard for distance [Michelson 94]. In 1960, the meter was redefined in terms of the emissive wavelength of krypton, replacing the platinium-iridium standard. Today, the meter is defined from the speed of light. Light became an even more widespread measurement tool since the advent of lasers, which brought a source of light that is highly coherent both spatially and temporally.

As a recent example, the usage of light as a tool to measure long distances with good accuracy has resulted in the estimation of the distance between the Earth and the Moon with an accuracy of a few millimeters [Murphy Jr 08]. This measurement was achieved by sending pulses of light on a retroreflector on the Moon and measuring their time of arrival. This measurement is called a *time-of-flight* measurement, which is less accurate than an interferometric measurement. The ability to distinguish between redundant in-

formation on distance, called *ambiguity range*, is on the order of the wavelength of light for an interferometric measurement, while it is on the order of the distance between subsequent pulses for a time-of-flight measurement. The latter then offer a better dynamics, since the spacing between pulses of light is much higher than its wavelength. Combining interferometric and time-of-flight measurements then allows to merge high dynamics and sub-wavelength precision.

In order to combine the dynamics of the time-of-flight measurement performed with pulsed light and the precision obtained by interferometric measurement, *optical frequency combs* appeared as ideal tools for the task. A frequency comb consists of a large number of equally spaced optical frequencies with a narrow linewidth, and a fixed phase relationship between them. In the temporal domain, this corresponds to a train of short pulses emitted at equal intervals. The development of mode-locked lasers, and in particular Titanium-Sapphire lasers in the 1990' [Spence 91], resulted in the realization of such frequency comb with pulses as short as a few femtosecond. The realization of many stabilization techniques allows today to produce very stable frequency combs, making them perfect tools for metrology and spectroscopy [Udem 02].

For the purpose of high precision measurement, the accuracy of an experiment accomplished using an optical frequency comb is limited mostly by the noise of the source. For a time-of-flight measurement, the accuracy is limited by the fluctuation of the repetition rate, called *timing jitter*, whereas an interferometric measurement is limited by the fluctuations in the each optical carrier, generally called *phase noise*. The ability to characterize and measure these fluctuations is essential to their stabilization [Paschotta 05].

These fluctuations can be described as arising from technical sources, such as thermal and mechanical variations, but also from the quantum nature of light, which poses the most fundamental limit, the one that remains when removing all sources of technical noise in the measurement. For instance, the random time-of-arrival of photons on a detector, commonly called the *shot noise* limit, defines the *standard quantum limit* in sensitivity in both amplitude and phase noise [Caves 81]. The field of quantum metrology studies how it is possible to engineer the quantum state of the system that results in a better sensitivity compared to classical methods. Recently, the usage of squeezed vacuum in an interferometer allowed to surpass the current sensitivity in gravitational wave detection [Aasi 13].

In this thesis, we investigate the usage of frequency comb for precision measurements at the quantum limit, as well as the fluctuations of the combs structure. We use a formalism that is borrowed from quantum optics to describe classical phenomenon. We show indeed that the comb structure can be decomposed on a basis of modes, where each of these is attached to a given physical parameters [Lamine 08, Jian 12]. In a projective measurement scheme, we show that it is then possible to measure an information car-

ried by the electromagnetic field (such as a delay in time) as well as fluctuations from the laser source (in that example, the timing jitter). We finally propose a scheme to generate two beams that are “squeezed in time”, since they allow to measure a delay with a better sensitivity than using classical ressources.

Outline of this thesis

The first part of this thesis concentrates on giving global definitions of the tools that are needed for the task of measurement using a multimode description of an optical frequency comb.

In the first chapter, we give a classical and a quantum formulation of the electromagnetic field. We define the notations that are used throughout this thesis.

In the second chapter, we describe the concepts of ultrafast optics. Since the work of this PhD was accomplished with short pulses (~ 20 fs), it is important to understand the physical phenomena that arise when such pulses propagate. We also outline how to characterize the spectral and temporal structure of the pulse, as well as its generation.

In the third chapter, we expose how we intend to measure the multimode structure of an ultrafast frequency comb. We give a global description of the experiment and we outline how to measure the optical quadratures of the different spectral components of the field.

The second part concentrates on the study of precision measurements at the quantum limit.

In the fourth chapter, we describe the multimode structure of the field when a perturbation is introduced. We cover the case of a displacement in time, in amplitude (*i.e.* energy), in optical frequency and in phase. We show that these parameters can be extracted by performing a projective measurement on a set of specific spectral modes. Moreover, we give a quantum description of the matter, which allows to show that these parameters are conjugated. We also show that the sensitivity of the projective measurement scheme coincides with the standard quantum limit.

In the fifth chapter, we present the experiments that were achieved on parameter estimation. We first give an optical method to measure the sensitivity of an interferometer, and show that it coincides with the limit defined by quantum mechanics. We then use a multimode approach to measure the sensitivity of an interferometric and of a time-of-flight measurement. We also construct a detection mode that combines interferometric and time-of-flight measurements, and show that a time measurement performed with that specific mode is indeed more sensitive. Using again a multimode description, we measure the value of index dispersion of a material with a reasonable precision. Finally, we use a different laser source that generates multimode squeezed vacuum, and show an increase in sensitivity when the mode that is attached to the detection of a parameter is squeezed.

The third part of this thesis is about characterizing the noise of an ultrafast frequency comb. We use a homodyne based scheme that compares the noise of a laser source to a

reference whose noise figures are either known or negligible.

The sixth chapter is about generating a reference beam to characterize the fluctuations of another. Since we use the same laser source to build the reference, we use an optical cavity to filter the noise. We describe in this chapter the filtering of the noise with optical cavities, and also characterize their properties when injected by an optical frequency comb.

In the seventh chapter, we measure the spectral amplitude and phase noise of an optical frequency comb, as well as their spectral correlations. We show how the noise of different spectral components of the spectrum is distributed and the correlations that exist between them. We also measure the correlations between the amplitude and the phase fluctuations of the comb.

The fourth and last part of this thesis is about perspective on the next part of the experiment, which aims at generating multimode squeezed light.

In the eighth and last chapter of this thesis, we present the general principle to generate squeezed light with frequency combs. Based on parametric down conversion, we show the multimode structure of the quantum field that is generated and its potential applications. We present the work that started on the elaboration of a synchronously pumped optical parametric amplifier.

Part I

Measuring with ultra-fast frequency combs

1 The modes and states of a beam of light

"You're looking for an intership ? Check this guy out, N. Treps [...] he's very smart and does really great research, I reckon he will rise quickly in academia."
– Clément "*Lil' Hud*" Jacquard

Contents

1.1 The classical electromagnetic field . . . 10
1.1.1 Description of the real electromagnetic field . . . 10
1.1.2 Fourier space formalism . . . 11
1.2 Modal description . . . 13
1.2.1 Temporal and spectral modes . . . 13
1.2.2 Spatial modes . . . 14
1.2.3 Spatio-temporal modes . . . 16
1.2.4 Basis change . . . 17
1.2.5 Power and energy . . . 17
1.3 The quadratures of the classical field . . . 19
1.3.1 Quadrature amplitudes . . . 19
1.3.2 Quadrature fluctuations . . . 20
1.4 Quantization of the field . . . 21
1.4.1 Bosonic operators . . . 21
1.4.2 Modal decomposition . . . 21
1.4.3 Quadrature operators . . . 23
1.4.4 Relation to the classical field . . . 24
1.5 Quantum states . . . 25
1.5.1 Density operator . . . 25
1.5.2 Wigner function . . . 26
1.6 Gaussian states . . . 27
1.6.1 Definition and quantum covariance matrix . . . 27
1.6.2 Examples of Gaussian states . . . 27
1.6.2.1 Vacuum state . . . 27
1.6.2.2 Coherent state . . . 28
1.6.2.3 Squeezed state . . . 29
1.6.2.4 Entangled states . . . 30

The aim of this chapter is to develop most of the conventions and notations that are used throughout this thesis. We begin by describing the notion of modes of the classical electromagnetic field, a concept that is essential to the understanding of the remaining. This is done both for the longitudinal and transverse part of the field representing a beam of light. We then write the quantum description of light by quantifying the field, introducing the operators and states that will be relevant to this work.

1.1 The classical electromagnetic field

Light being a form of electromagnetic radiation, its description may be achieved by Maxwell's equations. Throughout this manuscript, every boldface symbol $\mathbf{X}$ denotes a vector in the cartesian basis, unless specified otherwise.

1.1.1 Description of the real electromagnetic field

We begin by writing the electric field $\mathbf{E}(\mathbf{r},t)$, which is a 3-dimensional vector that depends on the spatial variable $\mathbf{r}$ and the temporal variable t.
In order to keep this description general, we consider that the field propagates through a medium of free charge density ρ and of polarization density $\mathbf{P}$, neglecting the magnetic part. The electric field will induce on matter an electric response $\mathbf{D}$, called the electric flux density, which is defined as

$$\mathbf{D}(\mathbf{r},t) = \varepsilon_0 \mathbf{E}(\mathbf{r},t) + \mathbf{P}(\mathbf{r},t) \tag{1.1}$$

More generally, the relationship between the applied electric field $\mathbf{E}$ and the response $\mathbf{D}$ is established through the electric permittivity tensor $\boldsymbol{\varepsilon}_r$:

$$\mathbf{D}(\mathbf{r},t) = \varepsilon_0 [\boldsymbol{\varepsilon}_r] \mathbf{E}(\mathbf{r},t) \tag{1.2}$$

The physics behind the field-matter interaction is then contained within the $\boldsymbol{\varepsilon}_r$ tensor, which describes the anisotropy of the medium. Its definition will be particulary useful for the description of non-linear effects that will be outlined in chapter 8.

For now, we specialize to the case of propagation through a charge free $\rho = 0$, isotropic and linear medium. This involves that the relation between the induced polarization and the applied field is linear:

$$\mathbf{P}(\mathbf{r},t) = \varepsilon_0 \chi_e \mathbf{E}(\mathbf{r},t) \tag{1.3}$$

Under these conditions, the relation between the electric field and the response of the medium is simply given by

$$\mathbf{D}(\mathbf{r},t) = \varepsilon_0 \varepsilon \mathbf{E}(\mathbf{r},t) \qquad \text{with} \qquad \varepsilon = 1 + \chi_e \tag{1.4}$$

This lead to the definition of the index of refraction n, which is more commonly used in optics:

$$n = \sqrt{\varepsilon} \tag{1.5}$$

The familiar propagation equation that governs the spatial and temporal propagation of the electric field through a medium is:

$$\triangle \mathbf{E} = \frac{1}{v_\varphi^2} \frac{\partial^2 \mathbf{E}}{\partial t^2} \tag{1.6}$$

where $\triangle$ stands for the vectorial laplacian operator and $v_\varphi = c/n$ is the phase velocity, i.e. the speed of light in the medium (in the case of vacuum, we have naturally $v_\varphi = c$).

A standard solution to (1.6) is the plane-wave solution:

$$\mathbf{E}(\mathbf{r},t) = \mathrm{Re}\left\{\mathbf{E}_0 e^{i(\mathbf{k}\cdot\mathbf{r}-\omega t+\phi)}\right\} \tag{1.7}$$

where $\mathbf{E}_0$ is a constant vector, $\mathbf{k}$ is the propagation vector whose magnitude $k = \omega n/c$ satisfies the dispersion relation for a plane-wave of pulsation ω. In this expression, an arbitrary phase ϕ will be expanded in more detail in section 2.2.

1.1.2 Fourier space formalism

On many occasions in this manuscript, it will be convenient to look at the representation of the electric field in the frequency-domain, which we shall describe in this part.

In this work, we will adopt the symmetric definition of the Fourier transform. Although not necessary, it is convenient to use this prescription in quantum optics with continuous variables as the commutation relations for the bosonic operators $\hat{a}(t)$ and $\hat{a}(\omega)$ are then symmetric (see section 1.4.2).

For a function $f(t)$ defined in the temporal domain, we write the Fourier transform $\widetilde{f}(\omega)$ defined in the conjugated space as:

$$f(\omega) = \int_{\mathbb{R}} \frac{\mathrm{d}t}{\sqrt{2\pi}} f(t) e^{i\omega t} \equiv \mathscr{F}[f(t)] \tag{1.8}$$

Conversely, the inverse Fourier transform is then given by[1]:

$$f(t) = \int_{\mathbb{R}} \frac{\mathrm{d}\omega}{\sqrt{2\pi}} f(\omega) e^{-i\omega t} \equiv \mathscr{F}^{-1}[f(\omega)] \tag{1.9}$$

Applying this to the real electric field yield its Fourier decomposition

$$\mathbf{E}(\mathbf{r},t) = \int_{\mathbb{R}} \frac{\mathrm{d}\omega}{\sqrt{2\pi}} \mathbf{E}(\mathbf{r},\omega)\, e^{-i\omega t} \tag{1.10}$$

Since $\mathbf{E}(t)$ is a real quantity, it follows that

$$[\mathbf{E}(\mathbf{r},\omega)]^* = \mathbf{E}(\mathbf{r},-\omega) \tag{1.11}$$

This definition of $\mathbf{E}(\omega)$ therefore contains some redundancy, which leads to the introduction of the analytic electric field $\mathbf{E}^{(+)}(\mathbf{r},t)$ where the negative frequencies are removed from the Fourier decomposition:

$$\mathbf{E}^{(+)}(\mathbf{r},t) = \int_{\mathbb{R}^+} \frac{\mathrm{d}\omega}{\sqrt{2\pi}} \mathbf{E}(\mathbf{r},\omega)\, e^{-i\omega t} \tag{1.12}$$

It is worth stressing that this quantity is now complex, so that the real field is defined by the relation

$$\mathbf{E}(\mathbf{r},t) = \mathbf{E}^{(+)}(\mathbf{r},t) + \mathbf{E}^{(-)}(\mathbf{r},t) \tag{1.13}$$

where $\mathbf{E}^{(-)}(\mathbf{r},t) = \left[\mathbf{E}^{(+)}(\mathbf{r},t)\right]^*$ corresponds to the integration over the negative frequencies.

Equivalently, one may define an analytic signal in the frequency domain by taking the Fourier transform of the temporal analytic signal:

$$\mathbf{E}^{(+)}(\mathbf{r},\omega) = \int_{\mathbb{R}} \frac{\mathrm{d}t}{\sqrt{2\pi}} \mathbf{E}^{(+)}(\mathbf{r},t)\, e^{i\omega t} \tag{1.14}$$

It follows that

$$\mathbf{E}(\mathbf{r},\omega) = \mathbf{E}^{(+)}(\mathbf{r},\omega) + \mathbf{E}^{(-)}(\mathbf{r},-\omega) \tag{1.15}$$

where $\mathbf{E}^{(-)}(\mathbf{r},\omega) = \left[\mathbf{E}^{(+)}(\mathbf{r},\omega)\right]^*$.

[1] For a better readability, we use the same notation to denote a function f in the real and in the Fourier domain.

1.2 Modal description

As introduced by equation (1.7), plane-waves satisfying the dispersion relation form a basis on which the field can be expanded. More generally, it may be expanded on any set of normalized modes, either spatial, temporal, or spatiotemporal, as long as they satisfy Maxwell's equations.

In this section, we show how to describe the electric field with modes in the longitudinal and transverse plane. We enclose the system in a box of volume V and of section S.

1.2.1 Temporal and spectral modes

A decomposition of the field in plane-waves may be achieved by expanding the analytic field (1.12) in spatial Fourier components, as it is done in [Grynberg 10]. The field is then written as

$$\mathbf{E}^{(+)}(\mathbf{r},t) = i\sum_{\ell} \mathscr{E}_\ell\, a_\ell\, \boldsymbol{\varepsilon}_\ell\, e^{i(\mathbf{k}_\ell\cdot\mathbf{r}-\omega_\ell t)} \tag{1.16}$$

where $\boldsymbol{\varepsilon}_\ell$ is the polarization of the component ℓ, $\mathbf{k}_\ell$ its wavevector, a_ℓ is the normal variable which corresponds to the complex amplitude of the component ℓ, and $\mathscr{E}_\ell$ is a normalization constant given by

$$\mathscr{E}_\ell = \sqrt{\frac{\hbar\omega_\ell}{2nc\varepsilon_0 V}} \tag{1.17}$$

This is called the normal mode decomposition and each mode of the basis is an independent monochromatic polarized wave. This definition of the field is very convenient when quantifying it, but for the scope of this thesis, we will rather decompose a light beam on a basis of envelope modes.

For the remaining of this manuscript, we will consider the field only in a given linear polarization, $\boldsymbol{E}$ is then reduced to a scalar. We also consider that the frequency spectrum in (1.16) is narrow and centered around ω_0, allowing the constant to be taken out of the sum $\mathscr{E}_\ell \simeq \mathscr{E}_0$. Finally, we rewrite (1.16) as a decomposition of envelope modes $u(t)$ relative to the carrier frequency:

$$\boxed{E^{(+)}(\mathbf{r},t) = \mathscr{E}_0 \sum_{\ell} a_\ell\, u_\ell(t) e^{i(\mathbf{k}\cdot\mathbf{r}-\omega_0 t)}} \tag{1.18}$$

where $\{u_\ell(t)\}$ is a set of orthonormal modes that satisfy the general condition (1.31) and a_ℓ is the complex amplitude of the field. We've also incorporated the imaginary unit

i in the mode u_ℓ, since these can always be defined up to a constant phase factor. It will sometimes be convenient to write the field as $\boldsymbol{E}^{(+)}(\mathbf{r},t) = \mathscr{E}_0 a(t) e^{i(\mathbf{k}\cdot\mathbf{r}-\omega_0 t)}$ where $a(t) \equiv \sum_\ell \alpha_\ell u_\ell(t)$ is the envelope of the field.

By taking the Fourier transform of (1.18), one may also define a spectral mode, or frequency mode:

$$\boxed{\boldsymbol{E}^{(+)}(\mathbf{r},\omega) = \mathscr{E}_0 \sum_\ell \alpha_\ell u_\ell(\omega-\omega_0) e^{i\mathbf{k}\cdot\mathbf{r}}} \tag{1.19}$$

with $u(\omega-\omega_0) = u(\Omega) = \mathscr{F}[u(t)]$ and $\Omega = \omega - \omega_0$ is the frequency relative to the optical carrier.

These temporal - or spectral - modes will be the main center of focus throughout this thesis. Their definition is very general at this point since the modes $\{u_\ell\}$ needs only to satisfy Maxwell's equation as well as the normalization and orthogonality conditions (1.31). However, in section 2.1.4, we will revise this spectro-temporal modes concept by applying it to the case of ultrashort laser pulses. In particular, we will use whenever possible the gaussian profile for the spectral and temporal envelopes, as every calculation will have an analytical solution in this case.

1.2.2 Spatial modes

The previous treatment only deals with plane waves whose wavefront is infinite. However, in practice, actual laser beams have a finite transverse extent and may not be considered as true plane waves.
Fortunately, in the present case, we may consider the laser beams as paraxial, meaning that they are made up of a superposition of plane waves with propagation vectors close to a single direction. This also implies that the field's variations in the transverse plane are much slower than in the longitudinal dimension.

We choose the propagation direction as z, and the transverse direction as the (x,y) plane where we define a unitary vector $\boldsymbol{\rho}$. Therefore, the position vector is written as $\mathbf{r} = (\boldsymbol{\rho}, z)$. A more complete description of the paraxial beams and the transverse structure of laser field may be found in [Yariv 67] or [Siegman 86].

We consider a monochromatic paraxial wave written as

$$\boldsymbol{E}^{(+)}(\mathbf{r},t) = \boldsymbol{E}_0 g(\mathbf{r}) e^{i(kz-\omega_0 t)} \tag{1.20}$$

where $\boldsymbol{E}_0 = \mathscr{E}_0 \alpha$ encompasses the field amplitude, k satisfies the dispersion relation and g is a slowly varying envelope in the longitudinal direction. Mathematically, this condition is written $\left|\partial_z^2 g\right| \ll 2k\left|\partial_z g\right|$ and allows to the neglect second order derivatives of g with respect to z.

Injecting the expression (1.20) into the propagation equation (1.6) under this approximation leads to the following paraxial wave equation

$$\triangle_{\boldsymbol{\rho}} g - 2ik\frac{\partial g}{\partial z} = 0 \tag{1.21}$$

where $\triangle_{\boldsymbol{\rho}} = \partial_x^2 + \partial_y^2$ is the laplacian operator in the transverse plane.
This equation has gaussian solutions that provide a good description of the laser beams that we are used to work with. In particular, the entire family of transverse electromagnetic mode (TEM) prove very useful as they correspond to the spatial eigenmodes of a laser cavity. The expression for the lowest order mode is written as follows:

$$g_{00}(x,y,z) = \frac{w_0}{w(z)} e^{-\rho^2/w^2(z)} e^{-ik\rho^2/2R(z)} e^{i\phi(z)} \tag{1.22}$$

where we defined the quantities

$$w^2(z) = w_0^2\left[1 + \left(\frac{z}{z_R}\right)\right] \tag{1.23}$$

$$\frac{1}{R(z)} = \frac{z}{z^2 + z_R^2} \tag{1.24}$$

$$\phi(z) = \arctan\left(\frac{z}{z_R}\right) \tag{1.25}$$

$$z_R = \frac{\pi w_0^2 n}{\lambda} \tag{1.26}$$

This describes a gaussian beam centered at $z = 0$ with a radius w_0 called waist (measured at $1/e$). The beam width variation is defined by $w(z)$. The confocal parameter or depth of focus $b = 2z_R$ is the length over which the radius is less than $\sqrt{2}\omega_0$. The geometry of the wavefront is given by the radius of curvature $R(z)$ and $\phi(z)$ is called the Gouy phase.

Higher order modes of the TEM_{mn} family are obtained by adding Hermite polynomials variation to the solution. The resulting modes then read

$$g_{mn}(x,y,z) = \frac{C_{nm}}{w(z)} H_m\left(\frac{\sqrt{2}x}{w(z)}\right) H_n\left(\frac{\sqrt{2}y}{w(z)}\right) e^{-\rho^2/w^2(z)} e^{-ik\rho^2/2R(z)} e^{i(m+n+1)\phi(z)} \tag{1.27}$$

where $C_{nm} = 1/\sqrt{\pi 2^{n+m+1} n! m!}$ ensures a proper normalization of the mode.

To show the effects that will be of interest to us in this thesis, we shall reduce the dimensions of the Hermite Gauss modes by constraining them to the x axis. We write our new basis as $\{g_n(x,z)\}$. It is linked to the two-dimensional modes (1.27) by assuming a fundamental profile over the y direction and integrating it out:

$$g_n(x,z) = \int_{\mathbb{R}} \mathrm{d}y\, g_{n0}(x,y,z) \tag{1.28}$$

The exact expression of the resulting modes, which may be found in [Delaubert 07], is not relevant to the scope of this thesis, as we shall only use their orthogonality properties.

1.2.3 Spatio-temporal modes

The previous definitions in the transverse and longitudinal domains are quite convenient, since they may be combined in a straightforward manner to build a new set of modes. This provides a complete model description of the electric field.

Under the previous descriptions and approximations, a linearly polarized electric field may be expanded on the basis of temporal $u_i(t)$ and spatial modes $v_n(x,z)$ as:

$$\boldsymbol{E}^{(+)}(x,z,t) = \mathscr{E}_0 \sum_{i,n} \alpha_{i,n} u_i(t) g_n(x,z) e^{i(kz-\omega_0 t)} \tag{1.29}$$

Alternatively, we are also able to define a new basis of modes $w_{i,n}(x,z,t)$ that encompasses every combination of the longitudinal and transverse modes:

$$w_{i,n}(x,z,t) = u_i(t) g_n(x,z) \tag{1.30}$$

Note that the spatial and temporal parts are factorized in w, which assumes no space-time coupling. This is a very reasonable assumption for the present work, where the light beam is in a well-defined spatial mode. At any position z and over a detection time T, these form an orthonormal set; introducing the standard L^2 inner product $\langle\cdot,\cdot\rangle$, it reads

$$\boxed{\left\langle w_{i,m}, w_{j,n} \right\rangle \equiv \int_T c\,\mathrm{d}t \iint_S \mathrm{d}^2\boldsymbol{\rho}\, w^*_{i,m}\, w_{j,n} = S c T\, \delta_{ij}\delta_{mn}} \tag{1.31}$$

1.2.4 Basis change

The modes that we chose, being the temporal $u(t)$ or spatial $v(x,z)$ modes, are not unique; the field may be expanded on any other basis. As an example, if we consider another temporal basis $\{v_i(t)\}$ of the field, the change from $\{u_i(t)\}$ to $\{v_i(t)\}$ is achieved by a unitary transform $\mathbf{U}$ defined by

$$\mathbf{U}_{ij} = \langle u_i(t), v_j(t) \rangle \equiv \int_T c \, \mathrm{d}t \, u_i^*(t) \, v_j(t) \tag{1.32}$$

which allows to write the change of basis as

$$v_j(t) = \sum_i \mathbf{U}_{ij} \, u_i(t) \tag{1.33}$$

1.2.5 Power and energy

Finally, we define some of the physical quantities related to the energy and the power contained in the field. These are important quantities since that are quite easy to access experimentally.

To lighten the notations , we write the complex field as

$$E^{(+)}(x,z,t) = \mathscr{E}_0 \, a(x,z,t) e^{-i\omega_0 t} \tag{1.34}$$

where $a(x,z,t) = \sum_{i,j} \alpha_{i,j} \, u_i(t) g_j(x,z)$ is the envelope of the field, proportional to the square root of the number of photons.

The energy density v (in J/m^3) contained in the electromagnetic field [Yariv 67] is given by

$$v = \frac{1}{2} \varepsilon_0 \left(E^2 + c^2 B^2 \right) \tag{1.35}$$

In term of the complex field, the energy density may be written as[2]

$$v(x,z,t) = 2\varepsilon_0 \left| E^{(+)}(x,z,t) \right|^2 \tag{1.36}$$

The energy W contained in the field is therefore equal to the integral of the energy density over the volume $V = ScT$ delimited by a section S and a detection time T. The index dependency comes from the fact that the light actually travels through the medium

[2] The "energy" in the real field is twice the one contained in the complex field $E^2 = 2\left|E^{(+)}\right|^2$, and since for plane waves, $B^2 = E^2/c^2$, the energy density as a function of the complex field is consequently written as (1.36).

an optical length dependent on the index n. Using the normalization condition (1.31) and the field constant (1.17), the energy reads

$$W = 2\varepsilon_0 n \mathscr{E}_0^2 \int_V \mathrm{d}V \, |a(x,z,t)|^2 = N\hbar\omega_0 \tag{1.37}$$

where N is the number of photon in the field over a time T. For temporal modes that are bounded, as it is the case for pulses of light, this integration time T allows to define specific quantities (see section 2.1.2).

The instantaneous intensity of the field (in J/s/cm^2) is then given by

$$I(x,z,t) = 2\varepsilon_0 n c \left| E^{(+)}(x,z,t) \right|^2 \tag{1.38}$$

For pulses, we are often interested in the integrated intensity or fluence F:

$$F(x,z) = \int_T I(x,z,t) \, \mathrm{d}t \tag{1.39}$$

Alternatively, we may define the power by integrating the intensity (1.38) over transverse coordinates:

$$P(z,t) = \int_S I(x,z,t) \, \mathrm{d}^2\boldsymbol{\rho} \tag{1.40}$$

The energy contained in the field may therefore be obtained by integrating either the power or the fluence on the proper variables:

$$W = \int_S F(x,z) \, \mathrm{d}^2\boldsymbol{\rho} \equiv \int_T P(z,t) \, \mathrm{d}t \tag{1.41}$$

Because of the dependency between the t and z variables, the integral over t cancels the longitudinal component of these quantities. Another useful quantity is the power that is obtained experimentally using a bolometer. These instruments measure power through heating, and are therefore incapable of resolving the power in a single pulse[3]. The result of such a measurement is the power averaged over a second P_{avg} (in W).

Note that all the previously defined quantities translate very well to the spectral domain, thanks to the symmetric Fourier transform defined in section 1.1.2. Using indeed this prescription, the Parseval theorem reads

$$\int_{\mathbb{R}} \mathrm{d}\Omega \left| E^{(+)}(\Omega) \right|^2 = \int_{\mathbb{R}} \mathrm{d}t \left| E^{(+)}(t) \right|^2 \tag{1.42}$$

[3] For relatively long pulses, a calibrated photodiode can resolve a single pulse. For pulses shorter than picosecond timescale, this method is no longer valid because of the slow response of the electronics.

meaning of course that computing the energy-related quantities in both spaces yields equivalent results.

1.3 The quadratures of the classical field

In section 1.2, we've seen that we can write the field in a particular spatio-temporal mode as the product of a slowly varying envelope and a phase factor that reflect the wave-like nature of light. In the following parts, it will be useful to break this phase factor into an absolute phase and the wave front curvature part. This leads to the introduction of the field quadratures [Bachor 04].

1.3.1 Quadrature amplitudes

Using the previous notations, we write the real electric field in the spatio-temporal modes basis $\{w_{i,n}(x,z,t)\}$ as

$$E(x,z,t) = \mathscr{E}_0 \sum_{i,n} \alpha_{i,n}\, w_{i,n}(x,z,t)\, e^{i(kz-\omega_0 t)} + \text{c.c.} \equiv \mathscr{E}_0\, a(x,z,t)\, e^{-i\omega_0 t} + \text{c.c.} \tag{1.43}$$

where c.c. stands for conjugated complex, and where we merged the spatial propagation with the envelope to form the complex amplitudes $a(x,z,t) = \sum_{i,n} \alpha_{i,n}\, w_{i,n}(x,z,t)\, e^{ikz}$. An equivalent form of this notation is given in terms of the quadrature amplitudes X and P associated to the sine and cosine waves:

$$E(x,z,t) = \mathscr{E}_0 \left[X(x,z,t)\cos(\omega_0 t) + P(x,z,t)\sin(\omega_0 t)\right] \tag{1.44}$$

The quadratures of the field are proportional to the real and imaginary part of the complex amplitude:

$$X(x,z,t) = a(x,z,t) + a^*(x,z,t) \tag{1.45}$$

$$P(x,z,t) = i\Big(a^*(x,z,t) - a(x,z,t)\Big) \tag{1.46}$$

This notation is convenient for describing the interaction between two fields (and also to quantify the electric field, see section 1.4). A common representation of the classical field decomposed on its quadratures is called the *Fresnel diagram*, or *phase space representation*.

In this diagram, the field is represented at a single point of space and time as a vector of magnitude $|a|$ making an angle $\phi = \arctan(P/X)$ with the X axis as outlined on figure 1.1a. In the case of interferences, the total field is sketched as the vectorial sum between the two individual fields. This helps to visualize on which quadrature lies the resulting field, as it is showed on figure 1.1b.

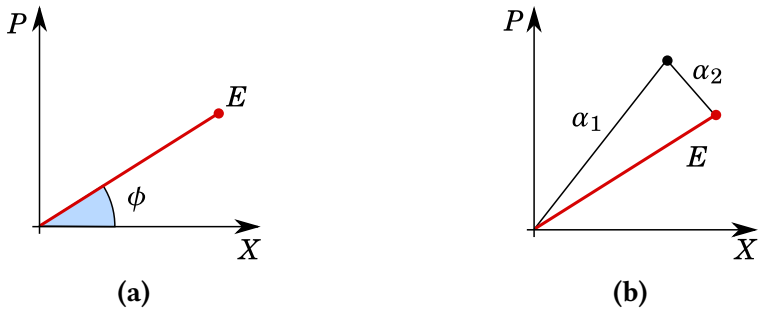

Figure 1.1: Phase space diagram of a single electric field $\boldsymbol{E}$ (a) and of the interference between two fields (b).

1.3.2 Quadrature fluctuations

Another elegant application of the field quadrature is when the wave has fluctuations in both amplitude and phase.

Consider a variation of the envelope in equation (1.44) (this means that the carrier remains unaffected). The fluctuations of $\boldsymbol{E}$ then read

$$\delta E(x,z,t) = \mathscr{E}_0\Big(\delta X(x,z,t)\cos(\omega_0 t) + i\delta P(x,z,t)\sin(\omega_0 t)\Big) \tag{1.47}$$

The fluctuations of the field quadratures δX and δP may then easily be linked to the fluctuations in amplitude and phase. Indeed, for the simplest expression of an electric field $\boldsymbol{E} = \mathscr{E}_0\,\alpha e^{i\varphi} + \text{c.c.}$, a fluctuation in both amplitude $\delta\alpha$ and phase $\delta\varphi$ leads to the following first order expansion:

$$\begin{aligned}\delta E &\approx \mathscr{E}_0\left(\delta\alpha\, e^{i\varphi} + i\alpha\,\delta\varphi\, e^{i\varphi}\right) + \text{c.c.} \\ &= 2\mathscr{E}_0\left(\delta X\cos\varphi + \delta P\sin\varphi\right)\end{aligned} \tag{1.48}$$

This description is again very relevant to the scope of this thesis, as the variations in amplitude δX and phase δP are easily accessible by usual measurements methods. From this point, we shall call respectively X and P the amplitude and phase quadratures of the electric field[4].

[4]Note that δP is actually proportional to the amplitude A of the field. As we will see in chapter 3, one does not exactly measure the phase of the field, but rather the phase as being "imprinted" on the amplitude.

1.4 Quantization of the field

In order to explore the ultimate limits in sensitivity when measuring with light, we need a quantum description of the electric field. The standard way to quantify the field is by identifying the field quadratures X and P as canonical variables in the sense of Hamiltonian mechanics, analogous to the quantification of a collection of harmonic oscillators. This allows to associate hermitian operators $\hat{X}$ and $\hat{P}$ which satisfy canonical commutation relations. The full treatment can be found in [Grynberg 10].

1.4.1 Bosonic operators

This begins by associating to the normal modes α_ℓ of (1.16) an operator $\hat{a}_\ell$. We impose these operators the canonical commutation relation, and we also impose a zero commutation for operators corresponding to different modes, since they are decoupled by construction:

$$\left[\hat{a}_\ell, \hat{a}_k^\dagger\right] = \delta_{\ell k} \tag{1.49}$$

$$[\hat{a}_\ell, \hat{a}_k] = 0 \tag{1.50}$$

The bosonic operators $\hat{a}_\ell$ and $\hat{a}_\ell^\dagger$ are called respectively *annihilation* and *creation* operators since they destroy or create a photon in the mode ℓ. This is again entirely similar to the harmonic oscillator where an excitation is represented by a photon.

It follows that we can define a real quantum electric field from the quantification of (1.13):

$$\hat{\mathbf{E}}(\mathbf{r},t) = \hat{\mathbf{E}}^{(+)}(\mathbf{r},t) + \hat{\mathbf{E}}^{(-)}(\mathbf{r},t) \tag{1.51}$$

where the quantum analytic field in the Heisenberg representation is given by

$$\boxed{\hat{\mathbf{E}}^{(+)}(\mathbf{r},t) = i\sum_\ell \mathscr{E}_\ell\, \hat{a}_\ell\, \boldsymbol{\varepsilon}_\ell\, e^{i(\mathbf{k}_\ell\cdot\mathbf{r}-\omega_\ell t)}} \tag{1.52}$$

1.4.2 Modal decomposition

In analogy to the classical treatment of 1.2, it is also possible to expand the quantum field on any basis of monochromatic modes $w_i(x,z,t)$ that still allow to diagonalize the energy of the system. Using the same considerations that were used to derive equation (1.18), we can write

$$\boxed{\hat{E}^{(+)}(x,z,t) = \mathscr{E}_0 \sum_i \hat{a}_i\, w_i(x,z,t)} \tag{1.53}$$

where $\mathscr{E}_0$ is also defined by (1.17).

The commutation relations (1.49) and (1.50) remain valid for the bosonic operator in the mode $\{w_i(x,z,t)\}$. In particular, considering that the field is in a well defined spatial mode $g_0(x,z)$, an even more concise notation may be obtained by considering the continuous mode annihilation operator [Loudon 00] $\hat{a}(x,z,t) = \hat{a}(t)g_0(x,z)$, allowing to write the commutation relations as

$$\left[\hat{a}(t), \hat{a}^\dagger(t')\right] = \delta(t-t') \tag{1.54}$$

$$\left[\hat{a}(t), \hat{a}(t')\right] = 0 \tag{1.55}$$

The Fourier transform formalism introduced in section 1.1.2 then allows to define the annihilation operator in the frequency domain $\hat{a}_\ell(\Omega)$ where the commutation relation is written the same way[5]:

$$\left[\hat{a}(\Omega), \hat{a}^\dagger(\Omega')\right] = \delta(\Omega-\Omega') \tag{1.56}$$

$$\left[\hat{a}(\Omega), \hat{a}(\Omega')\right] = 0 \tag{1.57}$$

The energy of the quantized system is given by the Hamiltonian that sums the contribution of every mode i:

$$\begin{aligned}\hat{H} &= \hbar\omega_0 \int_T \left(\hat{a}^\dagger(t)\hat{a}(t) + \frac{1}{2}\right) \\ &= \hbar\omega_0 \sum_i \left(\hat{a}_i^\dagger \hat{a}_i + \frac{1}{2}\right) \equiv \hbar\omega_0 \sum_i \left(\hat{N}_i + \frac{1}{2}\right)\end{aligned} \tag{1.58}$$

where $\hat{N}_i \equiv \hat{a}_i^\dagger \hat{a}_i$ is the operator for photon number in the mode i.

The continuous annihilation operator $\hat{a}(\Omega)$ may be decomposed as

$$\boxed{\hat{a}(\Omega) = \sum_i \hat{a}_i\, u_i(\Omega)} \tag{1.59}$$

The eigenstates of the Hamiltonian are the photon number states, or *Fock states*, $|N_1,\ldots,N_i,\ldots\rangle$ where N_i is the number of photons in the mode i. The bosonic operators action on the Fock states is mode dependent:

$$\hat{a}_i\,|n_1,\ldots,n_i,\ldots\rangle = \sqrt{n_i}\,|n_1,\ldots,n_i-1,\ldots\rangle \tag{1.60}$$

$$\hat{a}_i^\dagger\,|n_1,\ldots,n_i,\ldots\rangle = \sqrt{n_i+1}\,|n_1,\ldots,n_i+1,\ldots\rangle \tag{1.61}$$

[5] The non-symmetric definition of the Fourier transform would leave a factor 2π in the commutator.

A change of basis from $\{w_i(x,z,t)\}$ to $\{v_j(x,z,t)\}$ is done in a similar way as in the classical part 1.2.4 by associating another bosonic operator $\hat{b}_j$ to the new mode $v_j(x,z,t)$:

$$\hat{E}^{(+)}(x,z,t) = i\mathscr{E}_0 \sum_i \hat{b}_j v_j(x,z,t) \tag{1.62}$$

such that, for $\widetilde{w}_j$ defined as (1.33) with a unitary basis change matrix $\mathbf{U}$, the new bosonic operators write as :

$$\hat{b}_i^\dagger = \sum_i \mathbf{U}_{ij} a_i^\dagger \tag{1.63}$$

$$\hat{b}_i = \sum_i \left(\mathbf{U}^{-1}\right)_{ij} a_i \tag{1.64}$$

1.4.3 Quadrature operators

In quantum information, the Fock states are particularly interesting since they allow to picture photons as a natural representation of qubits. They also exhibit interesting quantum behavior for many applications in quantum optics [Kimble 77]. This regime is called the *discrete variable (DV) regime*.

In our case, we are more interested in a regime where we have a high photon flux since it leads to higher sensitivity in our measurement (see 4.1.2). We then classical a classical field of macroscopic energy and we picture the quantum effects as fluctuations in the light wave. This high photon number regime, also called the *continuous variable (CV) regime* is getting more and more used in the quantum optics community [Lloyd 99, Furusawa 11], as well as the hybrid regime that couples both the discrete and continuous description of the light [Morin 14, Jeong 14].

The standard approach in CV consists in assigning a bosonic operator $\hat{a}_i$ to a classical wave amplitude α_i such that $\alpha_i = \langle \hat{a}_i \rangle$. The quantum fluctuations $\delta\hat{a}_i$ of the quantum field are then written as

$$\delta\hat{a}_i = \hat{a}_i - \langle \hat{a}_i \rangle \tag{1.65}$$

where there is an implicit identity operator $\hat{\mathbb{1}}$ hidden after the expectation value of $\hat{a}_i$. In this thesis, we make use of the *semi-classical approximation* [Reynaud 92] that neglects any higher order term in $\delta\hat{a}$.

The bosonic operators are not hermitian, so they do not correspond to an observable and may not be measured. However, their real and imaginary parts are hermitian and correspond to the exact quantum counterpart of the field quadratures defined in (1.45) and (1.46):

$$\hat{x}_i = \hat{a}_i + \hat{a}_i^\dagger \tag{1.66}$$

$$\hat{p}_i = i\left(\hat{a}_i^\dagger - \hat{a}_i\right) \tag{1.67}$$

From (1.49) and (1.50), the commutator for the quadrature operators $\hat{x}_i$ and $\hat{p}_i$ is given by:

$$\left[\hat{x}_i\,,\hat{p}_j\right] = 2i\delta_{ij} \tag{1.68}$$
$$\left[\hat{x}_i\,,\hat{x}_j\right] = \left[\hat{p}_i\,,\hat{p}_j\right] = 0 \tag{1.69}$$

These conjugation relations allow to write the following Heisenberg inequality:

$$\sigma^2_{\hat{x}_i}\,\sigma^2_{\hat{p}_i} \geq 1 \tag{1.70}$$

where $\sigma_{\hat{O}} \equiv \left\langle \delta\hat{O}^2 \right\rangle$ is the variance of operator $\hat{O}$. Finally, we can define an arbitrary quadrature operator $\hat{q}_i^{\phi}$ at a ϕ angle in phase space:

$$\hat{q}_i^{\phi} = \hat{a}_i^{\dagger}\, e^{i\phi} + \hat{a}_i\, e^{-i\phi} \tag{1.71}$$

Using this notation, the amplitude (1.66) and phase (1.67) operators are dephased by $\pi/2$. For states that contain n-modes, the quadrature operators $\{\hat{x}_i\}$ and $\{\hat{p}_i\}$ are represented as vectorial operators of n components $\hat{\mathbf{x}}$ and $\hat{\mathbf{p}}$. It is also convenient to define a full quadratures vector of $2n$ components $\hat{\mathbf{X}} = (\hat{x}_1,\ldots,\hat{x}_n,\hat{p}_1,\ldots,\hat{p}_n)^{\intercal}$.

1.4.4 Relation to the classical field

In experimental quantum optics, it is quite convenient to be able to relate the quantum field (1.53) to the classical field (1.18). This allows to define what observable is being measured.

The expectation value of the electric field (1.53) is written as

$$\left\langle \hat{E}^{(+)}(x,z,t) \right\rangle = \mathscr{E}_0 \sum_i \langle \hat{a}_i \rangle\, w_i(x,z,t) \tag{1.72}$$

For single-mode Gaussian states (cf. section 1.6.2.2), it is always possible to find a basis of modes $\{v_i(x,z,t)\}$ where only the first mode $n=0$ is non-vacuum. This implies that

$$\langle \hat{a}_0 \rangle = \sqrt{N} \tag{1.73}$$

where N is the number of photons contained in the field. Using the definition of the quadrature operators (1.66) and (1.67), the annihilation operator can be written in term of observables:

$$\hat{a}_i = \frac{\hat{x}_i + i\,\hat{p}_i}{2} \tag{1.74}$$

Thus, the quantum electric field is written in term of amplitude and phase observables:

$$\hat{E}^{(+)}(x,z,t) = \mathscr{E}_0 \sum_i \frac{\hat{x}_i + i\hat{p}_i}{2} v_i(x,z,t) \tag{1.75}$$

For classical light, computing the expectation value of (1.75) should be equivalent to measuring the classical field (1.18). This defines the important relation:

$$\boxed{\langle \hat{x} \rangle = 2\,\mathrm{Re}\left\{E^{(+)}\right\}} \tag{1.76}$$

The expectation value of the quadrature amplitude of the quantum field is exactly equal to twice the real part of the complex classical field[6].

1.5 Quantum states

We introduce in this section the quantum states of interest in the continuous variable regime. For a more detailed description of the subject, [Braunstein 05] provides with a thorough review.

1.5.1 Density operator

Usually a quantum system is represented by a single state vector $|\psi\rangle$, called *pure state*. It is however not sufficient to describe a realistic system; the influence of the environment or fluctuations of various origin will degrade the purity of the state and lead to a statistical mixture of pure states, or *mixed state*. These may no longer be represented as single state vectors. A standard way of representing mixed states is by the density matrix or density operator $\hat{\rho}$, defined by

$$\boxed{\hat{\rho} = \sum_i c_i \, |\psi_i\rangle\langle\psi_i|} \tag{1.77}$$

where the c_i coefficients are the statistical weight of the pure state $|\psi_i\rangle$. The density matrix satisfies the condition $\mathrm{Tr}\left[\hat{\rho}\right] = 1$.

The purity P of the state can be deduced from the density matrix by

$$P = \mathrm{Tr}\left[\hat{\rho}^2\right] \tag{1.78}$$

For a pure state, $P = 1$; otherwise, $0 < P < 1$ for a mixed state.

[6] Obviously integrated over a finite spatial and temporal window.

The density matrix is a general tool that is especially convenient when describing mixed states in the discrete variable regime, as it may be expanded on the Fock states basis. However its usage in the continuous variables regime, where the number of photons and of modes increases, is more problematic, since it contains an infinite number of elements. Therefore, in this regime, it is more proper to make use of a representation in quadratures, which is a natural representation of continuous variables. It is outlined in the next section as the Wigner function, or Wigner distribution.

1.5.2 Wigner function

The Wigner function corresponds to another representation of the field in terms of quadratures. For a n-mode state, it may be written on the phase space of the outcomes of $\hat{\mathbf{x}}, \hat{\mathbf{p}}$ as [Schleich 11]:

$$W(\mathbf{x},\mathbf{p}) = \frac{1}{(2\pi)^n} \int \mathrm{d}^n\boldsymbol{\mu}\, \mathrm{d}^n\boldsymbol{\nu}\, \mathrm{Tr}\left[\hat{\rho}\, e^{-i(\hat{\mathbf{x}}\cdot\boldsymbol{\mu}+\hat{\mathbf{p}}\cdot\boldsymbol{\nu})}\right] e^{i(\mathbf{x}\cdot\boldsymbol{\mu}+\mathbf{p}\cdot\boldsymbol{\nu})} \tag{1.79}$$

This representation should ideally show the probability of measuring the outcome $\mathbf{x}$ and $\mathbf{p}$ of a measurement on $\hat{\mathbf{x}}$ and $\hat{\mathbf{p}}$. However, it is clear from (1.68) that these operators do not commute, therefore such a probability distribution cannot exist. The Wigner function W is a quasi-probability distribution such that the projection of W on any quadrature $\hat{x}_i^\phi$ corresponds to the marginal probability distribution of the outcome q_i^ϕ of the measurement. Like a probability distribution, the integral over all quadratures is equal to 1:

$$\int \mathrm{d}^n\mathbf{x}\, \mathrm{d}^n\mathbf{p} W(\mathbf{x},\mathbf{p}) = 1 \tag{1.80}$$

and the integral over all but one quadrature yields the probability to measure it; for example, by writing $\mathbf{p}^\phi = \mathbf{q}^{\phi+\pi/2}$ the orthogonal quadrature to $\mathbf{q}^\phi$, the probability to measure $\mathbf{q}^\phi$ is given by projecting the Wigner function:

$$P_\phi(\mathbf{q}^\phi) = \int W(\mathbf{q}^\phi,\mathbf{p}^\phi)\mathrm{d}^n\mathbf{p}^\phi \tag{1.81}$$

However, this distribution can be negative, hence the name of quasi-probability distribution. For more details on the Wigner function, see [Ourjoumtsev 07].
The Wigner function is a good tool to describe quantum states in term of the phase space variables, and many of the states relevant to continuous variables quantum optics may be represented through this function. It is worth stressing that the negativity of the Wigner function is not a necessary criterion do describe the "quantumness" of the state. Some states will exhibit highly non-classical behaviors such as entanglement and nonlocality, yet their Wigner function are positive. The most common belong to the class of Gaussian states that will be expanded in the following section.

1.6 Gaussian states

1.6.1 Definition and quantum covariance matrix

Simply put, *gaussian states* correspond to states whose Wigner function is Gaussian. They are efficiently producible in a laboratory and available on demand. As an example, the ground state of the Hamiltonian, or *vacuum state*, is Gaussian. Moreover, most operations we can apply on gaussian states of light preserves their Gaussian characteristics.

The most general form for a Gaussian Wigner distribution can be formulated as [Ferraro 05] :

$$W(\mathbf{X}) = \frac{1}{(2\pi)^n \sqrt{\det \mathbf{\Gamma}}} \exp\left[-\frac{1}{2}\left(\mathbf{X} - \langle \hat{\mathbf{X}} \rangle\right)^{\intercal} \mathbf{\Gamma}^{-1} \left(\mathbf{X} - \langle \hat{\mathbf{X}} \rangle\right)\right] \tag{1.82}$$

where $\langle \hat{\mathbf{X}} \rangle$ is the expectation value vector of the quadratures and $\mathbf{\Gamma}$ is the *symmetrized covariance matrix* which elements are defined the following way:

$$[\mathbf{\Gamma}]_{ij} \equiv \Gamma_{ij} = \frac{1}{2}\left\langle \{\hat{X}_i, \hat{X}_j\} - \langle \hat{X}_i \rangle \langle \hat{X}_j \rangle \right\rangle \tag{1.83}$$

where $\{\cdot, \cdot\}$ denotes the anti-commutator. By definition (and as for its classical counterpart, see section 7.2.1), the covariance matrix is a real, positive and semi-definite matrix which allows the spectral theorem to apply (this will be of great importance to us later on). The diagonal elements of this $2n \times 2n$ matrix correspond to the individual variance of each quadratures for every modes, and the off-diagonal represent correlations between those modes and quadratures. For our purposes, it contains all the information on the gaussian state that is considered.

Finally, the purity of the state in term of the covariance matrix is given by

$$P = \frac{1}{\sqrt{\det \mathbf{\Gamma}}} \tag{1.84}$$

1.6.2 Examples of Gaussian states

1.6.2.1 Vacuum state

The ground state of the radiation field is the state with zero photons $|0\rangle = |N_1 = 0, \ldots, N_n = 0\rangle$ in every modes. It is called a *vacuum state*. The covariance matrix associated to this state is the identity matrix, whatever the basis of modes in which it is represented:

$$\mathbf{\Gamma}_{|0\rangle} = \mathbb{1}_{2n} \tag{1.85}$$

It is a direct consequence of the way we defined the quadrature operators (1.66) and (1.67) : the variance of the fluctuations on both quadratures for a zero-photons state is equal to unity. Therefore, its Wigner function is given by

$$W(\mathbf{x},\mathbf{p}) = \frac{1}{(2\pi)^n} e^{-\frac{1}{2}(\mathbf{x}^2+\mathbf{p}^2)} \tag{1.86}$$

1.6.2.2 Coherent state

Introduced in [Glauber 63], *coherent states* $|\alpha_i\rangle$ are widely used in quantum optics since they are the quantum states that represent the state of light emitted by an ideal laser well above threshold. They are also called *quasi-classical states*. Moreover, they are the eigenstates of the annihilation operator $\hat{a}_i$:

$$\hat{a}_i \, |\alpha_i\rangle = \alpha_i \, |\alpha_i\rangle \tag{1.87}$$

The expression of such states may be obtained by displacing the vacuum state in phase space. This is achieved by applying the *displacement operator* $\hat{D}_i$ on the vacuum state:

$$|\alpha_i\rangle = \hat{D}_i(\alpha_i) \, |0\rangle \tag{1.88}$$

where

$$\hat{D}_i(\alpha_i) = \exp\left[\alpha_i \hat{a}_i^\dagger - \alpha_i^* \hat{a}_i\right] \tag{1.89}$$

A general coherent state is obtained by the tensor product of each individual coherent states (1.87)

$$|\alpha\rangle = \bigotimes_i |\alpha_i\rangle \tag{1.90}$$

Its covariance matrix is also equal to the identity matrix:

$$\mathbf{\Gamma}_{|\alpha\rangle} = \mathbb{1}_{2n} \tag{1.91}$$

and is therefore the same in each basis. In fact, it may be shown that there always exists a basis in which any coherent state can be represented with a coherent state in mode 1 and vacuum in all the other modes [Treps 05]:

$$\left|\psi\right\rangle = |\alpha\rangle \otimes |0,\ldots,0,\ldots\rangle \tag{1.92}$$

A coherent state may therefore be considered as a *single mode state*.[7]

[7] In contrast, a state is called multi mode if it is not single mode. Albeit amusing, this condition is strong in the sense that any state that cannot be written according to (1.92) is by definition multi mode. A good explanation of these conditions can be found in [Delaubert 07].

In this basis, the coherent state writes in terms of the Fock states as

$$|\alpha\rangle = e^{-|\alpha|^2/2} \sum_{n_1=0}^{\infty} \frac{\hat{a}_1^{n_1}}{\sqrt{n_1!}} |0\rangle \tag{1.93}$$

where the photons are created in the first mode. It is straightforward to show that

$$\langle \hat{N}_1 \rangle = |\alpha|^2 \tag{1.94}$$

and

$$\sigma^2_{\hat{N}_1} = |\alpha|^2 \tag{1.95}$$

The photon number distribution of a coherent state follow a Poisson distribution.

1.6.2.3 Squeezed state

The Heisenberg inequality (1.70) imposes a restriction on the value of the product of the variances of the quadratures in a given mode. And yet it does not constrain the variance of one single quadrature. In the case where the variance of one quadrature in a given mode is less than 1, this mode is said to be *squeezed*.

The squeezing operator for the quadrature $\hat{q}_i^{\phi_i}$ in mode i is written as

$$\hat{S}_i(\xi_i) = \exp\left[\frac{\xi_i \left(\hat{a}_i^\dagger\right)^2 - \xi_i^* (\hat{a}_i)^2}{2}\right] \tag{1.96}$$

where $\xi_i = r_i e^{i\theta_i}$ is the squeezing parameter; $r_i > 0$ is the amount of squeezing and θ_i is the direction.

On a vacuum state, the action of this operator yields the state $|\xi_i\rangle = \hat{S}_i(\xi_i)|0\rangle$, which may be expanded in terms of even Fock states [Ferraro 05]. Despite its name, the squeezed vacuum is not an empty state, as its mean number of photon is given by

$$\langle \hat{N}_i \rangle_{|\xi_i\rangle} = \sinh^2 r_i \tag{1.97}$$

whereas the expectation value of a quadrature operator at any angle in phase space vanishes : $\left\langle \hat{q}_i^{\phi} \right\rangle_{|\xi_i\rangle} = 0 \ \forall \ \phi$. However, the variances for the two orthogonal quadratures $\hat{q}_i^{\phi}$ and $\hat{p}_i^{\phi} \equiv \hat{q}_i^{\phi+\frac{\pi}{2}}$ read

$$\sigma^2_{\hat{q}_i^{\phi}} = e^{-2r_i} \equiv \sigma_i^2 \tag{1.98}$$

$$\sigma^2_{\hat{p}_i^{\phi}} = e^{2r_i} \equiv \frac{1}{\sigma_i^2} \tag{1.99}$$

The field is then "squeezed" along a given quadrature and "anti-squeezed" along the other. The special cases where $\phi = 0$ and $\phi = \frac{\pi}{2}$ correspond respectively to *amplitude* or *phase squeezed states*.

In the case where the state is pure and multimode, the covariance matrix is diagonal:

$$\mathbf{\Gamma}_{|\xi\rangle} = \mathrm{diag}\left(\sigma_1^2, \sigma_2^2, \ldots, \frac{1}{\sigma_1^2}, \frac{1}{\sigma_2^2}, \ldots\right) \tag{1.100}$$

A phase space diagram of coherent and squeezed states is shown on figure 1.2.

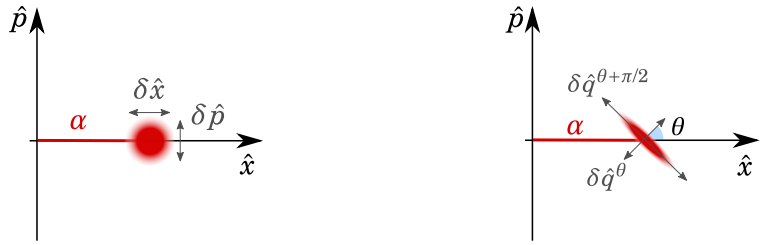

(a) **(b)**

Figure 1.2: Phase space representation of (a) a coherent state; (b) a coherent squeezed squeezed on the $\theta+\pi/2$ quadrature. A vacuum state is obtained by setting $\alpha = 0$ in these diagrams.

1.6.2.4 Entangled states

As it was pointed out, the off-diagonal terms in the covariance matrix display the correlations between the quadrature, whose origin may be classical or quantum. One of the most intriguing parts of quantum mechanics, the famous notion of *entanglement* as first described in [Einstein 35], emerges from quantum correlations. Formally speaking, an entangled state is a quantum state that cannot be described by the tensor product of density operators of its sub-ensembles; the state is then called *not separable*. While this feature is well described in the discrete variables regime, giving a formal definition of it in the continuous variables regime is a more challenging task. Current research studies a variety of criteria to define entanglement in this regime, such as inseparability, study of correlations, etc.

Although most of the work in this thesis is of classical nature, entangled states will be of interest in the next part of the experiment, and a more thorough explanation will be given in chapter 8.

2 Femtosecond ultrafast optics

(About ultrafast pulse-shaping) "There's about a million things that can go wrong."
– Jonathan "*Golden Goose*" Roslund

Contents

2.1 Description of pulses of light 32
2.1.1 Optical frequency combs 32
2.1.1.1 Ideal frequency comb 32
2.1.1.2 Realistic frequency comb 34
2.1.2 Energy and peak power 35
2.1.3 Moments of the field 36
2.1.4 Gaussian pulses 37
2.1.4.1 Temporal domain 37
2.1.4.2 Spectral domain 38
2.2 The influence of dispersion 38
2.2.1 Spectral and temporal phases 39
2.2.2 Effects on the pulse shape 39
2.2.2.1 Constant phase 40
2.2.2.2 Linear phase 41
2.2.2.3 Quadratic phase 41
2.2.2.4 Cubic phase 43
2.3 Representations of the pulse 44
2.3.1 Time-frequency distributions 44
2.3.1.1 Wigner distribution 45
2.3.1.2 Short-time Fourier Transform 45
2.3.2 Some examples 46
2.3.3 Experimental realizations 47
2.4 Generation of pulses of light 48
2.4.1 Steady-state laser cavity 48
2.4.2 Mode-locked lasers 50
2.4.2.1 General principles 50
2.4.2.2 Kerr-lens mode-locking 52

This thesis is all about precise measurements with light in the near infrared in the femtosecond regime and the analysis of its fluctuations. This domain has been growing and maturing for the last forty years and is now incredibly active. It is also very impressive how interdisciplinary this field has become, with its wide range of applications

in all sorts of research area. It involves a short time scale which allows one to make "stop-action" measurements of rapid phenomenon, and very high intensity, enough to strip the electrons from their nuclei, resulting in a laser-generated plasma. It also makes extreme nonlinear optics phenomena possible, where laser-matter interactions are sensitive to the non-instantaneous dynamics of bound motions of electrons. Although this thesis does not deal with these extreme behavior -attosecond time scales, XUV and X-Ray frequencies, high harmonics generation...-, ultrafast aspects need to be treated with care. The aim of this chapter is therefore to give the reader a "crash-course" in ultrafast optics, since most of the remaining chapters in this manuscript will rely heavily on the definitions that will follow. A more complete description may be found in [Rudolph 06] and [Weiner 11a].

2.1 Description of pulses of light

In this section, we introduce the notion of an optical frequency comb and give a mathematical description of its field. We then define power-related quantities that are specific to ultrashort pulses of light. We also put forward definitions to characterize the temporal and spectral envelopes, and end with a Gaussian description of the matter.

2.1.1 Optical frequency combs

In the case where the output spectrum of the laser corresponds to a large number of equally spaced longitudinal modes, the laser is designated as an *optical frequency comb* where every frequency mode is called a *tooth* of the comb. The process through which such lasers are generated is called *mode-locking*; it ensures a fixed phase relationship between each longitudinal mode of the comb. In this condition, in the temporal domain, it can be shown that the electric field consists of pulses of limited duration, whereas it would vanish if the phases were random. This mechanism will be outlined in more details in section 2.4.

Due to their very stable structure, frequency combs are tools of reference for metrology and spectroscopy. Their development led to the Nobel prize of Theodor W. Hänsch and John L. Hall in 2005.

2.1.1.1 Ideal frequency comb

In the following, we will give a mathematical description for the output of a mode-locked laser. The frequencies of the longitudinal modes are written as

$$\omega_n = n\,\omega_r \tag{2.1}$$

where ω_r is the free-spectral range of the laser cavity.

Considering only the temporal part, the electric field of a single pulse can be written from (1.18) as the product of a slowly varying envelope and an optical carrier at the frequency ω_0:

$$E^{(+)}_{pulse}(t) = \mathscr{E}_0\, a(t)\, e^{-i w_0 t} \tag{2.2}$$

which can be expanded in the Fourier space as previously:

$$E^{(+)}_{pulse}(\omega) = \mathscr{E}_0 \int_{\mathbb{R}} \frac{\mathrm{d}t}{\sqrt{2\pi}} a(t) e^{i(\omega-\omega_0)t} = a(\omega-\omega_0) \equiv a(\Omega) \tag{2.3}$$

The Fourier relation between time and frequency domains (or time-bandwidth product) imposes that short pulses have a broad spectrum.

In the spectral domain, assuming an infinitely narrow homogeneous linewidth for each longitudinal mode, the spectrum of an optical frequency comb is obtained by summing the contribution of each single pulse:

$$E^{(+)}(\omega) = E^{(+)}_{pulse}(\omega) \sum_n \delta(\omega - n\,\omega_r) \tag{2.4}$$

which corresponds to the spectrum sketched on figure 2.8.

In the temporal domain, this becomes

$$E^{(+)}(t) = \left(E^{(+)}_{pulse} \star \Delta_\tau\right)(t) \tag{2.5}$$

where $\star$ represents the convolution product and Δ_τ is the Fourier transform of the Dirac comb distribution $\sum_n \delta(\omega-\omega_n)$:

$$\Delta_\tau = \sum_n \delta(t - n\tau) \tag{2.6}$$

Consequently, the complex field in the temporal domain is written as

$$E^{(+)}(t) = \sum_n a(t-n\tau)\, e^{-i\omega_0(t-n\tau)} \tag{2.7}$$

This represents a train of pulses where $\tau = 2\pi/\omega_r$ is the time spacing between subsequent pulses.

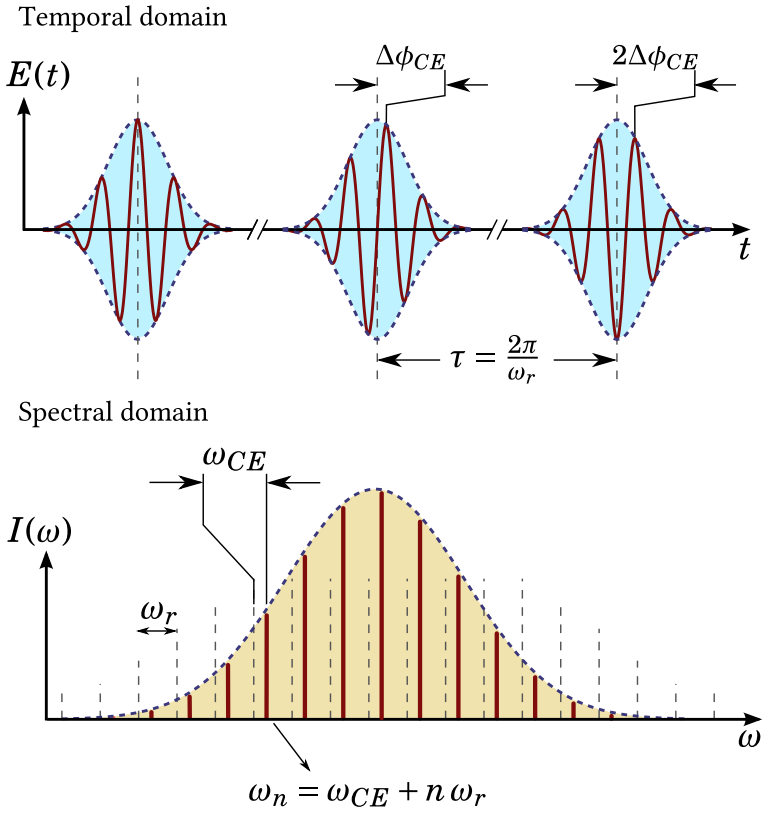

Figure 2.1: Temporal and spectral representation of a frequency comb.

2.1.1.2 Realistic frequency comb

The previous treatment is not entirely realistic since it does not take into account the effect of dispersion in the laser cavity. As we will expand into more details in section 2.2, both the envelope and the carrier of short pulses of light are changed by the effect of dispersion. Dispersion causes a difference between the phase velocity and the group velocity, therefore leading to an increasing dephasing between the carrier and the envelope from pulse to pulse[1]. The difference of dephasing between successive pulses is called carrier-envelope phase (CEP):

$$\Delta\phi_{CE} = \left(\frac{1}{v_g} - \frac{1}{v_\phi}\right)\omega_0 L \tag{2.8}$$

where v_ϕ and v_g are respectively the phase and group velocities in the laser cavity, and L is the length of the laser cavity.

[1]Note that the dispersion that is refered to here is inside the laser cavity, not outside.

As a result, the complex field reads

$$\boxed{E^{(+)}(t) = \sum_n a(t - n\tau)\, e^{-i\omega_0(t-n\tau)}\, e^{-in\Delta\phi_{CE}}} \tag{2.9}$$

It is important to point that as opposed to (2.7), the field is no longer periodic because of the CEP. In the spectral domain, this translates to

$$E^{(+)}(\omega) = E^{(+)}_{pulse}(\omega) \sum_n \delta\left(\omega - (n\omega_r + \omega_{CE})\right) \tag{2.10}$$

where ω_{CE} is the *carrier-envelope offset* (CEO) defined by

$$\boxed{\omega_{CE} = \Delta\phi_{CE} \frac{\omega_r}{2\pi}} \tag{2.11}$$

The longitudinal modes of a realistic frequency comb are then written as

$$\boxed{\omega_n = n\omega_r + \omega_{CE}} \tag{2.12}$$

The temporal and spectral representation of a frequency comb are shown on figure 2.1.

In precision measurements, the stabilization of both the repetition rate and the carrier-envelope offset are very important. It can be achieved through a variety of ways, for example by locking the comb on stabilized single-mode lasers [Nicolodi 14]. These quantities also belong to the global parameters of a frequency comb and their fluctuations will be analyzed in more details in the next part of this thesis.

2.1.2 Energy and peak power

This section is a complement to 1.2.5.

As it was suggested, for pulses of light, the detection time T need to be chosen with care as it allows to define specific power-related quantities. It can be useful to consider this detection time as $\tau/2$ *i.e.* half the time between subsequent pulses. Hence, computing the energy from (1.41) yields the energy W_p contained in a pulse:

$$W_p = \int_{\tau/2} P(z,t)\, \mathrm{d}t \tag{2.13}$$

For a frequency comb with a repetition rate f_r, the average detected power is given by:

$$P_{avg} = \frac{W_p}{T_r} \equiv W_p \times f_r \tag{2.14}$$

which is obviously equal to the energy in a pulse times the number of pulses per second.

Finally, for nonlinear effects, a very important characteristic of a pulse is its peak power P_{pk}, which is defined as the maximum occurring optical power. Since this quantity depends on the actual pulse shape, giving a mathematical description in the general case is not possible, but it has an analytical expression for gaussian pulses (c.f. (2.27)).

2.1.3 Moments of the field

When working with ultrashort pulses, it is useful to know the temporal and spectral characteristics of the field such as the width $\Delta\omega$ in the spectral domain and Δt in the temporal domain. There are multiple ways of defining these quantities, the most widely used being the full width at half maximum (FWHM). Though convenient because visual, it is not always the best way. That is for instance the case of pulses with substructures that causes a considerable part of the energy to lie well outside of the range defined by the FWHM. In these cases, it is preferable to use averaged values derived from the statistical moments of the field's intensity envelope.

The moments of the field can be defined for any variable ξ, being spatial, temporal and spectral. Therefore, for the sake of generality, let us write the field envelope as $f(\xi)$. The moment of order n for the variable ξ with respect to the intensity of the field is defined as

$$\boxed{\langle \xi^n \rangle = \frac{\int_{\mathbb{R}} \xi^n \, |f(\xi)|^2 \, \mathrm{d}\xi}{\int_{\mathbb{R}} |f(\xi)|^2 \, \mathrm{d}\xi}} \tag{2.15}$$

The first order moment $\langle \xi \rangle$ is the "center of mass" of the intensity distribution, generally chosen as a reference to give a zero value. As an example, the center of the transverse field as defined by (1.28) will be centered on $x = 0$, and the spectrum is usually centered on the carrier frequency ω_0. This definition can become very meaningful experimentally since we seldom work with perfectly symmetric spectra (and neither with perfectly symmetric pulses, for that matter).

A good criterium for the width in either domain is the standard deviation, defined as a function of the first and second order moments:

$$\sigma_\xi = \sqrt{\langle \xi^2 \rangle - \langle \xi \rangle^2} \tag{2.16}$$

In the temporal domain, when setting the first moment as zero, this is equivalent to the root mean square (RMS). The RMS duration has analytical expressions for well-defined envelopes [Sorokin 00]. The case of gaussian envelopes will be treated in the next section.

When defining the center of mass as the reference, the time width of the pulse is simply written as

$$\sigma_t^2 = \frac{\int_{\mathbb{R}} t^2 \, |a(t)|^2 \, \mathrm{d}t}{\int_{\mathbb{R}} |a(t)|^2 \, \mathrm{d}t} \tag{2.17}$$

Similarly, the bandwidth is defined as

$$\sigma_\omega^2 = \frac{\int_{\mathbb{R}^+} \omega^2 \, |a(\omega)|^2 \, \mathrm{d}\omega}{\int_{\mathbb{R}^+} |a(\omega)|^2 \, \mathrm{d}\omega} \tag{2.18}$$

Because of the conjugation relationships between the temporal and the spectral domains, the uncertainty principle in harmonic analysis [Appel 08] states that

$$\sigma_t^2 \cdot \sigma_\omega^2 \geq \frac{1}{4} \tag{2.19}$$

This inequality is saturated only in the case of gaussian pulses.

2.1.4 Gaussian pulses

Having presented the general characteristics of a pulse, it seems convenient to introduce a Gaussian temporal envelope $u(t)$ that we can use to do analytical calculations. The choice made here is indeed purely analytical, since the Gaussian shape is a reasonable approximation of the structure of the experimental pulses.

2.1.4.1 Temporal domain

The temporal mode $u(t)$ associated to a Gaussian shape is given by

$$u(t) = \frac{1}{(2\pi)^{1/4}} \frac{1}{\sqrt{\Delta t}} \exp\left(-\frac{t^2}{4\Delta t^2}\right) \equiv C_t \exp\left(-\frac{t^2}{4\Delta t^2}\right) \tag{2.20}$$

where Δt is the second moment and the coefficient C_t ensures that $u(t)$ satisfies the normalization condition[2] $\int_{\mathbb{R}} |u(t)|^2 \, \mathrm{d}t = 1$.

The FWHM of this distribution is related to the time bandwidth by

$$\Delta t_{FWHM} = 2\Delta t \sqrt{2 \ln 2} \tag{2.21}$$

Note that with this definition of the Gaussian field, the RMS width (2.17) and the second moment are equal

$$\sigma_t^2 = \int_{\mathbb{R}} t^2 \, |u(t)|^2 \, \mathrm{d}t = \Delta t^2 \tag{2.22}$$

With other definitions that are more common in the ultrafast community, there would be a factor of 2 between them.

[2] For simplicity, we take the normalization condition (1.31) and consider that $T = 1$.

2.1.4.2 Spectral domain

Taking the Fourier transform of (2.20) yields the field in the spectral domain:

$$u(\omega) = \frac{\sqrt{2\Delta t}}{(2\pi)^{1/4}} \exp\left(-\Delta t^2 \omega^2\right) \tag{2.23}$$

Computing the second moment then yields

$$\Delta\omega^2 = \frac{1}{4\Delta t^2} \tag{2.24}$$

which allows us to rewrite the spectrum as

$$u(\omega) = \frac{1}{(2\pi)^{1/4}} \frac{1}{\sqrt{\Delta\omega}} \exp\left(-\frac{\omega^2}{4\Delta\omega^2}\right) \equiv C_\omega \exp\left(-\frac{\omega^2}{4\Delta\omega^2}\right) \tag{2.25}$$

This representation is the exact counterpart of equation (2.20) and obeys the same normalization conditions. All the quantities from the temporal part may be transposed to the spectral domain by the substitution $\Delta t \rightarrow \Delta\omega$.

From (2.24), it is clear that the Gaussian case saturates the inequality (2.19). The time-bandwidth product may also be written in term of the FWHM:

$$\Delta t_{FWHM} \times \Delta\omega_{FWHM} \approx 2\pi \times 0.441 \tag{2.26}$$

This metric allows us to define the *transform limited pulse*, the shortest Gaussian pulse possible for a given spectral width. The value of the time-bandwidth product for other pulse shapes, such as hyperbolic secant or lorentzian, can be found in [Sorokin 00].

Finally, when writing the power of a Gaussian pulse according to (1.40), it becomes possible to write the peak power as

$$P_{pk} = \frac{W_p}{\sqrt{2\pi}\Delta t} \simeq 0.94 \frac{W_p}{\Delta t_{FWHM}} \equiv 0.94 \frac{P_{avg}}{f_r \times \Delta t_{FWHM}} \tag{2.27}$$

This expression as a function of the average power is convenient since, again, this quantity cannot be measured using usual electronics.

2.2 The influence of dispersion

As introduced in section 1.3, the electric field can carry information on both the amplitude and the phase quadrature. When doing measurement with ultrashort pulses, this information can be spectrally dependent. We will be particularly interested in the phase quadrature of the field, and therefore, we need to understand the phase variations in both the spectral and the temporal domains. It is also important to know whether or not a pulse is free of such phase variations.

2.2.1 Spectral and temporal phases

At the risk of sounding redundant, we write the complex field in the temporal domain as

$$E^{(+)}(t) = \mathscr{E}_0\, a(t)\, e^{-i\omega_0 t} \tag{2.28}$$

where $a(t)$ is the field envelope, *a priori* complex. In the spectral domain, relative to the carrier frequency, we also have

$$E^{(+)}(\Omega) = \mathscr{E}_0\, a(\Omega) \tag{2.29}$$

with $\Omega = \omega - \omega_0$. To add phase variations in either the frequency or time domains, we write these phases respectively $\phi(t)$ and $\phi(\omega)$ and include them in the envelope as follows:

$$a(t) = |a(t)|\, e^{i\psi(t)} \tag{2.30}$$

and

$$a(\Omega) = |a(\Omega)|\, e^{i\phi(\Omega)} \tag{2.31}$$

Two particular cases emerge: when $\psi(t)$ is a constant, the pulse is free of *phase modulation*, and when $\phi(\omega)$ is a constant, the pulse is said to be *bandwidth limited*[3].

When a pulse has a non trivial variation in both $\psi(t)$ and $\phi(\omega)$, we say it is *chirped*. The following section will list the effects that a spectral phase can have on the pulse shape.

2.2.2 Effects on the pulse shape

Let us consider that the spectral phase $\phi(\omega)$ can be Taylor expanded around the carrier frequency ω_0:

$$\phi(\omega) \simeq \phi(\omega_0) + (\omega-\omega_0)\left.\frac{\partial\phi}{\partial\omega}\right|_{\omega_0} + \frac{1}{2}(\omega-\omega_0)^2\left.\frac{\partial^2\phi}{\partial\omega^2}\right|_{\omega_0} + \frac{1}{6}(\omega-\omega_0)^3\left.\frac{\partial^3\phi}{\partial\omega^3}\right|_{\omega_0} \tag{2.32}$$

which can be rewritten in a more compact notation as

$$\phi(\Omega) \simeq \phi_0 + \Omega\,\phi_1 + \frac{\Omega^2}{2}\,\phi_2 + \frac{\Omega^3}{6}\,\phi_3 \tag{2.33}$$

[3] Here we stress the fact that a linear phase in either t or ω has the same effect on the pulse than a constant phase... As we will see in 2.2.2, a linear spectral phase shift is equivalent to a simple delay in the time domain, and a linear temporal phase shift is simply a shift of center frequency. As a result, it does not change this definition, and that is the reason why we kept the carrier $e^{-i\omega_0 t}$ outside of the envelope in (2.28).

The field's spectrum is consequently written as

$$E^{(+)}(\Omega) = \mathscr{E}_0 \, |a(\Omega)| \, e^{i\phi(\Omega)} \tag{2.34}$$

It is evident from computing the spectral intensity that the energy is not affected by this phase, nor is the intensity spectrum as observed with a spectrometer. However, such a phase can have a huge influence on the pulse shape. In the next section, we show the effect of each term of the phase expansion on the temporal pulse.

2.2.2.1 Constant phase

In the case of a constant phase $\phi(\Omega) = \phi_0$, there is no change in the pulse shape. The temporal field is directly given by

$$E^{(+)}(t) = \mathscr{E}_0 \, |a(t)| \, e^{-i(\omega_0 t - \phi_0)} \tag{2.35}$$

A constant spectral phase then results in a simple phase shift of the carrier in the temporal domain. The real field in the temporal domain is written

$$E(t) = 2\,\mathrm{Re}\left\{E^{(+)}(t)\right\} = 2\mathscr{E}_0 |a(t)| \cos\left(\omega_0 t - \phi_0\right) \tag{2.36}$$

The resulting pulse shape is depicted in figure 2.2 for a wavelength of 795 nm and a temporal FWHM of 6 fs.

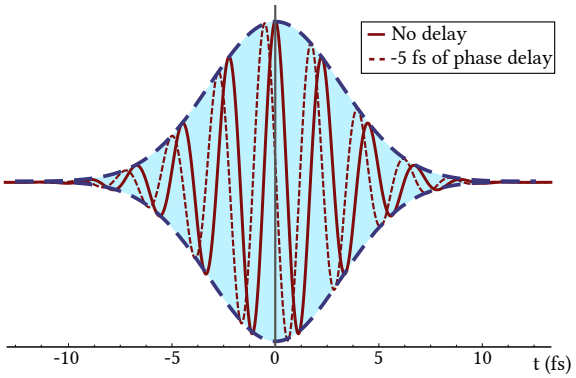

Figure 2.2: Pulse shape of a 6 fs pulse with and without a constant (negative) spectral phase.

2.2.2.2 Linear phase

For a linear spectral phase $\phi(\Omega) = \Omega\phi_1$, the complex field in the temporal domain is written as

$$E^{(+)}(t) = \mathscr{E}_0 \left|a\left(t-\phi_1\right)\right| e^{-i\omega_0 t} \tag{2.37}$$

This results in a global delay in the envelope of the pulse as shown by figure 2.3. Note that the carrier of the delayed pulse is not shifted with respect to the phase of the undelayed pulse.

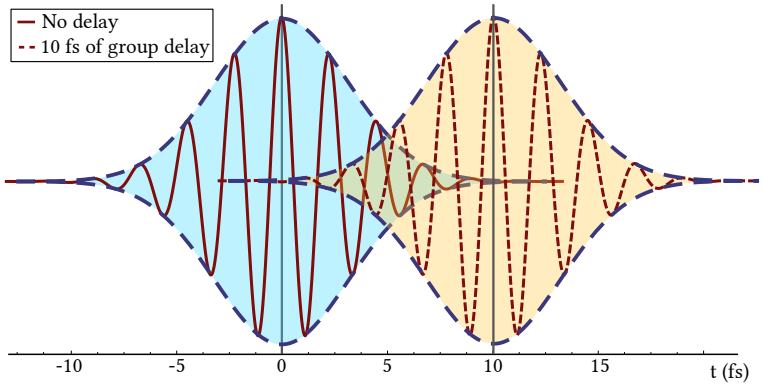

Figure 2.3: Pulse shape of a 6 fs pulse with and without a linear spectral phase.

A global delay in both phase and envelope, combining constant and linear spectral phases, will then result in a shift of the carrier in the delayed pulse.

2.2.2.3 Quadratic phase

A quadratic spectral phase $\phi(\Omega) = \frac{\Omega^2}{2}\phi_2$ affects both the envelope shape and the carrier frequency, as shown on figure 2.4. This is also the case for every higher order phase. The temporal field of a Gaussian pulse with a quadratic spectral phase reads

$$E^{(+)}(t) = \mathscr{E}_0\, a\, \frac{C_\varsigma}{\sqrt{\Delta t}} e^{-(t/2\varsigma)^2} e^{-i\omega_0 t} \tag{2.38}$$

Here we defined the envelope of the field as a Gaussian of second moment ς defined by

$$\varsigma = \Delta t \sqrt{1 - i\frac{\phi_2}{2\Delta t^2}} \tag{2.39}$$

Since this quantity is complex, the temporal field is not yet written in the form of (2.30).

To do so, we define an effective temporal width $\Delta t' = |\varsigma|$ for the chirped pulse, allowing to decompose the argument of the Gaussian in real and imaginary parts:

$$\left(\frac{1}{2\varsigma}\right)^2 = \left(\frac{1}{2\Delta t'}\right)^2 + i\frac{\phi_2}{8(\Delta t')^4} \tag{2.40}$$

where $\Delta t'$ is defined as

$$\boxed{\Delta t' = \Delta t\sqrt{1+\left(\frac{\phi_2}{2\Delta t^2}\right)^2}} \tag{2.41}$$

From equation (2.40), we see that a quadratic phase will have two effects on the pulse shape:

- The envelope becomes broader according to (2.41) independently of the sign of ϕ_2. A useful criterium is the amount of quadratic phase ϕ_c for which the pulse's envelope is twice bigger than the transform limited one. It reads:

  $$\phi_c = 2\sqrt{3}\Delta t^2 \tag{2.42}$$

  All these quantities may of course be put in term of temporal FWHM using (2.21).

- A linear frequency modulation occurs, given by

  $$\psi(t) = \frac{\phi_2}{8(\Delta t')^4}\, t \tag{2.43}$$

  This phenomenon is often referred to as *chirp*, as an analogy to acoustic waves. An up-chirp means that the instantaneous frequency increases with time, whereas a down-chirp is the contrary.

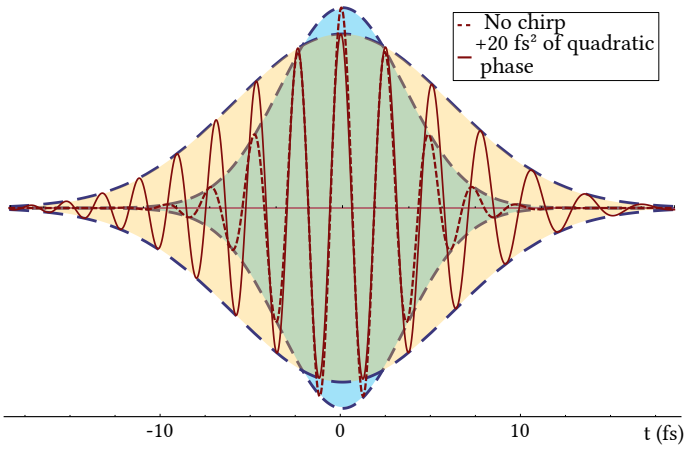

Figure 2.4: Pulse shape of a 6 fs pulse with and without a positive quadratic phase.

A pulse will acquire quadratic phase when it propagates through a dispersive medium. Since both positive and negative chirp induce a broadening of the envelope, the minimum pulse duration can only occur when there is no chirp, that is when there is no variation in instantaneous frequency and no spectral phase higher than the first order in ω.

To compensate a positive quadratic phase acquired through propagation, a pulse may be compressed down to the Fourier limit by using a negative group velocity dispersive medium. This is achieved by using either prisms or gratings [Martinez 84], or even by pulse shaping using a Spatial Light Modulator [Weiner 00].

2.2.2.4 Cubic phase

A cubic phase $\phi(\Omega) = \frac{\Omega^3}{6}\phi_3$ results in a radical change in the temporal envelope, making it non-Gaussian. The Fourier transform may still be analytically computed according to [McMullen 77].

Using a clever change of variables $\xi = \Omega + i\frac{\Delta t^2}{\tau^3}$, with $\tau^3 = \phi_3/2$, the Fourier transform of the spectral envelope reduces to

$$u(t) = C_\omega \int_{\mathbb{R}} \frac{\mathrm{d}\xi}{\sqrt{2\pi}} \exp\left[i\frac{\tau^3}{3}\xi^3 + i\left(\frac{\Delta t^4}{\tau^3} - t\right)\xi\right] \exp\left[\frac{2\Delta t^6}{3\tau^6} - \frac{\Delta t^2}{\tau^3}t\right] e^{-i\omega_o t} \tag{2.44}$$

The integral over ξ is known as the Airy integral in the complex plane $\mathrm{Ai}(t) = \int_{\mathbb{C}} \frac{\mathrm{d}z}{\sqrt{2\pi i}} e^{\frac{z^3}{3} - zt}$. Injecting this result, we then obtain:

$$u(t) = \frac{C_\omega}{\tau}\mathrm{Ai}\left(\frac{\Delta t^4/\tau^3 - t}{\tau}\right) \exp\left[\frac{\Delta t^2}{\tau^3}\left(\frac{2\Delta t^4}{3\tau^3} - t\right)\right] e^{-i\omega_o t} \tag{2.45}$$

For $\tau \to 0$, this function converges to the standard gaussian pulse. For non zero values of τ, we see that the carrier is unaffected, whereas the envelope acquires a complex shape, as shown in figure 2.5.

Upon propagating through a strongly dispersive medium, the third order dispersion will cause a delay of the pulse peak as well as an asymmetric broadening, creating replicas. For a negative cubic phase, these ripples arrive earlier in time, whereas it is the contrary for a positive phase. Generally, the cubic dispersion is weaker than the quadratic, so that effect always coincides with the broadening and chirp defined in the previous section. This may be modeled by the substitution $\Delta t \to \zeta$ in (2.45).

Cubic phase can therefore pose very serious problems in ultrafast optics. As was the case for quadratic phase, it is possible to compensate for it using a compressor or a pulse shaper.

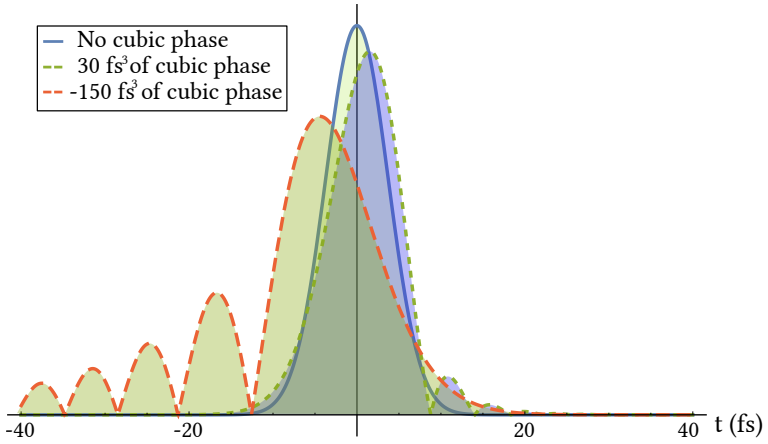

Figure 2.5: Envelope of a 6 fs pulse with and without a cubic phase.

2.3 Representations of the pulse

From the previous section, it is clear that a full representation of the pulsed field needs to include both the spectral and the temporal phases. Of course, once retrieved, one could plot the spectral and temporal phases of the pulse, but these can be hard to read. Although it does contain all the required information, it is not straightforward to know the temporal distribution of each frequency of the field. For example, temporal representations of the pulse in the previous section do not give easily away the arrival time of each color.

2.3.1 Time-frequency distributions

In many other fields such as quantum mechanics or acoustics, other representations were introduced to complement standard Fourier analysis. These distributions of time-varying spectra are called *spectrograms* (or equivalently *sonograms*). The concept has been widely used for the analysis of time-varying spectra

Over the years, a great number of distributions have been introduced and investigated, and it is still an evolving field. Here we only expose the general principle that lies behind time-frequency distributions since it also hints as to how to access the pulse shape experimentally. It also provides a good visual witness of the pulse shape and allows one to understand rapidly the structure that the pulse acquired during its propagation. For a review on all the different time-frequency distributions, see [Cohen 89].

2.3.1.1 Wigner distribution

The whole field of time-frequency distribution has been built upon the study of the Wigner function. First introduced by Wigner and applied to quantum mechanics, the Wigner function can be applied to any set of conjugated variables, for example, the wave-vector k and the position x, or the angular frequency ω and the time t. It has found some application in ultrafast optics for the description of pulses [Walmsley 96], but its usage has become limited since it is cumbersome to relate to the physical spectrum. Its mathematical definition is generally given by

$$\mathcal{W}(t,\omega) = \int_{\mathbb{R}} \frac{\mathrm{d}\tau}{2\pi} E^{(-)}\left(t-\frac{\tau}{2}\right) e^{-i\omega\tau} E^{(+)}\left(t+\frac{\tau}{2}\right) \tag{2.46}$$

$$= \int_{\mathbb{R}} \frac{\mathrm{d}\vartheta}{2\pi} E^{(-)}\left(\omega-\frac{\vartheta}{2}\right) e^{-i\vartheta t} E^{(+)}\left(\omega+\frac{\vartheta}{2}\right) \tag{2.47}$$

This definition is the counterpart of the quantum version.

Although this does provide a two-dimensional representation of the field, the Wigner function can prove hard to use and interpret. Because the distribution at a certain time usually reflects properties of the signal at other times, it is highly "non-local" in nature. Therefore, if there is noise on the signal for a small finite time, that noise will appear at other times. This means also that, at a certain point in time, the function can be non zero even when the signal is null. This noisy behavior is one of the main drawbacks of the Wigner distribution; it can be cleaned by smoothing, but this operation inevitably destroys some desirable structures.

2.3.1.2 Short-time Fourier Transform

A more widespread way of obtaining a spectrogram with better reliability is the so-called short-time Fourier transform. The concept is simple to understand and powerful. If one wants to analyze the behavior of a signal at a particular time, then one simply has to take a portion of the signal centered around that time, calculate its energy spectrum, and do this for every time.

Formally, let us consider the complex temporal envelope $a(t)$ of the field that we want to resolve and multiply it by a gating function $h(t-\tau)$. The spectrogram is then obtained by taking the energy of the Fourier transform of the signal:

$$S(\omega,t) = \left| \int_{\mathbb{R}} \frac{\mathrm{d}\tau}{\sqrt{2\pi}} a(\tau) h(\tau-t) e^{-i\omega\tau} \right|^2 \tag{2.48}$$

which, for specific filter function h, is the short-time Fourier transform (STFT) of the

signal. Alternatively[4], we may define S by taking the spectral envelope $a(\omega)$ and the Fourier transform of the filter $h(\omega)$:

$$S(\omega,t)=\left|\int_{\mathbb{R}}\frac{\mathrm{d}\vartheta}{\sqrt{2\pi}}a(\vartheta)h(\vartheta-\omega)e^{i\vartheta t}\right|^2 \tag{2.49}$$

The two definitions are equivalent. From an experimental point of view, there are many techniques that allows one to measure spectrograms and therefore to resolve both the amplitude and the phase of the pulse.

One needs to choose the filter function h with care. Once again, because of the uncertainty principle, the narrower the function, the better the resolution in a specific domain, but it cannot be arbitrarily narrow. In that case, any variation in either the spectral or the temporal phase will be much smaller than the spectrum of S and will then be difficult to resolve. Conversely, if the filter is too broad, the spectrogram will be identical to the original power spectrum, and no information over the phase can be gained. There is therefore a necessary tradeoff between time and resolution. In general, one should select a gate function whose duration is on the order of the inverse bandwidth of the pulse to be characterized. In other words, gating the pulse by its transform-limited version is a good choice.

2.3.2 Some examples

In this short section, we take some of the spectral phases that were investigated in section 2.2.2 and apply the STFT method to compute the spectrogram. We chose the gate function to be the transform limited version of the chirped pulse. We again restrict ourselves to the study of Gaussian envelopes.

The spectrograms shown on figure 2.6 represent three different cases. The first is the transform-limited pulse which has no chirp, but it can have either a constant or a linear spectral phase[5]. The second is a pulse with a positive quadratic phase, it is said to be linearly chirped. The third and last pulse has some cubic phase.

From these representations, the temporal distribution of each color[6] is more evident. It is very easy to notice that a positive quadratic phase will make the lower frequency part (*i.e.* the red wavelengths) to arrive earlier in time. In the cubic case, the colors propagate together, but the shape of the pulse is no longer gaussian as it was stressed earlier. The center of mass of the pulse is also noticeably shifted.

[4]This definition is sometimes called a sonogram.

[5]Naturally, a linear spectral phase would translate the spectrogram along the time axis.

[6]Note that the term color denotes here the spectrum of the electromagnetic field, not the colors used to represent the spectrograms in figure 2.6 !

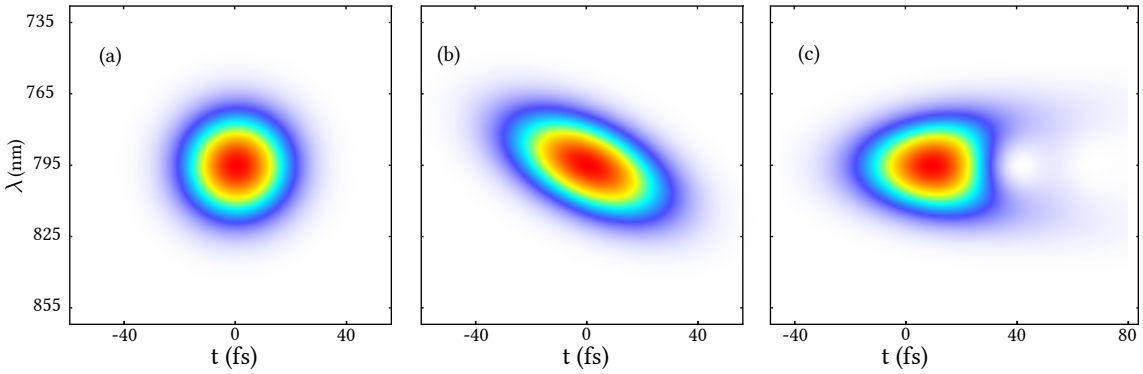

Figure 2.6: Spectrogram of three different pulse shapes. From left to right: (a) transform limited 20 fs pulse, (b) linear chirp (*i.e* quadratic phase), (c) cubic phase.

2.3.3 Experimental realizations

To conclude this chapter, we shall say a few words on how to experimentally retrieve the pulse shape. See [Trebino 02] for a much more complete list.

Knowing the exact structure of a pulse in both amplitude and phase can be very important for a lot of applications. Every non-linear process is highly dependent on the phase of the pulse, and the best efficiency is achieved when the pulse is transform-limited (c.f. section 8.3.2). In this situation, it is vital to know the absolute spectral (or temporal) phase.

There are no linear effects that can resolve the duration of a pulse or its phase in an absolute way. However, intensity correlation measurements will give information on the width of the pulse. This is realized by gating the pulse by itself within a $\chi^{(2)}$ medium and measuring the intensity of its second harmonic. The width of the resulting autocorrelation trace is proportional to the effective time-bandwidth of the pulse. Although it does not give the phase distribution, it is a simple technique that allows to infer whether or not a pulse is chirped with respect to its theoretical limit.

To access the phase profile, we usually resort to a technique called Frequency-Resolved Optical Grating (FROG) which gates the pulse to itself. Mathematically, what is measured at the output is very similar to (2.48). There exists a wide variety of FROG techniques that each offer some advantages and drawbacks. It is usually a technique similar to auto-correlation except that we measure the spectrum instead of the intensity. This allows to retrieve the absolute spectral and temporal phase of the pulse.

When the time-frequency distribution of the pulse is known, one can use it as a reference to measure the phase profile of another source using simpler techniques. For example, by beating an unknown pulse with a reference in an interferometer, in the spectral domain, the interference pattern allows one to retrieve the relative spectral

phase between the two (see section 3.1.3.4). Knowing the phase of the reference, it is therefore straightforward to plot the time-frequency distribution of the unknown pulse. This method can also be used to directly retrieve the spectrogram of the pulse by the xFROG procedure [Trebino 02].

2.4 Generation of pulses of light

In part III, we shall dive in more details into the noise characteristics of a laser source and we will need a decent knowledge on how the light of a femtosecond oscillator is generated. The aim of this section is to provide a description centered mainly on the type of lasers that have been used during this PhD (solid-state Titanium Sapphire laser, passive Kerr-lensing mode-locking), and does not pretend to review all of the laser theory.

2.4.1 Steady-state laser cavity

For our purposes, we consider laser sources that are made of a linear Fabry-Pérot cavity with a gain medium, as depicted by figure 2.7. Light passes through the gain medium twice per round-trip, and the electric field is periodic on this length. To achieve optical gain, a population inversion must occur in the gain medium. This corresponds to the situation where the number of electrons in an excited state exceeds the number of electrons in a lower level. This is usually achieved by optical pumping, where an external light source -e.g. a laser diode- is used to promote the electrons in an excited state.

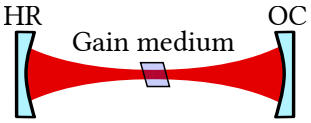

Figure 2.7: Linear laser cavity. HR: High Reflectivity ; OC: Output Coupler.

A steady-state is achieved if the two following conditions are fulfilled:

- The *gain condition* states that the round-trip gain balances exactly the round-trip losses.
- The *phase condition* allows only certain longitudinal modes to resonate inside the cavity. Their angular frequencies must satisfy

$$\omega_m = 2\pi m \frac{c}{L} \tag{2.50}$$

with $m \in \mathbb{N}$ and L is the total path traveled by the light in the cavity (in the case of a linear cavity, this distance is twice the cavity length). The spacing between each

longitudinal mode, or *free spectral range*, is given by $\omega_{FSR} = c/L$. It also corresponds to the laser *repetition rate*.

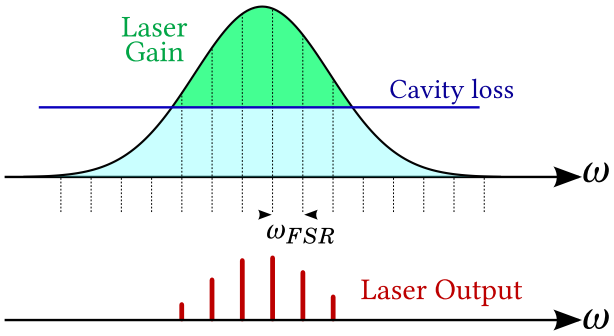

Figure 2.8: Sketch of the conditions for multimode lasing.

When the laser cavity is set such that the gain exceed losses only for a single longitudinal mode, the regime is called *single mode*. This results in the well-known monochromatic properties of lasers.

A basic laser operation is sketched schematically on figure 2.8 in the spectral domain. Laser oscillation happens only for modes where the gain lies above the loss line. In this broadband situation, multiple longitudinal modes satisfy the lasing conditions so that several output frequencies appear simultaneously. This regime is therefore called *multimode*.

This picture is a bit naive since in practice, the situation is a bit more complicated. Indeed, the gain condition requires that the gain exactly equals rather than exceeds the loss. This situation depends only on the properties of the laser medium and the pump level, and the level at which gain equal losses is called *threshold*. At this level, only weak light is emitted by the laser. To produce significant laser intensity, weak spontaneous emission needs to build up in the gain medium, and the gain must therefore exceed the loss.

However, above threshold, the intracavity field will extract more power that was stored by the pump in the gain medium and a saturation phenomenon occurs. As photons are amplified in the laser cavity by the gain medium through stimulated emission, electrons in the excited state are stimulated back to their low energy state. The gain is consequently reduced, and the actual gain, known as *saturated gain*, depends on the properties of the laser medium, the pump level and also the intracavity laser intensity. Thus, pump power above the threshold value is converted into stimulated emission[7] as laser intensity will build up just enough to maintain the saturated gain at exactly the

[7] This picture is similar to saturation phenomenon of electronic amplifiers; full gain is only possible for input signals below a certain voltage level, whereas higher input level will induce clipping of the output.

loss level. On figure 2.8, we assumed that the gain medium is broadened homogenously such that the saturated gain has the same spectral shape as the minimum gain required to achieve threshold.

This representation is however convenient, as to achieve short-pulse generation, a large number of modes need to oscillate simultaneously. As it was pointed in section 2.1.1, each of these longitudinal modes needs to have a fixed phase relationships in order to generate a frequency comb. This is achieved through the process of mode-locking.

2.4.2 Mode-locked lasers

To obtain a mode-locked laser generating ultrashort pulses, pulses need to form within the laser cavity using either active or passive elements. One also needs to take into account a number of different processes that affect the pulse as it propagates inside the cavity.

2.4.2.1 General principles

The mechanism of mode-locking is enabled when the gain is higher for the pulsed regime than for the continuous wave (CW) regime. This mechanism can either be an active element or be passively triggered by saturable absorption. Historically, active mode-locking was the first one to be demonstrated. Currently, passive mode-locking is widely used since it yields the shortest pulses through Kerr-lens mode-locking [Morgner 99]. The process of mode-locking is a complicated one: it involves a lot of different processes simultaneously, and describing its dynamics requires an elaborate treatment. A thorough description can be found in [Weiner 11a]. In the following, we briefly review the different key points that are required to achieve pulsed light generation.

Gain and bandwidth. As for single mode regime, both gain and linear loss are needed to generate short pulses, but their bandwidth are then important. According to the time-bandwidth product (2.19), shorter pulses have broader bandwidth and the laser needs to be set accordingly. Bandwidth limitation arises from a filtering effect, due to wavelength-dependent loss elements or from the finite bandwidth of the gain medium. Therefore, one has to maximize the bandwidth of the laser to achieve the shortest pulses generation.

Modulations. It is straightforward to see regularly spaced pulses of light as a CW wave whose amplitude is modulated at the repetition rate frequency. When this modulation happens inside the laser cavity, it introduces losses that are minimized when laser emission occurs in the form of short pulses that are synced with the modulation frequency. At each pass of the cavity, pulses get shortened up to a certain limit, and the

pulsed regime becomes favorable. That is why modulations play a key role in achieving and maintaining mode-locked operation[8].

Active modulations. This refers to externally driven modulators that modulate either the amplitude or the phase of the circulating pulse. The modulation frequency is usually chosen as the cavity round-trip time, and it needs to be set very precisely. This mode-locking technique, though quite simple, is not very robust since it is highly dependent on the stability of the cavity length. Moreover, the response of the modulator becomes ineffective for very short pulses and this limits the attainable pulse width.

Passive modulations. Conversely, this cavity loss modulation may be a function of the pulse intensity . As a consequence, the loss changes dynamically in response to the pulse, which itself is modulated in return. It is a nonlinear process that leads to a self-induced modulation with a period automatically synced to the cavity round-trip time. When the modulation happens in amplitude, we talk of *self-amplitude modulation* (SAM). These can be induced by adding a saturable loss element in the cavity, or *saturable absorber*. The phase can also vary dynamically with the time-dependent pulse intensity, leading to a *self-phase modulation* (SPM), occurring also at the pulse round-trip time. This process usually has a very fast response, such that only the instantaneous intensity matters in the nonlinear interaction. As a result, the pulse-shortening action can remain effective even for very short pulses. This mode-locking mechanism is therefore classified as passive, since the light itself initiates its own modulations through nonlinearities.

Dispersion. Finally, as we have seen in section 2.2.2, dispersion (due especially to quadratic and cubic phases) leads to serious consequences on the pulse shape and can therefore hinder short-pulse generation. In the laser cavity, dispersion comes from the gain medium, from the dielectric coating of the mirrors, or even simply from air. As the pulse gets broader after each round-trip, the temporal overlap in the cavity becomes weaker and this limits the efficiency of the lasing process. More importantly, this degrades the peak power and leads to weaker nonlinear effects. To minimize intracavity dispersion, a popular scheme for this is to use a shorter, more highly doped gain crystal. This minimizes the amount of dispersion acquired through the medium, but it does not compensate for other elements. Best results are then obtained by using a prism based compressor which material is carefully chosen, or by using specially designed chirped mirrors. The latter offer a very high and broadband reflectivity with the advantage of tailoring even better the phase they compensate and are usually prefered for few-cycles pulse generation.

[8]Note that since a Fabry-Perot cavity couples amplitude and phase, the modulations needed to achieve mode-locking can also be in phase.

To summarize, when a laser cavity is built with a broadband gain and a sufficient bandwidth, generation of short pulses can be achieved by modulating the intracavity field and a careful management of dispersion. We will now interest ourselves in one particular type of passive mode-locking, the solid-state Kerr mode-locking, as it might explain the correlations in the dynamics of amplitude and phase of the lasers that we investigate (cf. chapter 7).

2.4.2.2 Kerr-lens mode-locking

Nowadays, the most popular mode-locking technique with solid-states laser is called *Kerr-lens mode-locking* (KLM). KLM lasers based on titanium:sapphire (Ti:S) are particularly widespread. It consists of using the nonlinear response of the gain medium in which the nonlinear index leads to self-focusing in the laser cavity. This provides the modulation necessary to mode-lock the system. Note that this effect is an interplay between spatial and temporal properties of the field.

More precisely, the optical Kerr effect originates from the $\chi^{(3)}$ nonlinearity of the gain medium. The index of refraction of the medium depends on the intensity of the laser pulse. It is written as

$$n(\mathbf{r},t) = n_0 + n_2 I(\mathbf{r},t) \tag{2.51}$$

where $I(\mathbf{r},t)$ is the pulse intensity defined in (1.38). The pulse induces a change in the refractive index[9] of the material that is proportional to the instantaneous intensity. The response time of this nonlinear effect is not known exactly but is usually estimated to be 1 to 2 fs which can be considered as instantaneous.

As a result, after propagating in such a medium of length L, the field will acquire a nonlinear phase shift, given by

$$\boxed{\Delta\phi(\mathbf{r},t) = \frac{\omega}{c} n_2 I(\mathbf{r},t) L} \tag{2.52}$$

When approaching a pulsed regime, this effect induces both a fast SAM and a fast SPM, which may therefore be used as a mode-locking scheme. This process is highly dependent on the spatial profile of the lasing field. Once initiated, mode-locked operation is then self-sustaining.

Originally, the lasers that use this effect were described simply as "self-mode-locked" since the mode-locking mechanism was not identified at first. Afterwards, it was determined that a nonlinear lensing associated to the gain medium provides the fast amplitude modulation required for mode-locking. As pointed out earlier, because the response of

[9] In most laser materials, $n_2 > 0$ so the index actually increases with pulse power.

the medium is almost instantaneous, it is by this process that most of today's Ti:Sa lasers emit pulses of light in the sub 10-fs range.

From (2.52), it is clear that the KLM method is highly dependent on the temporal profile (*i.e* peak power) but also on the spatial profile of the lasing field. Indeed, when assuming a Gaussian profile such as (1.22), the intensity (hence the nonlinear effects) induced in the gain medium depends upon the radial coordinate. The change of index has therefore a radial dependency (and so does the phase) which is equivalent to a self-induced lens for the lasing mode. Under different conditions, this effect can reduce the loss or increase the gain, thus acting as a fast saturable absorber and resulting in self-amplitude modulation. When the loss is reduced, mode-locking becomes possible.

To reduce the loss using the spatial mode structure, a number of options are available. For example, it has been found quite remarkably that when a Ti:Sa laser cavity is slightly misaligned for a mixture of fundamental and higher order TEM modes to resonate, mode-locking could be induced by an external perturbation, such as tapping one of the cavity mirrors. This can be explained by the fact that a higher order mode has a wider spread and gets clipped somewhere in the cavity[10]. Self-lensing then improves the mode quality or decreases the beam size which in turn reduces the loss. There are also possibilities to accentuate and control the beam clipping effects by adding a slit close to the end mirror. This approach is called *hard-aperture KLM* and corresponds to one type of laser source that was used in this thesis (see 7.2.3). Finally, the gain can be increased since self-focusing may affect the overlap of the lasing mode with the spatial profile of the pump laser beam in the gain medium. The situation is in the end equivalent to the latter, and is called *soft-aperture KLM*. Such a laser is the other source used in this work (see 3.1.1).

What should be retained from this section is that the process by which ultra-short pulses of light are generated is a complicated one. It is a delicate interplay between non-linear effects (Kerr effect, self-amplitude and self-phase modulation, self-focussing, influence of the pump power...), spectral phase (negative group delay dispersion) and spatial characteristics of both laser and pump field. The full description of these effects is well beyond the scope of this thesis and we only need to remember that the dynamics of a laser field are obviously highly dependent upon them.

[10]This is one of the reasons that explain the poor spatial profile at the output of a mode-locked laser.

3 Revealing the multimode structure

(About doing experiments in the late evening) "It's not worth it; you think you have a good idea, but you just end up doing stupid things."

– Pu "*Pupu*" Jian

Contents

3.1 General experimental scheme 56
3.1.1 Laser source 57
3.1.2 Interferometric photodetection 59
3.1.3 Pulse shaping 62
3.1.3.1 Programmable mask pulse shaper 63
3.1.3.2 Pulse-shaping application to the experiment 64
3.1.3.3 Spectral phase compensation 64
3.1.3.4 Spectral interferometry 66
3.2 Signal measurement 68
3.2.1 Modulations of the field 68
3.2.1.1 Interferometric measurement of the modulations . . 68
3.2.1.2 The sidebands picture 69
3.2.2 Data acquisition 70
3.2.2.1 Demodulation of the signal 70
3.2.2.2 The power spectral density 72
3.3 Mode-dependent detection 73
3.3.1 Quantum derivation 73
3.3.2 Spectrally-resolved homodyne detection 75
3.3.2.1 Introduction 76
3.3.2.2 Multipixel basis 77
3.3.2.3 Multipixel homodyne signal 77
3.3.3 Temporally-resolved homodyne detection 78
3.3.3.1 Electric field cross-correlations 79
3.3.3.2 Application to homodyne detection 79
3.3.3.3 Experimental realization 80
3.3.4 Addendum: single diode homodyne detection 82

Having introduced the modal description of the field generated by an ultrafast frequency comb, we now present the experimental techniques to actually access this structure. This multimode description may be used to retrieve information encoded in the field.

Accessing experimentally these frequency-dependent quadratures have two prerequisites:

- Being able to measure the amplitude and the phase of the field. In practice, as it was stressed in equation (1.48), one may only measure the amplitude of the field. However, the phase quadrature information are experimentally transferred to an amplitude measurement. This is achieved by interferometric measurement called *homodyne detection*, a very widespread scheme in optics, and particularly in quantum optics[Adesso 14]. In this scheme, one field, called local oscillator, is used as a reference, while the other field, called signal, carries the information to be measured. One can then access the phase difference between the two fields.

- Resolving the temporal or the spectral structure of the field. The first solution is to disperse the spectrum on a diffraction grating and perform homodyne detection on a given spectral slice. This spectrally-resolved homodyne detection, called *multipixel homodyne detection* (MHD), is a very powerful and versatile tool to measure the multimode structure of the field. We present the working principle of the method in section 3.3.2. Another possibility is to physically change the spectral amplitude and phase of a field and perform a standard homodyne detection. This has been originally achieved in the group by shaping the spectrum of the local oscillator using a *pulse shaper*. In the homodyne detection, this allows selection of which spectral part of the field will interfere. Since already done in the past (see [Jian 14]), we only introduce the working principle of pulse-shaping in section 3.1.3, and we add a few details in appendix B. Although measuring from a spectral point of view seems easier, accessing it from the temporal side also yields interesting results. We call this last method *temporally-resolved homodyne detection*, and introduce it in section 3.3.3.

In this section, we focus on presenting the building blocks of the experiment that allow to extract this structure.

3.1 General experimental scheme

In this section, we present the general layout of the experiment. Subparts of it are built differently depending on the experiment but it can be summarized as shown on figure 3.1.

The beam generated by the femtosecond oscillator is split into the two arms of a Mach-Zehdner interferometer. 90% of the power is sent in the local oscillator (LO) arm, and the remaining 10% are sent into the signal beam. On the LO path, a pulse-shaper is introduced to address both the amplitude and the phase of the field.

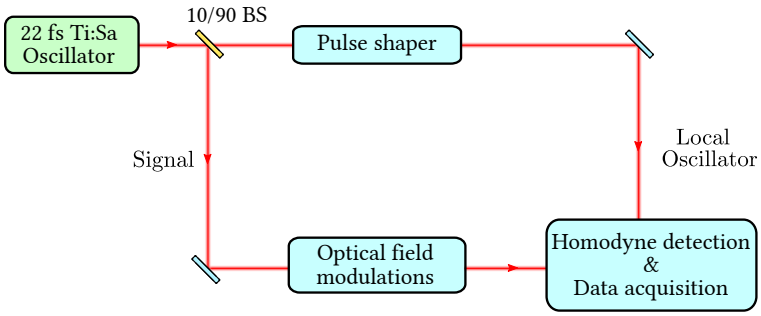

Figure 3.1: General experimental scheme, BS: beam-splitter.

On the signal path, we consider that, at some point, a spectrally-dependent perturbation occurs. It can be purposely introduced by an amplitude or phase modulator in the form of a modulation at a given frequency. This is what we opted for in parameter estimation, where we voluntarily modulate a physical parameter in order to measure it through a multimode description of the phenomenon. We develop this experiment in part II.

However, this modulation of the field does not need to be purposely introduced. Indeed, any source of noise (being mechanical, acoustical, thermal or technical in nature) can be represented as a modulation of the field on a range of frequencies (or equivalently, integration time). It is very natural to understand that at very high detection frequency (*i.e.* at a very short time scale), there can be no source of noise other that the quantum nature of light. Conversely, on a longer observation time (*i.e.* at low frequencies), influence from the surrounding environment becomes more noticeable. In part III, we use a similar scheme where one beam shows much lower noise figures (such that it can be taken as a reference) to actually extract the noise information of the other beam.

The two beams are then combined in a homodyne detection scheme and the resulting field is consequently measured.

We shall now present the different subparts of the experiment.

3.1.1 Laser source

The laser source is a Titanium-Sapphire based femtosecond oscillator from the Femtolasers company. It delivers pulses around 22 fs FWHM at a central wavelength of 795 nm for a repetition rate of 156 MHz. The average power is on the order of 1.1 W, therefore the energy contained in a pulse is about 7 nJ and the peak power is around 0.2 MW. The distance between subsequent pulses is then 1.92 m, *i.e.* 6 ns in the time domain. The spectrum is well approximated by a Gaussian of 42 nm width FWHM. The geometry of the laser cavity is depicted on figure 3.2.

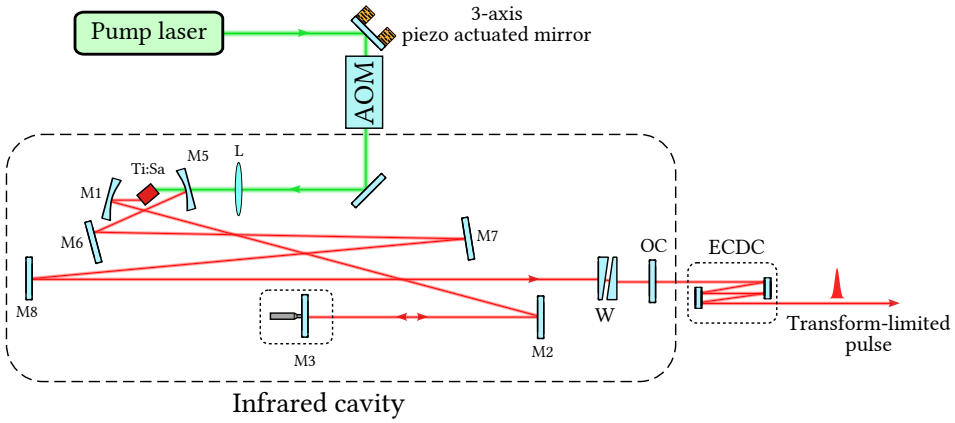

Figure 3.2: Laser cavity. M1 and M5 are curved mirrors, the other mirrors in the short and long arms are chirped. M3 is on a translation stage to fine-tune the stability range. OC: output coupler, W: wedge to adjust the CEP, ECDC: extra-cavity dispersion compensation to compress the pulse to the transform limit.

The gain medium is pumped by a Verdi V10 laser from Coherent. An acousto-optic modulator (AOM) is used to attenuate the pump power to around 5 W and can also be utilized to lock the CEO frequency of the comb [Helbing 02]. As the injection of the pump drifts on hours-time-scale, a quadrant detector is used on a leakage to detect the pointing drift, and a mirror mounted on piezo-electric actuators is used to lock the beam's position. The stability range of the cavity is controlled by changing the length of the short arm. The mode-locking mechanism is a soft-aperture KLM (see section 2.4.2.2). Intra-cavity dispersion compensation is achieved by chirped mirrors. At the output of the laser, the pulses are compressed to be transform-limited using an extra set of chirped mirrors.

Because this laser cavity is built using very short mounts and small optics, it is a very stable oscillator with good noise figures. It can remain modelocked over multiple days of operation as long as the environnement does not show abrupt variations. As it is usually the case with solide-state laser cavities, the main source of large time scale perturbation are thermal. A thorough analysis of the noise characteristics of this laser source may be found in [Schmeissner 14a].

This is not the only femtosecond source that was used in this thesis. In part III, we actually developed most of the experimental frame around another system that delivers longer pulses. The working principle of the laser cavity is however very similar to the one presented here.

3.1.2 Interferometric photodetection

Photodetection is a straightforward way to measure the field's intensity in optics. Since a standard detector integrates the intensity over a time much larger than the optical period, the information about the phase is then lost. To access the phase of the field, we make use of interferometric measurements. The beating of the two field results in an interference pattern which contains information on the phase difference between the two fields.

Consider the scheme depicted in figure 3.3. Two fields are mixed on a $50-50$ beamsplitter (BS). The first one, called *signal field*, is the field to be characterized. The second one, called *local oscillator*, serves as a reference. This denomination comes from the homodyne detection scheme that will be outlined in section 3.1.2, and we chose to keep this notation to describe the principle of interferometric measurements.

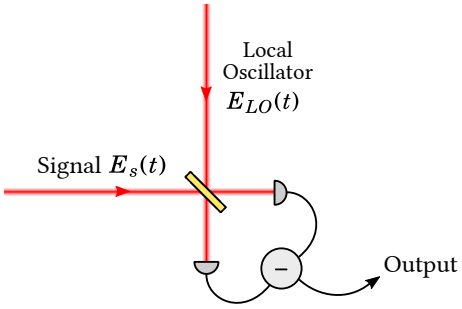

Figure 3.3: General homodyne detection scheme where two balanced photodiodes are used to detect the signal. The difference of the two photocurrent is subsequently taken to yield the homodyning signal.

The total field after the beamsplitter (that we consider a fixed longitudinal coordinate z, such that we may drop the z dependency) reads

$$E^{(+)}_{tot}(x,t) = \frac{E^{(+)}_s(x,t) \pm E^{(+)}_{LO}(x,t)}{\sqrt{2}} \tag{3.1}$$

where the $\pm$ sign depends on which output port of the beamsplitter is considered. Computing the intensity according to (1.38) yields:

$$I_{tot}(x,t) = \frac{I_s(x,t)}{2} + \frac{I_{LO}(x,t)}{2} \pm 2nc\varepsilon_0 \mathrm{Re}\left\{E^{(-)}_s(x,t)E^{(+)}_{LO}(x,t)\right\} \tag{3.2}$$

A standard square-law photodetector integrates the intensity over the detector size S and on a given integration time T. The efficiency of the photon-to-electron conver-

sion can be modeled by the responsivity $\mathscr{R}$ (in A/W) of the photodiode[1]. The retrieved photocurrent $\mathscr{I}$ is then written as

$$\mathscr{I}(t) = \mathscr{R} \int_S \mathrm{d}^2\boldsymbol{\rho} \int_t^{t+T} \mathrm{d}t' \, I(x,t') \equiv \mathscr{R} P(t) \tag{3.3}$$

where $P(t)$ is the detected power of the electric field.

The total photocurrent at one output of the beamsplitter is thus written as

$$\mathscr{I}_{tot}(t) = \frac{\mathscr{I}_s}{2}(t) + \frac{\mathscr{I}_{LO}}{2}(t) \pm \mathscr{R}\frac{\hbar\omega_0}{ST} \mathrm{Re}\left\{ \int_S \mathrm{d}^2\boldsymbol{\rho} \int_t^{t+T} \mathrm{d}t' \, a_s^*(x,t') a_{LO}(x,t') \right\} \tag{3.4}$$

where we injected the complex field expression and simplified some constant factors. Here, the envelopes a contain the phase of each field.

As we have seen in section 2.2.1, it seems more convenient to consider spectral phases rather than temporal phases, since the relation between the two is not always trivial. However, the concept of photodetection is more naturally put in the time domain since the signal is integrated over a finite time. To switch to the spectral domain, we inject the Fourier transform of $a(x,t)$ into (3.4). The temporal integral then writes as

$$\int_t^{t+T} \mathrm{d}t' \iint_{\mathbb{R}^2} \frac{\mathrm{d}\Omega}{\sqrt{2\pi}} \frac{\mathrm{d}\Omega'}{\sqrt{2\pi}} a_s^*(\Omega) a_{LO}(\Omega') e^{i(\Omega-\Omega')t'} \tag{3.5}$$

Since the bounds of the temporal integrals are not infinity, we need to apply a convenient approximation. We integrate over a time T a field whose spectral width is on the order of $\Delta\omega$. In the scope of this thesis where we do not require to resolve the pulsed regime, the detection time is on the order of the microsecond. For a laser source such as the one described in 3.1.1, the time-bandwidth product (2.24) implies that 20 fs pulses have a 50 THz bandwidth. It means that $\Delta w \times T \gg 1$ is valid over a very wide range of detection times T. Under this condition, we can consider the bounds of this integral as being infinite, allowing to consider the temporal integral as $\delta\left(\Omega - \Omega'\right)$[2].

Thus the photocurrent (3.4) is equivalently written as

$$\mathscr{I}_{tot} = \frac{\mathscr{I}_s}{2} + \frac{\mathscr{I}_{LO}}{2} \pm \mathscr{R}\frac{\hbar\omega_0}{ST} \mathrm{Re}\left\{ \int_S \mathrm{d}^2\boldsymbol{\rho} \int_{\mathbb{R}} \mathrm{d}\Omega \, a_s^*(x,\Omega) a_{LO}(x,\Omega) \right\} \tag{3.6}$$

[1] From (3.3), the responsivity $\mathscr{R}$ is defined by $\mathscr{R} = \frac{\mathscr{I}}{P}$. By writing both the photocurrent and the energy as containing respectively n electrons and N photons, the responsivity is defined by $\mathscr{R} = \eta\frac{q}{\hbar\omega_0}$. This introduces the quantum efficiency $\eta = \frac{n}{N}$ of the detector with $0 \geq \eta \geq 1$, a parameter that is more commonly referred to in the field of quantum optics.

[2] This approximation also allows to link the normalization condition (1.31) for spectral and temporal modes: $\int_{\mathbb{R}} \mathrm{d}\Omega \, u^*(\Omega)u(\Omega) = \int_t^{t+T} \mathrm{d}t' \, u^*(t')u(t') = T$

This expression still indicates that the measurement is taken over a finite detection time T. The two first terms in this equation contain only information about the energy in each field. To isolate the third term, we take the difference of the photocurrents at both outputs of the beamsplitter:

$$\mathscr{I}_- = 2\mathscr{R}\frac{\hbar\omega_0}{ST}\,\mathrm{Re}\left\{\int_S \mathrm{d}^2\boldsymbol{\rho}\int_{\mathbb{R}} \mathrm{d}\Omega\, a_s^*(x,\Omega)a_{LO}(x,\Omega)\right\} \tag{3.7}$$

The signal that is measured is then proportional to the cross-correlation between the two fields, which is necessarily phase-dependent. It is referred to as the *homodyne signal* and will be at the center of most experiments done in this thesis. A few relevant comments on this signal:

- This assumes that the beamsplitter is balanced, *i.e.* that the detected photocurrents associated to each field are equal on both detectors. It also involves that both detectors have the same responsivity $\mathscr{R}$.
- It is integrated over the full optical spectrum.
- Whereas the detection of a single beam would only yield the optical power, this interferometric scheme is sensitive to the phase of the field.

To further simplify the expression of the homodyne signal, let us write the signal field envelope as $a_s(x,\Omega) = \alpha_s w_s(x,\Omega)$ where the amplitude α_s is complex. We also consider the spatio-temporal mode is not coupled in space and time: $w(x,t) \equiv g(x)u(\Omega)$. Concerning the local oscillator field, in analogy to the quantum treatment, we write its complex amplitude as $\alpha_{LO} = \sqrt{N_{LO}}\,e^{i\phi_0}$. This notation allows to set the phase reference in this interferometric measurement. Finally, we choose to normalize every photocurrents by $\mathscr{R}\hbar\omega_0$, and we keep the same notation $\mathscr{I}_-$ for the normalized photocurrent.

Hence, the homodyne signal is written as

$$\boxed{\mathscr{I}_- = 2\sqrt{N_{LO}}\,\mathrm{Re}\left\{\alpha_s^*\,\Gamma_c\,e^{i\phi_0}\right\}} \tag{3.8}$$

where we introduced the homodyne overlap integral Γ_c. The overlap integral, also called *coherence* of the field, is factorized as follows:

$$\Gamma_c = \left(\frac{1}{S}\int_S \mathrm{d}^2\boldsymbol{\rho}\, g_s(x)^* g_{LO}(x)\right) \times \left(\frac{1}{T}\int_{\mathbb{R}} \mathrm{d}\Omega\, u_s^*(\Omega)u_{LO}(\Omega)\right) \equiv \gamma_\rho \times \gamma_\Omega \tag{3.9}$$

The spatial overlap integral γ_ρ denotes the spatial mode-matching between the two beams. Ideally, the two beams need to have the same transverse profile on the beamsplitter. In that case, this factor is equal to unity.

The γ_Ω integral contains a fair amount of information. It is quite similar to the spatial integral since it defines the spectral overlap between the two fields. To maximize it, one need to match both the spectral phases and the envelope. In the temporal domain, in analogy to the spatial case, this corresponds to the situation where both the envelopes and carriers of the two pulses overlap. This may be achieved through a variety of means, but the most efficient way to ensure a perfect temporal overlap is pulse shaping. We will develop this method in section 3.1.3.

Consider that we perfectly matched the two fields both spatially and spectrally. The coherence of the field is then unity. Hence, this interferometric measurement retrieves the signal

$$\mathscr{I}_- = 2\sqrt{N_{LO}}\,\mathrm{Re}\left\{\alpha_s^* e^{i\phi_0}\right\} \tag{3.10}$$

Having set the local oscillator as the field of reference[3], this allows to extract information on the amplitude and the phase of the signal field. Note that this signal is also amplified by the number of photons in the LO field. When this detection is operated in a configuration where the LO beam is stronger that the signal, this scheme is called a *homodyne detection*, that we expand in more details in section 3.3.

In this work, we look at fluctuations of the global mode $u(\Omega)$ which in the general case become accessible through Γ_c. In section 3.2.1, we give the example of modulating the signal field in either amplitude and phase, and apply this experimental scheme to retrieve information on the modulation.

In the following section, we present how the spectral overlap between the two fields can be experimentally optimized.

3.1.3 Pulse shaping

For the majority of applications in ultrafast optics, the necessity to carefully control the pulse shape is of great importance. The development of pulse shaping techniques has therefore been closely related to the advancements in ultrafast technologies. These techniques are complementary to ultrashort pulse generation and characterization methods. Their applications include amplified pulse compression, dispersion compensation for fiber optics communications, coherent control, spectroscopy and nonlinear microscopy, to name a few.

In this section, we present briefly the pulse shaping techniques that were used during this thesis and their purpose. More information on pulse shaping techniques can be found in [Weiner 95, Weiner 11b].

[3]The phase reference ϕ_0 can be defined so that $\alpha_s^* e^{i\phi_0}$ is real.

3.1.3.1 Programmable mask pulse shaper

For our applications, we chose to build a pulse shaper by using *spatial light modulation* (SLM) in a $4-f$ configuration, as depicted in figure 3.4. By diffracting the spectrum using diffraction gratings, we are able to address both the amplitude and the phase of each part of the spectrum. The resolution is limited by the one of the masks of the SLM. A more detailed description of the pulse shaper can be found in [Jian 14], and explanations on the alignment procedure in [Monmayrant 05] (although the chosen geometry differs). This pulse shaper was graciously lent to us by Béatrice Chatel.

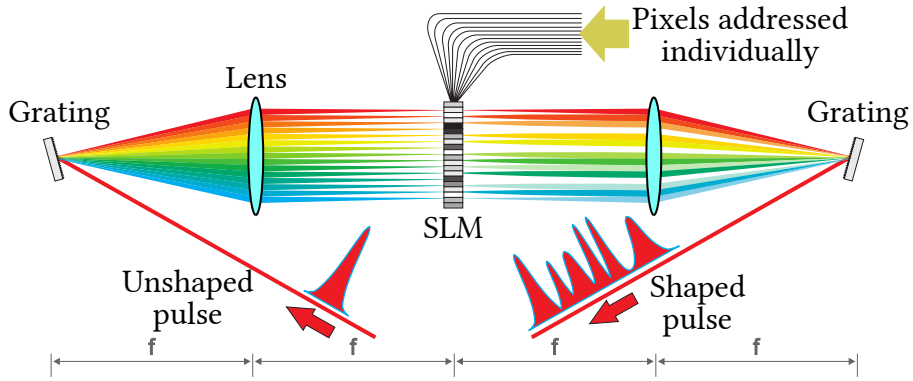

Figure 3.4: Schematic of a pulse-shaper in a 4-f configuration. [Figure by Jonathan Roslund]

The arrays, produced by the Jenoptik company, are composed of 640 pixels of nematic liquid crystals, comprised between two glass substrates. Transparent electrodes are deposited on the substrate as to control the voltage on each pixel. The total size of the mask is 64 × 10 mm. When applying a voltage between two electrodes, one can change the refractive index in the liquid crystal, and the array then acts as a phase mask. By combining two arrays with orthogonal polarizations and a polarizer at the output, it is possible to address both the amplitude and the phase of each "pixel" of the field.

This shaper has however some drawbacks. Being more than 10 years old, the delay between sending a command and the actual response of the crystal is on the order of 1 second, which is too long for complicated coherent control scheme or optimization procedure using evolutionary algorithm [Roslund 10]. It is also about 50 cm high, making it cumbersome to work with, whereas most recent pulse shapers can be as small as 10 cm. However, the use of a large SLM is vital when shaping short pulses; the spectrum being wide, in order to obtain a good resolution, one needs very diffractive gratings, therefore leading to short distances in the optical apparatus. Short distances are hard to work with when building a pulse shaper, since it will inevitably lead to a number of problems, such

as achromatism and spatial chirp. Therefore, we settled for a large mask that allowed for a more comfortable geometry in its design.

3.1.3.2 Pulse-shaping application to the experiment

While pulse shaping can be a very powerful tool to optimize light-matter interaction (for example, optimizing the temporal phase to maximize the efficiency in a non-linear process), our applications do not require a transform-limited pulse. Indeed, since we are dealing with linear interferometry, any common phase in each arm of the interferometer cancels out, and we need only to concern ourselves about the relative phase difference.

From equation (3.8) and (3.9), we set a perfect spatial overlap between the two fields (*i.e.* $\gamma_\rho = 1$). We also decompose the envelopes as amplitude and phase $a(\Omega) = |a(\Omega)|\, e^{i\phi(\Omega)}$. The phases defined here are spectrally dependent. The homodyne signal at the output of an interferometer is then proportional to

$$\mathscr{I}_- \propto \mathrm{Re}\left\{ \frac{1}{T} \int_{\mathbb{R}} \mathrm{d}\Omega\, |a_s(\Omega) a_{LO}(\Omega)|\, e^{i\delta\phi(\Omega)} e^{i\phi_0} \right\} \tag{3.11}$$

where we wrote the relative spectral phase between the two fields as $\delta\phi(\Omega) = \phi_{LO}(\Omega) - \phi_s(\Omega)$. As we pointed out in the previous section, the retrieved signal (3.8) is maximized when the overlap between the fields is optimal.

For our applications, we need to make absolutely sure that the relative spectral phase between the two arms of the interferometer is as flat as possible (*i.e.* shows no curvature, according to 2.2.1). This can be summarized by setting $\delta\phi = 0\, \forall\, \Omega$, and the most efficient way to achieve this condition is by pulse-shaping. Note that a mismatch in linear phase is easy to correct using a standard delay line. However, achieving a perfectly flat relative phase is problematic using standard compensation scheme such as prism compressors. Pulse shaping, though hard to implement, has the advantage of being versatile since any change in the dispersive elements can easily be accounted for.

As a complement to relative phase compensation, the pulse shaper can be also used to optimize the spectral overlap in amplitude between the two fields, although this has finally less of an impact on the resulting signal than phase mismatch. This spectral filter function has also been used to calibrate the multipixel detection (see section 5.3.1). Information and results on using the shaper to actually form the detection mode can be found in appendix B.

3.1.3.3 Spectral phase compensation

We quickly outline in this part the experimental procedure to match the phase between the two arms of the interferometer, since it has been routinely done when changing elements in the interferometer.

We start by setting the maximum voltage on the electrodes of the SLM such that its transmission is maximal (the pulse shaper is then equivalent to a zero-dispersion 4-f line). In the absence of any dispersive elements on the interferometer other than the strict necessary (achromatic mode-matching lenses for example), the phase between the two arms is relatively flat. When adding a dispersive element, two strategies can therefore be applied:

- Knowing the dispersive medium, it is possible to simulate how much phase it adds and write it on the shaper as a Taylor polynomial;
- Measure the relative phase by spectral interferometry, and apply it to the shaper as to minimize it.

To optimize the phase difference, a good metric is to look at the contrast of the optical fringes. This experimental quantity can be steadily measured by looking at the signal from a single diode at the output of the interferometer. To generate fringes, one needs to sweep the delay between the two fields. To do so, we set $\phi_0 = \omega_{mod}\tau$ which yields

$$\mathscr{I}_{tot}(\tau) = \frac{\mathscr{I}_s}{2} + \frac{\mathscr{I}_{LO}}{2} + 2\,\mathrm{Re}\left\{ \frac{1}{T}\int_{\mathbb{R}} \mathrm{d}\Omega\, |a_s(\Omega) a_{LO}(\Omega)|\, e^{i\delta\phi(\Omega)} e^{i\omega_{mod}\tau} \right\} \tag{3.12}$$

The interference term then oscillates at the modulation frequency ω_{mod}[4]. The contrast $\mathscr{C}$ of these fringes is given by the familiar formula

$$\mathscr{C} = \frac{\mathscr{I}_{tot}^{max} - \mathscr{I}_{tot}^{min}}{\mathscr{I}_{tot}^{max} + \mathscr{I}_{tot}^{min}} \tag{3.13}$$

The contrast can be easily linked to the coherence (3.9) using equation (3.12):

$$\mathscr{C} = \frac{2\sqrt{\mathscr{I}_s \mathscr{I}_{LO}}}{\mathscr{I}_s + \mathscr{I}_{LO}} \Gamma_c \tag{3.14}$$

Therefore, measuring the contrast of the balanced detection returns information on the spectral overlap in both amplitude and phase. For a constant phase $\Delta\phi$, the only remaining term that can influence the coherence is the spatial overlap between the two fields.

We stress however that this metric is not very sensitive to small shifts in the phase, and additional corrections are usually best achieved using spectral interferometry.

[4] This oscillation is easy to show in the monochromatic case. In our case, it can be deduced from (3.12) considering that a spectral phase difference lies obviously in the phase quadrature. Therefore, the interference term will be proportional to $\Gamma_c \sin\phi_0$.

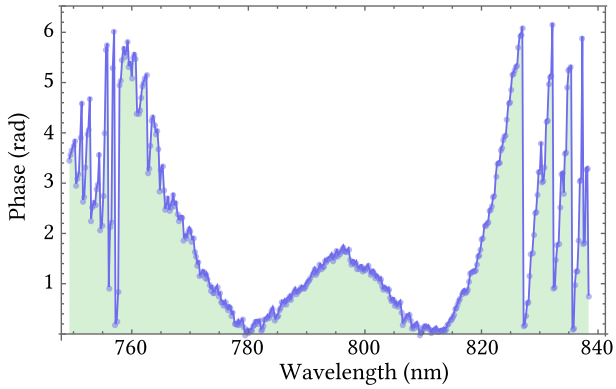

Figure 3.5: Experimental wrapped relative phase between the signal and LO fields of the Mach-Zehdner interferometer over the full width of the spectrum.

As an example, on figure (3.5) we show the spectral phase that is written on the shaper for the basic interferometer with the minimum dispersive elements in each arm. This correction ensures a contrast of more that 90%, limited only by the spatial mismatch of the two fields. We see that the phase is a balanced mix of quadratic and cubic components, probably because of the very thick achromatic lenses that are used for spatial mode-matching.

Note also that on this figure, the phase is wrapped every 2π. That is a consequence of the regime in which the shaper is operated, where the voltage applied in the electrodes is mapped in such a way that the phase is defined modulo 2π. In practice, this limits the maximum phase variation that can be written on it[5]: the neighbouring pixels of such discontinuities need to have their nematic crystal oriented in opposite directions. As a consequence, the field is diffracted and this causes a drop in the amplitude that appears as holes in the spectrum. This effect inevitably reduce the coherence between the two fields. Therefore, it has been preferable to compensate the quadratic dispersion as best as possible using linear optics (such as transparent glass), and only doing small corrections with the pulse shaper.

3.1.3.4 Spectral interferometry

As hinted at the end of section 2.3.3, spectral interferometry is a powerful and easy-to-implement technique when we only care about the relative spectral phase between two fields.

[5]The ultimate limit, however, is defined by the Nyquist limit. It can be summarized be stating that no phase difference greater that π may be imprinted on adjacent pixels. It is very similar to a sampling problem where undersampling will result in an ambiguity in the shaping process[Monmayrant 05].

Detecting one port of the beamsplitter with a spectrometer yields:

$$I_{tot}(\Omega) = \frac{I_s(\Omega)}{2} + \frac{I_{LO}(\Omega)}{2} + \mathscr{R}\frac{\hbar\omega_0}{S}\,\mathrm{Re}\left\{\int_S \mathrm{d}^2\boldsymbol{\rho}\, E_s^{(-)}(x,\Omega)E_{LO}^{(+)}(x,\Omega)\right\} \tag{3.15}$$

Doing a treatment similar to the photodetection, it is straightforward to obtain the detected signal:

$$I_{tot}(\Omega) = \frac{I_s(\Omega)}{2} + \frac{I_{LO}(\Omega)}{2} + |a_s(\Omega)a_{LO}(\Omega)|\cos\left[\phi_0 + \delta\phi(\Omega)\right] \tag{3.16}$$

We see that the overall spectrum shows an oscillation that is dependent on the relative spectral phase between the two fields. However, $\delta\phi(\Omega)$ is usually quite small and the spectrum modulation is experimentally masked by stronger fluctuations (such as air turbulences). A direct measurement of $\delta\phi(\Omega)$ is thus impossible to achieve using this signal.

A way around this limitation is to set a global delay between the two fields, *i.e.* $\phi_0 = \omega\tau$. In that case, the spectrum shows oscillations of a period $2\pi/\tau$ that are modulated by the spectral phase, which may then be extracted. This technique is called *spectral interferometry*.

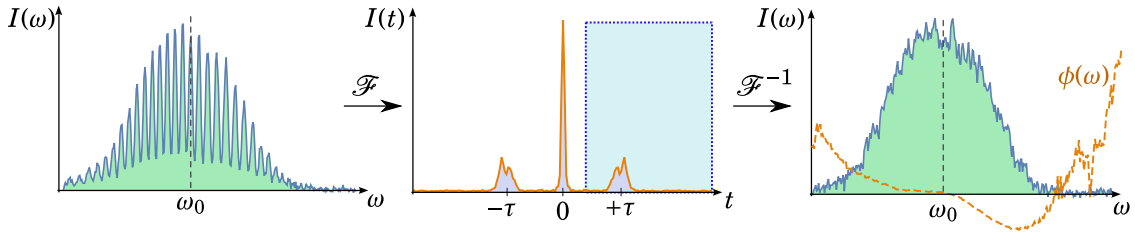

Figure 3.6: Fourier-transform spectral interferometry algorithm from experimental data. The delay between the two fields is on the order of 500 fs (*i.e.* 150 µm).

To show how the spectral phase is extracted, let us rewrite the interference part of equation (3.16) as

$$\frac{1}{2}|a_s(\Omega)a_{LO}(\Omega)|\left(e^{i(\Omega+\omega_0)\tau+i\delta\phi(\Omega)} + e^{-i(\Omega+\omega_0)\tau-i\delta\phi(\Omega)}\right) \tag{3.17}$$

Taking the Fourier transform of (3.17) transfers the signal to the temporal domain which exhibits sidebands at $\pm\tau$. We label them $f(t\pm\tau)$:

$$f(t\pm\tau) = \frac{1}{2}\int \mathrm{d}\Omega\, |a_s(\Omega)a_{LO}(\Omega)|\, e^{i\delta\phi(\Omega)}\, e^{i\Omega(t\pm\tau)} \tag{3.18}$$

By selecting one sideband and transferring it back to $t = 0$, another Fourier transform allows to retrieve the integrand $|a_s(\Omega)a_{LO}(\Omega)|\,e^{i\delta\phi(\Omega)}$. The modulus of that signal yields the product of the spectral envelopes whereas its argument gives directly the spectral phase.

This algorithm is called Fourier-transform spectral interferometry [Lepetit 95]. It is depicted on figure 3.6 for experimental data that eventually lead to the phase compensation shown on figure 3.5.

Using these methods, we are then able to ensure that the spectral overlap between the two mean fields is close to the optimum.

3.2 Signal measurement

In this section, we present how the information may be encoded either on the phase or on the amplitude quadrature of the field. We then show how this information may be retrieved using an interferometric measurement scheme.

We start by considering that the two fields are perfectly matched both temporally and spatially, such that the overlap integral (3.9) is equal to one.

3.2.1 Modulations of the field

As an analogy to radio frequencies, information may be hard-coded in the electric field by modulating it, either in amplitude or in phase. The description of the resulting field is necessary to properly retrieve this information.

The temporal representation of the signal field modulated in amplitude is written as

$$E^{(+)}_{AM}(t) = \mathscr{E}_0\Big(1 + m(t)\Big)\,\alpha_s\,u(t)\,e^{-i\omega_0 t} \tag{3.19}$$

where α_s is the complex envelope. Furthermore, a phase modulation reads

$$E^{(+)}_{PM}(t) = \mathscr{E}_0\,\alpha_s\,u(t)\,e^{-i(\omega_0 t - p(t))} \tag{3.20}$$

3.2.1.1 Interferometric measurement of the modulations

For a small modulation, we may expand the phase modulated field as

$$E^{(+)}_{PM}(t) \simeq \mathscr{E}_0\Big(1 + ip(t)\Big)\,\alpha_s\,u(t)\,e^{-i\omega_0 t} \tag{3.21}$$

Therefore, we can consider that the quantity that is being modulated is the complex amplitude of the field. It then becomes time-dependent and may be rewritten as

$$\alpha_s(t) = \alpha_s + \delta\alpha_s(t) \tag{3.22}$$

where $\delta\alpha_s(t)$ is equal to $m(t)\cdot\alpha_s$ for an amplitude modulation and $ip(t)\cdot\alpha_s$ for a phase modulation.

The signal at the output of the homodyne detection is obtained by replacing the complex envelope α_s in (3.8) by $\alpha_s(t)$. It is possible to do so for a modulation whose period is much slower than the response time of the detector. It is a reasonable assumption when modulating at MHz frequencies. The time-dependent homodyne signal then reads

$$\mathscr{I}_-(t) = 2\sqrt{N_{LO}}\,\mathrm{Re}\left\{\alpha_s^*(t)e^{i\phi_0}\right\} \equiv 2\sqrt{N_{LO}}\,\mathrm{Re}\left\{\alpha_s^* e^{i\phi_0} + \delta\alpha_s^*(t)e^{i\phi_0}\right\} \tag{3.23}$$

where we remind that we set the overlap integral $\Gamma_c = 1$.

If we define the phase reference ϕ_0 such that $\alpha_s^* e^{i\phi_0}$ is real, then for an amplitude modulation, the same phase ϕ_0 allows to retrieve the signal. On the contrary, for a phase modulation, the signal is maximal for a $\pi/2$ phase difference between the two fields.

3.2.1.2 The sidebands picture

The representation of the modulated field in the Fourier domain introduces the concept of sidebands of the optical carrier.

For that, we assume a sinusoidal profile for the modulations: $m(t) = m\cos\Omega_{RF}t$, and a similar expression for $p(t)$[6].

Using this expression, the phase modulated field may be expanded as

$$E_{PM}^{(+)}(t) = \mathscr{E}_0\, a(t)\, e^{-i\omega_0 t}\, e^{ip(t)} \tag{3.24}$$

For a small amplitude of modulation $p \ll 1$, the phase can be expanded, leading to (3.21).

In the Fourier domain, the phase modulated spectrum reads

$$E_{PM}^{(+)}(\Omega) = \mathscr{E}_0\left(a(\Omega) + i\frac{p}{2}a(\Omega-\Omega_{RF}) - i\frac{p}{2}a(\Omega+\Omega_{RF})\right) \tag{3.25}$$

In the case of a frequency comb, a phase modulation will result in sidebands appearing on both sides of each tooth with an imaginary amplitude. The situation is also very similar for an amplitude modulation where sidebands appear, but with a real amplitude :

$$E_{AM}^{(+)}(\Omega) = \mathscr{E}_0\left(a(\Omega) + \frac{m}{2}a(\Omega-\Omega_{RF}) + \frac{m}{2}a(\Omega+\Omega_{RF})\right) \tag{3.26}$$

This comb picture is sketched in figure 3.7.

The perturbation to the field therefore occurs at a given analysis frequency Ω_{RF} that can be differentiated from signals at baseband frequency.

[6]Note that this formulation of a modulation considers only one electrical quadrature. In the general case, either a phase or a sine term should be added.

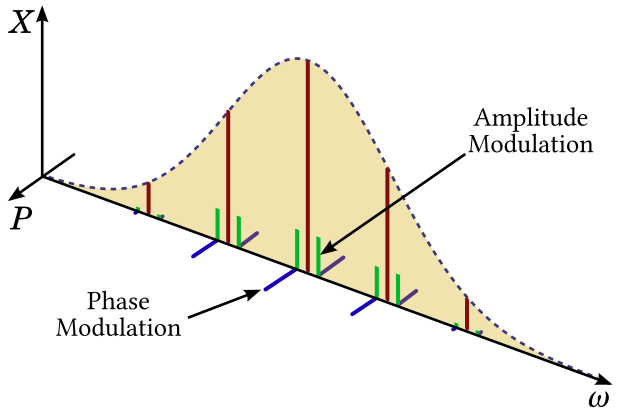

Figure 3.7: Phase-space representation of a frequency comb modulated in both amplitude (green lines) and phase (blue lines). The phase modulation switches sign on either side of a tooth.

3.2.2 Data acquisition

In equation (3.23), we showed that we can retrieve the information on the modulation through $\mathscr{I}_-(t)$. We now give more details on the tools at our disposal to characterize it. This leads naturally to some statistical consideration, the introduction of signal-to-noise (SNR) ratio and the concept of demodulation.

3.2.2.1 Demodulation of the signal

We consider that we retrieve the signal $\mathscr{I}_-(t)$ from (3.23) and we convert it to a voltage $V(t) = V_0 + \delta V(t)$ which encompasses the cases of both amplitude and phase optical quadrature measurements ($V_0 = 0$ in that case). This signal contains a DC term V_0 and some time-dependent variation.

We begin by considering a modulation such that $\delta V(t) = m\cos(\Omega_{RF}t)$. We are interested in retrieving the amplitude m of the modulation. A very common way in signal analysis is demodulation. It consists in multiplying the signal by another at the same frequency Ω_{RF} delivered by a reference (for example a function generator). Since there is no reason for these two signals to be synced, we need to set the phase φ of the reference. The mixing of the two signals can be done using an analogical mixer, but the process can also be digital.

The signal $X(t)$ at the output of the mixer reads

$$X(t) = V_0\cos\left(\Omega_{RF}t + \varphi\right) + m\cos(\Omega_{RF}t)\cos\left(\Omega_{RF}t + \varphi\right) \tag{3.27}$$

where we considered that the amplitude of the reference signal is 1[7]. Using product-to-sum trigonometric identities, the signal is rewritten as

$$X(t) = V_0 \cos\left(\Omega_{RF} t + \varphi\right) + \frac{m}{2}\Big(\cos\varphi + \cos\left(2\Omega_{RF} t + \varphi\right)\Big) \tag{3.28}$$

The resulting signal still shows oscillation, but we transferred the DC component to the quantity we want to measure. To isolate it, we apply a low-pass filter with a transfer function $h(f)$ of low cutoff frequency.

After low-pass filtering, the retrieved signal in the frequency domain is simply the product of the signal by the filter:

$$X(f)|_h = h(f) \cdot X(f) \tag{3.29}$$

Since the product of Fourier transforms is equal to the Fourier transform of their convolution product, the temporal signal at the output is directly the convolution of the signal by the filter:

$$X(t)|_h = \Big(h * X\Big)(t) \equiv \int_{\mathbb{R}} \mathrm{d}t' h(t'-t) X(t') \tag{3.30}$$

The filter function $h(f)$ has a low cutoff frequency, therefore its Fourier transform $h(t)$ is a very broad function[8]. As such, the integration on oscillating terms will be zero, and the only remaining term is

$$X(t)|_h = \frac{m}{2} \int_{\mathbb{R}} \mathrm{d}t' h(t'-t) \cos\varphi \tag{3.31}$$

By setting the demodulation phase φ, we select which electric quadrature is being measured. In that case, we measure m for $\varphi = 0$.

This signal is finally discretized by sampling at a given sampling rate f_s where each point X_i is the mean value $X_i = f_s \int_{1/f_s} X(t)|_h \ \mathrm{d}t$. This allows to characterize the signal by computing its mean and variance. We see that one would here always retrieve the exact value of m, since this model did not include any noise in the measurement (the variance of the detected signal is zero).

In order to take the noise into account, we simply add a stochastic variable $n(t)$ to $\delta V(t)$, leading to an extra term $\delta X(t)$ at the output of the mixer. It reads

$$\delta X(t)|_h = \int_{\mathbb{R}} \mathrm{d}t' h(t'-t) n(t') \cos\left(\Omega_{RF} t' + \varphi\right) \tag{3.32}$$

[7] In practice, an analogic mixer requires a specific power in the reference to be driven ,*i.e.* in order to extract the modulated signal above the noise.

[8] For a first-order low-pass filter with a cutoff frequency f_c, its transfer function is a lorentzian $h(f) = \frac{1}{1+\left(\frac{f}{f_c}\right)^2}$. Its temporal response is an exponential: $h(t) = \sqrt{\frac{\pi}{2}} f_c e^{-f_c|t|}$, which is therefore a function with a high temporal bandwidth for a small value of f_c.

which will retrieve the spectral component of $n(t)$ at the frequency Ω_{RF}. The amount of noise that is retrieved is dependent upon the width of the filter. For low cutoff frequencies (*i.e.* large temporal width), the fluctuations will average and the noise floor will then be lower. This bandwidth is called *resolution bandwidth*.

This picture including noise is more realistic, since the recovered distribution of X_i presents a certain variance σ_X^2. When no light hits the detector, at high analysis frequencies, the only present noise comes from the detection apparatus and is commonly referred to as *dark noise* $n_{dark}(t)$. When light hits the detector, at high analysis frequency, another noise source arises from the fluctuations of quantum vacuum, *i.e* the shot noise $n_{shot}(t)$. The baseline for noise may then be defined by measuring the variance of theses two signals. If the detection scheme allows to resolve the shot noise, taking the ratio of the variances of shot noise versus dark noise defines the clearance of the whole detection scheme.

In this work, we will rely heavily on this measurement scheme since it is quite easy to implement. Usually, to characterize a signal at multiple analysis frequencies, one would use a spectrum analyzer which functioning principle is very similar to what we developed here. This apparatus has the advantage of presenting a very low noise floor. It does however measure only a single signal at the same time, and in our work, we needed to acquire at most 16 signals simultaneously on a wide range of analysis frequencies.

3.2.2.2 The power spectral density

Some measurements were still done using a spectrum analyzer, mostly because of its very good noise figure. Therefore, we present here the working principle of a spectrum analyzer, which requires to consider the previous treatment in the frequency domain. Whereas the previous demodulation scheme retrieves a voltage, a spectrum analyzer retrieves the power.

The power spectral density (PSD) of $\mathscr{I}_-(t)$ is formally defined as:

$$S_{\mathscr{I}_-}(f) = \lim_{T\to\infty} \frac{1}{T} \left| \int_{-T/2}^{T/2} \frac{\mathrm{d}t}{\sqrt{2\pi}} \mathscr{I}_-(t) e^{2i\pi f t} \right|^2 \tag{3.33}$$

For a stationary process, the Wiener-Khinchin theorem allows to rewrite the power spectral density as the Fourier transform of the autocorrelation function of $\mathscr{I}_-$:

$$S_{\mathscr{I}_-}(f) = \iint_{\mathbb{R}^2} \frac{\mathrm{d}t}{\sqrt{2\pi}} \mathrm{d}t' \, \mathscr{I}_-(t') \mathscr{I}_-(t'-t) e^{2i\pi f t} \tag{3.34}$$

The variance of $\mathscr{I}_-(t)$ may be obtained from the PSD as:

$$\sigma^2_{\mathscr{I}_-} = \int_{\mathbb{R}} \mathrm{d}f \, S_{\mathscr{I}_-}(f) \tag{3.35}$$

$S_{\mathscr{I}_-}(f)$ is defined for both positive and negative values of f, and since $\mathscr{I}_-$ is real, its PSD contains redundant information. This description is called *double-sided*, in opposition to the *single-sided* description which considers only positive frequencies. Thus, the single-sided PSD is twice as large as the double-sided in order to conserve the total power contained in the sidebands.

This picture is similar to the one developed previously in the temporal domain except that it outputs a power distribution. If one requires the full distribution of the signal over a range of different RF frequencies, one would need to sweep the frequency of the local oscillator during the mixing process. This is precisely what a swept-tuned spectrum analyzer does: it aims to compute (3.35). In the same way, it needs to apply a filter function $h(f)$ such that this variance remains finite (very high frequency fluctuations such as white noise are usually present in such measurements). The measured variance is then equal to

$$\sigma^2_{\mathscr{I}_-}\Big|_h = \int_{\mathbb{R}} \mathrm{d}f\, S_{\mathscr{I}_-}(f)\,|h(f)|^2 \tag{3.36}$$

As previously, the shape and bandwidth of the filter defines for how long the acquisition window is opened and how high the noise floor is.

3.3 Mode-dependent detection

Having introduced the concept and outcome of an interferometric measurement scheme, we finally come to show that this detection is mode-dependent. Not only does it allows to retrieve information encoded on a specific quadrature of the field, it also enables to differentiate between different modes. To show this, we use a multimode quantum description of 3.1.2.

3.3.1 Quantum derivation

Similar to the quantization that was done in section 1.4, we consider the quantum counterpart of equation (3.7) where we assign a bosonic operator $\hat{a}(\Omega) = \sum_i \hat{a}_i u_i(\Omega)$ to the spectral envelope $a(\Omega)$. Considering again a perfect spatial overlap, the difference of photocurrent operator is given by

$$\hat{\mathscr{I}}_- = \frac{1}{T}\int \mathrm{d}\Omega\, \hat{a}_s^\dagger(\Omega)\hat{a}_{LO}(\Omega) + \text{h.c.} \tag{3.37}$$

where h.c. stands for hermitian conjugate.

Using the modal decomposition of the bosonic operator (1.59), this equation is written as

$$\hat{\mathscr{I}}_- = \frac{1}{T}\sum_{i,j}\hat{a}^\dagger_{i,s}\hat{a}_{j,LO}\int \mathrm{d}\Omega\, u^*_{i,s}(\Omega)\, u_{j,LO}(\Omega) + \text{h.c.} \tag{3.38}$$

Moreover, the normalization condition (1.31) allows to write the overlap integral in (3.38) as $\delta_{i,j}$. The quantum homodyne signal thus reduces to

$$\hat{\mathscr{I}}_- = \frac{1}{T}\sum_{i}\hat{a}^\dagger_{i,s}\hat{a}_{i,LO} + \text{h.c.} \tag{3.39}$$

We need to chose a proper basis to compute the noise in the measurement. We define the mean-field basis from the local oscillator, where only the first mode is non-vacuum:

$$\hat{a}_{LO} = \alpha_{LO}u_0(\Omega) + \sum_i \delta\hat{a}_{i,LO}\, u_i(\Omega) \tag{3.40}$$

where $\alpha_{LO} \equiv \sqrt{N_{LO}}\, e^{i\phi_{LO}}$ is the complex amplitude of the mean field and we expanded the annihilation operator as (1.65).

In the mean-field basis, the homodyne operator thus reads

$$\hat{\mathscr{I}}_- = \alpha_{LO}\,\hat{a}^\dagger_{0,s} + \sum_i \hat{a}^\dagger_{i,s}\,\delta\hat{a}_{i,LO} + \text{h.c.} \tag{3.41}$$

In the case where the LO beam is stronger than the signal (in other words, if N_{LO} is large enough), we may neglect the second term in this development. This approximation is at the center of homodyne detection. It implicates that the fluctuations of all the modes of the LO do not come into play in this measurement.

In term of quadratures operators (1.71), we can rewrite the homodyne operator as

$$\hat{\mathscr{I}}_- = \alpha_{LO}\,\hat{a}^\dagger_{0,s} + \alpha^*_{LO}\,\hat{a}_{0,s} \equiv \sqrt{N_{LO}}\,\hat{q}^{\phi_{LO}}_{0,s} \tag{3.42}$$

Therefore, computing the homodyne signal from the expectation value of (3.42) results in the expectation value of the signal quadrature operator in the quadrature defined by the local oscillator. This development also shows the mode selectivity of this scheme. Indeed, the detection only retrieves the mode of the signal field that is defined by the mean field mode of the local oscillator. Thus, we call this scheme a *projective measurement*.

Another relevant consideration is the quantum noise in this measurement. Considering the fluctuations of the homodyne signal $\delta\hat{\mathscr{I}}_- = \sqrt{N_{LO}}\,\delta\hat{q}^{\phi_{LO}}_{0,s}$, we can compute its variance:

$$\left\langle \left(\delta\hat{\mathscr{I}}_-\right)^2 \right\rangle = N_{LO}\left\langle \left(\delta\hat{q}^{\phi_{LO}}_{0,s}\right)^2 \right\rangle \tag{3.43}$$

Thus, the noise in the homodyne measurement is written as

$$\boxed{\Delta\mathscr{I}_- = \sqrt{N_{LO}}\,\sigma} \tag{3.44}$$

where σ is the noise in the mode of the signal field. When the noise originates only from the fluctuations of quantum vacuum, then $\sigma = 1$[9].

This quantum derivation is very useful to show the mode selectivity of the homodyne detection scheme. Although not straightforward, it can be linked to the classical treatment that was done in this chapter. Indeed, we adopted a purely monomode approach in the form of a single spectral mode. From this point of view, the homodyne detection measures the fluctuations (either in amplitude or in phase) of the global mode, that is accessible through the overlap integral Γ_c. In the quantum description, the overlap integral is always equal to unity by the construction of the detection basis. The signal that is measured is actually dependent on the expectation value of the bosonic operator in each mode of the signal field. Since this basis is constructed from the spectrum of the global mode, it is therefore entirely similar to the classical description.

Finally, another important fact to be retained from this section is that the local oscillator field needs to be stronger than the signal field in a homodyne detection scheme. It is vital to ensure that the noise from the LO field does not come into play.

3.3.2 Spectrally-resolved homodyne detection

In analogy to (3.38), for a local oscillator in a given mode $w_{LO}(x,t)$ and a multimode description of the signal field, the classical homodyne signal can be written as

$$\mathscr{I}_- = 2\sqrt{N_{LO}}\,\mathrm{Re}\left\{\sum_{i,n}\alpha^*_{i,n}\alpha_{LO}\left\langle w^*_{i,n}(x,t), w_{LO}(x,t)\right\rangle\right\} \tag{3.45}$$

where the inner product is defined as (1.31) and the $\{w_{i,n}\}$ modes form an orthonormal basis. Thus, to measure the amplitude of a given mode of the signal field, one has to set the LO in that same mode.

We consider the temporal part of this scalar product and are interested in how the local oscillator mode can be constructed. As it was hinted earlier, a first strategy is pulse-shaping to construct the projection mode and to perform the measurement. This means however that a new configuration needs to be established for each different mode. We present here a way to perform this projection after the measurement, which then allows to extract any mode from a single measurement.

[9] The quantum treatment is needed to properly identify the noise in this measurement. However, a similar result can be obtained from a monomode classical derivation.

The starting point is to notices that, in an interferometric measurement, once the beams are combined, the nature of the signal remains unchanged for linear operation. Therefore, if one could resolve each spectral component of the combined field, the result would be strictly equivalent to combine the same spectral component of each field on a different beamsplitter and then separately measure the different colors.

Thus, a spectrally-resolved homodyne detection is achieved by spatially dispersing the spectral component of the light (using either a grating or a prism[10]), focussing each of these colors on a linear array of detectors, and performing the detection. The general setup is sketched on figure 3.8.

Since this detection is done using a finite number of detectors, or *pixels*, we call this scheme *multipixel homodyne detection* (MHD).

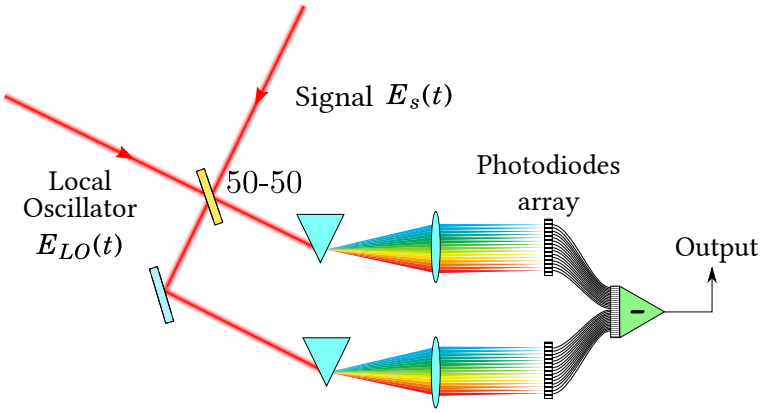

Figure 3.8: Spectrally-resolved homodyne detection.

3.3.2.1 Introduction

This detection was first introduced in the spatial domain for quantum state tomography [Beck 00]. Quantum state tomography is a technique based on homodyne detection to measure the quantum state of light and reconstruct the Wigner function of the state. As we will see in the next section, homodyne detection is sensitive to the mode mismatch between the two fields (represented by the overlap integral), and any mismatch will lead to a loss of efficiency and degrade the quality of the reconstruction. Optimization of the mode-matching (in that case, spatial, but in our case, it is spectral / temporal) can be achieved by shaping the beam, but it may not be an easy or robust task.

The solution proposed in [Beck 00] relies on using an array of detectors in the homodyne detection instead of single diodes, such that the mode-mismatch may actually be

[10] A prism cut at Brewster angle and properly placed in the beam will be less lossy than a grating, but less dispersive.

corrected *post facto*. For a more complete description of spatial multipixel detection, see [Morizur 11]. In the following, we give a description of spectral multipixel detection, which we will simply refer to as MHD.

3.3.2.2 Multipixel basis

We consider an array of N pixels, where N is an even integer. We assume it is centered on the carrier frequency ω_0 and it is subdivided so that each pixel corresponds to a spectral slice of width $\delta\omega$. We index each pixel by $n \in \mathbb{Z}$. This defines subset of the optical spectrum whose center frequencies are given by $\omega_n = \omega_0 + n\delta\omega$.

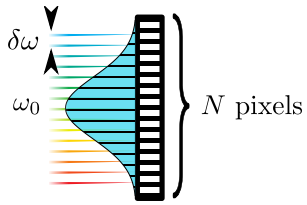

Figure 3.9: Multipixel array.

This defines a new set of modes, called *pixel-modes*, that we label $u_n(\omega)$. They can be defined from the whole spectrum:

$$u(\omega) = \sum_n^N u_n(\omega) \tag{3.46}$$

where a pixel-mode is obtained by "pixelization" of the envelope:

$$u_n(\omega) = \begin{cases} C_n\, u(\omega) & \text{if } \omega_n \le \omega < \omega_{n+1} \\ 0 & \text{otherwise} \end{cases} \tag{3.47}$$

where c_n ensures that each pixel-mode is normalized.

Any basis may therefore be represented in the multipixel basis using the same method.

3.3.2.3 Multipixel homodyne signal

To reconstructing the homodyne signal in the multipixel case, we first write (3.8) for a single pixel. It reads

$$\mathscr{I}_{-,n} = 2\sqrt{N_{LO}}\, \mathrm{Re}\left\{ \alpha^*_{s,n} \int_{\delta\omega} \mathrm{d}\omega\, u^*_{s,n}(\omega) u_{LO,n}(\omega) e^{i\phi_{LO}} \right\} \tag{3.48}$$

where we set once again a perfect spatial overlap (which doesn't depend on the pixel number in the absence of spatial chirp[11]). In theory, one would have to account for the dependency of the responsivity $\mathscr{R}$ on the pixel number, but it can be taken care of by an experimental calibration of the detector.

Usually, the two fields are in the same spectral mode (experimentally, that may not exactly be the case, but this mismatch can be compensated, as we will discover in section 5.4.2). Therefore, to introduce an arbitrary mode in the LO field, one has to reconstruct the homodyne signal by applying an arbitrary gain to the single-pixel signal :

$$\begin{aligned}\mathscr{I}_- &= \sum_{n=1}^{N} g_n \mathscr{I}_{-,n} \\ &= 2\sqrt{N_{LO}}\,\mathrm{Re}\left\{ \alpha_s^* \int_{\delta\omega} \mathrm{d}\omega\, u_s(\omega)\, u_{MP}(\omega)\, e^{i\Delta\phi(\omega)} \times \gamma_\rho \right\}\end{aligned} \tag{3.49}$$

where we wrote the effective mode of the LO field as

$$\boxed{u_{MP}(\omega) = \sum_n g_n\, u_{n,LO}(\omega)} \tag{3.50}$$

Again, it is reasonable to consider that the LO field is in the mean field mode, such that any projection mode can be constructed knowing the mean field mode. It is clear that modes that show a structure varying faster than the resolution of the array cannot be reconstructed.

In our case, we do not wish to reconstruct very complicated modes, such that meaningful information can be obtained even with only 4 pixels. Indeed, the strongest condition for reconstructing a basis is the orthogonality between its modes. One therefore needs as many pixels as there are peaks and valleys in the modes to construct them unambiguously.

3.3.3 Temporally-resolved homodyne detection

Finally, a very useful measurement scheme that was used during this PhD is a temporally-resolved homodyne detection. The general scheme is based on cross-correlations measurements, which derivation is similar to the one done for spectral interferometry in section 3.1.3.4. For our applications, it provides an incredibly convenient way to measure the homodyne signal independently of the optical quadrature.

[11] Spatial chirp can be a very serious problem when dealing with ultrashort pulses. It corresponds to the situation where different wavelengths are mapped to different part of the transverse beam, as an analogy to temporal chirp (2.2.2.3). It can be very easily introduced when working with diffracting elements such as pulse compressors.

3.3.3.1 Electric field cross-correlations

When scanning the delay between the two fields, the homodyne signal reads

$$\mathscr{I}_{-}(\tau) \propto \int_{\mathbb{R}} \mathrm{d}\Omega\, a_s^*(\Omega) a_{LO}(\Omega) e^{i\Omega\tau} + \text{c.c.} \tag{3.51}$$

where both envelopes are complex and contain their respective phases. Injecting the Fourier transforms of each envelopes yields the temporal representation:

$$\mathscr{I}_{-}(\tau) \propto \int_{T} \mathrm{d}t\, a_s^*(t) a_{LO}(t-\tau) e^{-i\omega_0\tau} + \text{c.c.} \tag{3.52}$$

For pulse characterization, if one field is known, then it is possible to extract both the amplitude and the phase of the other. For example, by considering that the LO pulse is a delta function, then the result of the measurement is proportional to $\mathrm{Re}\left\{a_s(\tau)e^{-i\omega_0\tau}\right\}$ (in the spectral domain, this means the spectrum of LO is much broader, and the signal spectrum is obtained by deconvolution). Therefore, the envelope of the crosscorrelation signal gives access to the amplitude of the field, while the argument gives access to its temporal phase. However, in the general case, nothing conclusive may be extracted about the pulse shape without making assumptions.

3.3.3.2 Application to homodyne detection

Nonetheless, we do not concern ourselves with the actual pulse shape, but we are rather interested in the relative phase between the two fields. Recording the homodyne signal as a function of the delay between the two fields has the great advantage of retrieving all the information at once.

We want to compute the homodyne signal as function of the delay τ between the two fields. This is done by setting $\phi_0 = \omega\tau \equiv (\Omega + \omega_0)\tau$ in (3.8). The signal then reads

$$\mathscr{I}_{-}(\tau) = 2\sqrt{N_{LO}}\,\mathrm{Re}\left\{\alpha_s^* \int \mathrm{d}\Omega\, u_s^*(\Omega) u_{LO}(\Omega) e^{i\Omega\tau} e^{i\omega_0\tau}\right\} \tag{3.53}$$

If we consider also a perfect spectral overlap, this simply reduces to

$$\mathscr{I}_{-}(\tau) = 2\sqrt{N_{LO}}\,\mathrm{Re}\left\{\alpha_s^* u_{cc}(\tau) e^{i\omega_0\tau}\right\} \tag{3.54}$$

where $u_{cc}(\tau)$ is the cross-correlation of the envelopes[12].

[12] If both fields are defined by the same Gaussian envelope of width Δt, the autocorrelation is another Gaussian of width $\sqrt{2}\Delta t$. Note however that this does not retrieve the absolute width of the pulse since this is a relative measurement.

This expression shows that all the information on the complex envelope α_s of the signal field may be retrieved in the envelope and the phase of the retrieved signal. More importantly, this method allows to measure every optical quadratures "simultaneously". To show this, we consider that the signal field is modulated either in amplitude or in phase, similar to (3.23). This signal is then written as

$$\mathscr{I}_-(\tau) = 2\sqrt{N_{LO}}\left(\mathrm{Re}\left\{\alpha_s^* u_{cc}(\tau)e^{i\omega_0\tau}\right\} + \mathrm{Re}\left\{\delta a_s^*(\tau)u_{cc}(\tau)e^{i\omega_0\tau}\right\}\right) \tag{3.55}$$

The information on the modulation is contained in the second term which can be isolated by demodulation. Whereas in the previous description, we need to set ϕ_0 to differentiate between an amplitude and a phase modulation, here they can both be accessed.

Moreover, this method can also be used to extract the spectral structure of the signal field, in the same way the multipixel homodyne does. Indeed, taking the Fourier transform of the cross-correlation signal (3.53) with respect to τ yields directly the integrand:

$$I^-(\Omega) = \mathscr{F}[I^-(\tau)] \equiv 2\sqrt{N_{LO}}\,\mathrm{Re}\left\{\alpha_s^*\, u_s^*(\Omega)\, u_{LO}(\Omega)\right\} \tag{3.56}$$

As we will see later, measuring this temporally resolved homodyne signal is an incredibly powerful and versatile tool that will allow to measure parameters precisely without resorting to complex experimental techniques. Indeed, the result is virtually identical to the multipixel scheme and can be used with a single detection. It may then prove to be an alternative to multipixel detection since it is possible to extract the spectral part from the signal.

3.3.3.3 Experimental realization

To actually measure the temporally-resolved homodyne signal, one needs to scan the delay between the two fields. Different methods are available, each presenting different constraints:

- This displacement needs to be purely longitudinal. If it induces an angular shift, then the spatial overlap will not be uniform over the range of the scan thus introducing errors.
- The best way to achieve such a delay scan is by putting a retroreflector on a motorized delay line. This allows to achieve displacements over a large range, more than enough to resolve the full pulse width. The drawback of this method is its speed: motorized translation stages do not respond fast enough to make such a measurement real-time.
- A mirror mounted on a piezoelectric actuator can offer micrometers of displacement on a millisecond timescale. This offer the fastest possible response, but it need to be introduced in the beam path with a minimum angle.

For our experiment, we decided to build a retroreflector on a motorized delay line. Initially, it was used solely for the purpose of crosscorrelations measurements, before this temporally-resolved homodyne detection was even considered. To account for the slow response, we chose to stabilize the relative phase between the two fields before the stage by building two consecutive homodyne detections. The experimental scheme is shown on figure 3.10.

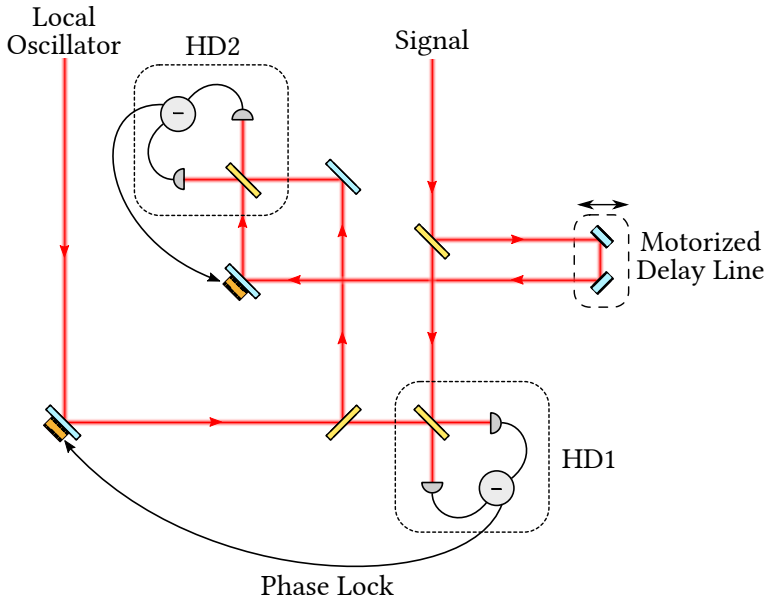

Figure 3.10: Experimental layout for the relative phase lock between signal and LO fields. The two fields are first separated by beamsplitter of 90% reflectivity. The transmitted 10% are combined in a first homodyne detection. The difference of the photocurrent is used to lock the delay between the two fields. Once the phases are stabilized, measurements can be done on a second homodyne detection.

Both signal and LO beams are split on a 90/10% beam splitter. On part goes to a first homodyne detection (HD1) while the second goes to the second homodyne detection (HD2) which has the retroreflector built into the signal beam's path. Using the low frequency signal from HD1, the relative phase between the two field is locked by acting on a piezo-mounted mirror. In such a configuration, the only phase fluctuations left come from the propagation of the two beams on a very short distance, and they are therefore very small. This allows to perform the crosscorrelation measurement with a very good reproducibility.

We specify that the second homodyne detection can either be single diode or spectrally-resolved.

3.3.4 Addendum: single diode homodyne detection

To close that part on homodyne detection, we explain one last relevant point. In homodyne detection, we take the difference of the two photocurrents to measure the interferometric term. It is not only to remove the signal coming from the power of both fields, but rather to get rid of any classical noise that might be contained in the fields.

It is clear from the signal of a single detector (3.16) and from the difference signal (3.8) that both contain the same interference term. The only difference between these two expressions reside in the power contained in each field, which is a term that does not oscillate. Therefore, when demodulating as described in section 3.2.2, the mean signal retrieved would be similar in both cases. The only important difference resides in the variance.

Indeed, if any amplitude classical noise is present, it will show when measuring the noise from a single diode, but not from the difference. The latter then present a higher SNR[13]. Nevertheless, if the analysis frequency is high enough, the only noise comes from quantum fluctuations. Thus, looking at only one photocurrent in the homodyne detection yields the same result than taking the difference at the expense of lower photon number.

[13]Note that classical noise will be present in the measured mean signal in whichever case. However, the noise floor is different, hence the signal-to-noise is higher in the real homodyne configuration.

Part II

Quantum metrology

4 Parameter estimation at the quantum limit

*(About the amount of squeezing required in quantum computation)"From what I got from the experimentalists, we don't have infinite squeezing **yet**."*

– Giulia "*Flash Dance*" Ferrini

Contents

4.1 Projective measurements 86
4.1.1 Displacements of the field in specific modes 86
4.1.2 Sensitivity 88
4.1.3 The Cramér-Rao bound 89
4.2 Spectral and temporal displacements 89
4.2.1 Temporal displacements 90
4.2.2 Spectral displacements 92
4.2.3 Conjugated parameters 94
4.2.4 Application to range-finding 96
4.2.4.1 Existing schemes 96
4.2.4.2 Ultimate limit in sensitivity 97
4.2.4.3 Addendum: higher order modes 99
4.3 Space-time coupling: a source of contamination 102
4.3.1 Transverse displacements 102
4.3.2 Homodyne contamination 104

In the previous chapter, we introduced how the multimode structure of the field can be experimentally accessed. In the present chapter, we shall describe the particular case of parameters that are willingly encoded in the field. It introduces the concept of projective measurement, detection modes, limits in sensitivity and efficient measurements.

We then concentrate our study to the case of perturbations of the pulse both in amplitude and in phase that originate from phase and energy shifts. We put forward the conjugated variables amplitude / phase and time / frequency that naturally arise, and give a proposal for a quantum formulation.

Then, we look at more precise examples of parameter estimation, such as distance and frequency. We define the detection modes for these quantities and compute their sensitivities.

Finally, we put forward a drawback in the projective measurement scheme where the

spatial part of the field can contain information that contaminates the measurement on its longitudinal part.

4.1 Projective measurements

In this section, we present in a more detailed way how the variation of a small parameter encoded in the field may be seen as photons being displaced in a given mode of the field. This defines the projections modes required in a homodyne detection scheme 3.3 to extract this parameter.

4.1.1 Displacements of the field in specific modes

In a way very similar to the modulations introduced in 3.2, let us consider that through propagation in a dispersive medium, the field is affected by a parameter p. Whether this perturbation happens in the amplitude or in the phase quadrature is of no importance for this general treatment. We also assume that the field is in a given spatial mode such that the transverse dependency of the field can be implicit[1]. The general scheme is depicted on figure 4.1.

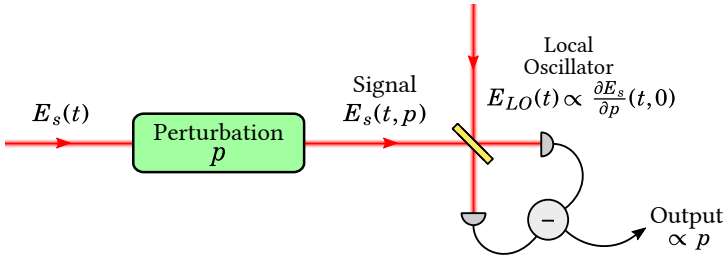

Figure 4.1: Projective measurement scheme.

The field after propagation reads

$$E^{(+)}(t,p) = \mathscr{E}_0\, a(t,p)\, e^{-i\omega_0 t} \tag{4.1}$$

To remain consistent with previous definitions, we again keep the carrier outside of the complex envelope $a(t)$. The parameter p may however be a perturbation of the carrier.

The general problem of estimating a parameter p encoded in a light beam $E(p)$ has been treated for example in [Helstrom 68]. The ultimate limit in sensitivity in the measurement is given by the so-called quantum Cramér-Rao bound for specific quantum

[1]Note that the present treatment can also be applied to the transverse profile of the field. It's only a matter of changing the considered variable from time to space.

states of light. For Gaussian states, it can be shown [Jian 14] that this bound can be experimentally reached with a balanced homodyne detection scheme.

For a small variation of p, the field (4.1) may be Taylor expanded as follows:

$$E^{(+)}(t,p) \simeq E^{(+)}(t,0) + p\,\frac{\partial E^{(+)}}{\partial p}(t,p=0) \tag{4.2}$$

The modal structure appears by writing (4.2) in term of the complex envelope:

$$\boxed{E^{(+)}(t,p) \simeq \mathscr{E}_0\left(a(t,0) + p\,\frac{\partial a}{\partial p}(t,0)\right) \equiv \mathscr{E}_0\alpha_s\left(u_0(t) + p\,K\,v(t)\right)e^{-i\omega_0 t}} \tag{4.3}$$

where we introduced the normalized mode $v(t) = \frac{1}{K}\frac{\partial u}{\partial p}(t,p=0)$ and K is a dimensional normalization constant which reads $K = \sqrt{\left\langle \left|\frac{\partial u}{\partial p}\right|, \left|\frac{\partial u}{\partial p}\right| \right\rangle}$, where the inner product is defined as (1.31). The mode $u_0(t) = u(t,0)$ corresponds to the mean-field, *i.e.* the envelope of the non-displaced field. The mode $v(t)$ is called the *detection mode* attached to the detection of the parameter p.

In the general case where multiple parameters $p_i \in \vec{p}$ are encoded in the field, the previous derivation applies and reads

$$E^{(+)}(t,\mathbf{p}) \simeq \mathscr{E}_0\left(a(t,\mathbf{0}) + \mathbf{p}\cdot\boldsymbol{\nabla}_{\mathbf{p}}\,a(t,\mathbf{0})\right) \equiv \mathscr{E}_0\alpha_s\left(u_0(t) + \sum_i p_i\,K_i\,v_i(t)\right)e^{-i\omega_0 t} \tag{4.4}$$

One should note that, in general, the modes v do not form an orthogonal basis. In this equation, the displaced field is defined as a superposition of the undisplaced field in the mean field mode and a set of different modes with a small contribution. We can thus image the fact that this perturbation is displacing photons into other modes (which is similar to power being pushed in sidebands in the spectral domain in the case of a modulation).

We also consider that the signal field is in a coherent state, such that $\alpha_s = \sqrt{N}$.

The retrieved signal in a homodyne configuration scheme is computed by considering that the signal field is given by (4.3) and the LO is in the mode $v(t)$. The situation is then similar to (3.43), where we retrieve the information carried by the signal field in the mode defined by the mean-field of the local oscillator. The optical quadrature that we retrieve is set by the phase of the local oscillator.

In this picture, the signal may also be written as the inner product of the signal envelope by the local oscillator mode:

$$\mathfrak{I}_- = 2\sqrt{N N_{LO}}\,\mathrm{Re}\left\{\langle u(t), v(t)\rangle\right\} \tag{4.5}$$

with $u(t) = u_0(t) + pKv(t)$.

As an example, let us consider the special case where $v(t)$ is orthogonal to $u_0(t)$. We then have $\langle u_0(t), v(t)\rangle = 0$ and $\langle v(t), v(t)\rangle = 1$. The homodyne signal then directly retrieves the value of p:

$$\mathfrak{I}_- = 2\sqrt{N N_{LO}}\, pK \tag{4.6}$$

To compute the signal-to-noise ratio Σ, one has to compute the noise in the experiment, which is given by (3.44):

$$\Delta\mathfrak{I}_- = \sqrt{N_{LO}}\,\sigma \tag{4.7}$$

where σ represents the noise in the detection mode. Thus, the signal-to-noise ratio reads

$$\boxed{\Sigma = \frac{2\sqrt{N}K}{\sigma}\cdot p} \tag{4.8}$$

If the only noise present arises from fluctuations of quantum vacuum, then we have $\sigma = 1$.

In the multi-parameters case described by (4.4), in the particular case where the modes $v_i(t)$ form an orthogonal basis, it is straightforward to see that a homodyne detection with the local oscillator in the mode $v_i(t)$ allows to retrieve unambiguously any parameter p_i encoded in the signal field.

4.1.2 Sensitivity

One can then determine the sensitivity with which we retrieve the parameter p. It is defined from the minimum value p_{min} of p that can be measured using this method, that is, for a signal-to-noise ratio of 1:

$$p_{min} = \frac{\sigma}{2\sqrt{N}K} \tag{4.9}$$

The sensitivity is then given by the inverse of p_{min}. In the quantum-limited case, we have:

$$\boxed{p_{min} = \frac{1}{2\sqrt{N}K}} \tag{4.10}$$

This important relation shows that the sensitivity increases with the photon number N and with the normalization constant K. In the more general case (4.9), we see that the sensitivity is also governed by the variance of the detection mode. It means that when

classical noise is present (*i.e.* $\sigma > 1$), sensitivity decreases, however, if squeezed quantum light is used ($\sigma < 1$), then sensitivity is increased. This is a standard result in quantum metrology, first demonstrated in [Caves 81], and a recent application example can be found in [Aasi 13].

Since the sensitivity (4.10) scales with the number of photons, we took the experimental strategy to work with strong coherent states rather than to use squeezed vacuum.

4.1.3 The Cramér-Rao bound

As hinted in the beginning of this section, the ultimate limit in sensitivity that one may achieve in the parameter estimation problem is given by the Cramér-Rao bound. Indeed, to know whether or not a given measurement scheme is optimal, one usually resorts to information theory. A good outlook into the classical Cramér-Rao bound may be found in [Réfrégier 02] whereas a quantum development and an application to this experiment is done in [Jian 14].

In information theory, the classical Cramér-Rao bound corresponds to the best precision that one can achieve using every possible estimator for a given parameter. This estimator is then said to be *unbiased* since it gives the correct value of the parameter that is estimated. This allows to determine which measurement apparatus or strategy is best suited to determine the value of a parameter.

This can then be redefined in the quantum realm in term of density operators. The measurement is described by a set of operators known as positive operator-value measure (POVM) [Barnett 02]. The derivation of this bound is more subtle than in the classical case, but it gives a stronger result. Indeed, the limit that one obtains is measurement independent, since the quantum Cramér-Rao bound is given whatever the measurement apparatus. This bound can be saturated, and has been extensively used in the field of quantum metrology [Anisimov 10].

In the case of multimode Gaussian states (for example, coherent states), this bound can be computed. More importantly, it has been demonstrated that the best sensitivity of parameter estimation using a balanced homodyne detection scheme equals the quantum Cramér-Rao bound, making this detection scheme an efficient measurement strategy.

The main result here is that the chosen projective measurement scheme yields the best possible outcome in the parameter estimation problem.

4.2 Spectral and temporal displacements

In this section, we concentrate our study to small displacements of the field in time (carrier and envelope) and to small displacements of the spectrum.

4.2.1 Temporal displacements

We use the results that were obtained in section 2.2.2 about spectral phase effects on the pulse shape. Let us Taylor expand the accumulated phase to the first order as in (2.33). For convenience, we identify characteristic times in the following way:

$$\phi(\Omega) \simeq \omega_0 t_\varphi + \Omega t_g \tag{4.11}$$

We identify t_φ as a displacement of the carrier and t_g as a displacement of the envelope.

The displaced field in the spectral domain is simply given by

$$E_s^{(+)}(\Omega) = \mathscr{E}_0 a(\Omega) e^{i(\omega_0 t_\varphi + \Omega t_g)} \tag{4.12}$$

Equivalently, in the temporal domain:

$$E_s^{(+)}(t) = \mathscr{E}_0 a(t - t_g) e^{-i\omega_0 (t - t_\varphi)} \tag{4.13}$$

which clearly shows the displacements in both carrier and envelope.

Since t_φ and t_g are supposedly small compared to the optical period, we then proceed to expand the amplitude and the phase of the temporal representation of the field. We then obtain

$$\begin{aligned} E_s^{(+)}(t) &\simeq \mathscr{E}_0 \sqrt{N} \left(u_0(t) - t_g \frac{\partial u_0}{\partial t} \right) \cdot \left(1 + i\omega_0 t_\varphi\right) e^{-i\omega_0 t} \\ &= \mathscr{E}_0 \sqrt{N} \left(u_0(t) + \omega_0 t_\varphi \cdot i u_0(t) - t_g \frac{\partial u_0}{\partial t} \right) e^{-i\omega_0 t} \end{aligned} \tag{4.14}$$

where we neglected the second order term $t_\varphi \cdot t_g$. We labeled u_0 the unperturbed field envelope, such that the total field is written as $E_s^{(+)}(t) = \mathscr{E}_0 \sqrt{N}\, u(t)$. We can see that equation (4.14) is similar to (4.3), except that not all modes are normalized.

After normalization of the modes on which (4.14) is expanded, the field then writes as

$$E_s^{(+)}(t) = \mathscr{E}_0 \sqrt{N}\, \alpha_s \left(u_0(t) + \omega_0 t_\varphi \cdot v_\varphi(t) + K_g t_g \cdot v_g(t) \right) e^{-i\omega_0 t} \tag{4.15}$$

The mode attached to the detection of a phase shift t_φ is called *phase mode* $v_\varphi(t)$, and is defined by

$$\boxed{v_\varphi(t) = i\, u_0(t)} \tag{4.16}$$

Note that v_φ is not orthogonal to the mean-field mode u_0.

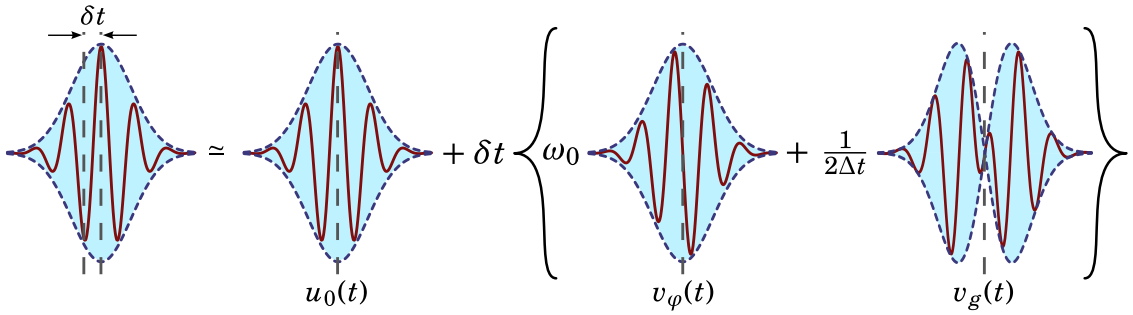

Figure 4.2: Schematic picture of a delayed pulse expanded on the basis of the detection modes.

As a reference to measurements that consider the time of arrival of pulses of light, we call the mode attached to the detection of a shift in the envelope t_g the *time-of-flight mode* $v_g(t)$. It is defined as

$$v_g(t) = -\frac{1}{K_g}\frac{\partial u_0}{\partial t}e^{-i\omega_0 t} \tag{4.17}$$

whose normalization constant K_g is given by $K_g = \sqrt{\int \mathrm{d}t \left|\frac{\partial u_0}{\partial t}\right|^2}$. In the Gaussian case given by (2.20), the normalization constant is actually proportional to the temporal bandwidth: $K_g = \frac{1}{2\Delta t}$ and the time-of-flight mode is consequently given by

$$\boxed{v_g(t) = \frac{t}{\Delta t}u_0(t) \equiv -2\Delta t\frac{\partial u_0}{\partial t}} \tag{4.18}$$

In that case, the field is written as

$$\boxed{E_s^{(+)}(t) = \mathscr{E}_0\sqrt{N}\left(u_0(t) + \omega_0 t_\varphi \cdot v_\varphi(t) + \frac{t_g}{2\Delta t}\cdot v_g(t)\right)e^{-i\omega_0 t}} \tag{4.19}$$

As an example, on figure 4.2 is depicted a representation of the real part of (4.19) in the case of a global delay of the pulse $t_\varphi = t_g = \delta t$.

In the same manner, the expansion of the Gaussian field in the spectral domain from (4.12) yields

$$\begin{aligned} E_s^{(+)}(\Omega) &\simeq \mathscr{E}_0\sqrt{N}\,u_0(\Omega)\big(1 + i\omega_0 t_\varphi + i\Omega t_g\big) \\ &\equiv \mathscr{E}_0\sqrt{N}\Big(u_0(\Omega) + \omega_0 t_\varphi \cdot v_\varphi(\Omega) + \Delta\omega\, t_g \cdot v_g(\Omega)\Big) \end{aligned} \tag{4.20}$$

The detection modes in the spectral domain are then given by

$$\boxed{v_\varphi(\Omega) = i\, u_0(\Omega)} \tag{4.21}$$

$$\boxed{v_g(\Omega) = i\frac{\Omega}{\Delta\omega} u_0(\Omega)} \tag{4.22}$$

Using the previously defined Fourier transform formalism, it is easy to show that the Gaussian detection modes are directly linked by Fourier transforms.

Note that every spectral mode is pure imaginary, whereas the temporal time-of-flight mode is real. Although surprising, it is understandable that a perturbation in the arrival time of a train of pulses can be resolved with a single detector; it is therefore an amplitude quadrature measurement in the temporal domain, but it cannot be resolved as easily in the spectral domain[2].

4.2.2 Spectral displacements

The previous derivation has an exact counterpart in the spectral domain.

Consider a displacement in the spectrum that manifests itself in the form of a global change ϵ of the amplitude. The envelope of the field is then written as $(1+\epsilon)a(\Omega)$, where we chose ϵ to be independent on wavelength for simplicity. Consider also a change $\delta\omega$ in the central wavelength, which then changes the amplitude to $a(\Omega-\delta\omega)$.

Using these notations, the displaced spectral field is consequently written as

$$E_s^{(+)}(\Omega) = \mathscr{E}_0\,(1+\epsilon)a(\Omega-\delta\omega) \tag{4.23}$$

Taking the Fourier transform simply yields

$$E_s^{(+)}(t) = \mathscr{E}_0\,(1+\epsilon)a(t)e^{-i(\omega_0-\delta\omega)t} \tag{4.24}$$

When expanding the field (4.23) and neglecting second-order terms, we then obtain

$$E_s^{(+)}(\Omega) \simeq \mathscr{E}_0\sqrt{N}\left(u_0(\Omega)+\epsilon\cdot u_0(\Omega)-\delta\omega\cdot\frac{\partial u_0}{\partial\Omega}\right) \tag{4.25}$$

A treatment identical to (4.19) allows to write the displaced spectrum as

$$\boxed{E_s^{(+)}(\Omega) = \mathscr{E}_0\sqrt{N}\left(u_0(\Omega)+\epsilon\cdot v_\epsilon(\Omega)+\frac{\delta\omega}{2\Delta\omega}\cdot v_{\delta\omega}(\Omega)\right)} \tag{4.26}$$

[2]One can also consider an infinitely accurate detector in the temporal domain. It could potentially resolve any effect on the pulse shape, being a delay, a broadening or a change in its structure. A spectrometer on the other hand cannot resolve any spectral phase without using interferometric measurements. A time measurement is then sensitive to the relative phase between each color.

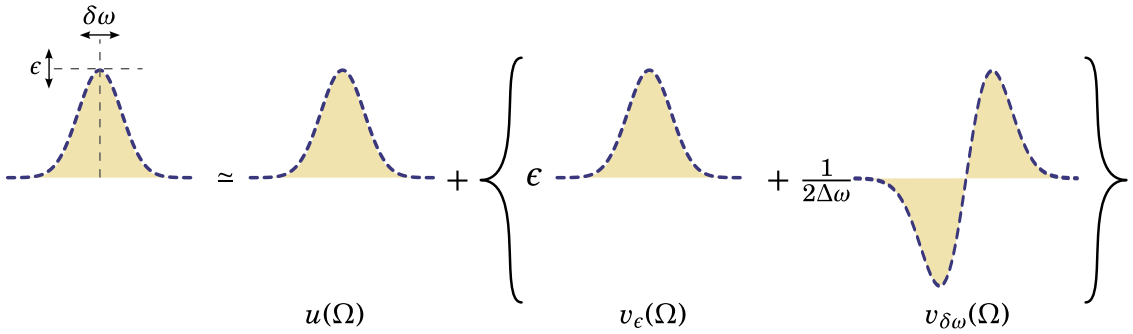

Figure 4.3: Schematic picture of a spectrum displaced in energy and in center wavelength expanded on the basis of the detection modes.

which defines the detection mode v_ϵ for a perturbation ϵ in the amplitude of the field

$$\boxed{v_\epsilon(\Omega) = u_0(\Omega)} \tag{4.27}$$

and the mode $v_{\delta\omega}$ attached to a shift of the central wavelength

$$\boxed{v_{\delta\omega}(\Omega) = \frac{\Omega}{\Delta\omega} u_0(\Omega)} \tag{4.28}$$

In the same way as before, figure 4.3 provides a schematic representation of equation (4.26).

In the temporal domain, equation (4.24) allows to define the temporal detection modes

$$v_\epsilon(t) = u_0(t) \quad \text{and} \quad v_{\delta\omega}(t) = i\frac{t}{\Delta t} u_0(t) \tag{4.29}$$

We see that the exact set of modes are used to detect these fours parameters. They differ in their definition by the imaginary unit i which specifies on which optical quadrature the information resides. More importantly, it also reveals that these parameters are conjugated in the sense of hamiltonian mechanics. Therefore, they are also observable of conjugated operators in a quantum description (see section 4.2.3).

Using (4.10), we compute the ultimate limit in sensitivity for these measurements. For the temporal displacements, we obtain

$$\boxed{\left(t_\varphi\right)_{min} = \frac{1}{2\sqrt{N}\,\omega_0} \quad \text{and} \quad \left(t_g\right)_{min} = \frac{1}{2\sqrt{N}\,\Delta\omega}} \tag{4.30}$$

and for the amplitude / spectrum displacements, we have

$$\boxed{\left(t_\epsilon\right)_{min} = \frac{1}{2\sqrt{N}} \quad \text{and} \quad \left(t_{\delta\omega}\right)_{min} = \frac{\Delta\omega}{\sqrt{N}}} \tag{4.31}$$

Using this modal description, we find the standard result for the ultimate sensitivity for an interferometric measurement of amplitude and phase[3].

Moreover, using a Gaussian mean-field mode allows to easily construct the detection basis. One may note that the detection basis that we derived here is similar to the Hermite-Gauss basis. This is quite convenient since these modes are directly orthogonal. For a non-Gaussian mean-field, the construction of the basis is not as straightforward. Indeed, there is no guarantee that the modes attached to the estimation of parameters are orthogonal. In that case, the construction of the basis needs to be adapted to the parameters that need to be measured. Albeit less general, we will keep the Gaussian definition for analytical reasons, but the same results may be obtained for an arbitrary mean-field.

4.2.3 Conjugated parameters

Introducing the Hermite-Gauss modes $v_n(\Omega)$[4], we have

$$v_0(\Omega) = u_0(\Omega) \quad \text{and} \quad v_1(\Omega) = \frac{\Omega}{\Delta\omega} u_0(\Omega) \tag{4.32}$$

which allows to rewrite the displaced fields in the same basis.

In the spectral domain, we consider a field displaced in all four of the previous parameters :

$$\boldsymbol{E}_s^{(+)}(\Omega) = \mathscr{E}_0 \sqrt{N} \left(v_0(\Omega) + \left(\epsilon + i\omega_0 t_\varphi\right) \cdot v_0(\Omega) + \left(\frac{\delta\omega}{2\Delta\omega} + i\Delta\omega t_g \right) \cdot v_1(\Omega) \right) \tag{4.33}$$

where we used the modes $\{v_n\}$ from the Hermite-Gauss basis.

This equation puts forward the conjugated parameters. The mean field mode v_0 is associated naturally to variations of amplitude, whose conjugate quantity is a shift in phase. Similarly, the mode v_1 carries the information on a shift in the envelope of the pulse. The conjugate parameter is a shift of the spectrum. In quantum mechanics, conjugate variables are observable that do not commute and satisfy Heisenberg's principle. The field of quantum metrology has usually focused on the measurement of a single variable. Its orthogonal observable may however contain information from a different origin that can be used to enhance the measurement result[Steinlechner 13].

[3] It is worth noting that the standard interferometer limit scales as $1/\sqrt{N}$. This difference by a factor of two arises from the fact that the homodyne-based measurement places the N signal photons into a single arm of the interferometer, whereas the standard interferometric detection distributes them equally between both arms.

[4] $v_n(\Omega) = \frac{1}{\sqrt{2^n n!}} H_n\left(\frac{\Omega}{\sqrt{2}\Delta\omega}\right) \cdot u(\Omega)$

To formulate the quantum counterpart of (4.33), we write $\langle \hat{a}_0 \rangle = \sqrt{N}$, and assume that only v_0 and v_1 are non-vacuum modes. Under the small parameter approximation, it reads

$$\hat{E}_s^{(+)}(\Omega) = \mathscr{E}_0 \left\{ \sqrt{N} \left[\left(1 + \epsilon + i\omega_0 t_\varphi\right) \cdot v_0(\Omega) + \left(\frac{\delta\omega}{2\Delta\omega} + i\Delta\omega t_g \right) \cdot v_1(\Omega) \right] + \sum_n \delta\hat{a}_n v_n(\Omega) \right\} \tag{4.34}$$

Ideally, we would like to define observables to measure the parameters encoded in the field. Using the quadrature operators (1.66) and (1.67), for a field in the Hermite-Gauss basis where the mean-field mode is v_0, we have

$$\hat{E}_s^{(+)}(\Omega) = \mathscr{E}_0 \sum_i \hat{a}_i \, v_i(\Omega) = \mathscr{E}_0 \sum_i \frac{\hat{x}_i + i\hat{p}_i}{2} \, v_i(\Omega) \tag{4.35}$$

Thus, in term of quantum observables, the field (4.34) is written as

$$\hat{E}_s^{(+)}(\Omega) = \mathscr{E}_0 \left(\frac{\langle \hat{x}_0 \rangle + i \, \langle \hat{p}_0 \rangle}{2} \, v_0(\Omega) + \frac{\langle \hat{x}_1 \rangle + i \, \langle \hat{p}_1 \rangle}{2} \, v_1(\Omega) + \sum_n \delta\hat{a}_n v_n(\Omega) \right) \tag{4.36}$$

By identification, we have the following relations:

$$\langle \hat{x}_0 \rangle = 2\sqrt{N}\,(1+\epsilon) \qquad \text{and} \qquad \langle \hat{p}_0 \rangle = 2\sqrt{N}\,\omega_0\, t_\varphi \tag{4.37}$$

$$\langle \hat{x}_1 \rangle = \sqrt{N}\,\frac{\delta\omega}{\Delta\omega} \qquad \text{and} \qquad \langle \hat{p}_1 \rangle = 2\sqrt{N}\,\Delta\omega\, t_g \tag{4.38}$$

We see that the mean-field mode v_0 is naturally used to detect the amplitude and the phase of the field. The next mode in the basis is used to detect slippage in time and in frequency. We may then define new conjugate operators $\hat{X}_i$ and $\hat{P}_i$ such that computing their expectation value yields the parameter of interest:

$$\hat{X}_0 = \frac{1}{2\sqrt{N}}\,\hat{x}_0 \qquad \text{and} \qquad \hat{P}_0 = \frac{1}{2\sqrt{N}\,\omega_0}\,\hat{p}_0 \tag{4.39}$$

$$\hat{X}_1 = \frac{\Delta\omega}{\sqrt{N}}\,\hat{x}_1 \qquad \text{and} \qquad \hat{P}_1 = \frac{1}{2\sqrt{N}\,\Delta\omega}\,\hat{p}_1 \tag{4.40}$$

This introduces clearly the couples of conjugate variables amplitude / phase and time / frequency as carried by different spectral modes. To perform a measurement below the standard quantum limit on one quantity, one would have to introduce squeezing in the same mode (the quantity retrieved in the other field quadrature would then show excess noise).

Being conjugate observables, using (1.68), the commutation relations for these new operators read

$$[\hat{X}_0, \hat{P}_0] = \frac{i}{2N\omega_0} \quad \text{and} \quad [\hat{X}_1, \hat{P}_1] = \frac{i}{N} \tag{4.41}$$

leading to the following uncertainty relations:

$$\sigma_{\hat{X}_0} \cdot \sigma_{\hat{P}_0} \geq \frac{1}{4N\omega_0} \quad \text{and} \quad \sigma_{\hat{X}_1} \cdot \sigma_{\hat{P}_1} \geq \frac{1}{2N} \tag{4.42}$$

In addition to the enhancement in sensitivity, the identification of conjugated observable allows to generate entanglement between them. We investigate this possibility in the last part of this thesis.

4.2.4 Application to range-finding

An application to our projective measurement scheme is space-time positionning, as proposed in [Lamine 08]. In the perspective of exchanging pulses of light between two observers, it is possible to determine the delay in time or in space between their time of arrival and a reference. In our description, it is similar to measuring t_φ and t_g.

In the first case, one uses the wave-like nature of light and uses interferometry to determine the offset between the carriers. The ambiguity range of such a measurement is on the order of the wavelength. In the second case, one considers the arrival time of the pulses envelope, leading to an ambiguity range dictated by the spacing between subsequent pulses. Naturally, combing the two methods leads to a more precise measurement.

In our vocabulary, it means that there exists a mode that combines the phase mode and the time-of-flight mode, which presents a higher sensitivity for measuring a global delay (or displacement).

4.2.4.1 Existing schemes

Combining interferometric with time-of-flight measurement is common method in absolute distance estimation. The first experiment from [Chekhovsky 98] uses picosecond pulses in a time-of-flight measurement, giving a rough estimation of distance, combined with white-light interferometry, thus enhancing precision.

As an example of a scheme combining interferometric and time-of-flight measurement using femtosecond pulses, we can cite the one proposed by Jun Ye in [Ye 04]. It is based on the fact that in an interferometer, when a distance difference is introduced between the two arms, the delay in the arrival of the two pulses depends also on the repetition rate of the laser. Monitoring the delay as a function of the repetition rate then

allows to retrieve the distance. The first estimate on distance is done using a fast detector while higher precision is achieved by measuring the contrast of the optical fringes. An experimental realization has been done in [Cui 08]. The precision of this scheme is limited by the timing jitter of the laser source.

This scheme is best suited for use in vacuum since it is sensitive to dispersion. To account for that effect, it is possible to consider the spectral phase accumulated. The distance can be retrieved by comparing the spectral phase between the reference arm and the target arm of an interferometer for different wavelengths. It is another application of spectral interferometry 3.1.3.4 to distance estimation [Cui 11]. The precision is however limited by the knowledge of the environnement parameter in order to compensate for it.

Another scheme derived from dual comb spectroscopy techniques has been demonstrated in [Coddington 09]. Two frequency combs with slightly different repetition rates are used: one is sent into an interferometer while the other is used as the local oscillator of an heterodyne cross-correlation scheme to analyze the output of the interferometer. The pulses from the two sources are then overlayed at different times. This technique can be seen as down-sampling of the signals which may be measured using slow detectors and electronics.

Finally, a purely time-of-flight technique can be mentioned [Kim 08]. It is called a balanced optical cross-correlator. Pulses coming from a target whose distance we want to determine are combined with a reference in a nonlinear $\chi^{(2)}$ crystal. A cross-correlation is obtained between the two pulses by measuring the sum frequency signal out of the crystal. The delay is retrieved by scanning the repetition rate between the two lasers and identifying zero cross-correlations signal. This method directly measures the group delay and no knowledge on the dispersives properties of the propagation medium is required. However, since it is a non-linear process, it is dependent on the pulses duration.

4.2.4.2 Ultimate limit in sensitivity

We compute the ultimate limits of sensitivity for an interferometric phase measurement or a time-of-flight measurement. We consider that light propagates in a weakly dispersive medium with a refractive index $n(\omega)$. Introducing a perturbation of propagation distance δL in the signal beam, the phase difference between the two fields writes as

$$\delta\phi(\omega) = \frac{\omega n(\omega)}{c}\delta L \tag{4.43}$$

We expand this phase, similar to (4.11):

$$\begin{aligned}\delta\phi(\omega) &\simeq \frac{\delta L}{c}\omega_0\, n(\omega_0) + (\omega-\omega_0)\left(n(\omega_0) + \omega_0 \left.\frac{\partial n}{\partial \omega}\right|_{\omega_0}\right) \\ &\equiv \omega_0\, t_\varphi + \Omega\, t_g \end{aligned} \tag{4.44}$$

where we neglected the second order dispersion. The time shifts of the carrier t_φ and of the envelope t_g are given by

$$t_\varphi = \frac{\delta L}{c}\, n_0 = \frac{\delta L}{\mathrm{v}_\varphi} \tag{4.45}$$

$$t_g = \frac{\delta L}{c}\left(n_0 + \omega_0\, n_0'\right) = \frac{\delta L}{\mathrm{v}_g} \tag{4.46}$$

where we introduced the phase and group velocities of light in the medium, and we wrote derivatives with respect to ω with a prime.

Using the derivation of the previous section, the delayed signal field is consequently written in the Hermite-Gauss basis $\{v_n\}$ as

$$E_s^{(+)}(\Omega) = \mathscr{E}_0\sqrt{N}\left(v_0(\Omega) + i\omega_0 t_\varphi \cdot v_0(\Omega) + i\Delta\omega t_g \cdot v_1(\Omega)\right) = \mathscr{E}_0\sqrt{N}\, u(\Omega) \tag{4.47}$$

where $u(\Omega)$ is the mode of the signal field[5]. Performing a projective measurement on iv_0 and iv_1 will retrieve respectively t_φ and t_g, thus giving information on δL with shot-noise limits given by (4.30). More precisely, the limit in sensitivity for a phase and a time-of-flight measurement are written as

$$(\delta L)^{\varphi}_{min} = \frac{\mathrm{v}_\varphi}{2\sqrt{N}\,\omega_0} \tag{4.48}$$

$$(\delta L)^{g}_{min} = \frac{\mathrm{v}_g}{2\sqrt{N}\,\Delta\omega} \tag{4.49}$$

Since the information on δL is carried by both modes, we can construct another detection mode corresponding to δL. We compute:

$$\left.\frac{\partial u}{\partial(\delta L)}\right|_{\delta L=0} = i\left(\frac{\omega_0}{\mathrm{v}_\varphi}\cdot v_0(\Omega) + \frac{\Delta\omega}{\mathrm{v}_g}\cdot v_1(\Omega)\right) \tag{4.50}$$

$$\equiv \left(\frac{\omega_0}{\mathrm{v}_\varphi}\cdot v_\varphi(\Omega) + \frac{\Delta\omega}{\mathrm{v}_g}\cdot v_g(\Omega)\right) \tag{4.51}$$

[5]Note that $u(\Omega)$ results from a Taylor expansion of a normalized mode. Therefore, it is no longer normalized.

For measuring δL, the ultimate limit of sensitivity is thus given by

$$\boxed{(\delta L)_{SQL} = \frac{1}{2\sqrt{N}} \frac{1}{\sqrt{\left(\frac{\omega_0}{\mathrm{v}_\varphi}\right)^2 + \left(\frac{\Delta\omega}{\mathrm{v}_g}\right)^2}}} \tag{4.52}$$

and the detection mode allowing to reach this sensitivity is given by

$$\boxed{v_{\delta L}(\Omega) = \frac{1}{\sqrt{\left(\frac{\omega_0}{\mathrm{v}_\varphi}\right)^2 + \left(\frac{\Delta\omega}{\mathrm{v}_g}\right)^2}} \left(\frac{\omega_0}{\mathrm{v}_\varphi} \cdot v_\varphi(\Omega) + \frac{\Delta\omega}{\mathrm{v}_g} \cdot v_g(\Omega)\right)} \tag{4.53}$$

We see indeed that the detection mode combines the phase mode and the time-of-flight mode to yield a more sensitive measurement of δL. The enhancement depends on the properties of the light source (by its wavelength and bandwidth) and on the properties of the dispersive medium. In the case of air, the dependency of index with wavelength is negligible such that $\mathrm{v}_\varphi \simeq \mathrm{v}_g$.

It is then similar to vacuum, where the phase velocities and group velocities of light are equal. And the detection mode is then given by

$$v_{\delta L}(\Omega) = \frac{1}{\sqrt{1 + \left(\frac{\Delta\omega}{\omega_0}\right)^2}} \left(v_\varphi(\Omega) + \frac{\Delta\omega}{\omega_0} \cdot v_g(\Omega)\right) \tag{4.54}$$

Here, the enhancement is only dependent on the wavelength and bandwidth of the laser. To make best use of this scheme using a coherent broadband source, the technical limitation to the enhancement is obtained for single-cycle pulses[6].

Since this scheme relies on linear interferometry, the pulse duration is not relevant, and spectrum broadening techniques, such as supercontinuum generation, can be used in order to increase even more the sensitivity.

Note that the description for a perturbation in mean wavelength and energy given in 4.2.2 may be written such that the amplitude of the field is affected by the change in wavelength. Since the parameter $\delta\omega$ would appear on both the amplitude and the time-of-flight mode, a similar development to the one done here would result in a detection mode to detect $\delta\omega$.

4.2.4.3 Addendum: higher order modes

In the previous treatment, we neglected the influence of dispersion. The main reason for that simplification is mostly technical. Experimentally, it is already difficult to measure

[6] A single-cycle pulse can be defined as $\Delta t_{FWHM} = \frac{2\pi}{\omega_0}$ [Brabec 97]. For Gaussian pulses, this yields $\frac{\Delta\omega}{\omega_0} \approx 0.2$.

the group delay term, and accessing the information about group delay dispersion using this scheme is not possible. One would need either a very dispersive material or a very high number of photons in the signal beam in order to extract the signal above the noise floor.

However, taking into account the dispersion results in another interesting application of the projective measurement scheme, that we propose to develop here.

Expanding the phase perturbation (4.43) to the second order yields

$$\delta\phi(\omega) \simeq \frac{\delta L}{c}\left\{\omega_0\, n(\omega_0) + (\omega-\omega_0)\left(n(\omega_0) + \omega_0 \left.\frac{\partial n}{\partial \omega}\right|_{\omega_0}\right) + \frac{(\omega-\omega_0)^2}{2}\left(2\left.\frac{\partial n}{\partial \omega}\right|_{\omega_0} + \omega_0 \left.\frac{\partial^2 n}{\partial \omega^2}\right|_{\omega_0}\right)\right\}$$

which can be rewritten as

$$\delta\phi(\Omega) = \omega_0\, t_\varphi + \Omega\, t_g + \frac{\Omega^2}{\omega_0}\, t_{GVD} \tag{4.55}$$

with

$$t_{GVD} = \omega_0 \left(n_0' + \frac{\omega_0}{2}\, n_0''\right)\frac{\delta L}{c} \tag{4.56}$$

With the previous treatment, the detection mode for t_{GVD} is given by

$$\begin{aligned} v_{GVD}(\Omega) &= i\frac{1}{\sqrt{3}}\frac{\Omega^2}{\Delta\omega^2}u_0(\Omega) \\ &= \frac{1}{\sqrt{3}}v_0(\Omega) + \sqrt{\frac{2}{3}}\,v_2(\Omega) \end{aligned} \tag{4.57}$$

where the mode of the field is written as

$$u(\Omega) = v_0(\Omega) + i\left(\omega_0 t_\varphi \cdot v_0(\Omega) + \Delta\omega t_g \cdot v_1(\Omega) + \sqrt{3}\,\frac{\Delta\omega^2}{\omega_0} t_{GVD} \cdot v_{GVD}(\Omega)\right) \tag{4.58}$$

The detection mode for a perturbation of group delay dispersion combines the first and third modes of the Hermite-Gauss basis. It is then clear that this mode is not orthogonal to the phase mode iv_0, but it is orthogonal to the time-of-flight mode iv_1. This mode description is another derivation to show that a time-of-flight measurement is insensitive to the effect of group-velocity dispersion. However, performing a measurement using the phase mode will be contaminated by dispersion. More precisely, it would retrieve

$$\langle u, v_\varphi \rangle = \omega_0\, t_\varphi + \frac{\Delta\omega^2}{\omega_0}\, t_{GVD} \tag{4.59}$$

and a projection on the dispersion mode would yield

$$\langle u, v_{GVD} \rangle = \frac{\omega_0}{\sqrt{3}} t_\varphi + \sqrt{3} \frac{\Delta\omega^2}{\omega_0} t_{GVD} \tag{4.60}$$

which would then be contaminated by the pure phase displacement.

The modal decomposition of the field allows to define purified modes to measure only one parameter independently of the other. In the case of GVD, it is straightforward to see that the purified mode is directly

$$v^p_{GVD}(\Omega) = v_2(\Omega) \tag{4.61}$$

The sensitivity of this purified mode is obtained by computing its normalization contant $K^p_{GVD} = K_{GVD} \langle v^p_{GVD}, v_{GVD} \rangle = \sqrt{2} \frac{\Delta\omega^2}{\omega_0}$. It is proportional to the constant of the original mode K_{GVD} by a factor equal to the overlap between the original and the purified modes. The measurement is thus more accurate but less precise.

Similarly, a purified phase mode v^p_φ would retrieve only the pure phase information without the dispersion. It is obtained by orthogonalization as follows:

$$v^p_\varphi(\Omega) \propto v_\varphi(\Omega) - \langle v_\varphi, v_{GVD} \rangle \cdot v_{GVD}(\Omega) \tag{4.62}$$

After normalization, the purified mode for phase detection is given by

$$v^p_\varphi(\Omega) = \sqrt{\frac{2}{3}} v_0(\Omega) - \frac{1}{\sqrt{3}} v_2(\Omega) \tag{4.63}$$

The sensitivity for this phase measurement is scaled by $K^p_\varphi = \sqrt{\frac{2}{3}} \omega_0$, leading to

$$\left(t^p_\varphi\right)_{min} = \frac{1}{2\sqrt{N}\sqrt{\frac{2}{3}}\omega_0} \tag{4.64}$$

Comparing to (4.30), we can see that the sensitivity for a phase measurement independent of dispersion is indeed degraded.

With this treatment, we showed the feasibility to use projective measurements as a mean to increase the accuracy of a ranging experiment in a dispersive medium at the expense of precision[7]. It is also possible to add other parameters to the development, thus building another detection modes basis. Two strategies can then be adopted.

[7] We stress that this modal description is another derivation of already existing schemes. For example, the fact that the time-of-flight mode is independent of dispersion is another representation of multiwavelengths interferometry that combines interferometric measurements at different wavelength.

The first one is to use an established model to define the detection modes. In [Jian 12], the Edlén model is used to characterize the dependency of the index of refraction of air on parameters such as pressure, humidity and temperature. It is then possible to construct a variety of modes that measure the variation of only a single parameter independently of the others.

Otherwise, it seems conceivable to adopt an evolutionary algorithm to build the detection mode. For example, if one were to dynamically address the projection mode on a ranging experiment in a dispersive medium, an optimization of that mode could potentially increase the signal to the optimal.

Obviously, all of these schemes are dependent on the amount of noise in the experiment, and the ability to distinguish the effects of other sources of noise to the fluctuations that we want to access.

4.3 Space-time coupling: a source of contamination

To conclude, we need to address the influence of the transverse profile of the field in the projective measurement scheme.

In most of our calculations, we considered that both beams in the interferometers were in the same spatial mode, such that the overlap integral γ_ρ is unity. When the beams are spatially multimode, not only does it degrade the signal, it can also cause a contamination on both optical quadratures. As a consequence, a phase measurement no longer retrieves a pure longitudinal information, but rather a mixture of longitudinal and transverse displacement.

4.3.1 Transverse displacements

Thanks to the symmetry between the spatial and the temporal description of the electric field, our previous treatment can be applied to the spatial domain. For a more detailed description, see [Delaubert 07]. For our purpose, we consider spatial perturbation only as displacement and tilt of the beam relative to a reference, as shown on figure 4.4.

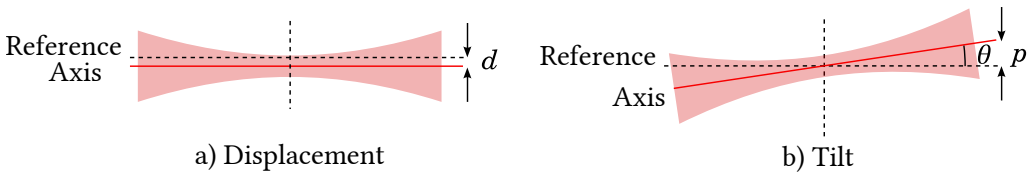

Figure 4.4: Representation of simple spatial modifications for a Gaussian beam relative to a reference axis. a) Displacement of the beam. b) Tilt or angular displacement θ.

We write the transverse envelope of the field as $a(x,z) = \alpha\, g_0(x,z)$ where we define the transverse mode as a TEM_{00} (1.27). In analogy to a displacement in time, we first consider that the beam is displacement along the x axis by a quantity d. The reference is naturally defined as $x = 0$. For simplicity, we center the longitudinal coordinate $z = 0$ at the beam waist. Although the beam's displacement does not depend on the longitudinal coordinate, the tilt of the beam needs to be defined around a pivot point, which we will define as the beam's waist.

The displaced transverse field is then expanded as

$$a(x) \simeq \alpha \left(g_0(x) + d \cdot \frac{\partial g_0}{\partial x}(x) \right) \tag{4.65}$$

The information on displacement is carried by $\frac{\partial g_0}{\partial x}$, which for TEM modes, is found to be exactly the TEM_{01} mode. The displaced field then writes as

$$a(x) \simeq \alpha \left(g_0(x) + \frac{d}{w_0} \cdot g_1(x) \right) \tag{4.66}$$

Note that the amplitude of the displacement is real.

On the other hand, the expression of a beam that is tilted by an angle θ with respect to a reference reads

$$a(x) = \alpha\, g_0(x\cos\theta)\, e^{ikx\sin\theta} \tag{4.67}$$

where $k = \frac{2\pi}{\lambda}$ is the norm of the wavevector at a wavelength λ. Here, the wavefront is tilted both in amplitude and in phase. In similar way as previously, we expand this phase considering that the angle θ is small[8], and we obtain the tilted field:

$$g(x) = \alpha \Big(g_0(x) + ip \cdot x g_0(x) \Big) \quad \text{with} \quad p = \frac{2\pi}{\lambda}\theta \tag{4.68}$$

The tilt information p is carried again by the mode $x g_0(x)$ which is directly proportional to the TEM_{01} mode for a TEM_{00} reference beam. It is carried in the phase quadrature of the field.

The expression of the field for a beam both displaced and tilted then reads

$$E(x) = \mathscr{E}_0 \alpha \left[g_0(x) + \left(\frac{d}{w_0} + i\frac{w_0 p}{2} \right) g_1(x) \right] \tag{4.69}$$

which is schematically depicted in figure 4.5.

It is obvious that, from the point of view of an experimentalist, a change in the position of a beam can come either from a global displacement and/or from a tilt of the beam.

[8] More precisely, the condition writes as $\lambda/w_0 \ll 1$.

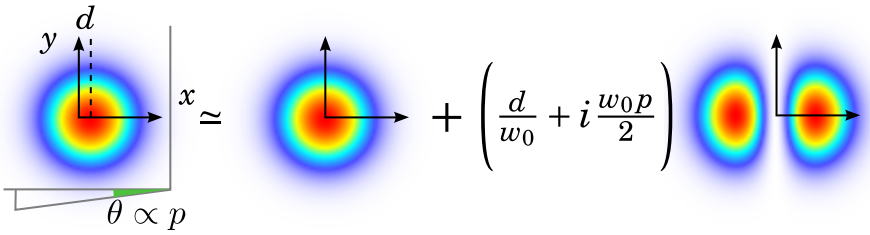

Figure 4.5: Representation of a displaced and tilted beam in the transverse plane. The tilt is represented here by an angle of the wavefront's plane with respect to a reference. The information about the displacement and the tilt are both carried by the TEM_{01} mode, but on orthogonal optical quadratures.

From equation (4.69), we see that one is distinguishable from another by accessing the amplitude or the phase quadrature of the TEM_{01} mode. As in the temporal domain, performing a projective measurement by projecting the displaced field on a local oscillator in the TEM_{01} mode allows to retrieve the information.

A displacement or a tilt of the beam can always be seen as a simple displacement in the detection plane. Hence, to properly distinguish between them experimentally, careful imaging needs to be achieved. Otherwise, if the detection plane is not at a well-defined point in space, a physical displacement and tilt of the beam translate into different quantities.

The important point is that both amplitude and phase optical quadratures contain information on the displacement of the beam. Again, this displacement can be described as photons being transferred to the TEM_{01} mode[9].

If one were to continue the expansion (4.65) up to the second order, it would show that the TEM_{02} mode carries information about a change in the waist size in the amplitude quadrature and a change in the longitudinal waist position in the phase quadrature.

4.3.2 Homodyne contamination

Let us consider that we want to detect a longitudinal displacement in a projective homodyne detection, as introduced in 4.2.1 and 4.2.4. We consider that whatever mean utilized to generate the longitudinal displacement in the signal field also induces a transverse displacement. We chose the longitudinal reference $z = 0$ as the point where the beams are combined. We write the signal mode as

$$g_s(x) = g_0(x) + \left(s_d + i s_p\right) \cdot g_1(x) \tag{4.70}$$

[9]The displacement and tilt of the beam also correspond to conjugated observables in a quantum description[Delaubert 06].

We also consider that the transverse mode of the local oscillator is mostly in a TEM_{00} mode with a small TEM_{01} contribution. We write:

$$g_{LO}(x,z) = \mu\, g_0(x,z) + \nu\, g_1(x,z) \equiv \mu\Big(g_0(x,z) + \eta g_1(x,z)\Big) \tag{4.71}$$

with $\left|\mu\right|^2 + |\nu|^2 = 1$, $\nu \ll 1$ and $\eta = \frac{\nu}{\mu} \ll 1$.

Since we did not specify the pivot point for the tilt, we simply write the two displacement parameters as s_d and s_p, as way to identify the optical quadrature. Note that these correspond in the general case to a mixture of displacement and tilt. In our experiment, we did not carefully image the displacement, therefore it is not possible to infer whether or not the information on the spatial amplitude and phase quadrature originate from displacement or tilt.

Computing the spatial overlap integral, as defined in (3.9), we then obtain

$$\gamma_\rho = \mu\Big(1 + \eta\left(s_d - i s_p\right)\Big) \tag{4.72}$$

where we remind that $\mu \simeq 1$ and $\eta \ll 1$[10]. In the following, we remove the dependency on μ since it is close to unity, and does not add anything relevant.

We remind that the spectral envelope of the signal field is written in the Hermite-Gauss basis as

$$u_s(\Omega) = v_0(\Omega) + i\Big(\omega_0\, t_\varphi \cdot v_0(\Omega) + \Delta\omega\, t_g \cdot v_1(\Omega)\Big) \tag{4.73}$$

The signal field is then found to be in the following spatio-temporal mode:

$$\begin{aligned} u_s(\Omega)\cdot g_s(x) = {} & v_0(\Omega)\Big[g_0(x) + \left(s_d - \omega_0 t_\varphi s_p\right)\cdot g_1(x)\Big] \\ & + i v_0(\Omega)\Big[\omega_0 t_\varphi \cdot g_0(x) + \left(s_p + \omega_0 t_\varphi s_d\right)\cdot g_1(x)\Big] \\ & - \; v_1(\Omega)\,\Delta\omega t_g s_p \cdot g_1(x) \\ & + i v_1(\Omega)\Big[\Delta\omega t_g \cdot g_0(x) + \Delta\omega t_g s_d\, g_1(x)\Big] \end{aligned} \tag{4.74}$$

We can see that the amplitude and phase quadratures of the signal field now contain both temporal and spatial parameters. By neglecting second order terms (*i.e.* terms similar to $t_\varphi s_d$ which are supposed to be small), we compute the overlap between the signal field (4.73) and the spatial part of the local oscillator (4.71):

$$\begin{aligned} u_s(\Omega)\cdot\gamma_\rho = {} & v_0(\Omega)\cdot\Big[1 + \eta\, s_d\Big] \\ & + i v_0(\Omega)\cdot\Big[\omega_0 t_\varphi + \eta\, s_p\Big] \\ & + i v_1(\Omega)\cdot\Delta\omega t_g \end{aligned} \tag{4.75}$$

[10] Note also that s_d and s_p are real quantities.

It is now clear from (4.75) that performing a projective measurement on the mode iv_0 attached to a phase measurement will not retrieve only a information on a longitudinal displacement. The measurement is then contaminated by the spatial displacement, depending on how much TEM_{01} component there is in the local oscillator beam.

For no TEM_{01} contribution in the local oscillator ($\eta = 0$), as before, we retrieve either t_φ or t_g by projecting on respectively the phase mode iv_0 and the time-of-flight mode iv_1. However, when $\eta \neq 0$, projecting on the phase mode retrieves

$$\mathscr{I}_- \propto \eta s_p + \omega_0 t_\varphi \tag{4.76}$$

Even though η is supposed to be small, for a precision measurement, the contamination can become significant. In the time domain, this spatial effect can be seen as an additional delay of the carrier.

Interestingly enough, projecting on the time-of-flight mode does not retrieve any spatial information (at the first order). This mode will retrieve purely a timing information, independently on the amount of spatial displacement.

Since we interest ourselves into the ultimate limits in the sensitivity to measure a purely longitudinal displacement, these spatial effects can affect the result. It is therefore of utmost importance to control the transverse displacement of the beam in our sensitivity measurements.

5 Measuring the multimode field

*"The starting point is to do just a **simple** time measurement."*
– Nicolas "*The Boss*" Treps

Contents

5.1 Experimental details . . . 108
5.1.1 Measurement strategy . . . 109
5.1.2 Phase modulation at high frequencies . . . 110
5.1.3 Spatial filtering . . . 114
5.2 Interferometer calibration . . . 115
5.2.1 Calibration of displacement . . . 116
5.2.1.1 Methodology . . . 116
5.2.1.2 Experimental procedure . . . 118
5.2.1.3 Results . . . 119
5.2.2 Sensitivity measurement . . . 120
5.3 Multipixel detection . . . 122
5.3.1 Design and construction . . . 122
5.3.1.1 Optical and electrical design . . . 122
5.3.1.2 Alignement procedure . . . 124
5.3.2 Gain calibration . . . 125
5.3.3 Space-wavelength mapping . . . 127
5.3.4 Clearance . . . 128
5.4 Spectrally-resolved multimode parameter estimation . . . 128
5.4.1 A glimpse at the multimode structure . . . 129
5.4.2 Signal extraction . . . 132
5.4.3 Heterodyne measurements: the need for a stable reference . . . 134
5.4.4 Space-time positioning . . . 136
5.4.4.1 Phase and time-of-flight measurements . . . 136
5.4.4.2 Detection mode . . . 139
5.4.5 Dispersion . . . 141
5.4.6 Quantum spectrometer . . . 144

In this chapter, we present the main results of the parameter estimation experiment. It is in the continuity of the range-finding experiment done by Pu Jian during her PhD [Jian 14]. Back then, the main experimental setup was built, and the goal was to show the application of projective measurements to parameter estimation, and in particular to range-finding. The ultimate objective was to use different modes to measure different

parameters that are encoded into the beam of light. For example, one can assign different modes sensitive to a variety of different physical effects that arise due to propagation through a dispersive medium [Jian 12].

The proof-of-principle experiment was realized using a pulse-shaper to create a local oscillator mode that shows different sensitivities to a path difference between the two arms of the interferometer. It relied on a careful calibration of this displacement. The next step was to use projective measurements to differentiate between a displacement in free-space or in vacuum, i.e. to differentiate between a difference in true path or in optical path.

In the work that we present here, the main objective remains, but we had to make different choices on the experimental side. A lot of the original ideas proved difficult to implement, and the parameters that we wanted to access ended up being too small to be measured with good confidence. Moreover, the spatial contamination described in (4.3) proved to be significant, even though the spatial overlap seemed sufficiently high. In this section, we therefore settle to show the following points:

- Using the mean-field mode, we measure the sensitivity of a Mach-Zehdner interferometer, and we show that it coincides with the Cramér-Rao bound for coherent states (4.30). This calibration is done in an absolute manner, without assuming anything about the losses in the measurement process.

- Making use of a spectrally resolved homodyne detection, we show that the multimode structure of the field is accessible with a single shot measurement, and that we can therefore do a post-facto projective measurement.

- We apply this experimental scheme to the original range-finding experiment, and derive the sensitivity of a mode attached to a displacement in phase, a displacement in the envelope, and finally we show that the ultimate sensitivity is attained using the detection mode. We then measure the same parameter with different modes, resulting in different sensitivities.

- Finally, we show that one can effectively measure different parameters using different projection modes. Using a spectral and time-resolved homodyne detection, we measure the difference in optical path between two arms of the interferometers when a heavily dispersive material is introduced.

5.1 Experimental details

As we hinted in the introduction, the whole experiment proved to be more difficult than first expected. It eventually grew more and more in complexity in order to show even

the simplest results with reproducibility and confidence. For example, the spatial contamination required the experiment to be adapted to the new constraints rather than being entirely rebuilt.

In this section, we outline details on the experimental scheme, the way it is constructed and the way the information is measured.

5.1.1 Measurement strategy

To summarize, we want to measure the parameters outlined in section 4.2 using a projective measurement scheme. Ideally, we would like this measurement to be quantum-limited since we are interested in the ultimate limits in sensitivity. These limits are only achieved when the only noise present in the light source is the fluctuations of quantum vacuum (*i.e.* $\sigma = 1$ in equation (4.9)).

In a homodyne configuration scheme, the noise of importance in the measurement is the amplitude noise. Indeed, since the two arms of the interferometer comes from the same source, the phase noise does not come into play.

To determine the frequency at which the laser source is shot-noise limited in amplitude, a standard measurement is a balanced detection. It consists in splitting equally on a beamsplitter the field and measure the power spectral density of the noise with two balanced diodes. Taking the sum of the photocurrents yields the classical noise of the original beam, whereas taking the difference yields the shot noise. Indeed, since any classical noise subtracts when taking the difference, what remains is the quantum nature of light. The result, using a homebuilt photodetector, is shown on figure 5.1.

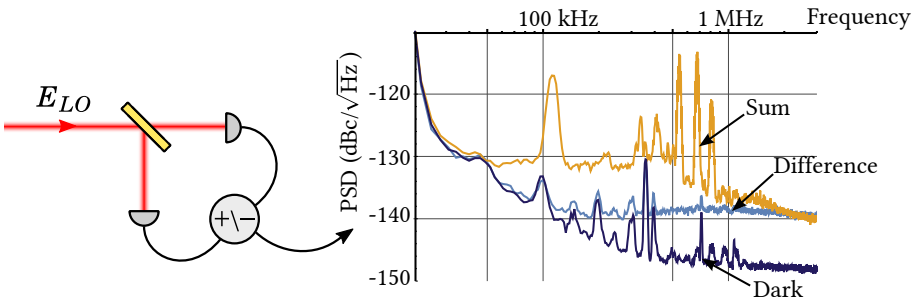

Figure 5.1: Balanced detection and resulting noise traces. The sum gives the amplitude noise, difference gives the shot noise. The laser source is shown to be shot-noise limited in amplitude at 2 MHz.

On this plot, we show the amplitude noise, the shot noise and the dark noise of the detector. The amount of light on the detector is on the order of 200 µW, and the noise level is given in Decibel-Carrier dBc, *i.e.* the noise level relative to the power contained in the optical carrier. We can see that the amplitude noise is at the same level than the

shot noise at around 2 MHz. We also added the dark noise of the detection to confirm that the clearance is high enough to assert the shot noise level.

This shows that, in order to perform a quantum limited measurement, we need to measure the parameters at a frequency around 2 MHz. The homodyne signal is then retrieved either using a spectrum analyzer or by demodulation, as described in section 3.2.2.

5.1.2 Phase modulation at high frequencies

We then need to achieve a modulation of the optical path at 2 MHz. A standard way to do so is to use an electro-optic modulator (EOM), which is able to deliver a strong phase modulation at high frequency. Rather than modulating the optical path, such a device modulates the index of refraction of the propagating medium, thus creating a phase shift. Although it results in considerable depth of modulation, for our purposes of multimode parameter estimation, it may not be the best choice.

By applying a strong electric field $\boldsymbol{E}_{ext}$ to a crystal, the linear Pockels effect induces a change Δn in the refractive index. The change in phase is then found to be written as

$$\Delta\phi(\omega) = \frac{\omega}{c}\Delta n(\omega) \tag{5.1}$$

where $\Delta n(\omega)$ is defined as [Boyd 03]:

$$\Delta n(\omega) = \frac{1}{2}n^3(\omega) r_{33} \boldsymbol{E}_{ext} \tag{5.2}$$

The phase modulation is then proportional to the cube of the index of refraction of the medium and to the appropriate element of the electro-optic tensor r_{33} (which can be defined as a function of $\chi^{(2)}$). Even though this phase shift may be rewritten as a longitudinal displacement, it is not as straightforward as physically delaying the pulse.

For example, if we want to measure the ultimate sensitivity for a distance or a delay using our scheme, that is, using the detection mode defined in section 4.2.4.2, the description of the phase and group velocities is then entirely dependent on the model described by (5.1). In particular, the type of crystal and its composition needs to be known (which consist usually of doped materials to achieve a strong phase displacement) with precision, and the dependency of the electro-optic tensor with the wavelength should also be taken into account. Moreover, the polarization needs to be carefully set to avoid unwanted amplitude modulations.

Hence, to generate a displacement at high frequency, we settled for the most straightforward method which consists of physically displacing a mirror. This is best achieved by mounting a mirror on a piezoelectric actuator at zero incidence with the beam, as

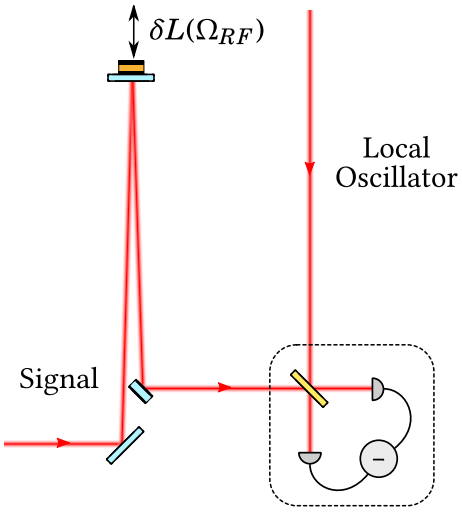

Figure 5.2: Experimental scheme for modulating the delay between the two arms of the interferometer.

shown on figure 5.2. By applying a voltage to the actuator, its ceramic material expands or contracts, thus displacing the beam.

This apparatus generates a true displacement that is straightforward to understand, but it does have some drawbacks too.

- First, to generate a pure longitudinal displacement, one has to make sure that the mirror is perfectly normal to the incident beam, which is not an easy feature to achieve. This will inevitably displace the beam in the transverse plan, leading to the unwanted coupling described in section 4.3.

- Though a piezoelectric actuator is supposed to expand and contract longitudinally, there is no guarantee that it does not move in the transverse plane. Indeed, in [PI 14], it is shown that piezoelectric stacks possess other vibration modes than longitudinal. The amount of excitation of these unwanted modes depends largely on how the resonator is mounted. The resonator consists of the association of the mirror, the actuator and the mount. Different mounting strategies can be adopted to insure a better stability, such as a strong, stable mount [Briles 10], or a lateral clamping of the actuator [Chadi 13].

- Applications of a piezo is best suited for low frequencies. When high voltage is applied, a displacement on the order of 1 µm is achievable. However, at high frequencies, the response is severely reduced. For sensitivity measurements, this limit does not matter since even a small displacement may be sufficient. Neverthe-

less, the response can be erratic, and the linearity of displacement with the applied voltage needs to be experimentally verified.

Therefore, a mirror mounted on a piezo actuator induces a change in both the longitudinal and the transverse planes. These displacements happen at the same modulation frequency, such that it is not straightforward to distinguish between a pure phase modulation (*i.e.* a change in propagation) to a transverse displacement. Moreover, with a high enough sensitivity (which is the case in the scope of this thesis), an amplitude modulation can be observed simply because the angle of incidence of the beam on optics is being modulated [Ivanov 03]. Albeit small, this effect is not negligible in our applications.

To evaluate our experimental scheme, we modulated the phase of the signal field using different elements and measured the signal on both optical quadratures. We also measured the spatial displacement. The experimental scheme for these measurements is outlined on figure 5.3.

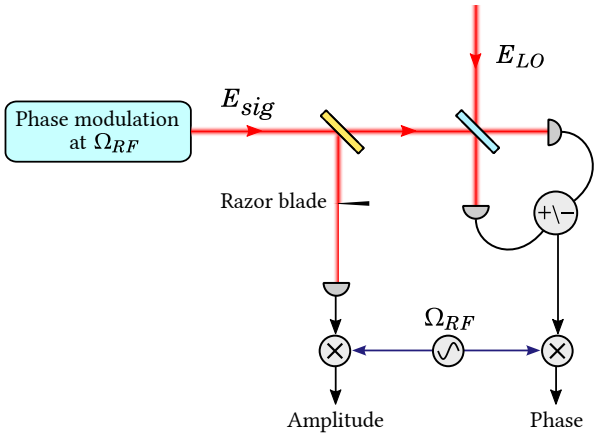

Figure 5.3: Experimental scheme to measure the amount of phase, amplitude and spatial modulations. The amplitude response is obtained by removing the razor blade. Note that the photon number needs to be equal in each measurement in order to be consistent. Also, the signal at the output of the mixer goes through a 15 kHz first order low-pass filter before collecting the data.

The phase quadrature information was retrieved using a homodyne detection with the relative phase between the signal and LO locked on $\pi/2$. Note that this measurement is done without any mode construction, so the projection mode is simply the mean-field mode, which is best suited for a phase detection. The amplitude quadrature was obtained with a single diode with the same optical power than in the homodyne case. The spatial information was obtained by adding a sharp razor blade in the beam. The blade is moved in the beam until half the power is blocked. It then gives information

on how much the beam is being displaced (but does not distinguish displacement or tilt without proper imaging). This was done for both x and y directions. We then took this data set for a range of modulation frequencies around 2 MHz. The data was acquired by demodulating each signal[1]. Note that since the modulation of the field is small, the output of the photodiode needs to be amplified before the mixing procedure. This is achieved with a low noise amplifier ZFL-1000LN from Mini-circuits.

On figure 5.4, we plotted the detected signals for these cases when a piezoelectric actuator is being modulated.

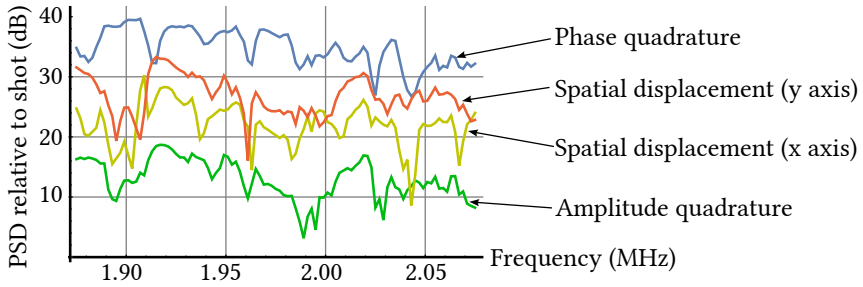

Figure 5.4: Power spectral density obtained by demodulation of the amplitude and phase optical quadratures for a piezoelectric actuator (Physik Instrumente, PL055.30).

We can see on this plot that the phase quadrature (*i.e.* the homodyne signal) yields the higher stsignal. It is also noticeable that the response is not flat with respect to modulation frequency. This is to be expected for any resonator, which will show resonances. The signal on the amplitude quadrature is lower by at least two orders of magnitude, which is quite small but it can be measured without any difficulty. It means that, in an homodyne detection scheme, if the relative phase between the two arms is not set perfectly for a phase quadrature measurement, not only is there a loss of signal, we would also retrieve information from the amplitude quadrature.

More surprising is the amount of spatial modulation that is present. Note that these traces are corrected from the amount of amplitude modulation since it should appear on all measurements. Both axis show a signal level that is only one order of magnitude lower than the homodyne signal, which is not negligible. We can see that the transverse and longitudinal displacements are structured, which is yet another witness of resonances. However, the relationship between the phase quadrature structure and the transverse displacement does not appear to be trivial: for example, there is a clear resonance at 2.03 MHz for the phase quadrature which does not appear on both spatial signals.

We add that similar measurements were done for different types of piezo actuators, which showed very different responses. The one that was eventually chosen and plotted

[1]The demodulation phase (*i.e.* electronic quadrature) was set such that the retrieved signal is maximal.

on figure 5.4 showed the lowest transverse modulation. We also characterized different EOMs the same way. Though the phase modulation is much flatter with frequency, it isn't exempt of amplitude or transverse modulation, as shown on figure 5.5. This is a confirmation that an electro-optic modulator is not a perfect phase modulator either.

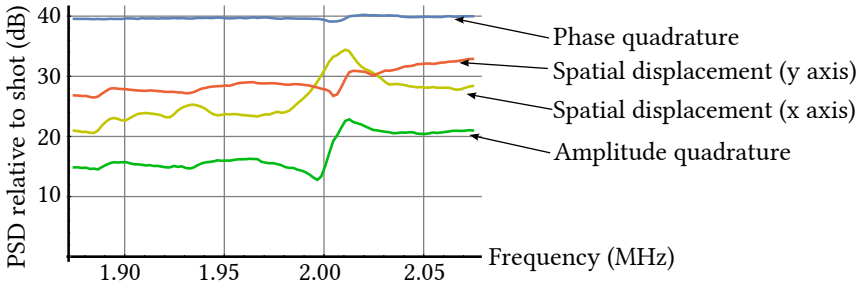

Figure 5.5: Power spectral density obtained by demodulation of the amplitude and phase optical quadratures for an electro-optic modulator (resonant, but operated at a frequency far from resonance).

We conclude that getting a purely longitudinal displacement required a very careful control of both imaging and the way the displacement is generated. We opted for a spatial filtering technique to remove the transverse displacement rather than try to generate a pure phase modulation.

5.1.3 Spatial filtering

The analysis of the previous section and the theoretical analysis of 4.3 shows that the transverse displacement is a real effect that comes into play in our experimental scheme.

In order to be confident in the fact that no spatial contamination remains, the best option would be to ensure a perfect TEM_{00} mode in the local oscillator arm. A possible way to do so is to build a Fabry-Pérot cavity in this arm, which acts as a spatial filter. However, it is a cumbersome solution in ultrafast optics, since this cavity would need to match the laser's cavity (especially in length) in order to transmit the entire the spectrum. It also adds complexity to the experimental setup with the need of an active lock.

We then opted for a single-mode fiber, which also acts as a spatial filter, but can prove to be cumbersome. In particular, these are quite dispersive, and would need to be compensated. One solution would be to put fibers on both arms of the interferometer and use the pulse-shaper to fine tune the relative phase.

As we pointed in section 3.3.2, in a homodyne measurement, once the beams are combined, no linear element can affect the information contained in the interference pattern. Therefore, it is convenient to put the filter fiber at the output of the beamsplitter, where

the dispersion does not matter anymore, as depicted by figure 5.6. Doing so, we noticed a consequent increase in the contrast of the interference fringes. By introducing a narrow bandpass filter of 1.5 nm FWHM, the temporal overlap integral can be considered as being unity, such that the measured contrast depends only on the spatial coherence. Without spatial filtering, we measured a contrast of 92%, whereas with a single-mode fiber, we measured a contrast close to 100%.

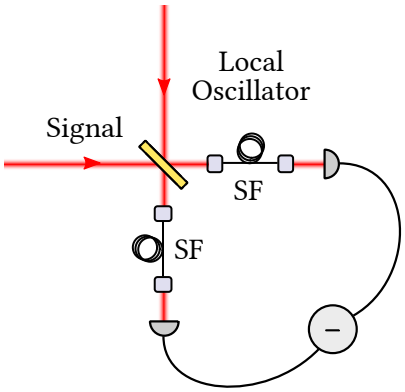

Figure 5.6: Spatial filtering scheme for homodyne detection. SF: single-mode fiber.

This allows us to consider that both beams are in the same spatial mode (defined by the fiber), such that no contamination of the homodyne signal can come from transverse effects. Note that these unwanted spatial modulations on the phase quadrature at the input of the fiber are however pushed into the amplitude quadrature at the output. Therefore, the lock of the relative phase between the two arms of the interferometer still needs to be set with care.

5.2 Interferometer calibration

Before proceeding to multimode parameter estimation, we need to calibrate the phase modulation. Simply put, one needs to be able to relate what is measured to physical quantities. We restrict our calibration to the case of a mirror mounted on a piezo actuator, but the same strategy can be applied to an EOM.

What is being measured at the output of the homodyne detection is an optical phase, and we would like to relate it to a longitudinal displacement. For large displacements (*i.e.* on the order of the optical wavelength), the phase shift can be observed from the interference fringes, and therefore be measured with a good precision. However, at high modulation frequency, the response is very diminished and the resulting longitudinal displacement is much smaller than the optical wavelength. Hence, it may not directly

be measured. Extrapolating from a calibration obtained from a large displacement is conditioned by the linearity of both the piezo element and the electronics that are used.

A possible strategy is to use a quadrant detector which allows to detect small displacements [Treps 03]. We place the actuator at a 45° angle and measure the transverse displacement. However, relating the measured signal to an actual longitudinal displacement requires a knowledge of the distances and the geometry of the optical layout. The precision on the calibration is then dependent on the ability to measure distances on the optical table. Such a calibration, albeit precise and simple to execute, is thus not done in an absolute manner. It also requires to move the mirror at a different place, and the calibration is not done with the same optical scheme than the measurement.

In [Roslund 15], we propose a methodology to enable an absolute measurement of a subwavelength longitudinal displacement introduced by a piezo-electric actuator. It is based on the fact that all the information on the displacement is contained within the relative strength of the various harmonics that arise due to the phase modulation. This method does not require any assumption regarding the nature of the light source.

With the calibration in hand, it is straightforward to estimate the limit of sensitivity of the interferometer given by (4.10). Usually, the ultimate limit of detection (which scales with $\frac{1}{\sqrt{N}}$) is estimated by measuring the optical power contained in the signal field[Verlot 09]. Doing so necessitate to know the responsivity of the photodiode and also to precisely measure all the field quantities that define the detection limit such as the fringes contrast for mode-matching. The method that we propose here does not require any of this knowledge.

5.2.1 Calibration of displacement

5.2.1.1 Methodology

We begin by considering that the signal field is phase modulated. Under the assumption that the phase modulation is linear with the voltage applied to the piezo element, we write the optical phase as

$$\phi_{mod} = k \cdot n \cdot d(V) \cdot \sin[\Omega_{RF} t] \tag{5.3}$$

where $k = \frac{2\pi}{\lambda}$ is the field's wavenumber, n is the index of refraction of air, $d(V)$ is the longitudinal displacement that we need to determine, and Ω_{RF} is the modulation frequency. The signal field is consequently written as

$$E^{(+)}_{sig}(x,t) = \mathscr{E}_0 \, \alpha_s \, w_s(x,t) \, e^{i\phi_{mod}} \tag{5.4}$$

where we set α_s as a real quantity. Therefore, the homodyne signal (3.8) writes as

$$\mathscr{I}_- = 2\sqrt{N_{LO}}\,\Gamma_c \cdot \alpha_s \cos\left[\phi_0 + \phi_{mod}\right] \tag{5.5}$$

where Γ_c is the coherence between the two fields and ϕ_0 is the phase of the local oscillator. We remind that the responsivity of the detector is contained implicitly in the definition of the photocurrent. Note also that this measurement is done with no mode construction: the mode in the signal field is supposed to be similar to the mode in the local oscillator field, *i.e.* the mean-field mode. Any mismatch in amplitude or in phase between the fields is contained in the coherence Γ_c.

For a displacement smaller than the optical wavelength $k\dot{d} \ll 1$, the homodyne signal may be expanded on a Bessel function basis. It yields:

$$\begin{aligned}\mathscr{I}_- \simeq 2\sqrt{N_{LO}}\,\Gamma_c \cdot \alpha_s \,\big[&J_0(k\,n\,d)\cos\phi_0 \\ &-2J_1(k\,n\,d)\sin\phi_0\,\sin[\Omega_{RF}t] + 2\,J_2(k\,n\,d)\cos\phi_0\,\cos[2\,\Omega_{RF}t] + \ldots\big]\end{aligned} \tag{5.6}$$

We can see that the signal at the fundamental frequency Ω_{RF} is maximal for a relative phase offset between the two fields $\phi_0 = \frac{\pi}{2}$. It means that the LO needs to be overlapped with the phase quadrature of the signal field.

The amplitude quadrature of the field contains a DC term which corresponds to the energy in the two fields and the second harmonic of the modulation, which contains information about the longitudinal displacement d.

At an analysis frequency where the only noise present arises from fluctuations of quantum vacuum, the noise in the detection is given from (4.7) with $\sigma = 1$:

$$\Delta\mathfrak{I}_- = \sqrt{N_{LO}} \tag{5.7}$$

which allows to write the signal to noise ratio as

$$\begin{aligned}\Sigma = 2\,\Gamma_c \cdot \alpha_s \,\big[&J_0(k\,n\,d)\cos\phi_0 \\ &-2J_1(k\,n\,d)\sin\phi_0\,\sin[\Omega_{RF}t] + 2\,J_2(k\,n\,d)\cos\phi_0\,\cos[2\,\Omega_{RF}t] + \ldots\big] \\ \equiv\ &\Sigma^{(0)} + \Sigma^{(1)} + \Sigma^{(2)}\end{aligned} \tag{5.8}$$

This expression shows that the signal-to-noise shows different harmonics which depend on the energy contained in the signal field.

By computing the ratio of the first and second harmonic, we have

$$\frac{\Sigma^{(2)}}{\Sigma^{(1)}} = \left|\frac{J_2(k\,n\,d)}{J_1(k\,n\,d)}\right| \simeq \frac{k\,n\,d}{4} \tag{5.9}$$

which is independent on the energy in the signal field and varies linearly with the optical displacement d.

Therefore, the relative strength of the harmonics of the signal-to-noise ratio is linearly related to the displacement, which enables a direct calibration.

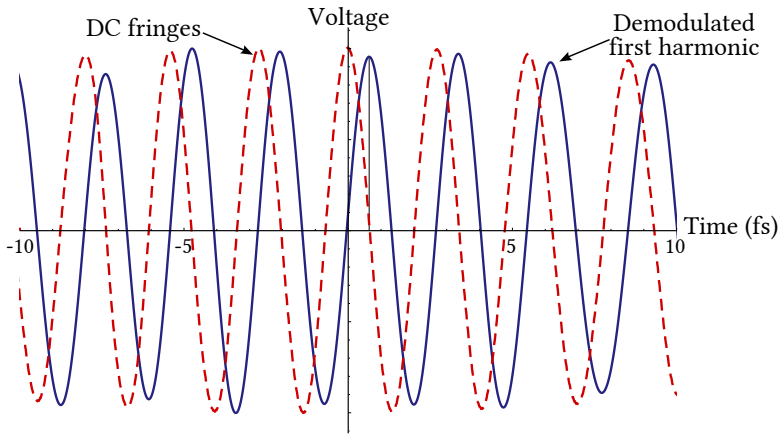

Figure 5.7: Retrieved traces at the output of the interferometer when sweeping the relative phase between the two arms. Dashed: DC signal of a single photodiode. Straight: Demodulation of the first harmonic for a phase modulation. Note that the two signals are in perfect quadrature.

5.2.1.2 Experimental procedure

To retrieve the displacement $d(V)$ as a function of the applied voltage V, we then need to measure the power of the first and second harmonics of the signal-to-noise ratio for different voltages.

Measuring the first harmonic is straightforward. We set the interferometer in homodyne configuration by setting approximately 10 times more power in the local oscillator arm than in the signal arm (as to be insensitive to the noise in the local oscillator, as it was discussed in section 3.3.1). The output of both photodiodes are split at 10 kHz using a biased-tee. This allows to separate the DC to the high frequency components of (5.8).

On figure 5.7, we plot the DC term and the demodulated first harmonic of equation (5.8). Using the scheme introduced by figure 3.10, we sweep the relative phase between the two arms of the interferometer while retrieving simultaneously the DC fringes and we demodulated the first harmonic[2]. We see that both are in quadrature, such that the DC may be used as an error signal to lock the delay. When the DC term is zero, the signal from the first harmonic is maximal. This allows to pinpoint the phase quadrature with a good precision.

We drive the piezo-electric actuator[3] at a frequency of 2 MHz and we ramp the voltage

[2]The relative amplitude of these two traces is not meaningful in this plot since we normalized them to 1.

[3]We stress that this method does not only calibrate a displacement: it may more generally be utilized to calibrate a phase offset. It can thus be used to calibrate the response of an electro-optic modulator using the same scheme.

from 0 to 10 V using a function generator. Note that this signal is not amplified, which guarantees that the electric signal that is sent to the piezo element is linear. The relative phase ϕ_0 is locked on the phase quadrature using a PI lockbox NEWFOCUS LB1005.

To measure the second harmonic, we need to lock the relative phase on the amplitude quadrature. To do so, we utilize the demodulated signal of the first harmonic, which is in quadrature with the DC fringes. This demodulated signal then provides the error signal to lock on the amplitude quadrature.

Therefore, using this signal, it is possible to lock the interferometer on the amplitude quadrature and measure the power contained in the second harmonic. This is achieved by adding another modulating element to the interferometer (such as another piezoelectric actuator or an EOM). It is modulated at a different RF frequency such that it does not influence the modulation of the first one, and used to generate the error signal. That way, the locking apparatus is different from the one that we measure.

Note also that the strength of the second harmonic is much lower than the fundamental. It is therefore necessary to have both a strong phase modulation and a detection with a low noise floor in order to measure this amplitude modulation. Therefore, we use a spectrum analyzer for this calibration. Demodulation is used only to lock on the amplitude quadrature.

We add that an ultrafast source is not required for this calibration procedure.

5.2.1.3 Results

To compute the signal-to-noise using a spectrum analyzer, we need to consider how the noise is retrieved.

On a general manner, we can write the measurement $M(t)$ as a sum of signal $S(t)$ and noise $N(t)$: $M(t) = S(t) + N(t)$. Computing the PSD from (3.34) yields $M^2(f) = S^2(f) + N^2(f)$ in the absence of correlation between signal and noise. The signal-to-noise ratio is then simply given by

$$\boxed{\frac{S}{N}(f) \equiv \Sigma(f) = \sqrt{\left(\frac{M}{N}(f)\right)^2 - 1}} \tag{5.10}$$

Therefore, we need to measure the signal $S_{\mathscr{I}_}(f_{RF})$ at the f_{RF} frequency given by (3.33) and the noise in the measurement by measuring the homodyne signal in the absence of a modulation. The signal-to-noise is then computed using (5.10).

The evolution of the amplitude of both the fundamental and second harmonic peaks are depicted on figure 5.8a and b as a function of the applied voltage.

We can see that the first harmonic grows linearly for small values of the displacement (in agreement with $J_1(d) \simeq \frac{d}{2}$). This also confirms our assumption that the modulating element responds linearly to voltage on the investigated range.

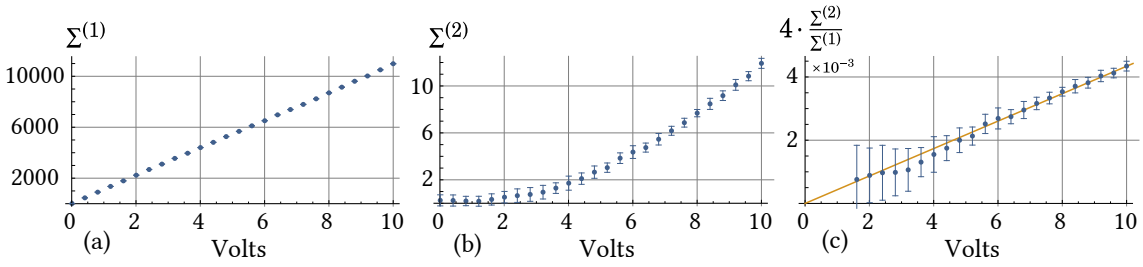

Figure 5.8: Phase modulation harmonics observed in the homodyne signal as a function of the voltage applied to the piezo-electric actuator. The fundamental harmonic (a) grows linearly with displacement, whereas the second harmonic (b) grows quadratically. The ratio (c) of the two signal-to-noise shows a linear response to the displacement, and allows to retrieve the calibration.

The growth of the second harmonic is considerably smaller and scales quadratically with displacement (in agreement with $J_2(d) \simeq \frac{d^2}{8}$). Both those signals are dependent on the power contained in the signal field, as shown by (5.8).

The ratio of the two harmonics depicted by 5.8c, however, is independent on the strength of the signal field. As expected, the ratio grows linearly with displacement, and a linear fit according to (5.9) retrieves an optical displacement of

$$\boxed{d(V) = 0.55 \pm 0.01 \text{ Å} \Big/ \text{Volt}} \tag{5.11}$$

for a center wavelength $\lambda = \frac{2\pi}{k} = 795$ nm. Since the experiment was done in laboratory air, we set the index of refraction $n = 1$. The calibration was achieved at 1.95 MHz.

5.2.2 Sensitivity measurement

With the calibration in hand, it is then possible to estimate the sensitivity of the interferometer to a phase measurement. We again lock the relative phase on the phase quadrature and ramp the voltage as in 5.8a, albeit over a reduced range. This is achieved with a 42 dB electric attenuator at the output of the function generator. The scan result is shown on figure 5.9.

The smallest amplitude d_{min} that is measurable occurs for a modulation amplitude that is equal to the background quantum noise, *i.e.* $\Sigma^{(1)} = 1.0$. We find that the minimum sensitivity is $d_{min} = 5.0 \pm 0.1 \cdot 10^{-14}$ m. The retrieved signal results from collecting photons within a time interval corresponding to a resolution bandwidth of $\Delta\nu_{RBW} = 50$ Hz. After renormalization by the resolution bandwidth, the minimum detectable

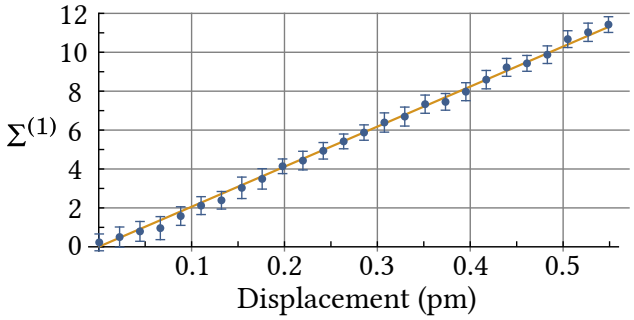

Figure 5.9: Time-averaged displacement sensitivity of the mirror-mounted piezo actuator. The displacement at which the signal-to-noise is equal to 1 is found to be $d_{min} = 5.0 \pm 0.1 \cdot 10^{-14}$ m. The integration time is 9 ms which amount to $\sim 10^{12}$ photons.

longitudinal displacement becomes

$$\boxed{d_{min} = 7.0 \pm 0.1 \cdot 10^{-15} \text{ m} \Big/ \sqrt{\text{Hz}}} \tag{5.12}$$

We want to compare this value to the one predicted by the Cramér-Rao bound for phase estimation. Using (4.30), it is given by

$$d_{min}^{SQL} = \frac{\lambda_0}{4\pi\sqrt{N}} \tag{5.13}$$

where λ_0 is the center wavelength of the light. We then need to evaluate the number of photons that are detected during the calibration.

As we hinted in the introduction to this section, estimating the photon number necessitates to take into account the quantum efficiency of the detector as well as the fringe contrast. For detectors PDA36A from Thorlabs, the responsivity at 795 nm is $\mathscr{R} = 0.5$ A/W, leading to a quantum efficiency of $\eta = 78\%$.

The contrast of the optical fringes that we measured is $\mathscr{C} = 51\%$. This allows to compute the coherence of the field using (3.14). The DC output of the detectors shows a voltage of 0.365 V in the signal beam and 4.13 V in the local oscillator field. We therefore estimate a coherence of $\Gamma_c \approx 94\%$.

Moreover, we need to estimate the acquisition time of the spectrum analyzer. Since it utilizes a Gaussian filter, the acquisition window is opened for a time Δt that can be calculated from the time-bandwidth product of the filter. Namely, we have $\Delta t \Delta \nu_{RBW} = 0.44$ where $\Delta \nu_{RBW}$ corresponds to the resolution bandwidth of the apparatus. We then estimate the width of the time window to be $\Delta t = 9$ ms.

The number of detected photons during the time Δt is therefore given by

$$N = \eta \cdot \Gamma_c^2 \cdot \frac{P_s}{\hbar\omega_0} \cdot \Delta t \tag{5.14}$$

where $P_s = 115$ µW is the power in the signal field. We then estimate $N \simeq 2.7 \cdot 10^{12}$ photons.

Plugging the detected number of photons into the theoretical detection limit (5.13) and normalizing by the resolution bandwidth then yields

$$\boxed{d_{min}^{SQL} = 5.5 \cdot 10^{-15} \text{ m} \Big/ \sqrt{\text{Hz}}} \tag{5.15}$$

Thus, the experimentally recovered sensitivity is in fair agreement with the one estimated from the standard quantum limit $\left(d_{min} \Big/ d_{min}^{SQL} \simeq 1.27\right)$.

We stress that the observed displacement is a time-average over the detection time in the millisecond scale. This measurement does not resolve an absolute variation on an ultrafast timescale. Also, we add that the retrieved sensitivity is very dependent on the purity of the phase modulation. Indeed, if the retrieved signal contains a mixture of longitudinal and transverse displacement (that we've seen in section 4.3.1 can lie in the phase quadrature of the field), the measured sensitivity won't coincide with the Cramér-Rao bound anymore.

Still, it is quite remarkable that the retrieved sensitivity is in very good agreement with the theoretical expectation.

5.3 Multipixel detection

Having a way to calibrate the longitudinal displacement with a good precision, we may now move on to extracting parameters from the field using a modal approach. Toward that aim, we first need to develop the design and construction of the multipixel detection.

5.3.1 Design and construction

5.3.1.1 Optical and electrical design

The multipixel homodyne detection of figure 3.8 is put instead of the second homodyne detection on figure 3.10. The two beams are focussed on two plane-ruled gratings (RG-1200-1000 from Newport) which are then imaged on microlenses arrays. These allow to precisely focus the spectral slices on each pixel of the detector array without any gaps[4]. This optical layout is shown on figure 5.10.

[4]Though not mandatory, this focussing increases the signal for quantum application, when detecting squeezed vacuum. In our case, we noticed inconsistent signals at high frequency when the light is being diffracted on the border of pixels. We therefore opted for the additional microlenses array.

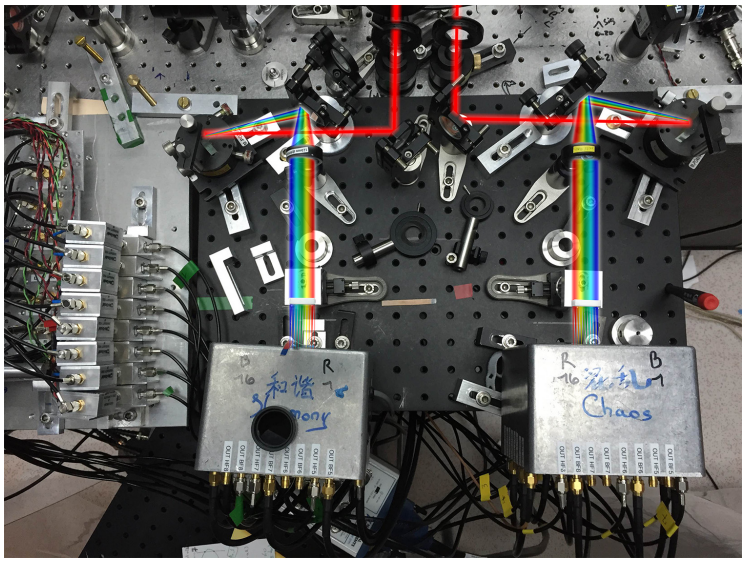

Figure 5.10: Picture of the multipixel homodyne detection. The beams are schematically overlayed. The left detector is at a noticeable angle in the beam because of the way the photodiode array is clamped. Both diffracted beams are actually at zero incidence on the arrays to maximize efficiency.

We chose a mirror-symmetry for the construction of both detectors for an easier alignment. To ensure a proper alignment, we aligned carefully the diffraction grating as not to introduce any tilt in the diffracted beams.

Each detector and each microlenses array are mounted on lateral translation stages, which is very important for alignement. There is no need for a longitudinal translation stage on the detectors.

The photodiodes array, built by HAMAMATSU, are composed of 16 Si photodiodes with a quantum efficiency of 90%. They are plugged into a self-built motherboard. Each pixel is connected to a transimpedance amplifier which split the signal into a DC and high-frequency part (cutoff frequency of ~ 200 kHz). The gain of the amplifier may be adjusted using a potentiometer. It allows to calibrate the gain of each pixel.

On the left side of picture 5.10, we can see the demodulation electronics. For simplicity, we operated the detection with 8 pixels, plugging only every other pixels. Each HF signal is demodulated. The path starts with taking the difference of the photocurrents of both detectors (with a passive subtractor ZFSC-2-1 from MINI-CIRCUITS), and a 20 kHz high-pass filter is added to ensure no saturation of the demodulation electronics. The difference signal is subsequently amplified and mixed with the electronic local oscillator. The output of the mixer is then low-pass filtered with a 15 kHz bandwidth. This scheme is identical for all the 16 pixels that result in the 8 signals. These are digitalized using

an acquisition card PCIe-6361 from National Instrument. This card can acquire 16 channels simultaneously at an acquisition rate of 2 MHz[5]. The analogical signals from the demodulation are acquired using a BNC connector block BNC-2110.

The DC output of the photodiodes are connected into another connector block BNC-2111 which allows for the acquisition of 16 simultaneous signals. As we will see, the acquisition of all of the DC allows to precisely align the detection, and serves as a good reference before starting a measurement.

We also take two DC signals from the center pixels of each detectors to lock the delay between the arms of the interferometer (by taking the difference to generate an error signal, see figure 5.7).

The data acquisition is then accomplished using Labview.

5.3.1.2 Alignement procedure

Once the optical layout is set, we need to carefully align the detection. When constructing a homodyne detection, it is necessary to ensure that the photons are distributed equally between the two outputs of the combining beamsplitter. This is required to nullify the energy terms of signal and LO field in (3.4) when taking the difference of the photocurrents. Failing to do so would result in an unbalanced detection where the noise from the local oscillator remains.

When using two detectors, this is achieved by fine-tuning the angle on the beamsplitter until the energy detected by both detector is equal[6]. However, since this scheme integrates over the full optical spectrum, it does not ensure that every part of the spectrum is perfectly balanced.

To balance the power on the multipixel detection, we first confirmed that each DC output of the detector was balanced, *i.e.* that the same voltage was read for the same optical power. This was accomplished by using the pulse-shaper as an interference filter, selecting a very narrow spectral slice centered at 795 nm, and using the translation stages to move each pixel in the beam. Therefore, we were able to confirm that each DC were balanced and could be used as a reference.

We then maximized the sum of the DC voltages of each detector by fine-tuning the position of the microlenses array. Then, by summing the signal received by both detectors (thus computing the total received), we balanced the beamsplitter by tuning its angle.

Eventually, we need to find a way to ensure that the power in each spectral slice rather than the total power is balanced. By monitoring every DC simultaneously, we compared

[5]For a single channel, thus, the simultaneous acquisition rate for 8 pixels is limited to 250 kHz per channel.

[6]Since the stronger beam is the local oscillator, this procedure is accomplished using this beam only.

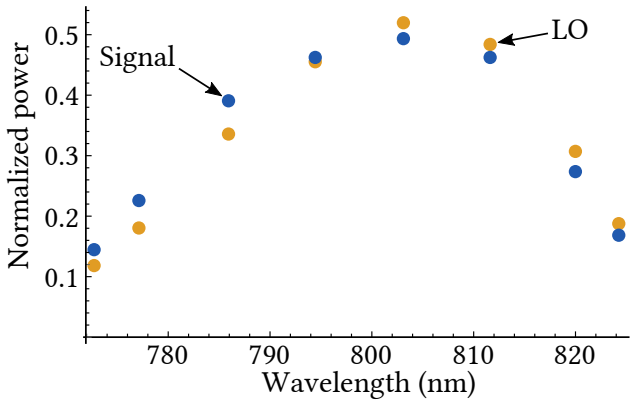

Figure 5.11: Acquisition of the DC signal of signal and local oscillator fields for a single detector. Each points represents a pixel of the detector.

the power pixel by pixel. By playing with the lateral position of both detectors and microlenses arrays, we are able to overlap the two spectra perfectly[7].

However, this procedure does not ensure that the signal field is also balanced. It has been previously observed and confirmed in this experiment. It is believed to originate from polarization imbalance between the two fields. Fortunately, this has no effect on the final measurement, since the signal field is weaker than the local oscillator. It does however come into play for locking the relative phase. Indeed, since we use the difference of the DC (which is proportional to power), the proper lock point is thus not defined as being exactly zero. The offset can be determined by measuring the imbalance of the signal field. Albeit small, this difference is enough to considerably change the outcome in a sensitive measurement.

The mismatch between the signal and local oscillator spectra is shown on figure 5.11. This particular effect is important for modes construction and needs to be accounted for.

5.3.2 Gain calibration

Now that the power received by both detector is balanced, we move on to the gain calibration procedure.

As it was described in 5.3.1.1, the high frequency output of the detectors have a variable gain that may be tuned. This is important to ensure that the retrieved signal is equal on all pixel for the same optical power. We therefore need to balance the gain of all pixels of a single detector, but we also need to balance both detectors. If they are not balanced, the situation is equivalent to an unbalanced beamsplitter.

[7]Note that this overlapping procedure is easier with short spectra. Large bandwidth means that the uncertainty in the reflectivity of all optics gets more noticeable.

To calibrate the gain, we again use the pulse shaper as an interference filter, allowing to focus a fixed amount of power on a single pixel. A possible strategy from there is to record the variance of the demodulated signal at a quantum limited frequency while moving the detector laterally. Since this variance is proportional to the photon number, assuming that the photodiodes have the same response, it is possible to tune the gain to set each variance on the same value.

This method is easy to implement, yet does not yield the best result. Indeed, measuring the variance of the demodulated signal is not very stable, and the measurement needs to be averaged over a few seconds in order to be reproducible. The whole calibration procedure thus takes longer to achieve, and is subject to slow power fluctuations of the laser source.

We adopted another technique which is widespread to calibrate photodiodes. Since we need only the local oscillator beam to calibrate, we may introduce any dispersive element in the beam without being concerned about overlap. We then introduced an acousto-optic modulator (MT110-A1.5-IR from AA Opto-Electronic) before the beam splitter. We optimized its alignement such that the efficiency of diffraction is maximum. Blocking the diffracted beam, we may then modulate its amplitude, such that it introduces an amplitude modulation on the beam[8]. For consistency, we chose to modulate the amplitude of the field at the same frequency that we want to do the measurement, *i.e.* around 2 MHz.

Demodulating this signal, we then have a stable reference to do the calibration. We send light to a single detector and move it such that the beam hits a single pixel at a time, and tune the gain to put the demodulated signal on the reference. This method allows to calibrate not only the photodiode's amplifier, but also all the detection scheme.

With a single detector calibrated, we then put the light on the same pixel of both detector and look at the difference of the photocurrents. We tune the gain of the second detector to make that signal zero, ensuring that both detectors are balanced. Iterating that procedure over all pixels allows to complete the calibration procedure.

To confirm that the calibration is successful, we remove the AOM and measure the variance of the difference of the photocurrents for a given optical power. We then compare the retrieved spectral shape to the DC spectrum. As we said, both are proportional to the photon number and should therefore be similar. The measurement is shown on figure 5.12.

We can see on this plot that the DC spectrum overlaps very well with the HF variance[9].

[8] We remind that we inject only a single spectral slice of the spectrum. We then do not need to take into account the response of the AOM with respect to optical wavelength.

[9] Note that the variance retrieved for a single detector rather than the difference of both also retrieves the shot noise at a high enough detection frequency. The signal is however divided by two since it receives half the number of photons.

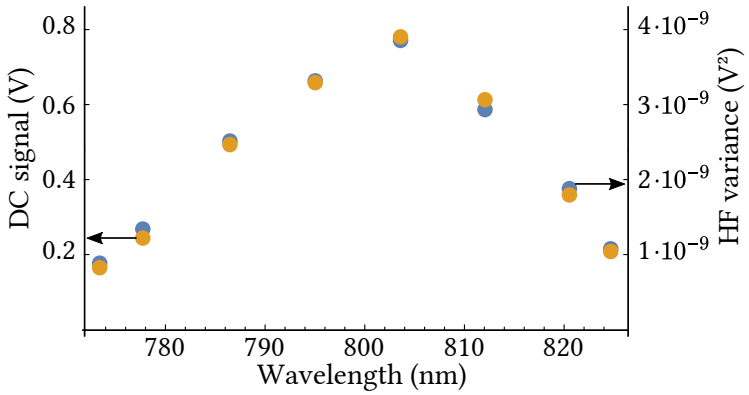

Figure 5.12: Measurement of the DC signal of the local oscillator for a single detector and the variance of the difference of photocurrents. Both overlap, showing a succesful calibration.

This means that measuring the variance of the homodyne signal at a high enough frequency (without any element modulating) does indeed retrieve the shot noise statistics, and may be used to compute the signal-to-noise in our measurements.

5.3.3 Space-wavelength mapping

Another important part of the procedure is to map pixels to wavelength. This is achieved using again the pulse shaper. Since it is already calibrated, we chose to use it as a reference to calibrate the mapping of the pixels.

To do so, we use again the shaper as an interference filter where we sweep its central wavelength. For each point, we record the DC of each pixels for both detectors. The result is shown on figure 5.13a.

We fit a Gaussian through each signal of 5.13a and map the mean wavelength as a function of the pixel number. This is done for both detectors. The resulting calibration is shown on 5.13b. Note that the mapping of both detectors is symmetric, thanks to the good optical design.

We can see from the mapping that we indeed plugged every other pixels, except for the ones on the edge. This is intentional, since the amount of power is reduced at the edge of the spectrum. Therefore, we moved the edge pixel inwards, allowing to have enough optical power to rise the signal above the noise level.

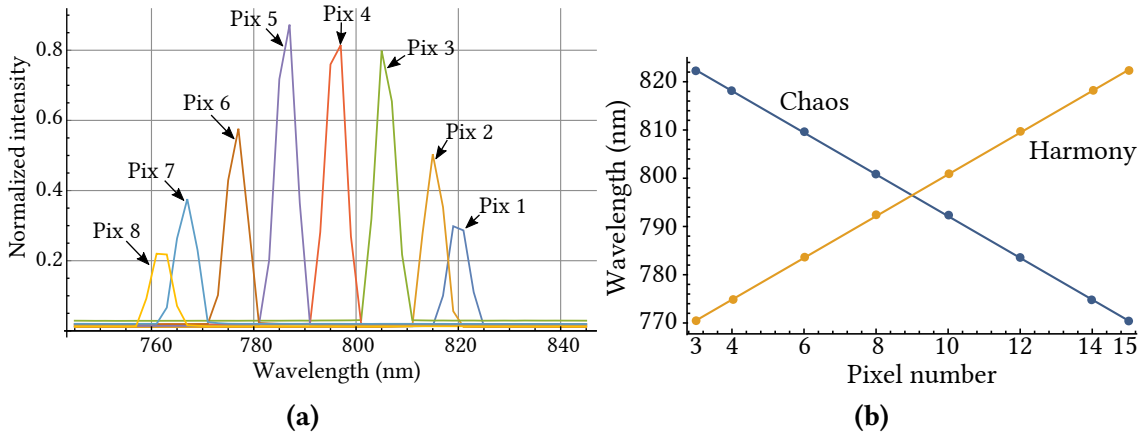

Figure 5.13: Space to wavelength mapping of the detectors. (a) Acquisition of the detected DC signal when the center wavelength of a small spectral slice is sweeped on a detector. (b) Resulting calibration for both detectors.

5.3.4 Clearance

Finally, another important step in characterizing a photodiode amplifier is to determine its saturation point.

To determine this point, we measure the variance of each signal while increasing the optical power. The retrieved signal should increase linearly with power. Saturation occurs when the amplified signal does no longer grow linearly with power.

With the amplifier than is used, the saturation phenomena occurs when the variance of the signal drops suddenly to the noise floor of the detection. The amount of optical power at which the signal crashes defines the maximum power at which the detection may be operated. In turn, this defines the maximum clearance of the system. Doing so, we found the saturation point of the system to be 8 dB above the dark noise (per pixel). This value, even if it is not very high for very sensitive quantum application, such as detection of squeezed vacuum, is more than enough for our applications.

Knowing the saturation point, we usually operated our homodyne detection with a power level that maximizes the signal while keeping a safe distance from saturation.

5.4 Spectrally-resolved multimode parameter estimation

We are now equipped to investigate the multimode structure of the field using spectrally-resolved detection. We first use the multipixel detection to show the existence of a higher

order mode in which photons are displaced when the optical path is modulated.

We then develop how the modes are constructed under the restriction that both spectra from the signal and local oscillator fields are not exactly similar. Finally, we apply this scheme to the measurement of phase and group delay independently, and to construct the detection mode for space-time positioning.

5.4.1 A glimpse at the multimode structure

We first consider the homodyne signal out of the multipixel detection when the phase of the field is modulated, as developed in 4.2.1. Let us write the integrand of the homodyne signal as

$$i(\Omega) = \sqrt{N_{LO}}\,\alpha_s^* \cdot \Big[v_0(\Omega) - i\left(\omega_0 t_\varphi \cdot v_0(\Omega) + \Delta\omega t_g \cdot v_1(\Omega)\right)\Big] \cdot u_{LO}(\Omega) e^{i\phi_0} + \text{c.c.} \quad (5.16)$$

where c.c. stands for conjugated complex. The homodyne signal is written $\mathscr{I}_- = \int \mathrm{d}\Omega i(\Omega)$.

We can see in this expression that the time-of-flight mode carries information. However, the signal is dominated by the phase mode, since $\omega_0 \gg \Delta\omega$. We propose here to experimentally suppress the contribution of the phase mode from (5.16). What should remain is the time-of-flight mode (and higher order modes not written in (5.16)), confirming the validity of the modal expansion of the field.

For a phase modulation occurring at a quantum limited frequency, the noise in the measurement at an optical frequency Ω may be written as $\Delta i(\Omega) = \sqrt{N_{LO}}\,u_{LO}(\Omega)$. The signal-to-noise is consequently given by

$$\Sigma(\Omega) = \alpha_s^* \cdot \Big[v_0(\Omega) - i\left(\omega_0 t_\varphi \cdot v_0(\Omega) + \Delta\omega t_g \cdot v_1(\Omega)\right)\Big] e^{i\phi_0} + \text{c.c.} \equiv 2\,\mathrm{Re}\left\{a_s(\Omega) e^{i\phi_0}\right\} \quad (5.17)$$

which is found to be the signal's field envelope (4.1) in the quadrature defined by the local oscillator's phase. This quantity can be steadily evaluated using the multipixel detection and setting the relative phase between the two arms of the interferometer.

The signal-to-noise 5.17 can be decomposed as a part independent of the modulation (*i.e.* DC) in the amplitude quadrature of the field and a part the is modulated at a high frequency that lies in the phase quadrature. On the amplitude quadrature, we have

$$\Sigma_X(\Omega) = 2\,\mathrm{Re}\left\{\alpha_s^* v_0(\Omega)\right\} \quad (5.18)$$

which does not contain any high frequency modulation. On the contrary, the phase quadrature's signal-to-noise writes as

$$\Sigma_P(\Omega) = 2\,\mathrm{Re}\left\{\alpha_s^* \left(\omega_0 t_\varphi \cdot v_0(\Omega) + \Delta\omega t_g \cdot v_1(\Omega)\right)\right\} \quad (5.19)$$

which contains the modulated terms t_φ and t_g. The signal given by equation 5.19 may thus be measured by locking the interferometer on the phase quadrature and demodulating at the modulation frequency. As we pointed earlier, the main contribution in this signal comes from the phase mode v_0, and the displacement contained in v_1 is small in comparison. However, the DC signal actually contains the first mode without the longitudinal displacement. At the DC output of the photodiodes, we measure the square of (5.18) (since it measures power) with a proportionality factor due to the different response in electronics.

To extract higher order components from (5.16), one may subtract the DC signal with a proper gain as to cancel the phase mode contribution. What should remain is the contribution of higher order modes.

Consider that we record the signal-to-noise given by (5.19) for a given phase modulation. We then use the DC of signal's field $P_s(\Omega)$, which we write as a function of (5.18) as $P_s(\Omega) = \kappa \cdot \left(\Sigma_{DC}\right)^2$, where κ is a proportionality factor.

To remove the phase mode's contribution from (5.16), we write the difference signal $\mathscr{D}$ as

$$\mathscr{D}(\Omega) = \Sigma_{HF}(\Omega) - g \cdot \sqrt{P_s(\Omega)} = \alpha_s^* \left[\left(\omega_0 t_\varphi - g\sqrt{\kappa}\right) \cdot v_0(\Omega) + \Delta\omega t_g \cdot v_1(\Omega) \right] \tag{5.20}$$

where g is an arbitrary gain in post-processing that we propose to determine. More precisely, the phase mode contribution is zero for:

$$g = \frac{\omega_0 t_\varphi}{\sqrt{\kappa}} \tag{5.21}$$

At first glance, it seems like determining g requires to know the values of unknown parameters. However, one may note that the integral of the phase mode $\int \mathrm{d}\Omega v_0(\Omega)$ is non-zero, since it is an even function for the considered spectrum. Conversely, the integral of the time-of-flight mode yields zero by construction $\int \mathrm{d}\Omega v_1(\Omega) = 0$. We stress that this last remark is exact for Gaussian spectra. In the case where the optical spectrum is a little asymmetric, we may still consider that the integral of the time-of-flight mode, which is an odd function, is much smaller than the integral of the phase mode. It is therefore a reasonable hypothesis to neglect this term.

Using this assertion, the gain is then found to be:

$$\boxed{g = \frac{\int \mathrm{d}\Omega\, \Sigma_{HF}(\Omega)}{\int \mathrm{d}\Omega\, \sqrt{P_s(\Omega)}}} \tag{5.22}$$

In term of our experimental setup where we have 8 pixels, these integrals are discrete summation over the pixels.

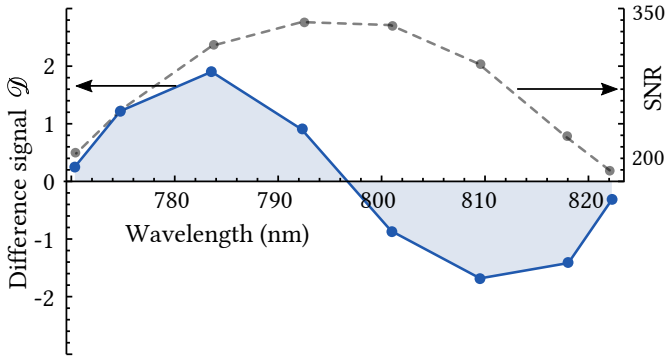

Figure 5.14: Homodyne signal without the phase mode contribution, given by (5.20) with the proper gain (5.21). The spectral structure clearly resembles the time-of-flight mode. Higher order modes are also contained in this spectrum, but are not as obvious to the eye. For comparison, we overlayed the signal-to-noise of the acquisition which is clearly dominated by the phase mode. It is clearly not obvious that such spectrum contains a time-of-flight component.

The result of this procedure when modulating the piezo actuator that was calibrated in section (5.2.1) is presented in figure 5.14.

We can see that the remaining spectral structure in the difference signal $\mathscr{D}$ shows a strong contribution from a time-of-flight mode. The first moment of the DC spectrum is found to be $\mu = 796$ nm, which is in good agreement with the point at which the structure of (5.2.1) crosses zero. The right scale of this plot is attached to the signal-to-noise (5.19) which is overlayed. The left scale is therefore also in the same units of signal relative to noise. Note that the difference signal is much smaller, which is to be expected since the group velocity modulation in air is negligible. It is remarkable however that it may still be extracted.

We stress also that although the sign of the extracted mode 5.14 (*i.e.* $\mathscr{D} < 0$ for $\lambda > \lambda_0$) is right on this figure, it depends on the lock point. More specifically, looking back at figure 5.7, we see that the two sides of the DC fringes are equivalent respectively to a maximum and to a minimum of the demodulated signal. Therefore, depending on which side of the DC fringe we lock on (which we remind is our error signal), the sign of the retrieved signal switches. On the measurement that yielded the result 5.14, we were locked on an "up-fringe", corresponding to a positive HF signal.

This measurement is merely to show that the multimode structure of the field is indeed contained in our spectrally-resolved measurement. We do not try to extract any physical value at this point since we want to construct projection modes to do so.

5.4.2 Signal extraction

We now present the method to construct the projection modes. As we discussed in 4.2, the modes may be constructed from a Hermite-Gauss basis, but only for a Gaussian mean field mode. In the general case, we need to know the spectrum of the mean field and define the next mode in the basis using the theoretical derivation from section 4.2.

In the previous experiment, we showed that it is possible to retrieve the time-of-flight mode using the spectrum from the signal field. Such a method could then potentially be used to construct the detection basis. We experimented with various ways to construct this basis, and we expand in this section the method that was eventually chosen.

Using the multipixel homodyne detection, what is measured is the signal (5.16) integrated on each spectral slice. To properly extract the information carried by the signal field, we remind that we need to set a gain g_n on each signal, as depicted by equation (3.49). The homodyne signal of the n$^{\text{th}}$ pixel is written as

$$\mathscr{I}_{-,n} = \sqrt{N_{LO}}\,\alpha_s^*\, g_n \int_{\Omega_n-\delta\omega/2}^{\Omega_n+\delta\omega/2} \mathrm{d}\Omega\, u_s^*(\Omega)\cdot u_{LO}(\Omega) e^{i\phi_0} \quad + \quad \text{c.c.} \tag{5.23}$$

where $\delta\omega$ is the spectral width of a pixel and u_s is the envelope of the signal field, which may be expanded on the projection modes basis $\{v_i\}$ as $u_s(\Omega) = \sum_i p_i\, v_i(\Omega)$.

The total homodyne signal is obtained by summing the individual contribution from each pixel. It reads:

$$\mathscr{I}_- = \sqrt{N_{LO}}\,\alpha_s^* \sum_n g_n \int_{\Omega_n-\delta\omega/2}^{\Omega_n+\delta\omega/2} \mathrm{d}\Omega \left(\sum_i p_i\, v_i^*(\Omega)\right)\cdot u_{LO}(\Omega) \;+\; \text{c.c.} \tag{5.24}$$

$$\equiv \sqrt{N_{LO}}\,\alpha_s^* \sum_{n,i} p_i\, g_n\, \Gamma_{n,i} \;+\; \text{c.c.} \tag{5.25}$$

where $\Gamma_{n,i}$ is the overlap integral between the local oscillator mode and the i$^{\text{th}}$ mode of the signal field over the n$^{\text{th}}$ spectral band. To show how to chose the gain g in order to extract a given mode j, we rewrite (5.24) as:

$$\mathscr{I}_- = \sqrt{N_{LO}}\,\alpha_s^* \sum_i p_i \cdot \left(\sum_n g_n \cdot \Gamma_{n,i}\right) \quad + \quad \text{c.c.} \tag{5.26}$$

Since p_i are physical parameters, they are real quantities, and we also defined the gains g_n as real numbers. This allows to write:

$$\mathscr{I}_- = 2\sqrt{N_{LO}}\,\alpha_s^* \sum_i p_i \cdot \left(\sum_n g_n \cdot \mathrm{Re}\{\Gamma_{n,i}\}\right) \tag{5.27}$$

$$\equiv 2\sqrt{N_{LO}}\,\alpha_s^* \sum_i p_i \cdot \langle g\,, \Gamma_i \rangle \tag{5.28}$$

We can see from this last expression that the homodyne signal is proportional to the scalar product between the gain function and the overlap integral in the i$^{\text{th}}$ mode. In the case were the local oscillator is a flat function, the gain that allows to retrieve a given mode j of the projection basis is $g = \int v_j$, such that $\langle g, \Gamma_i \rangle = \delta_{ij}$. This gain g then selects a single term in the sum, but it needs to be constructed knowing the shape of v_j, which is deduced from v_0.

Hence, to reconstruct a given mode v_j from the signal field, we need to know the local oscillator's envelope u_{LO}, but also the mean-field mode v_0. In the continuous limit of an infinite number of pixels n, this reconstruction is exact. In our case, the pixelization of the detection can only approximate the structure of the modes, such that the reconstruction is not exact. It is however sufficient to ensure orthogonality between the projection modes, which is the most important in parameter estimations.

The noise in the measurement is given by $\Delta\mathscr{I}_- = N_{LO} \sum_n g_n^2 \int_{\delta\omega} \mathrm{d}\Omega\, |u_{LO}(\Omega)|^2$. Consequently, the signal-to-noise is given by

$$\Sigma = \alpha_s^* \frac{\sum_n g_n \int \mathrm{d}\Omega\, u_s^*(\Omega) \cdot u_{LO}(\Omega)}{\sqrt{\sum_n g_n^2 \int \mathrm{d}\Omega\, |u_{LO}(\Omega)|^2}} e^{i\phi_0} + \text{c.c.} \tag{5.29}$$

where the integrals are over the spectral width $\delta\omega$ around the n$^{\text{th}}$ pixel. Note that the gain function needs to be considered in the noise of the measurement.

In principle, the knowledge of the envelopes v_0 and u_{LO} should be acquired by measuring the DC of the signal and local oscillator's fields. The mode v_i can then be predicted, and the gain that needs to be applied to u_{LO} can be computed.

However, we have discovered that this method did not yield the best reproducibility. The measured homodyne signal is quite sensitive to different parameters such as turbulences that slightly affect the lock point. As a consequence, the signal-to-noise (5.17) shows a different spectral shape than the signal's spectrum recovered by the DC output of the detectors. This small offset is enough to make the output of each measurement very different, and as a consequence, we had to devise another way to construct the modes.

The solution that we eventually picked is to use the demodulated homodyne signal to extract the mean-field mode. This method requires the assumption that demodulated signal is a pure phase modulation, which is a very reasonable hypothesis with our spatial filtering. More specifically, we consider the phase modulation as $\phi_m(\omega) = \omega \cdot t_m$, where $t_m = \delta L n/c$.

We divide the signal-to-noise (5.29) of each individual pixel by the optical frequency ω_n. This treatment does not exactly retrieve the signal envelope because of the pixelization of the signal to noise. It does however provide a stable reference that is specific to each measurement and that takes systematic errors into account. For simplicity, we refer to that retrieved spectrum as the signal field envelope.

Having obtained the signal spectrum, we may now construct the modes basis by applying a proper gain g_n to each pixel. We remind that, in the Gaussian case, this basis is defined by the Hermite-Gauss basis, and the gains g_n are therefore given by the Hermite polynomials.

In the case where the envelope of the signal field is not Gaussian, the modes are more difficult to construct. The time-of-flight mode is formally defined by (4.18) as the derivative of the mean-field mode with respect to frequency. Computing the derivative of the retrieved mean-field mode would be a possibility, however, it is not a stable solution. Indeed, dealing with a discretized spectrum, a numerical derivation is very unstable. Hence, this method does not ensure the best reproducibility.

Another convenient approximation may be done here, considering that our spectra are close to being Gaussian. Therefore, the gain that needs to be applied must also be close to Hermite polynomials. To construct the modes, we then multiply the envelope of the signal field by the proper Hermite polynomial. The obtained spectrum is then orthogonalized to the mean-field mode and normalized.

Such an algorithm does not ensure that the constructed time-of-flight mode is exactly the derivative of the mean-field. However, for our applications, we want to extract the information carried by a given mode, independently of another. Doing so requires perfect orthogonality between the projection modes. It is therefore logical that the experiment is very sensitive to the orthogonality between the modes. Moreover, the most important feature of the time-of-flight mode is the π phase shift at the center of the spectrum, which is easy to achieve using this method.

Finally, one last problem to address is the fact that the local oscillator spectrum is different from the signal, as shown by figure 5.11. Fortunately, this mismatch is easy to account for when constructing the gain[10]. By dividing the projection mode by the local oscillator's spectrum, we multiply the result to the homodyne signal (5.23). This allows to make sure that the envelope of the local oscillator simplifies in the process, and we project on the proper mode defined by the signal's mean-field mode.

This process is detailed in appendix C.

5.4.3 Heterodyne measurements: the need for a stable reference

Before proceeding even further, we need to address yet another complexity in the measurement scheme.

We aim to measure small parameters, which as we have discovered in 5.4.1 is possible. We indeed extracted a small signal (on the order of a signal to noise ratio of 1) from a

[10]For posterity, it is worth mentioning that an interesting way to tackle this problem would be to use the shaper to match both spectra. We did not investigate this method, but it may be worthwhile to pursue it.

much stronger signal (SNR of ~ 300). The result that was presented in that section is however hard to reproduce. It is subject to numerous systematic errors, such as turbulences and dependency on the lock point of the interferometer. Moreover, it is not surprising that the outcome of this measurement is highly dependent on how the filtering fiber is injected. Such a device is quite sensitive to alignement and is subject to variations. It has been observed that a small change in the injection of the fiber (small enough that the coupling is not noticeably affected) results in a totally different measurement. This may be explained by the difference in mode-matching between the two beams of the interferometer. The local oscillator beam is smaller than the signal and is then coupled differently into the fiber. Small changes in the injection therefore result in a different interference pattern.

It is thus very difficult to find a good witness to the proper alignement of the experiment in this configuration. We therefore needed to find a way to ensure good operation of the experiment with a solid reproducibility, in an effort to gain in precision.

What usually provides a good reference is the DC signal from the detectors. However, using such a reference requires to somehow know the result of the experiment before measuring it. Indeed, a possibility would be to monitor the difference signal from figure 5.14 while tweaking the alignement and the lock point of the interferometer. Computing before hand the amount of signal that should remain on the time-of-flight mode, this would provide a reference. More than just being not an exceptionally rigorous experimental procedure, it is cumbersome to do so, since we need to measure multiple quantities to compute the difference signal (like the shot noise).

We then tried to find other references, considering that the experiment would work better if everything were measured simultaneously, in order to account for stability issues. The idea then came to simultaneously measure two modulations which should be similar. For example, if one were to modulate the phase of the field using two similar modulators, one would retrieve exactly the same signal[11]. If not, it then means that the experiment is not properly aligned (different spatial components couple differently into the fiber).

We consequently modulated two different piezo actuators at different RF frequencies. These two actuators are placed at very different distances in the interferometers, such that their amount of spatial displacement is different. If, for example, we do not inject properly the fiber, their higher order spatial components will be transmitted with different weight, resulting in a different measurement.

We heterodyne the two modulations as to detect them simultaneously. The first actuator is modulated at Ω_{RF}, while the other is modulated at $\Omega_{RF} + \Omega_h$, where Ω_h is

[11] We remind that the most relevant measurement is the spectral shape of the phase modulation. The amplitude of this high-frequency spectrum is not as relevant as its shape, which contains the modal structure.

called the heterodyne frequency, and is on the order of a few hundred Hz such that the signal is not filtered by the low-pass filter at the output of the demodulation process. We demodulate the signal at Ω_{RF}, which then shows a modulation at the Ω_h frequency. By Fourier transforming this signal, isolating the peak at the heterodyne frequency and Fourier transforming back, we extract the two different signals without any losses[12].

It is then possible to monitor these two modulations at the same time. This allows to tweak in real-time the injection and the lock point of the interferometer until both signals overlap perfectly. Doing so resulted in the best possible reproducibility in this experiment.

5.4.4 Space-time positioning

At last, we have what is necessary to extract the parameters carried by the multimode field. To perform the measurement, we adopt a strategy similar to the one used for the calibration (5.2.1.2). We ramp the amplitude of the modulation of a phase modulating element and record the demodulated signal for each pixel.

Note that modulating an element different than the one that we calibrated does not require to perform another calibration. By assuming that both modulate the phase of the field in the same way, we just ratio the signal-to-noises of the first harmonics to deduce the displacement.

We then compute the signal-to-noise (5.29) for a given gain function, defining a given projection mode.

5.4.4.1 Phase and time-of-flight measurements

We propose to first measure the minimum variation of distance distance that is possible to measure using either the phase mode or the time-of-flight mode. We remind that the theoretical expression for these is given by equation (4.48) and (4.49). Their reconstructed spectral shape is plotted on figure 5.15. By ramping the amplitude of the modulation, we record the strength of the phase modulation for each part of the spectrum. We then compute their signal-to-noise, as shown on figure 5.16a. By summing each pixel (figure 5.16b), we should recover the same sensitivity that we measured using a non spectrally-resolved homodyne detection for the calibration.

To confirm that assertion, we measured the power in the signal beam and found 346 µW. Taking into account a quantum efficiency of the detectors of 90%, a contrast of 90% and a resolution bandwidth (specified by the low-pass filter for demodulation) of

[12]Note that during this process, there is a digital demodulation phase that needs to be determined to maximize the retrieved heterodyne signal.

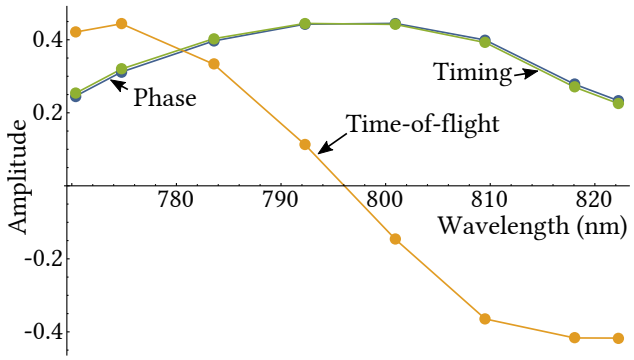

Figure 5.15: Detection modes for space-time positioning. Because of the limited bandwidth, the difference between the timing mode and the phase mode is negligible but still noticeable.

15 kHz[13], we estimate a detected photon number of $\sim 10^{10}$.

The minimum theoretical detectable displacement is then found to be

$$d_{min}^{SQL} = 5.2 \text{ fm} \Big/ \sqrt{\text{Hz}} \tag{5.30}$$

Taking the longitudinal displacement for which the signal-to-noise of figure 5.16b is equal to 1 and normalizing by the resolution bandwidth, we measure an ultimate sensitivity of

$$d_{min,XP} = 7.2 \pm 0.1 \text{ fm} \Big/ \sqrt{\text{Hz}} \tag{5.31}$$

which is once more in good agreement with the theoretical value.

To perform the projective measurement, we take the raw acquisition (*i.e.* not the signal-to-noise 5.16a), and linearly fit the response of each pixel. We then perform the scalar product of these fits to the filter of the mode we want to project on. Indeed, the acquisition already contains the spectral shape of the local oscillator, hence we need only the filter part of the modes to perform the projection. This gives the signal for which we then need to compute the signal-to-noise

The noise is obtained by projecting on the projection mode the variance of vacuum for each pixel. Note that, from (5.29), we need to take the square of the gain function to do this projection, the variance is proportional to the number of photon (it is therefore a power measurement) and the signal is proportional to the square root of the number

[13]It is worth stressing that the filter has a Lorentzian transfer function, in contrast with the spectrum analyzer that acquires in a Gaussian window. The time-bandwidth product of a Lorentzian is 0.142.

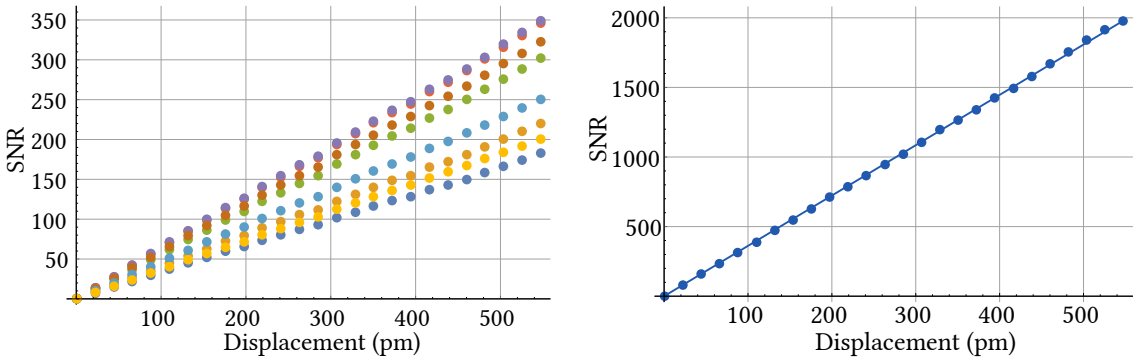

Figure 5.16: Signal recovered by each pixel of the detection while scanning the amplitude of the calibrated piezo actuator. (a) Retrieved signal-to-noise for each pixel. (b) Total signal-to-noise and linear fit.

of photon (it is a measurement of the field). We then obtain the shot-noise projected on the desired mode[14].

We may then compute the signal-to-noise of the displaced field projected on a given mode. The signal-to-noise once projected on the phase and time-of-flight modes is outlined on figure 5.17.

We remind that the limits in sensitivity for measuring a distance using the phase and time-of-flight modes are respectively given by (4.48) and (4.49). In this case, we modulate the distance in air, hence $v_\varphi \simeq v_g$ is a very reasonable approximation. The ratio of these two sensitivities is then given by

$$\boxed{\frac{(\delta L)^g_{min}}{(\delta L)^\varphi_{min}} = \frac{\omega_0}{\Delta\omega}} \tag{5.32}$$

Experimentally, from (5.31), the retrieved sensitivity while projecting on the phase mode is $d^\varphi_{min,XP} = 7.2 \pm 0.1 \text{ fm}/\sqrt{\text{Hz}}$ and when projecting on the time-of-flight mode, we have $d^g_{min,XP} = 382.6 \pm 0.5 \text{ fm}/\sqrt{\text{Hz}}$. The ratio of these sensitivities then reads

$$\boxed{\frac{(\delta L)^g_{XP}}{(\delta L)^\varphi_{XP}} \simeq 53 \pm 2} \tag{5.33}$$

[14]Note that the value of the shot noise obviously does not change a lot when projecting it onto the filters. Nevertheless, the small variation still needs to be accounted for.

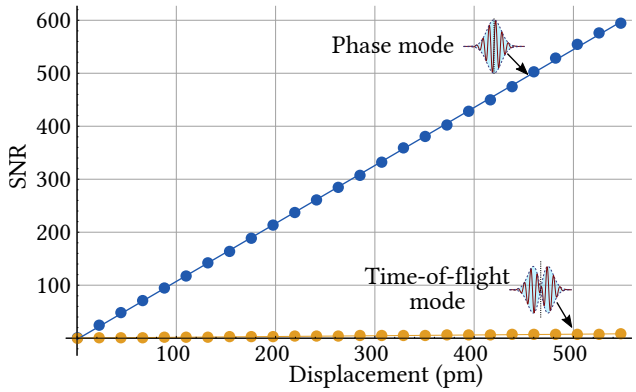

Figure 5.17: Signal-to-noise of the phase modulation projected on the detection modes attached to a phase and a time-of-flight measurement.

To compare to the theoretical ratio, we need to compute the first and second moment of the spectrum that is received by the detector. We use the DC output of the detector when detecting the signal's spectrum. We find $\mu = 796.5$ nm for the first moment and $\sigma = 15$ nm for the second moment. This defines an effective center frequency and bandwidths as $\omega_0^{XP} = 2.37$ PHz and $\Delta\omega^{XP} = 44.5$ THz. This allows to compute the ratio

$$\frac{\omega_0^{XP}}{\Delta\omega^{XP}} \simeq 53.2 \tag{5.34}$$

which is in excellent agreement with the retrieved ratio (5.33).

This result serves as a proof-of-principle for projective measurement. We measured the minimum detectable displacement in a homodyne measurement scheme when projecting on the two modes attached to a phase and a time-of-flight measurement. We found obviously that a time-of-flight measurement is less sensitive that a phase measurement, and the difference in sensitivities is found to be dependent on the bandwidth and the center wavelength of the detected light.

5.4.4.2 Detection mode

We now propose to go one step further and try to compute the ultimate sensitivity for space-time positioning when projecting on the detection mode defined in 4.2.4.2. We name that mode *timing mode*.

We remind that this detection mode is a superposition of the phase mode and the time-of-flight mode, with a weight defined by the ratio (5.34). Having measured the experimental moments of the field and having constructed the phase and time-of-flight modes, it is then straightforward to build the detection mode. We plot it on figure 5.15.

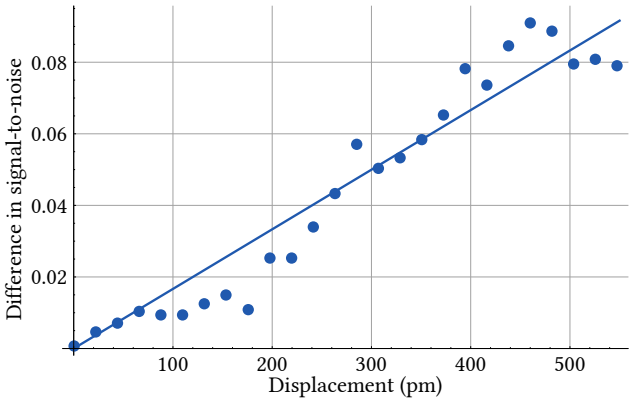

Figure 5.18: Enhancement in sensitivity between the detection mode for space-time positioning and the phase mode.

We can see that it is very similar to the phase mode, since the bandwidth of the spectrum is relatively small. There is still a noticeable difference in the shape, and as a direct consequence, a projective measurement using this mode will result in a different sensitivity.

For a modulation in air, the ratio of sensitivities for a phase detection and a detection on the timing mode is given by

$$\frac{(\delta L)^{\varphi}_{min}}{(\delta L)_{SQL}} = \sqrt{1+\left(\frac{\Delta\omega}{\omega_0}\right)^2} \simeq 1+\frac{1}{2}\left(\frac{\Delta\omega}{\omega_0}\right)^2 \tag{5.35}$$

As such, the enhancement is quantified by $\frac{1}{2}\left(\frac{\Delta\omega}{\omega_0}\right)^2$, which with our experimental moments amount to $1.8\cdot 10^{-4}$, which is very small. A way to show this enhancement experimentally is to plot the difference between a projection of the homodyne signal on the timing mode and on the phase mode $\Sigma_{\delta L}-\Sigma_{\varphi}$ as a function of the displacement. This is plotted on figure 5.18. We can see that the slope of this function is positive, showing that the detection mode has indeed a higher sensitivity.

We compute the minimum detectable displacement with the timing mode and ratio it to the sensitivity of the phase mode. The measured enhancement is found to be $(1.5\pm 0.2)\cdot 10^{-4}$, which is in good agreement to the expected value.

We have then showed the applicability of projective measurements with the example of space-time positioning. We measured the smallest displacement possible using the modes attached to a phase and a time-of-flight detection, and constructed another mode that combines both methods to obtain an even better sensitivity.

5.4.5 Dispersion

We now propose to use the time-of-flight mode to measure a different parameter. As shown by (4.45) and (4.46), the retrieved information for a perturbation of distance depends on the phase or the group velocity of light in the medium. For air, these are equal. However, if it were possible to introduce a path variation in a strongly dispersive medium, then the two velocities are no longer equal, and the time-of-flight mode would retrieve a different information.

Moreover, knowing the value of the phase velocity by projecting on the phase mode, it seems possible to measure the group velocity by subtracting the projection on the phase mode to the projection on the time-of-flight mode. The original idea for that application is depicted in appendix D, which proved difficult to implement.

We had to devise another way to induce a strong modulation of the group velocity. Since it does not seem possible to modulate the group velocity independently of the phase velocity, we chose to introduce a modulation of path by introducing a dispersive material in the beam. We settled for a prism made of SF-10, which we mounted on a piezo-actuator as shown on figure 5.19. With careful alignement, we were able to achieve a deep phase modulation.

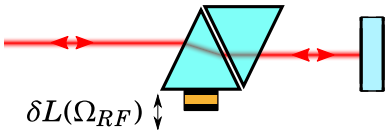

Figure 5.19: Modulation of path in a strongly dispersive medium. The two prisms are places as close to possible as not to introduce any problems when the colors are recombined.

Using such a device to modulate the path, the phase and time-of-flight modes will retrieve a different parameter. To show this, we propose to make use of another detection scheme than the multipixel detection. Namely, we use a single diode homodyne detection and resolve the spectral structure of the field by resolving it temporally, as introduced in section 3.3.3. Such a scheme is not dependent on lock point and allows to retrieve the spectrum with less ambiguity than the multipixel. Note that the multipixel detection also works for this application and has the advantage of resolving the spectral structure in a single-shot, but the representation is pixelized rather than continuous.

We retrieve the cross-correlation of the signal and local oscillator field when modulating the calibrated piezo actuator and the prism. Both modulations are retrieved simultaneously through heterodyning. We also measure the DC output of the photodiodes. Performing a Fourier transform then allows to retrieve the spectrum, as depicted by figure 5.20. Note that the spectral resolution of the retrieved spectrum is much better than

the multipixel, since it is defined by the time window on which the cross-correlation is measured, which can be made arbitrarily large.

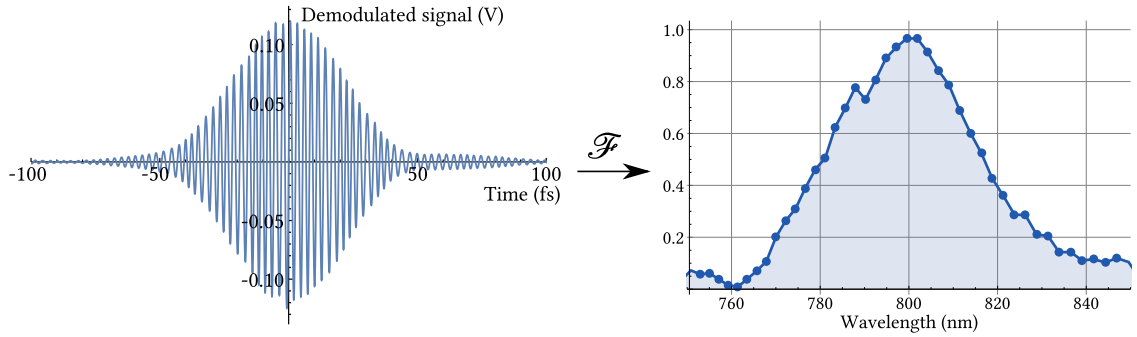

Figure 5.20: Demodulated signal of the cross-correlation between the signal and the local oscillator fields. The retrieved fringes are those of the high-frequency phase modulation. The Fourier transform is directly the spectrally resolved homodyne signal.

By heterodyning, we retrieve simultaneously the signal-to-noise spectra for the modulation of a calibrated piezo-mounted mirror and the prism. Using a procedure similar to (5.20), it is possible to isolate the dispersion term.

More precisely, we write as Σ_1 and Σ_2 respectively the signal to noise of the piezo actuator and the prism. It writes:

$$\Sigma_n(\Omega) = 2\sqrt{N}\left[\omega_0\, t_{\varphi,n}\cdot v_0(\Omega) + \Delta\omega\, t_{g,n}\cdot v_1(\Omega)\right] \tag{5.36}$$

where n denotes which element is modulated. Computing the difference signal $\mathscr{D}$ between the signal-to-noise ratios then yields

$$\begin{aligned}\mathscr{D}(\Omega) &= \Sigma_2(\Omega) - g\cdot\Sigma_1(\Omega) \\ &= 2\sqrt{N}\left[\omega_0\left(t_{\varphi,2} - g\, t_{\varphi,1}\right)\cdot v_0(\Omega) + \Delta\omega\left(t_{g,2} - g\, t_{g,1}\right)\cdot v_1(\Omega)\right]\end{aligned} \tag{5.37}$$

Similarly to (5.22), the gain to be digitally added in order to nullify the phase mode's contribution to the difference signal is found to be

$$g = \frac{t_{\varphi,2}}{t_{\varphi,1}} \equiv \frac{\int \mathrm{d}\Omega\, \Sigma_2}{\int \mathrm{d}\Omega\, \Sigma_1} \tag{5.38}$$

Since in air, group and phase velocities are equal, we have $t_{\varphi,1} = t_{g,1}$. Upon application of the gain, the difference signal simplifies to

$$\begin{aligned}\mathscr{D}(\Omega) &= 2\sqrt{N}\,\Delta\omega\left(t_{g,2} - t_{\varphi,2}\right)\cdot v_1(\Omega) \\ &\equiv 2\sqrt{N}\,\Delta\omega\cdot\frac{\omega_0\, n_0'\,\delta L_2}{c}\cdot v_1(\Omega)\end{aligned} \tag{5.39}$$

We can see that the difference signal should in theory contain a single contribution on the time-of-flight mode which is directly proportional to the index dispersion at the center wavelength.

Using projections, it is possible to suppress the dependency on the displacement δL_2. Indeed, projecting the signal to noise on the phase mode yields

$$\langle \Sigma_2, v_0 \rangle = 2\sqrt{N}\,\omega_0 t_{\varphi,2} \equiv 2\sqrt{N}\,\omega_0 \frac{n_0 \delta L_2}{c} \tag{5.40}$$

Dividing the difference signal projected on the time-of-flight mode by this quantity then yields

$$\boxed{\frac{\langle \mathscr{D}, v_1 \rangle}{\langle \Sigma_2, v_0 \rangle} = \frac{n_0'}{n_0}\Delta\omega} \tag{5.41}$$

which is only dependent on the bandwidth of the field and on the index properties of the medium.

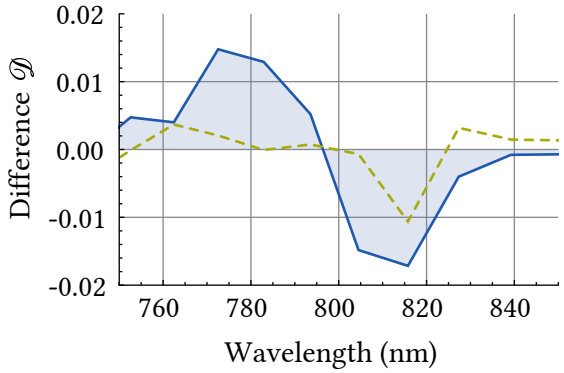

Figure 5.21: Heterodyne difference signal. The retrieved shape clearly ressembles to a time-of-flight mode. Dashed line correspond to the retrieved spectrum with the same procedure but when modulating two similar piezo-mounted mirrors.

On figure 5.21, we show the difference signal (5.39) which shows obviously principally a time-of-flight structure. In dashed lines, we applied the same gain procedure when we heterodyne and demodulate two similar piezo-mounted mirrors. This allows to show that the retrieved signal is indeed dependent on the difference between the two modulating elements.

Using the projections defined by (5.41), we retrieve a value of

$$\frac{\langle \mathscr{D}, v_1 \rangle_{XP}}{\langle \Sigma_2, v_0 \rangle_{XP}} \simeq (1.2 \pm 0.2) \cdot 10^{-2} \tag{5.42}$$

Using Sellmeyer's equations and the values of index and index dispersion given in table A.1, we find that, for SF10, $\frac{n_0'}{n_0} \approx 9.9 \cdot 10^{-3}$ fs. For the considered bandwidth, the theoretical value of (5.42) is therefore $3.9 \cdot 10^{-3}$. The experimental value is too important by a factor of 3. There are multiple leads to explain this discrepancy. Among the most relevant is the fact that this measurement is slow compared to the single shot acquisition of the previous experiments. In order to obtain a good resolution, the delay line needs to be swept over a long range, resulting in a longer acquisition time (on the order of 2 seconds). Such a measurement is prone to turbulences and fluctuations. Moreover, since it is not spectrally-resolved, the shot noise needs to be reconstructed from the DC signal.

The influence of all the sources of error has not been investigated in details since this method was applied near the end of this thesis. It would however benefit from being studied further, since it presents an interesting alternative to the multipixel detection.

5.4.6 Quantum spectrometer

To conclude on this part on parameter estimation, we consider the same experiment on the amplitude quadrature.

As described in (4.2.2), the time-of-flight mode can be used in the amplitude quadrature to detect a shift in the spectrum. Using the multipixel detectors, such a measurement is quite easy to achieve, since it is an amplitude measurement and thus does not require any homodyne detection or delay lock. We took this measurement one step further by using squeezed vacuum in order to perform a measurement below the standard quantum limit.

This experiment was accomplished with a different laser source, delivering longer pulses on the order of 100 fs. The reason being that this source is injecting a synchronously pumped optical parametric oscillator, which delivers under threshold multimode squeezed vacuum[Roslund 13]. The modal structure of this quantum light is well approximated by the Hermite-Gauss basis, which also happens to be the basis on which the previous detection modes are expanded. Therefore, it is possible to use such field that is squeezed in the proper mode to enhance the sensitivity of projective measurement, as described by (4.9).

For this experiment, we chose to modulate the center wavelength of the laser, again at a high frequency of ~ 1.5 MHz. This is achieved by modulating a mirror inside the laser cavity, usually used to lock the spectrum's center[15]. The modulation was added to the retrocontrol loop of the lock, small enough such that it does not hinder the stability.

Since the wavelength parameter lies on the amplitude quadrature, the measurement

[15] On this source, this lock actually also stabilizes the CEO.

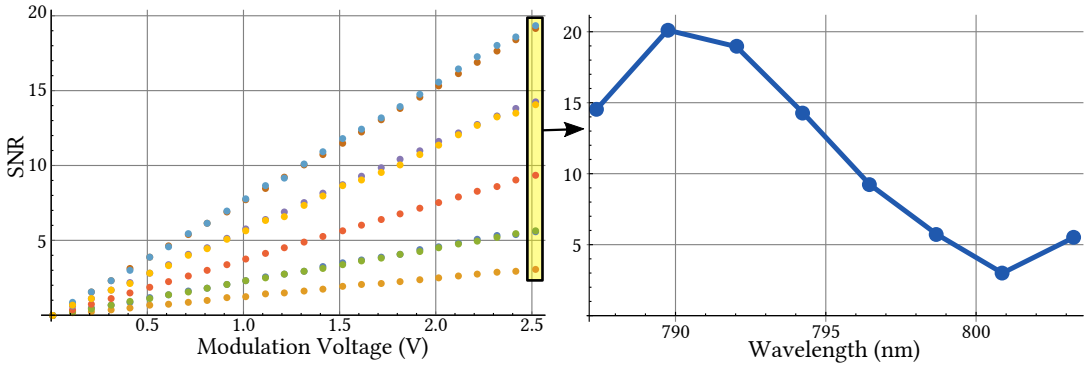

Figure 5.22: Signal-to-noise ratio for each pixel when the center wavelength is being modulated by a variable amplitude. On the right, the last point of the scan (*i.e.* maximum modulation strength) is plotted as a function of wavelength. It shows a non-Gaussian shape.

is performed using a single multipixel detector, greatly simplifying the scheme[16]. However, since it is dealing with quantum resources, the experiment still comprises a lot of complications. The first one it to be able to generate a bright beam which is squeezed on the proper mode. This was achieved by combining the multimode squeezed vacuum output of the OPO with a strong beam on a 93-7% beamsplitter. These two beams had to be locked together. For a more complete description of the experiment, see [Cai 15].

As a first step, the experiment was made using classical resources, much like what was described in the previous section. The amplitude of the modulated element is ramped, and the signal received by each pixel (on the amplitude quadrature) is subsequently demodulated. The retrieved signals are plotted on figure 5.22.

In contrast with our previous measurements on the phase quadrature, we directly retrieve a high frequency spectrum that has a shape similar to the time-of-flight mode. That is to be expected from (4.25), since demodulating this field and computing its signal-to-noise would retrieve directly

$$\Sigma(\Omega) = \frac{\delta\omega}{2\Delta\omega} \cdot v_1(\Omega) \tag{5.43}$$

In this scheme where only a single beam is used, the modes construction is easier: it can be constructed from the spectral shape of the shot-noise. Doing so allows to construct the amplitude mode and the time-of-flight mode without having to resort to a complicated construction as in 5.4.2.

[16]Note that, since it is using a single detector, the measurement needs to be performed at a quantum limited frequency in order to be shot-noise limited.

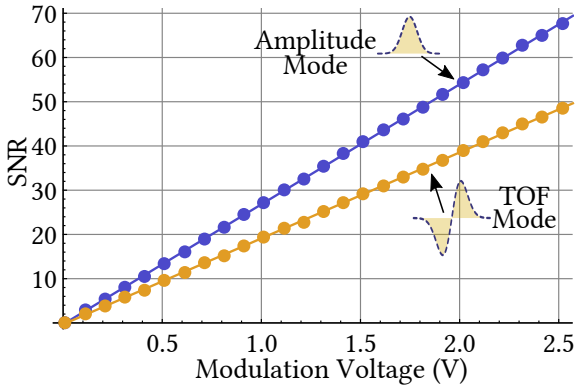

Figure 5.23: Signal-to-noise ratios after projection on the phase mode and on the time-of-flight mode. The modulation induces variations in both amplitude and wavelength.

After projecting on these two modes, we retrieve the signal-to-noise ratios depicted by figure 5.23. We can see that projecting on the amplitude mode results in a higher signal than the time-of-flight mode. Therefore, the way the wavelength is modulated in this experiment does also induce a variation of amplitude that is subsequently detected.

Note also that we did not calibrate the displacement, since we are interested mostly in the quantum enhancement. Therefore, we consider that this measurement on the time-of-flight mode is quantum limited, and we retrieve for a signal-to-noise ratio of 1 the ultimate value given by (4.31). Computing again the first moment from the reconstructed modes and considering a number of photons of $4{\cdot}10^{16}$ (corresponding to 10 mW detected over a second), the ultimate limit for the detection of a spectral displacement is

$$(\delta\omega)_{min}^{SQL} \simeq 61 \text{ kHz} \Big/ \sqrt{\text{Hz}} \tag{5.44}$$

Interestingly, this value is smaller than the tooth spacing.

We then perform the same measurement when squeezed vacuum is injected. The sensitivity will then be proportional to the variance of the detection mode. The way squeezed vacuum is generated, in order to have a noise reduction in the second mode, the first mode must necessarily show excess noise (see section 8.1.1).

The first mode is antisqueezed and shows an excess noise of +4.4 dB, whereas the second mode is squeezed, and has a reduced noise of −1.4 dB. The result upon projecting on these modes is shown on figure 5.24 along with the case when vacuum is injected.

We can see that the amplitude mode does indeed show excess noise, since the sensitivity is reduced with respect to the vacuum case. On the other hand, the time-of-flight mode increases the sensitivity by a considerable amount of 21%. The sensitivity limit is

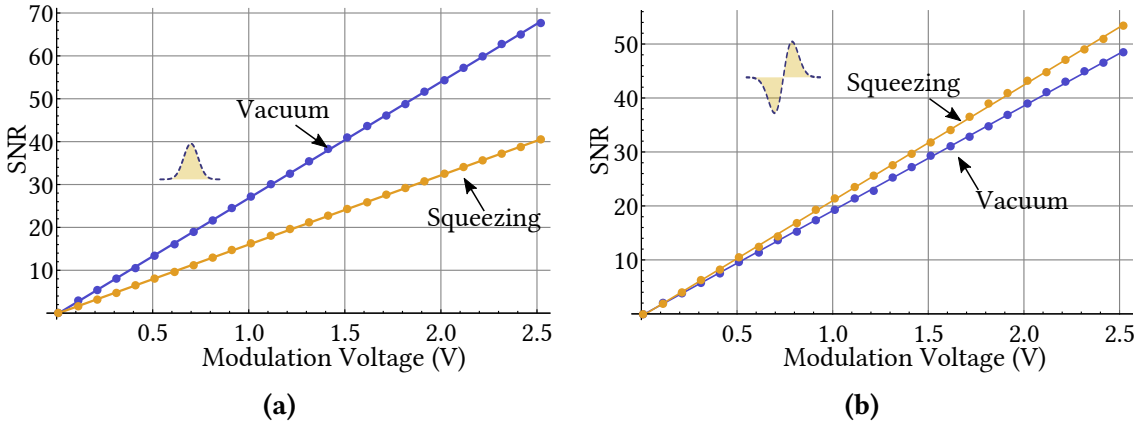

Figure 5.24: Comparison between vacuum and squeezed vacuum input upon projection on (a) the amplitude mode (b) the time-of-flight mode.

then given by

$$\boxed{(\delta\omega)_{min}^{sqz} \simeq 50 \text{ kHz}\Big/\sqrt{\text{Hz}}} \tag{5.45}$$

This resulting sensitivity is below the standard quantum limit.

Part III

Noise analysis of an ultra-fast frequency comb

6 Optical cavities

(Upon observing the transverse modes of a particularly misaligned cavity, looking incredibly similar to the Batman sign[Jacquard 12]) "I don't think I can ever do better than that."

– Clément "*Game Over Man*" Jacquard

Contents

6.1 Fabry-Perot cavities 152
6.1.1 Input-output relations 152
6.1.2 Characteristic quantities 154
6.1.3 Spatial mode 155
6.1.4 Noise filtering 156
6.1.5 Quadrature conversion 156
6.2 Synchronous cavities 157
6.2.1 Resonance condition 158
6.2.2 The cavity's comb 158
6.2.3 Simulations 160
6.3 Experimental realization 162
6.3.1 Motivations 162
6.3.2 Design and construction 162
6.3.3 Cavity lock 163
6.3.4 Environnemental pressure dependency 163
6.3.5 Noise properties 165

In the previous part, we used a modal description of the field to extract information that was hard-coded in it. In this part, we show that the same formalism may be applied to the noise analysis of a frequency comb, in both amplitude and in phase.

For that purpose, we need to develop tools to access the noise characteristics. We have already seen that accessing the amplitude noise is straightforward. However, resolving phase noise necessitates to compare a signal to a reference, being electrical or optical. As it was hinted in section 3.1, in a homodyne detection scheme, if the phase noise of one field in the interferometer is known, then we can deduce the phase noise of the other field. Such a scheme would allow to apply our modal characterization to noise characteristics of a laser source.

To decouple the noise, we chose to introduce a Fabry-Perot cavity in the signal arm of the interferometer. It acts as a low-pass filter in both amplitude and phase, whose output

shows different noise properties than its input. From a specific analysis frequencies defined by the cavity's finesse, we can consider that the noise properties of the filtered beam are quantum limited, and may thus be used in a homodyne measurement to access the noise distribution of the local oscillator.

In this part, we focus on the description of Fabry-Perot cavities in the femtosecond regime. We also present experimental details on the characterization of a high finesse cavity injected by a broad spectrum.

6.1 Fabry-Perot cavities

In this section, we remind the basic equations that describe a Fabry-Perot cavity and its filtering behavior. The general theory can be found in many optics book, such as [Siegman 86].

6.1.1 Input-output relations

We consider a ring Fabry-Perot cavity of length L made of three mirrors. We label two input and output mirrors with Fresnel coefficients in energy[1] R_1,R_2 and T_1,T_2, such that $R_i + T_i = 1$. The third mirror is supposed have a perfect reflectivity. The amplitude coefficient are assumed to be real and are written as $r_i = \sqrt{R_i}$, $t_i = \sqrt{T_i}$. A representation of such cavity is done on figure 6.1.

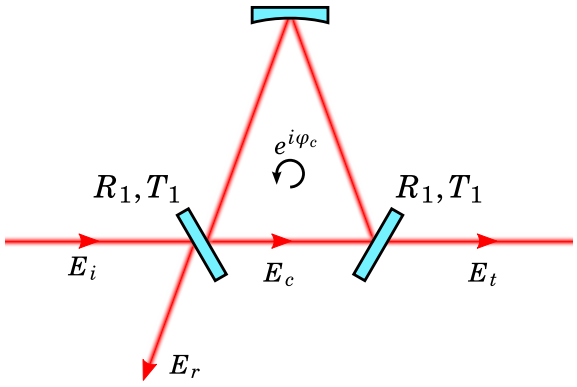

Figure 6.1: Schematic drawing of a ring cavity. The back mirror is supposed to have a perfect reflectivity. The phase accumulated on one round-trip is written φ_c.

[1]For simplicity, we do not assume that the Fresnel coefficients are dependent on wavelength. Nevertheless, for a full simulation of a high finesse cavity injected by a broad spectrum, the reflectivity curve of the mirrors needs to be taken into account.

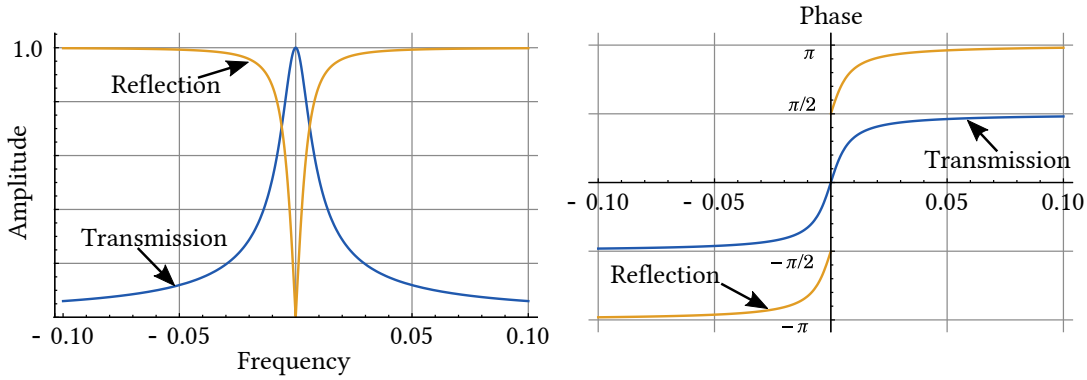

Figure 6.2: Amplitude and phase of the complex transfer coefficients in transmission and in reflection for an impedance matched cavity of finesse 1000. The phase of the reflected field is not defined at resonance, since all the incident field is transmitted. If losses are included in this model, there exists a reflected field at resonance.

We are interested in the incident, transmitted and reflected fields, that we write respectively $E_i^{(+)}$, $E_t^{(+)}$ and $E_r^{(+)}$. We write the phase accumulated over a round-trip as $\varphi_c(\Omega)$, and the field inside the cavity is written as $E_c(\Omega)$. The input-output relations of the cavity are written as

$$E_t^{(+)}(\Omega) = t_c(\Omega) \cdot E_i^{(+)}(\Omega) \quad \text{and} \quad E_r^{(+)}(\Omega) = r_c(\Omega) \cdot E_i^{(+)}(\Omega) \tag{6.1}$$

These fields are linked by the following coefficients:

$$t_c(\Omega) = \frac{t_1 t_2 e^{i\varphi_c(\Omega)/2}}{1 - r_1 r_2 e^{i\varphi(\Omega)}} = \tau(\Omega)\, e^{i\Phi_t(\Omega)} \tag{6.2}$$

$$r_c(\Omega) = \frac{r_2 e^{i\varphi_c(\Omega)} - r_1}{1 - r_1 r_2 e^{i\varphi(\Omega)}} = \rho(\Omega)\, e^{i\Phi_r(\Omega)} \tag{6.3}$$

We decomposed both coefficients in amplitude and in phase. The phase accumulated one round-trip is noted $\varphi_c(\Omega)$. As before, the frequencies are taken relative to the carrier $\Omega = \omega - \omega_0$.

By computing the amplitude and the phase of the transfer coefficients, it can be shown that $\tau(\Omega)$ and $\rho(\Omega)$ are even functions, while $\Phi_t(\Omega)$ and $\Phi_r(\Omega)$ are odd functions. The coefficients are depicted on figure 6.2.

When the cavity is impedance matched, *i.e.* $t_1 = t_2 = t$ and $r_1 = r_2 = r$, the equations are greatly simplified. The transmission coefficient in energy is given by: :

$$T_c(\Omega) = |t_c(\Omega)|^2 = \frac{T^2}{(1-R)^2 + 4R \sin^2\left(\frac{\varphi_c(\Omega)}{2}\right)} \tag{6.4}$$

which is maximal for $\varphi_c(\Omega) = 0\ [2\pi]$.

In the remaining, it will be convenient to consider the input-output relations in term of the quadratures of the field.

We remind that the real field is decomposed in the spectral domain as a sum of the analytic fields as:

$$E(\omega) = E^{(+)}(\omega) + E^{(-)}(-\omega) \tag{6.5}$$

In term of the field's amplitude, we have $E^{(+)}(\omega) = \mathscr{E}_0\, a(\omega - \omega_0)$. The input-output relations may the be written as

$$a_t(\Omega) = t_c(\Omega) \cdot a_i(\Omega) \tag{6.6}$$

Using the expressions of the field quadratures (1.45) and (1.46), it is possible to rewrite the input-output relations as a function of the quadratures of the incident and transmitted / reflected fields. A simple expression is obtained by considering the parity of the transfer coefficients. The relation linking the field quadratures is then written as

$$\begin{pmatrix} X_t \\ P_t \end{pmatrix}(\Omega) = \tau(\Omega) \begin{bmatrix} \cos\Phi_t(\Omega) & -\sin\Phi_t(\Omega) \\ \sin\Phi_t(\Omega) & \cos\Phi_t(\Omega) \end{bmatrix} \cdot \begin{pmatrix} X_i \\ P_i \end{pmatrix}(\Omega) \tag{6.7}$$

A similar expression may be obtained for the reflected field's quadratures.

6.1.2 Characteristic quantities

A cavity is defined intrinsically by its mirrors and its length, which allow to defined quantities to characterize it.

The phase accumulated over one round-trip of a cavity in vacuum writes as

$$\varphi_c(\Omega) = (\Omega + \omega_0)\frac{L}{c} \tag{6.8}$$

For the cavity to be resonant at the frequency ω_0, its length L needs to satisfy the condition:

$$L = p\,\lambda_o \tag{6.9}$$

This length defines the spacing in frequency between two resonances as the free spectral range (FSR):

$$\nu_{FSR} = \frac{c}{L} \tag{6.10}$$

We introduce the finesse $\mathscr{F}$ of the cavity, which is an intrinsic quantity only dependent on the properties of the cavity. For a global reflectivity R in power[2] (i.e. a fraction $1-R$ in power is lost after one round-trip), the finesse reads:

$$\mathscr{F} = \frac{\pi}{2\arcsin\left(\frac{1-\sqrt{\rho}}{2\sqrt{\sqrt{\rho}}}\right)} \tag{6.11}$$

In the high reflectivity approximation, this formula approximates to:

$$\mathscr{F} \simeq \frac{2\pi}{1-\rho} = \frac{2\pi}{T+P} \tag{6.12}$$

where we noted T the global transmission, and P the round-trip losses. This formula is only valid for a high finesse. A common way to describe the finesse is the average number of round-trip of a single photon inside the cavity before being transmitted. The higher the finesse, the longer the light is trapped inside the cavity. This properties is useful to understand the filtering properties of a cavity.

6.1.3 Spatial mode

In order for a cavity to be a stable resonator, the intra-cavity field needs to be periodic on the cavity length: the accumulated phase needs to be a multiple of 2π, and the transverse profile of the cavity beam must overlap with the incident beam.

The stability condition for a cavity is obtained by modeling the propagation of the beam using the ABCD formalism, and solving for the complex beam parameter to be unchanged after a round-trip. This defines the distances between the optics that result in a stable resonator.

Usually, the spatial mode of the cavity is a TEM_{00}. Proper injection of the cavity consists in overlapping the incident beam with the cavity's mode. To do so, one needs to align the input beam properly, and to ensure that the mode matches the one of the cavity by setting its waist size and position on the proper values.

Misaligning the input beam puts energy in odd modes (such as TEM_{01}), whereas incorrect mode-matching transfers energy in the even modes (such as TEM_{02}). It is therefore possible to distinguish experimentally between an error in alignement and an error in mode-matching by looking at the transmitted spatial modes[3]. Such properties can be used to change the mode of the input beam, which is obviously a lossy process[Treps 03].

[2] For the cavity sketched on figure 6.1, the global reflectivity writes as $R = R_1 R_2$. Losses can be introduced in this factor.

[3] Note that distinguishing between an mismatch in waist size and in waist position requires to access the amplitude and the phase quadrature of the TEM_{02} mode.

6.1.4 Noise filtering

The spatial profile of the transmitted beam is defined by the mode of the cavity. The behavior may be seen as a filter of the transverse profile of the input beam. Indeed, if the mode at input shows other modes than the one of the cavity, then these components will propagate away and not resonate in the cavity. The efficiency of this filtering is dependent on the finesse. The higher the finesse, the more efficient the filtering.

In the spectral domain, the same phenomenon occurs, even though it is not as straightforward to describe. Using the sidebands picture 3.2.1.2, any noise can be represented as a sideband of the optical frequency. If the frequency of the noise is high enough such that the sidebands are not resonant, according to (6.7), the sidebands won't be transmitted by the cavity.

Therefore, the cavity will act as a low-pass filter in noise, which cutoff frequency can be defined from the point at which the amplitude transfer coefficient of figure 6.2 is reduced by a factor of 2, in analogy to electric filters. This frequency defines the bandwidth ν_c of the cavity, and is related to the finesse and the free spectral range of the cavity by:

$$\nu_c = \frac{\nu_{FSR}}{\mathscr{F}} \tag{6.13}$$

A higher finesse thus leads to a stronger filtering of the noise. In the temporal domain, a similar treatment allows to consider that the fluctuations of the field are averaged over the time the light is trapped in the cavity. This time is the inverse of the bandwidth of the cavity.

Using the quadratures description (6.7), we then see that this low-pass filtering occurs in both quadratures, thus filtering the amplitude and the phase noise of the incident field.

6.1.5 Quadrature conversion

In term of quadratures, the noise filtering is described another way. Consider amplitude and phase noise of the incident field, written as δX_i and δP_i. The variance of the amplitude and phase noise of the transmitted field (6.7) are then written:

$$\langle \delta X_t^2 \rangle = c_1^2 \langle \delta X_i^2 \rangle + c_2^2 \langle \delta P_i^2 \rangle - 2c_1 c_2 \langle \delta X_i \cdot \delta P_i \rangle \tag{6.14}$$

$$\langle \delta P_t^2 \rangle = c_1^2 \langle \delta P_i^2 \rangle + c_2^2 \langle \delta X_i^2 \rangle + 2c_1 c_2 \langle \delta X_i \cdot \delta P_i \rangle \tag{6.15}$$

where we wrote the conversion coefficients $c_1 = \tau(\Omega)\cos\Phi_t(\Omega)$ and $c_2 = \tau(\Omega)\sin\Phi_t(\Omega)$. We can see that the amplitude quadrature of the transmitted field contains information about both optical quadratures of the incident field and also correlations between amplitude and phase noise. As it is shown in section 7.3.4, these correlations are considerably smaller than the individual noise in amplitude or in phase.

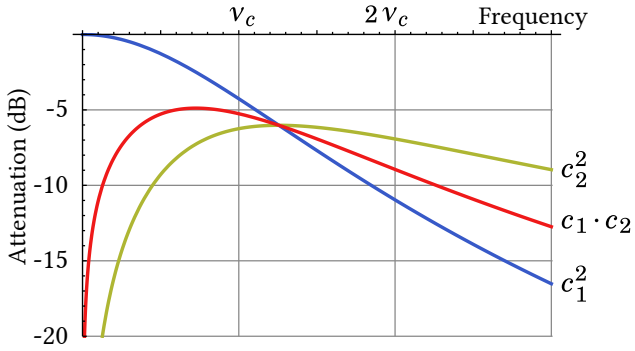

Figure 6.3: Amplitude of the coefficients that convert noise from one optical quadrature to the other.

On figure 6.3, we plotted the conversion coefficients. We can see for example that on the amplitude quadrature of the transmitted field (6.14), the amplitude noise is filtered by the coefficient c_1. However, the amount of phase noise conversion increases with analysis frequency, up to approximately $\sim \frac{\nu_c}{2}$. At this frequency, the value of the two coefficients differs by about 2 dB. In the case where phase noise is much higher than amplitude noise (which is the case with a modelocked Ti:Sa laser), the amplitude quadrature of the transmitted field should therefore show excess noise. On the phase quadrature (6.15), the input phase noise is attenuated, and a portion of the input amplitude noise is converted.

Thus, the noise switches quadrature between the input and the output of the cavity. Nevertheless, the noise is still attenuated, such that the total noise is diminished. This quadrature conversion effect will be of importance later.

6.2 Synchronous cavities

In order for a cavity to be resonant for multiple optical frequencies, the resonance condition (6.9) needs to be revised. In the time domain, it is straightforward to see that a resonant cavity injected by a train of pulse corresponds to the situation where the pulse inside the cavity overlaps with the next pulse in the train. In order to be perfectly resonant, both the carrier and the envelope of the pulses need to overlap. Such cavities are then said to be synchronous, since they need to be synced with the repetition rate of the laser.

In this section, we write the theory for synchronous cavities, and do simulations to predict the behavior of high finesse synchronous cavities. A more complete treatment may be found in [Medeiros de Araujo 12].

6.2.1 Resonance condition

We consider that the cavity is injected by a frequency comb whose CEO is zero, such that the frequencies of the comb are written simply as $\omega_n = n\omega_r$ (see (2.1)). In order for the cavity to be resonant for the entire comb, the phase accumulated on a round-trip needs to be a multiple of 2π for each frequency :

$$\varphi_c(\omega_n) = 0 \ [2\pi] \ \forall \ n \tag{6.16}$$

Solving this condition with (6.8) allows to deduce that the cavity length needs to satisfy

$$L = \frac{2\pi c}{\omega_r} \equiv L_r \tag{6.17}$$

The length of the cavity needs to equal the length between two pulses, which is also the length of the laser cavity. Note that this solution is also valid for any multiple integer of the repetition length. Such a cavity would also transmit the entire spectrum, the only complications are experimental, since longer cavities are more subject to turbulences.

6.2.2 The cavity's comb

When considering the physical parameters that arise when describing the phase accumulated in a round-trip, it can be shown that the cavity defines a frequency comb. Achieving perfect resonance is then equivalent to overlapping perfectly the comb defined by the cavity with the comb of the laser source.

We write the phase due to propagation in a dispersive medium (6.8) as

$$\phi_c(\omega) = \frac{\omega L}{c}\Big(1 + \delta n(\omega)\Big) \equiv \omega\frac{L}{c} + \varphi(\omega) \tag{6.18}$$

The first term of this phase corresponds to the vacuum case, whereas the second term is the perturbation induced by the dispersive medium. This description is convenient since in the vacuum case, the resonance condition is well-defined.

The round-trip phase is then written as

$$\varphi_c(\omega) = \phi_{Gouy} + \omega\frac{L}{c} + \varphi(\omega) \tag{6.19}$$

We considered the Gouy phase that is a result from the propagation of the transverse modes[4]. It is a constant that depends only on the geometry of the cavity. The term ϕ_{vac}

[4]Note that when considering the Gouy phase, the cavity length (6.17) does not ensure resonance. The incident comb thus needs to have a non-zero CEO.

corresponds to the propagation in vacuum, while the term φ contains the information about the medium.

We propose to solve the resonance condition for this accumulated phase, when the cavity is injected by a frequency comb with a non-zero CEO.

To do so, we Taylor-expand $\varphi(\omega)$ around ω_0 as it was done previously, for example in (2.32). The accumulated phase then writes as

$$\begin{aligned}\varphi_c(\omega) &= \phi_{Gouy} + \varphi_0 - \omega_0\varphi_0' + \frac{\omega}{c}\left(L + c\varphi_0'\right) + \frac{1}{2}(\omega-\omega_0)^2\varphi_0'' + \dots \\ &\equiv \alpha + \frac{\omega}{c}L_{eff} + \frac{1}{2}(\omega-\omega_0)^2\varphi_0'' + \dots \end{aligned} \tag{6.20}$$

where $\varphi_0 = \varphi(\omega_0)$, φ_0' and φ_0'' correspond respectively to the first and second derivatives of φ with respect to ω taken at ω_0. We can see a constant phase term described by

$$\alpha = \phi_{Gouy} + \varphi_0 - \omega_0\varphi_0' \tag{6.21}$$

and a effective optical path defined by

$$\boxed{L_{eff} = L + c\varphi_0'} \tag{6.22}$$

This apparent cavity length is due to the first order dispersion.

If we neglect higher orders of this development, we may solve analytically the resonance condition. We see that we can define the cavity's frequency combs, which frequencies ω_n^c satisfy $\varphi_c(\omega_n^c) = 2n\pi$. They read

$$\begin{aligned}\omega_n^c &= n\frac{2\pi c}{L_{eff}} - \alpha\frac{c}{L_{eff}} \\ &\equiv n\omega_r^c + \omega_{CE}^c \end{aligned} \tag{6.23}$$

This frequency comb has its own repetition rate and carrier-to-envelope offset that are dependent on the properties of the cavities and of the dispersive medium.

To ensure perfect resonance of the incident light, we need to overlap the frequency comb defined by the cavity to the frequency comb of the laser. It means that we must simultaneously set $\omega_{CE}^c = \omega_{CE}$ and $\omega_r^c = \omega_r$. Experimentally, one may match the repetition rates by either locking the length L of the cavity to the repetition rate of the laser, or the other way around. For the carrier-to-envelope phase, since it is a constant parameter, one may change the amount of dispersion in the cavity to match the CEO of the laser. However, for high finesse cavity, this parameter usually fluctuates, such that it is better to be able to lock the CEO of the laser on a stable reference, and tune this value such that it matches the cavity's.

When taking into account higher order dispersion, the frequencies that are resonant in the cavity do not form a comb anymore, since the spacing between the teeth of the comb is not constant. There are no other strategies than minimize the dispersion accumulated on a round-trip. This parameter is very important to control when conceiving a high finesse cavity.

6.2.3 Simulations

Even though solving the resonance condition is no longer analytical for realistic conditions (*i.e.* propagation in a dispersive medium), it may be simulated easily. Such simulations are essential when building synchronous high finesse cavity, since it allows to predict how the spectrum will be transmitted. The only unknown parameters in such simulations is the actual finesse, which always turns out to be smaller in the experiments, due to various sources of losses that are not easily modeled.

A parameter that is easy to change experimentally is the cavity length, using for example a translation stage. Small variations of the cavity length is commonly achieved by introducing a piezo-mounted mirror inside the cavity. This also allows to control the cavity length's in a retrocontrol loop in order to lock it to the laser. We remind that the contrary procedure (*i.e.* changing the laser's cavity length) results in the same situation, such that the problem may be modeled in a similar way.

When simulating cavities injected by broad spectra, a useful representation is to plot the transfer function (6.4) as a function of the wavelength and of the detuning of the cavity[5]. This results in a two-dimensional map which is easy to relate to experimental quantities. This is inspired by [Schliesser 06].

We consider a high-finesse cavity injected by the frequency comb described in 3.1.1, which has a spectral width of 40 nm FWHM. We then compute the transfer function (6.4) considering that the cavity is in lab air. We define the incident frequency comb according to experimental parameters, and we set the cavity's parameters (6.23) to satisfy the resonance conditions without dispersion.

We then consider small variations δL around L and plot the transfer function in transmission for each wavelength. The result, which we call *resonance map*, is shown on figure 6.4. The simulation is done for a cavity of finesse ~ 200 in air at standard atmospheric pressure. Since a cavity is sensitive to the phase accumulated over one round-trip, a resonance map is an indirect representation of this phase. We can see on this figure that the resonance is curved with respect to wavelength, which is representative of residual dispersion.

Taking projections of the map at a given cavity length gives the transmitted spectrum. It is equivalent to setting the cavity length experimentally by locking. On the right side

[5] This detuning may be defined as an offset in its length around resonance.

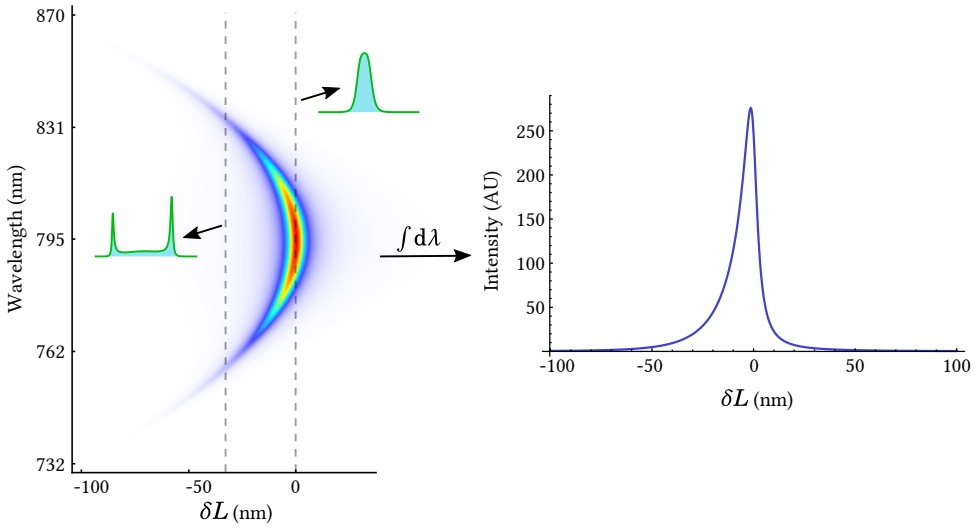

Figure 6.4: Resonance map for a cavity of finesse ~ 200 in air. On the right is the integral of the resonance map over wavelength. The insets are projections at a given cavity length.

of figure 6.4, we integrated the resonance map over wavelength. This result is also accessible experimentally by sweeping the cavity length at a resonnably high speed (which can be done by ramping the piezo inside the cavity and measuring the transmitted power with a photodiode). The transmission peak, which is a Lorentzian without dispersion, is clearly assymetric, which is another witness of intra cavity dispersion.

We can see from the map that there is no cavity length (*i.e.* no lock point) that allows to transmit the whole spectrum because of second order dispersion. Without quadratic phase, the resonance map would be straight, without curvature, meaning that it is possible to transmit the entire spectrum, as predicted by (6.23).

In this model, we only considered the accumulated phase results from propagation through air. Experimentally, we need to take into account all the elements inside the cavity, especially the dielectric coating on all the mirrors, which always adds dispersion. Therefore, a possible strategy to ensure resonance of every tooth of the comb is to use specially designed mirrors with the lowest possible dispersion, and put the cavity in vacuum. Another possibility is to use chirped mirrors which phase is tailored to compensate the propagation through air. However, this usually results in an oscillating GDD which, for high finesse cavities, introduces higher order dispersion to the accumulated phase.

6.3 Experimental realization

6.3.1 Motivations

In this last section, we present experimental results on the construction and the characterization of a cavity of finesse ~ 1200 injected by a ~ 45 nm FWHM spectrum. More details may be found in [Schmeissner 14a]. It was constructed to take advantage of the noise filtering properties described in 6.1.4.

We remind that, from section 4.1.2, the sensitivity in a projective measurement scheme is governed by the noise in the detection mode. In our experiment described in chapter 5, we split the field out of the laser source to generate the beam where information is encoded and the beam used to measure it. In a more general scheme, the two fields do not come from the same source and thus do not share common noise properties. As a result, for space-time positioning, the phase noise of the source needs to be minimized since the detection mode is on the phase quadrature. This may be achieved by introducing a filtering cavity in the signal's arm of the interferometer

6.3.2 Design and construction

As we developed in section 6.2.1, in order to transmit the entire spectrum, the cavity length needs to match the free spectral range of the laser source. We chose to set a cavity length of 1.92 m, matching the laser's cavity (free spectral range of 156 MHz).

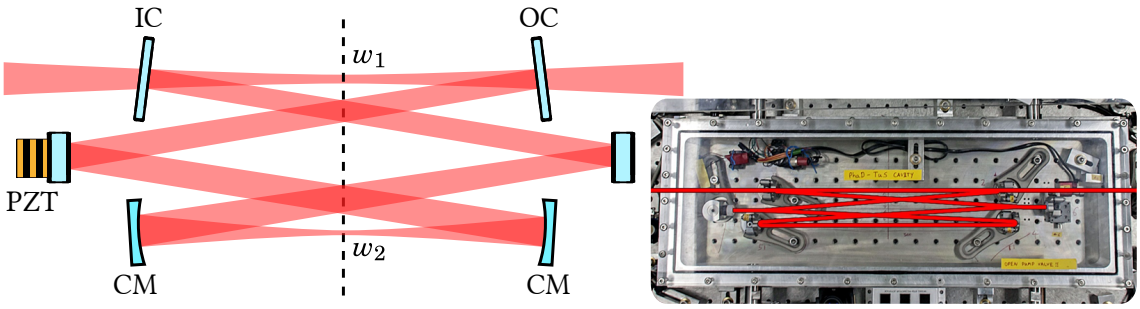

Figure 6.5: Drawing of the bow-tie ring cavity. IC : input coupler, OC : output coupler; PZT : piezo-mounted mirror; CM : curved mirror. The waists in the cavity are written w_1 and w_2. Not shown : one mirror is on a remote controlled translation stage with picometer precision to match the free spectral range of the cavity to the laser.

The geometry that was chosen is a ring cavity in a bow-tie configuration. The reason for a ring cavity instead of a linear is that it is possible to inject two counter-propagating beams. Therefore, one beam may be used to lock the cavity's length, while the other one

is used for measurements. Working with short pulses, this solution is convenient since the locking beam can propagate through very dispersive materials such as EOMs while keeping the studied pulse transform-limited. The cavity is sketched on figure 6.5.

The cavity is put in a vacuum chamber built of Invar to minimize the influence of the environnement. The mirrors are coated by Layertec, and are optimized for zero dispersion on a large spectral bandwidth. The reflectivity of the couplers is 99.8%, which using (6.11) results in a theoretical finesse of ~ 1600.

To match the free spectral range of the cavity, one of the mirrors is mounted on a motor translation stage with a picometer precision. Another mirror is mounted on a piezo actuator to lock the cavity length.

We estimated the finesse using an optical ring-down technique to a value of ≃ 1250, which is smaller than the theoretical value. There are consequently losses in the cavity, which is to be expected when building a high finesse cavity. Nevertheless, the measured finesse is very acceptable for applications to ultrafast optics. The bandwidth of the cavity is then approximately $\nu_c \approx 125$ kHz.

6.3.3 Cavity lock

A weaker second beam is injected from the output coupler, used as a reference. It is phase modulated outside of the cavity bandwidth using an EOM. Its reflection is diffracted on a grating, and a selected spectral slice is detected using an APD. The phase modulation is demodulated to generate the error signal used to lock the cavity in a Pound-Drever-Hall (PDF) scheme[Black 01].

This allows to set the cavity length, which is one of two parameters that need to be set to ensure full transmission of the incident spectrum. As we described in 6.2.2, the other parameter that needs to be fixed is the carrier-envelope-offset. We do so by changing the CEO of the laser by modulation of the pump laser[Helbing 02].

This stabilization of the CEO is done with a commercial system from Menlo. A photonic crystal fiber is injected by a portion of the laser's output to generate a supercontinuum. It is octave spanning, and may therefore be self-referenced. Doing so, we realize a $f - 2f$ scheme that retrieves the fluctuations of the carrier-envelope offset frequency[Jones 00]. As usual, this signal is demodulated by a stable reference (Agilent N5181A) and used in a retrocontrol loop on the pump AOM to lock the CEO. The proper offset is found by maximizing the transmission of the cavity.

6.3.4 Environnemental pressure dependency

As we described it in 6.2.2, the environnemental conditions are of the utmost importance when realizing a high finesse cavity in the femtosecond regime. Naturally, the best op-

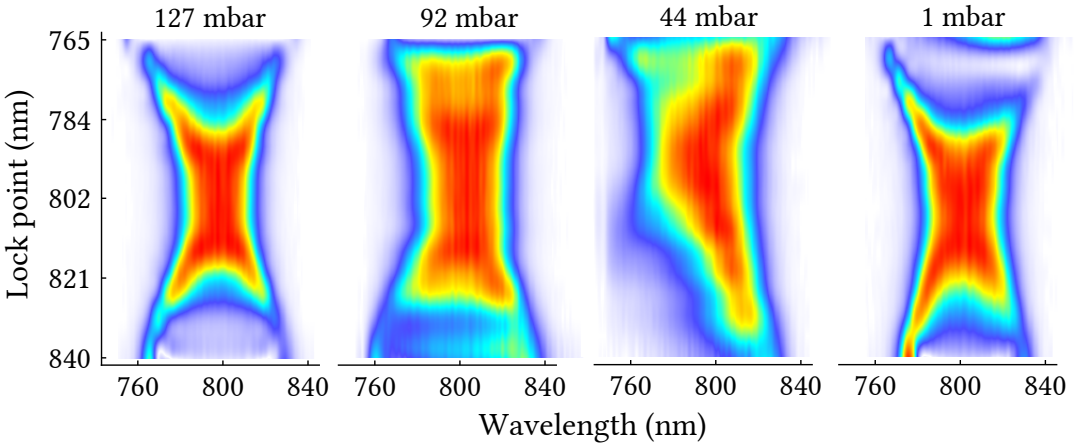

Figure 6.6: Experimental resonance maps for different intra-cavity air pressure. The striped structure is a result of the interpolation technique used to plot, and is not a real physical effect.

eration should be obtained when the cavity is under vacuum, since there wouldn't be any source of dispersion.

In practice however, we noticed that the best operation (*i.e.* maximum transmitted power and spectral width) is obtained for a weak vacuum of ~ 50 mbar. To investigate this behavior, we propose to measure the resonance map of figure 6.4 for different air pressure inside the cavity.

To achieve such a map, we need to change the length where the cavity is locked, which we refer to as the lock point. The way to do so is to change the spectral slice that is used to generate the error signal. However, we stress that this method does not allow to lock the cavity on an arbitrary point. Indeed, from figure 6.4, we can see that a certain cavity length is resonant for two ranges of frequency. Using our locking method, it means that using the error signal of these two spectral slices result in the same lock point. This situation occurs if the accumulated phase is quadratic. The simulation can be easily adapted to that constraint, as shown by figure 6.7a. The resonance map is then symmetric in the situation where two distinct spectral slices are transmitted at a given cavity length.

Setting different intra-cavity pressure, we acquire the transmitted spectrum using a spectrometer for different lock points. We then plot the resonance maps, as shown on figure 6.6.

For the highest and lowest pressure, the experiment maps are consistent with the observation that we made about symmetric resonance maps. We can then conclude that there is a fair amount of quadratic phase accumulated at 130 mbar. However, we can also see that there is a residual negative quadratic phase at lower pressure.

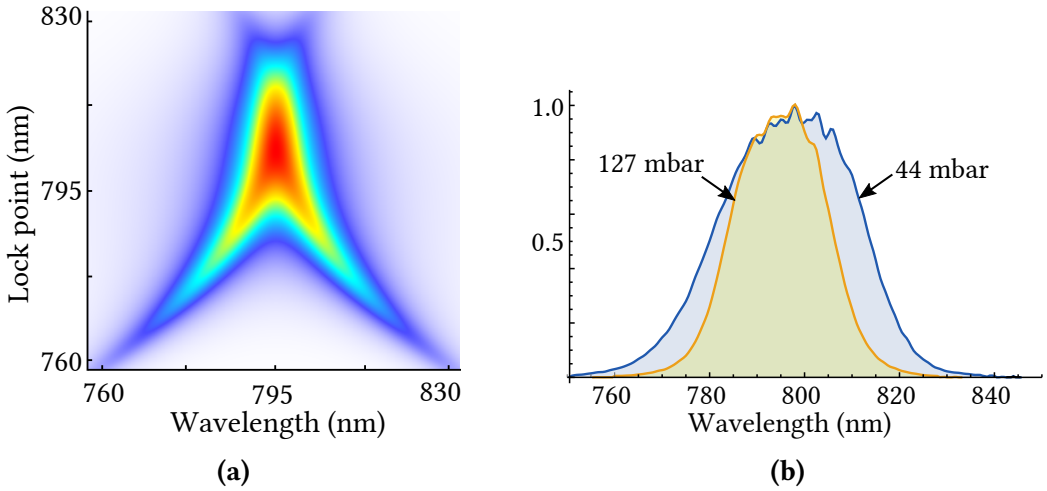

Figure 6.7: (a) Theoretical resonance map for a cavity of finesse ~ 200 in 100 mbar of air. Instead of the cavity length, we plotted it as a function of the lock point, obtained by mapping the transmitted spectrum to the cavity length. (b) Projection of the experimental resonance maps of figure 6.6 for a lock point of 795 nm.

This residual quadratic phase must come from the optical elements inside the cavity. There are 6 mirrors in the cavity, and small residual quadratic phase on each reflection can result in a considerable amount over a round-trip, which is even more noticeable for a high finesse cavity. Therefore, the remaining negative dispersion from the mirrors is compensated by the positive dispersion of the air inside the cavity.

On figure 6.7b, we selected a lock point of 795 nm and plotted the spectrum transmitted by the cavity. At a pressure of ~ 50 mbar, the cavity transmits the entire spectrum, whereas it is reduced for higher or lower air pressure because of dispersion. The transmitted power is also higher. We also injected the cavity with a broader source generated by a photonic crystal fiber, and found the maximum bandwidth of the cavity to be around 100 nm.

With this method, we fully characterized the cavity. It allows to retrieve indirectly the phase accumulated on a round-trip without introducing any element inside the cavity.

6.3.5 Noise properties

Finally, we take interest in the noise of the field transmitted by the cavity. The results presented in this part are investigated in greater details in [Schmeissner 14c] and [Schmeissner 14a].

We first compare the amplitude noise of the transmitted and incident fields by acquiring the power spectrum distribution with a single detector. The result is shown on

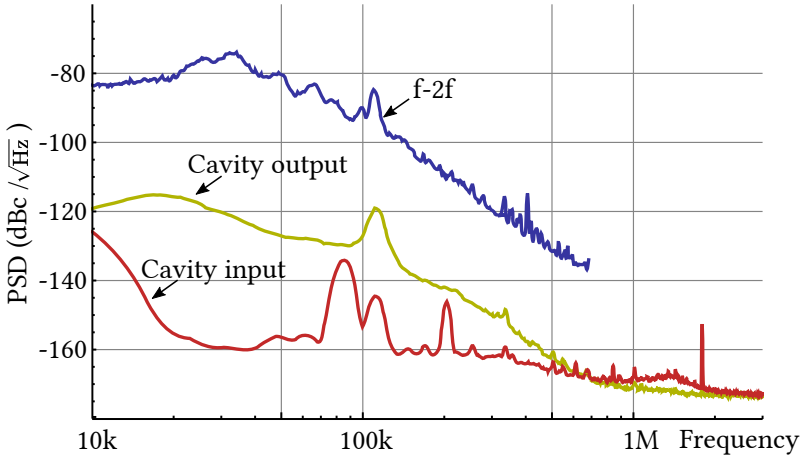

Figure 6.8: Power spectrum distribution of the amplitude noise for the same amount of power of the laser and the cavity transmission. The higher signal comes from the free-running variations of the CEO frequency, normalized for an equivalent power. The CEO noise's trace is cut before 1 MHz because the detected beating hits the noise floor of the detection scheme.

figure 6.8.

We see that at high frequencies, there is indeed a filtering of the amplitude noise of the laser. Notably, the structure at 1.5 MHz which originates from the relaxation oscillations of the laser is totally suppressed. However, at lower frequencies, the amplitude noise of the field transmitted by the cavity is considerably higher. We see an excess noise of ~ 40 dB.

This result can be expected from equation (6.14). For a high phase noise and low amplitude noise at the input, the amplitude quadrature of the output of the cavity will show higher noise than the original amplitude noise.

In [Schmeissner 14a], using what is called the rubber-band model[Newbury 07], it is shown that the main driver of phase noise of this laser source comes from fluctuations of CEO rather than repetition rate. In order to lock the cavity, the CEO of the laser has to be locked with a PID whose bandwidth is on the order of 100 kHz. Any fluctuations in CEO higher than this frequency can thus be considered to be free-running.

Using a phase-lock loop (PLL) scheme, we analyze the power spectrum distribution of the carrier-to-envelope offset noise detected at the output of the $f-2f$ interfermometer, and we plot it also on figure 6.8. Above 100 kHz, we can see that the slope of the CEO noise is similar to the amplitude noise transmitted by the cavity. Comparing the noise level is not straightforward since the beating signal in the $f-2f$ is detected using an APD, and renormalizing the power is prone to measurements error. However, comparing

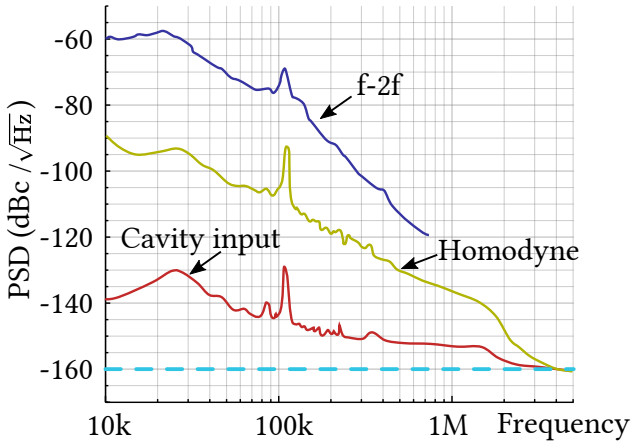

Figure 6.9: Power spectrum distribution of the amplitude noise of the laser source, the homodyne signal of the output of the cavity versus its input and the CEO phase noise measured from the signal at the output of the $f-2f$ interferometer.

the slopes is enough to infer that the transmitted field by the cavity is indeed dominated by the conversion of high phase noise of the laser source.

To conclude, we perform a homodyne detection between the transmitted field (as the signal field) and the laser's output (as the local oscillator). On the phase quadrature, we should measure the relative phase noise $\langle \delta\phi^2_{rel} \rangle$ between the two fields. We analyze the beam at the output of the cavity which contains the filtered phase noise of the laser. Indeed, if the phase noise of the local oscillator is written $\langle \delta\phi^2_0 \rangle$, then the phase noise of the signal field is $\langle [H(f)\cdot\phi_0]^2 \rangle$, where $H(f)$ is the filter function of the phase quadrature. The relative phase noise that is measured is thus:

$$\langle \delta\phi^2_{rel} \rangle = [1-H(f)]^2 \langle \delta\phi^2_0 \rangle \tag{6.24}$$

We then do not actually measure the noise of the source, but rather the remaining phase noise after filtering. At low sideband frequencies, the cavity does not filter anything ($H \to 1$) and the two arms of the interferometer are correlated and no meaningful information about phase noise may be retrieved. However, above the cutoff frequency, the retrieved phase noise contains information on the original phase noise attenuated by the filter function. The result is shown on figure 6.9.

We observe that the homodyne signal follows a specific attenuation above the cutoff frequency, whose slope is different than the one retrieved from the PLL of the carrier-to-envelope offset frequency noise. The difference in slopes is found to agree with the filtering of the CEO phase noise[Schmeissner 14c].

7 Experimental study of correlations in spectral noise

"It's all about the noise..."

– Roman "*Herr Schmeissner*" Schmeissner

Contents

7.1 The modal structure of noise 170
7.1.1 Introduction and motivations 170
7.1.2 The noise modes 170
7.2 Measuring spectral correlations in the noise 171
7.2.1 Classical covariance matrix 171
7.2.2 Retrieving the fluctuations 173
7.2.3 Experimental scheme 175
7.2.3.1 Measurement strategy 175
7.2.3.2 Normalization 176
7.3 Experimental results 177
7.3.1 Amplitude and phase spectral noise 177
7.3.2 The noise modes 179
7.3.3 Collective parameters projection 180
7.3.4 Phase-amplitude correlations 181
7.3.5 Real-time laser dynamics analysis 183

We use in this chapter a multimode description of an optical frequency comb to describe its noise. We show that both its amplitude and phase fluctuations may be decomposed on a basis of modes, each attached to a different parameter. We pursue the strategy that was adopted in [Schmeissner 14b] to characterize the spectral distribution of noise of a frequency comb, bringing novel insight on the matter.

In particular, we adapt our spectrally-resolved measurement scheme to simultaneous measurement of the spectral structure of amplitude and phase noise. This allows to glean the correlations between the amplitude and the phase noise of an optical frequency comb which is, to our knowledge, an undocumented subject.

The scheme that we investigate in this section allows to retrieve the fluctuations of the

collective parameters that define an optical frequency comb. Accessing their variations in real-time grants the possibility to precisely characterize and potentially stabilize the laser source.

7.1 The modal structure of noise

7.1.1 Introduction and motivations

When assessing the noise of a laser source, it is usually separated in fluctuations in amplitude (*i.e.* variation in photon number) and in phase (*i.e.* variation in frequency).

In the case of a frequency comb, such a description needs to be applied to each individual comb line, resulting in fluctuations in the global comb structure. Typically, the noise dynamics are described with a number of collective properties[Haus 93] such as pulse energy, carrier-envelope offset or the temporal jitter of the pulse train.

In a manner similar to that presented in 4.2, it has been theorized in [Haus 90] that a variation of one of these collective parameters affects the comb structure in a way that consists of adding a particular noise mode to the mean-field mode. The noise dynamics of an optical frequency comb may thus be theoretically represented by a unique set of noise modes, exactly like a perturbation in the propagation distance of a pulse may be decomposed on a set of modes.

The existence of such modes would imply that correlations must exist between individual comb lines. Strictly speaking, this would mean that the sum of the noise of individual spectral slices is not equal to the noise of the sum of the spectral slices. Whereas the distribution of noise across a frequency comb is an already well-documented subject[Bartels 04, Swann 06], the role of correlations among individual comb lines is a research subject to be explored in more details[Martin 09].

7.1.2 The noise modes

To fully describe the dynamics of a frequency comb, we use four collective parameters. The theory of Haus and Lai[Haus 90] describes the noise that arises due to the generation and propagation of a soliton pulse in a laser cavity. The variables considered for a pulse are its photon number, phase, position (in time) and momentum (*i.e.* frequency). These four variables may be linked to four collective parameters of the pulse train as mean power, central wavelength, timing jitter and phase (CEO).

On figure 7.1, we show a schematic representation of the variations in amplitude and in phase of individual comb lines. In insets, we reproduced the corresponding noise mode from [Haus 90] describing the fluctuations of power, wavelength, CEO phase and timing jitter.

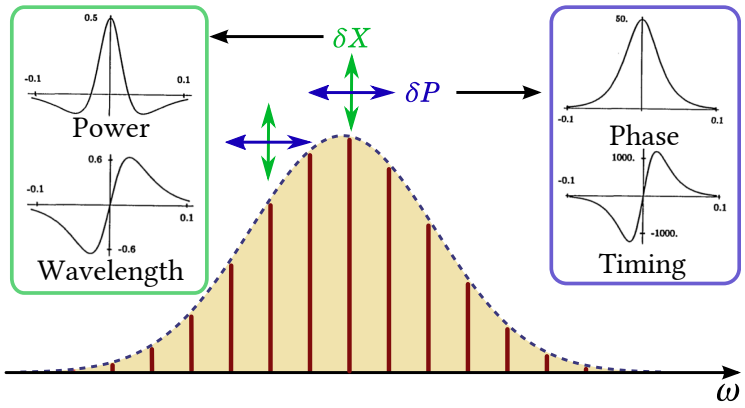

Figure 7.1: Schematic representation of the four collective parameters that describe the noise dynamics of a frequency comb.

As it should, these modes show a close resemblance to the ones outlines in section 4.2. The differences arise from the fact the Haus theory describes a soliton pulse that propagates inside the laser cavity while we look at the field at the output.

The description of this theory is beyond the scope of this thesis, the important point being the existence and shape of such noise modes.

7.2 Measuring spectral correlations in the noise

To reveal the modal structure in the noise dynamics of a frequency comb, one has to simultaneously measure and compare the fluctuation (in amplitude and in phase) of every comb line. Since resolving a single frequency is not experimentally feasible with our sources, we consider spectral bands. The collective properties of the comb lines that populate these bands should remain. To do so, we propose to make use of the multipixel detection presented in 3.3.2.

7.2.1 Classical covariance matrix

As usual, we represent the field as:

$$E^{(+)}(\Omega) = \mathscr{E}_0\, a(\Omega)\, e^{i\varphi(\Omega)} \tag{7.1}$$

The fluctuations of the field $\delta E = E - \langle E \rangle$ are thus given to the first order by

$$\begin{aligned}\delta E(\Omega) &= \mathscr{E}_0 \Big(\delta a(\Omega) + i\delta\varphi(\Omega)\cdot a(\Omega)\Big) e^{i\varphi(\Omega)} + \text{c.c.} \\ &= 2\delta X \cos\big[\varphi(\Omega)\big] + 2\delta P \sin\big[\varphi(\Omega)\big]\end{aligned} \tag{7.2}$$

Consider that we measure simultaneously the fluctuations of the field in amplitude and in phase in a given spectral band. We write the retrieved amplitude and phase noise for the n^{th} spectral band respectively as δX_n and δP_n. These fluctuations are retrieved at a given sideband frequency.

We investigate a sideband RF frequency range of ~ 100 kHz to ~ 3 MHz. We do not wish to resolve fluctuations at lower frequencies that originate from technical noise, such as vibrations, turbulence, acoustics and thermal effects. The investigated range is mostly dominated by laser dynamics such as spontaneous emission and noise from the pump transferred to the oscillator.

Over that range, the observed noise fluctuations closely follow Gaussian statistics. As a consequence, a proper representation of these spectrally dependent fluctuations is a covariance matrix. The elements of the covariance matrices in amplitude and in phase are written as

$$[\mathbf{\Gamma}_X]_{ij} = \langle \delta X_i \cdot \delta X_j \rangle \tag{7.3}$$

$$[\mathbf{\Gamma}_P]_{ij} = \langle \delta P_i \cdot \delta P_j \rangle \tag{7.4}$$

The diagonal elements of this matrix represent the spectrally-resolved variance. The notation $\langle \cdot \rangle$ denotes the averaging of the demodulated fluctuations at a given sideband frequency over the acquisition time.

Since the phase $\langle (\delta P)^2 \rangle$ and amplitude $\langle (\delta X)^2 \rangle$ fluctuations are acquired simultaneously, it is possible to compute the correlations $\langle \delta X \cdot \delta P \rangle$ for every frequency bands. We write the obtained matrix $\mathbf{C}$ as

$$[\mathbf{C}]_{ij} = \langle \delta X_i \cdot \delta P_j \rangle \tag{7.5}$$

Note that this matrix is not symmetric, and may thus not be diagonalized. However, the full matrix $\mathbf{M}$ defined by:

$$\mathbf{\Gamma} = \begin{bmatrix} \mathbf{\Gamma}_X & \mathbf{C} \\ \mathbf{C}^{\mathrm{T}} & \mathbf{\Gamma}_P \end{bmatrix} \tag{7.6}$$

which represents the collective fluctuations in amplitude and in phase. This matrix is symmetric and may therefore be diagonalized.

Indeed, since covariance matrices are positive-semidefinite and symmetric, they may consequently by decomposed on an eigenbasis:

$$\boxed{\mathbf{\Gamma} = \mathbf{V}\,\mathbf{\Lambda}\,\mathbf{V}^{-1}} \tag{7.7}$$

where the i^{th} column $\mathbf{v}_i$ of $\mathbf{V}$ is the i^{th} eigenvector of $\mathbf{\Gamma}$ associated to the eigenvalue Λ_{ii}. The eigenvector then correspond to a noise mode whose eigenvalue depict its contribution to the global noise description. Note that this matrix needs to be normalized, which

we will do in section 7.2.3.2 relative to the shot noise level. Also, the amount of modes that are accessible using the multipixel detector is limited by the number of pixels.

With such a decomposition in hand, it is possible to project the modes attached to the fluctuation of a parameter that we constructed in chapter 5 on the eigenmodes of the noise matrices to estimate their contributions. This is in essence what was done in section 5.4.6 to know the noise in the time-of-flight mode in the amplitude squeezed beam. Albeit the noise was quantum in nature, the strategy adopted here to extract classical noise structure is globally inspired by the quantum method.

Note that the decomposition of the full covariance matrix (7.6) results in a basis of modes that couple both amplitude and phase noise. Since these are not easy to interpret, we chose to diagonalize independently $\mathbf{\Gamma}_X$ and $\mathbf{\Gamma}_X$ which gives the modal distribution of amplitude and phase noise whose analysis is more accessible.

7.2.2 Retrieving the fluctuations

Up until now, we used a homodyne detection to retrieve the information on the phase quadrature of the field by taking the difference of the photocurrents, or the amplitude noise by taking the sum. Such measurement were done independently. Here, we show that this same scheme may be used to retrieve simultaneously the information on both field quadrature by acquiring the signal at both output of the interferometer. We name this scheme as *superdyne detection*.

In the interferometer, we want to retrieve the noise in the local oscillator beam (*i.e.* the strong field) while the signal field is used as a reference to access the phase quadrature. As we will demonstrate in this section, this optical setup allows to retrieve the fluctuations both in amplitude and in phase of the local oscillator field. To measure the noise in individual spectral bands, we use the same spectrally-resolved homodyne detection as before (see 3.3.2). The details on the experimental procedure are given in section 7.2.3.1.

In [Schmeissner 14b], measuring the previously-described covariance matrices was achieved using the same homodyne detection based optical setup. Two balanced photodiodes were used at the output of the interferometer, such that the detection of individual spectral bands was achieved with a pulse shaper in the local oscillator arm. . The measurement was accomplished using a spectrum analyzer. Both amplitude and phase noise were measured, but not simultaneously, such that the correlations between the two was not measured. The scheme that we present here consists in an upgrade of that previous setup since a single measurement retrieves the noise in both quadrature simultaneously and is much quicker to achieve.

To retrieve both quadratures at the same time, for one given spectral band, we measure simultaneously the signals coming from both detectors. So instead of measuring a single signal coming from the analogical difference of both photocurrents, we retrieves the two

photocurrents. This is done for all of the 8 spectral bands, resulting in the simultaneous acquisition of 16 signals. The sum and the difference are then done in post-processing.

More specifically, going back to equation (3.4), taking the sum of the photocurrents (for a given spectral slice) yields

$$\mathscr{I}_{+,n} = \mathscr{I}_{s,n} + \mathscr{I}_{LO,n} \tag{7.8}$$

where the contribution from individual field is integrated over the spectral band of the detector. This obviously yields the total power contained in both beams of the interferometer, such that the fluctuations of this photocurrent are found to be directly proportional to the noise on the amplitude quadrature of the fields. In the case where the local oscillator is stronger than the signal field, the noise if dominated by its amplitude fluctuations. Hence, it follows that

$$\boxed{\left\langle \left(\delta\mathscr{I}_{+,n}\right)^2 \right\rangle = N_{LO} \left\langle \left(\delta X_{LO,n}\right)^2 \right\rangle} \tag{7.9}$$

Taking the difference of the photocurrent results in the now familiar homodyne signal:

$$\mathscr{I}_{-,n} = 2\sqrt{N_{LO}}\,\mathrm{Re}\left\{\alpha_s^*\,\Gamma_{c,n}\,e^{i\phi_0}\right\} \tag{7.10}$$

Note that in contrast with parameter estimation, the modal structure of the fluctuations of the signal field is not known, since this is what we aim to determine. When the interferometer is locked on the phase quadrature, we see that the fluctuations in phase noise are carried by the term $i\alpha(\Omega)\cdot\delta\varphi(\Omega)$ (cf. equation (7.2)). The measured phase is the relative phase between the two arms of the interferometer: $\delta\varphi(\Omega) = \delta\varphi_{LO}(\Omega) - \delta\varphi_s(\Omega)$. If we consider that there is no phase noise in the signal field, which may be achieved by filtering, then the measured phase is $\delta\varphi(\Omega) = \delta\varphi_{LO}(\Omega)$, which is the absolute phase noise of the local oscillator.

When the relative phase between the two arms is $\pi/2$, the noise in the detected signal is given by

$$\boxed{\left\langle \left(\delta\mathscr{I}_{-,n}\right)^2 \right\rangle = N_{LO} \left\langle \left(\delta P_{s,n}\right)^2 \right\rangle} \tag{7.11}$$

Note that this is contingent upon the local oscillator being in the same mean-field mode than the signal field. More importantly, we can see that this scheme measures the phase quadrature of the signal field rather than the local oscillator field. Hence it needs to be renormalized. From (7.2), we can see that the phase quadrature is proportional to the envelope of the signal field, as such, $\delta P_s \propto \sqrt{N}$. Therefore, when the two fields are in the same mean-field mode, their phase fluctuations are linked by

$$\delta P_{LO,n} = \sqrt{\frac{N_{LO}}{N}}\,\delta P_{s,n} \tag{7.12}$$

This allows to renormalize our measurement (7.11) such that the fluctuations of the same field are retrieved.

7.2.3 Experimental scheme

7.2.3.1 Measurement strategy

As we hinted earlier, to measure the fluctuations, we use our superdyne detection to acquire simultaneously the sum and the difference of the photocurrents. The experimental scheme is depicted on figure 7.2.

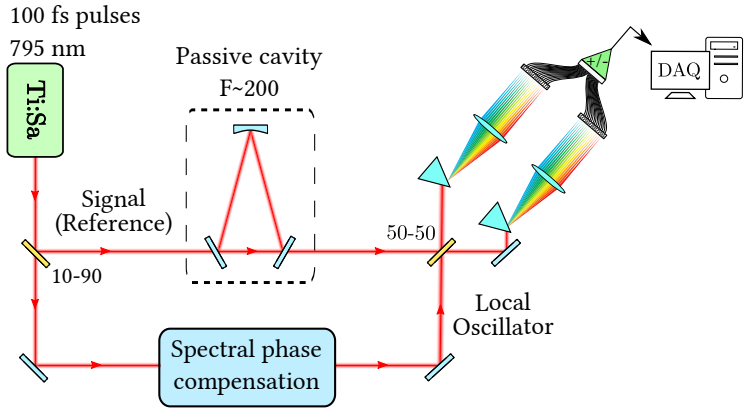

Figure 7.2: Experimental scheme of the superdyne detection that measures simultaneously the fluctuations in amplitude and in phase of the laser field. The field that is being characterized is the local oscillator, while the signal field serves as a reference.

The laser source that we characterize is different of the one used in the experiments from part III. It is a solid-state Titanium-Sapphire laser MIRA from COHERENT pumped by a VERDI V18. It delivers pulses of ~ 100 fs at a center wavelength of 795 nm with a repetition rate of 76 MHz. The spectral width is 10 nm FWHM, and the mean mode-locked power that is delivered is around 2 W.

On the local oscillator arm, a spatial light modulator from BNS is introduced to compensate the spectral phase between the two fields by pulse shaping.

In order to decouple the fluctuations of the two arms, we introduce a Fabry-Pérot cavity of finesse ~ 200 to filter the signal's field. The cutoff frequency ν_c is consequently around 200 kHz. We remind that, when using a cavity in a homodyne detection, the relative phase that is measured is given by equation (6.24), which is dependent on the transfer function in phase $H(f)$ of the cavity.

The analysis frequency f_l at which the phase noise in both beams is non longer correlated may be obtained by solving the frequency at which the phase noise of the trans-

mitted field is reduced by a factor of 2 from the incident:

$$[1 - H(f_l)]^2 = \frac{1}{2} \tag{7.13}$$

By approximating the transfer function to the case of high finesse cavities, this yields $f_l \simeq 1.55 \cdot \nu_c$. Therefore, at a frequency of ~ 300 kHz, the two beams can be considered as decoupled in phase, such that the measurement on the phase quadrature retrieves the fluctuations of the local oscillator.

On the amplitude quadrature, we remind that this quadrature shows excess noise from the quadrature conversion (6.14) induced by the cavity. Consequently, the noise level has to be characterized and attenuated properly to ensure that taking the sum of the photocurrents yields only the noise of the local oscillator. To ensure no contamination due to the different noise levels, we introduced different level of optical attenuation in the signal beam when measuring. The optimal attenuation is obtained when the retrieved noise spectrum for the sum of the photocurrent is equivalent (in the distribution, not in amplitude) to the one retrieved with the signal beam blocked[1].

7.2.3.2 Normalization

As it was outlined in section 3.3.1, the variances of the quadrature operators in amplitude and in phase are equivalently equal to 1 for vacuum. Hence, it is a logical choice to normalize the fluctuations to the shot-noise level. Moreover, since the clearance of the detection scheme is not exceptionnally high (8 dB at maximum power, about 2 dB only for the side pixels that receive less power), the dark noise in the measurement needs to be carefully removed.

The normalization process consists in computing a gain function that allows to retrieve the signal. As before, we write the measured signal m_i for a single pixel, with an optical signal s_i and noise[2] d_i. The measurement then yields $m_i = \alpha_i s_i + d_i$, where α_i is gain resulting from the conversion of the optical signal into an electrical signal. In term of covariance, without correlation between the signal and the noise, we have:

$$\mathrm{Cov}_{ij}[m] = \alpha_i \alpha_j \cdot \mathrm{Cov}_{ij}[s] + \mathrm{Cov}_{ij}[d] \tag{7.14}$$

where $\mathrm{Cov}_{ij}[x]$ is the element (i, j) of the covariance matrix of x. When the fluctuations of the signal arise from quantum vacuum, then $\mathrm{Cov}[s] = \mathbb{1}$ is the identity matrix. For any

[1] We also add that the introduction of a high-pass filter at the input of the demodulation stage was necessary because the very high phase noise at lower frequencies saturated the electronics.

[2] The noise that is referred to here is the dark noise of the detection. The term signal obviously describes the noise that arises from measuring the fluctuations of the light field, which are not correlated to the noise of the detection.

measurement to yield the value of 1 when measuring vacuum, the gain α is thus found to be

$$\alpha_i = \sqrt{\mathrm{Cov}_{ii}[m_{vac}] - \mathrm{Cov}_{ii}[d]} \tag{7.15}$$

where m_{vac} is the measure covariance matrix of vacuum.

The covariance matrices normalized to the shot-noise level are therefore given by

$$\boxed{\mathrm{Cov}_{ij}[s] = \frac{\mathrm{Cov}_{ij}[m] - \mathrm{Cov}_{ij}[d]}{\alpha_i \cdot \alpha_j}} \tag{7.16}$$

which is the noise relative to shot noise (RSN).

The amplitude covariance matrix directly retrieves the amplitude fluctuations of the local oscillator field. However, the phase covariance matrix needs to be renormalized according to (7.12) such that the phase noise that is measured is for the number of photons contained in the local oscillator field and no the signal field.

Note that, from a quantum point of view, this situation is equivalent to mixing an unit of vacuum in the signal port of the beamsplitter. As a consequence, the sensitivity is reduced according to Heisenberg principle. This is a consequence of the simultaneous measurement of both optical quadratures. For classical noise, this is however not an issue.

Once this renormalization of the phase fluctuations is done, the correlation matrix $\mathbf{C}$ is also normalized to shot noise using to (7.16) because of the isotropy of vacuum.

7.3 Experimental results

7.3.1 Amplitude and phase spectral noise

On figure 7.3, we represent the covariance matrices in amplitude (top panel) and in phase (bottom panel) for a range of three sideband frequencies. The noise is estimated relative to the shot noise level in a linear scale. We also included as inset a two-dimensional heatmap representation of each matrices.

We can see that at high frequency, neither the amplitude nor the phase matrix exhibit correlations between wavelengths. For the amplitude matrix, the diagonal elements are equal to 1, confirming that the laser source is shot noise limited in amplitude on this corresponding time-scale. The absence of correlation terms is also consistent with the fact that the fluctuations of vacuum are entirely uncorrelated. The same observation can be done for the phase covariance matrix, although the diagonal elements are equal to 10. This is a consequence of the power renormalization (7.12) that decreases the sensitivity

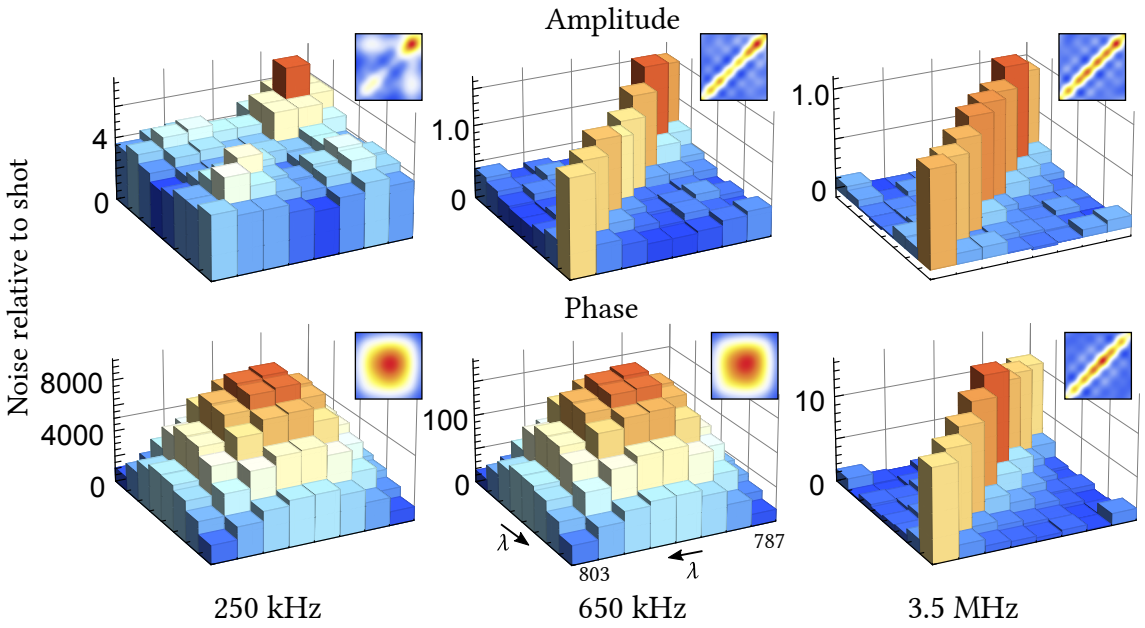

Figure 7.3: Covariance matrix representation of the fluctuations in amplitude (top row) and in phase (bottom row) at three different sideband frequencies.

of the measurement. When not normalizing, the diagonal elements are equal to 1, and the source is therefore also shot-noise limited in phase noise at this sideband frequency.

Conversely, on longer time scale, it appears that the amplitude fluctuations of every considered spectral band are correlated, as it is depicted by the flat structure of the top left matrix. For the phase quadrature, not only is the noise considerably higher, the correlations are largely confined to the spectral center. Both quadrature show a very different noise level and spectral distribution.

Note also that the amplitude noise appears to reach the shot noise level quicker than the phase noise, which is in accord with figure 6.9. Although the laser source that was investigated in chapter 6 is different than the present one, both are still Titanium-Sapphire based laser and thus exhibit similar disparities in the noise level.

However, the two sources do not share the same mode-locking mechanism, hence there is no reason to assume that their spectral noise distribution should be similar. Unfortunately, the phase noise of the source that delivers 20 fs pulses was not yet acquired at the time of the writing of this thesis. However, measuring the amplitude noise is quite straightforward and has been steadily achieved. Its amplitude noise matrices are plotted on figure 7.4

We see indeed a different spectral distribution than the ones depicted by figure 7.3. Most noticeably, the noise seems concentrated toward the infrared wavelengths, even

more than the other laser source. At 1.5 MHz, the amplitude noise is dominated by the relaxation oscillations. Whereas the amplitude noise retrieved with a single detector does not appear to be that different for both laser sources, their spectral correlations can show different structure.

By this method, the noise figure of two laser source may be compared in details since information about correlations between different parts of the spectrum are not easily retrieved using standard methods. More importantly, the difference in the mode-locking process may be the reason for the differences that are witnessed here, and more information will be gained by acquiring the spectral phase fluctuations in the near future.

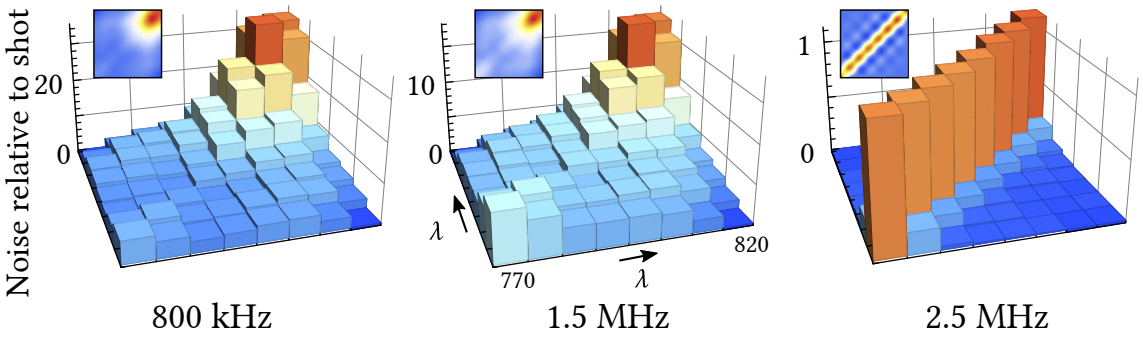

Figure 7.4: Covariance matrix representation of the fluctuations in amplitude only of the laser source described in 3.1.1.

7.3.2 The noise modes

We now want to extract the modal structure of this noise, which becomes accessible upon eigendecomposition of the noise matrices. The eigenvalues reflect the noise power, and are dependent on analysis frequency. They are shown on figure 7.5. At high frequency, the noise in both quadratures is equal to the shot noise[3] as it should. At longer timescale, the eigenvalues rise well above shot noise level in a non-degenerate manner. In both cases, the main noise mode is clearly identified as the one with the highest eigenvalue. The eigenmode attached to the highest eigenvalues (at a particular analysis frequency) are also shown on the plot 7.5. We can see that the main amplitude noise mode closely resembles the mean-field mode while the next eigenstructure is similar to the time-of-flight mode. The phase quadrature shows the same eigenmodes.

The eigenstructures are very similar to the theoretical prediction of [Haus 90] shown on figure 7.1. The amplitude noise is clearly dominated by amplitude fluctuations while

[3]The offset with respect to shot in the noise value for the main eigenvalue of the phase quadrature comes from excess noise from the cavity. It may be suppressed by attenuating the signal's beam.

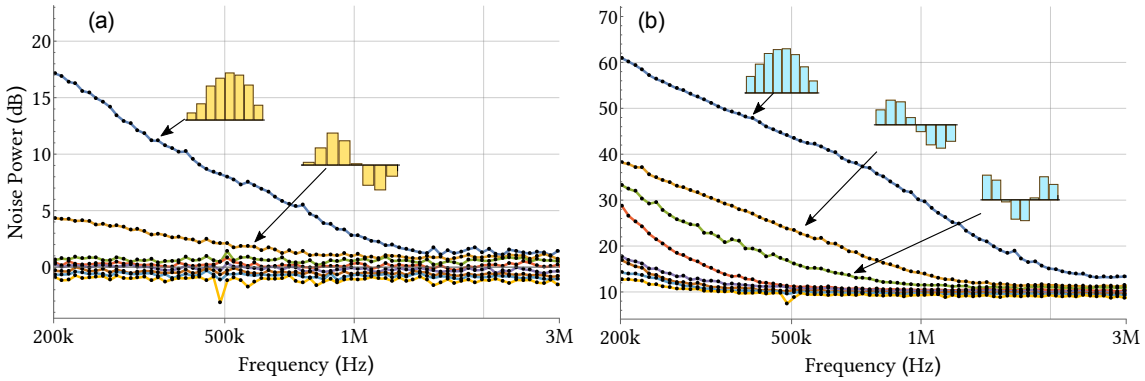

Figure 7.5: Eigenvalue distribution of the covariance matrices in amplitude (a) and in phase (b). The corresponding eigenmodes at 500 kHz are also plotted.

the fluctuations of wavelength are much lower. In the phase quadrature, the CEO phase noise largely dominates whereas the timing jitter is less important but still noticeable. Interestingly, we show the clear existence of a third mode not predicted by Haus theory, which, in analogy to 4.2.4.3, may be attached the fluctuations of dispersion inside the laser cavity.

Note that this method of eigendecomposition does not ensure that the variation of each eigenvalue in figure (7.5) is always attached to the same mode. Nevertheless, no crossing in the noise power is observed, and the modal structure is not affected by the analysis frequency[4] .

Since the noise is represented relatively to the quantum limit, this method also allows to compare the noise power in both quadrature. We can infer from the decomposition that the fluctuations in CEO and in time of arrival of the pulses are more intense than the fluctuations in power and in center frequency.

We note also that the general structure of the amplitude covariance matrix and eigenmodes are different from the one presented in [Schmeissner 14b] despite the laser source being identical. In addition to the difference in sensitivity, this disparity may be explained by the fact that this previous experiment was accomplished with pump diodes at the end of their life cycle, resulting in very different noise characteristics.

7.3.3 Collective parameters projection

It is also possible to derive which parameter fluctuates given knowledge of the previous noise distribution. Indeed, the modes attached to the fluctuations of a parameters may be

[4]Except of course when shot noise is reached and every eigenvalue is degenerated. Consequently, the modal structure is meaningless.

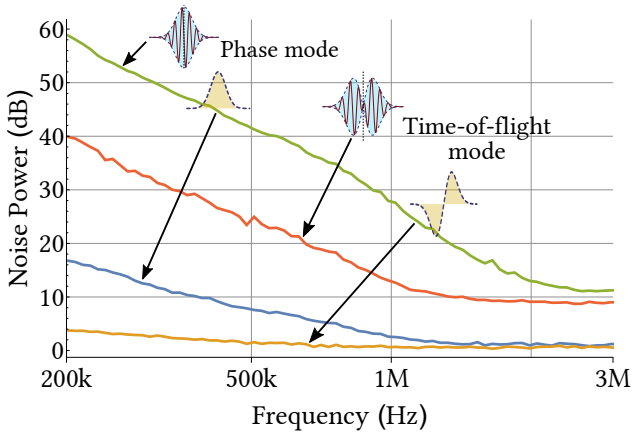

Figure 7.6: Experimental evolution of the fluctuations of the four collective parameters of an optical frequency comb with respect to sideband frequency. The phase mode corresponds on the amplitude and phase quadratures respectively to variations in mean power and in CEO phase. The time-of-flight mode corresponds to timing jitter and center wavelength fluctuations.

computed, as it was done in 4.2. Computing the inner product (*i.e* the overlap) between the parameter mode and the eigenmodes of the noise matrices then allows to retrieve the noise associated to the fluctuation of the said parameter. This is in essence a basis change of the covariance matrix. The retrieved eigenvalue is then directly the noise power attached to the fluctuations of a physical parameter.

On figure 7.6, we projected the previous eigendecomposition into the basis defined by the phase mode and time-of-flight modes v_0 and v_1 as previously defined. This projection is done for every analysis frequency, hence the distribution in noise is always attached to the proper mode. It is clear from this figure that the noise variation is quite similar to the one depicted in figure 7.5, thus demonstrating a very good overlap between the eigenmodes and the projection modes attached to a specific parameter.

This allows to directly compare the noise in amplitude and in phase. The global noise structure is strongly dominated by the fluctuations of CEO and timing jitter that lie on the phase quadrature.

7.3.4 Phase-amplitude correlations

The concurrent acquisition of amplitude and phase fluctuations allows to compute the correlations between the two. Note that the quadrature noises have very different intensities. Retrieving the correlations between signals very contrasted does not yield a precise result. To increase the dynamic range, it is preferable to compute the cor-

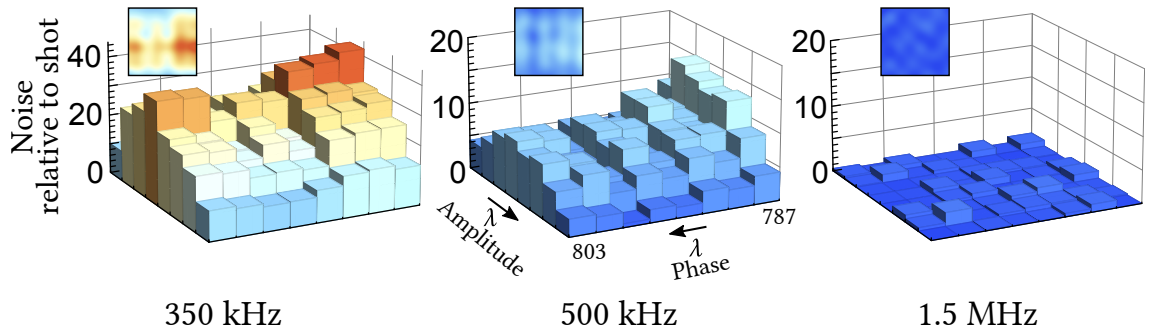

Figure 7.7: Matrix of correlations between amplitude and phase noise. The correlations vanish at high sideband frequencies since the fluctuations of quantum vacuum are uncorrelated.

relations between two signals with similar variations. In our setup, the strongest noise comes from the phase noise, which is retrieved by the amplitude of the signal field. Consequently, this beam was significantely attenuated. The power ratio between the local oscillator and the signal fields was set to ~ 300 for the acquisition of correlations. On figure 7.7, we plot the matrices of correlations for three different analysis frequencies. As expected, beyond sideband frequencies of ~ 1 MHz, no correlations are observed since the quadrature of vacuum are not tied. At lower frequencies however, a distinct structure is observed along the amplitude quadrature. We can see a variation in amplitude seemingly similar to a Gaussian for every frequency band of the phase quadrature. Note that the global sign of this correlation matrix has no meaning since the variations in phase are dependent upon the lock point of the interferometer. As it was discussed in 5.4.1, the side of the fringe on which we lock determines the sign of the recovered signal, hence the sign of the retrieved correlations may be switched by changing the lock fringe. The polarity of each pixel within the correlation matrix is however relevant, and every spectral bands are correlated the same way.

The Gaussian structure along the phase quadrature may be explained by the mode-locking mechanism of the laser. As it was outlined in 2.4.2.2, the Kerr-lensing effect is in essence a phase response dependent on the amplitude, as described by equation (2.52). This may explain that the phase and amplitude quadrature are correlated within the same spectral band, with a progression that follows the mean-field spectrum.

An animation of the amplitude and phase noise matrices as well as the correlation matrix as a function of sideband frequency may be found online at [Thiel 15].

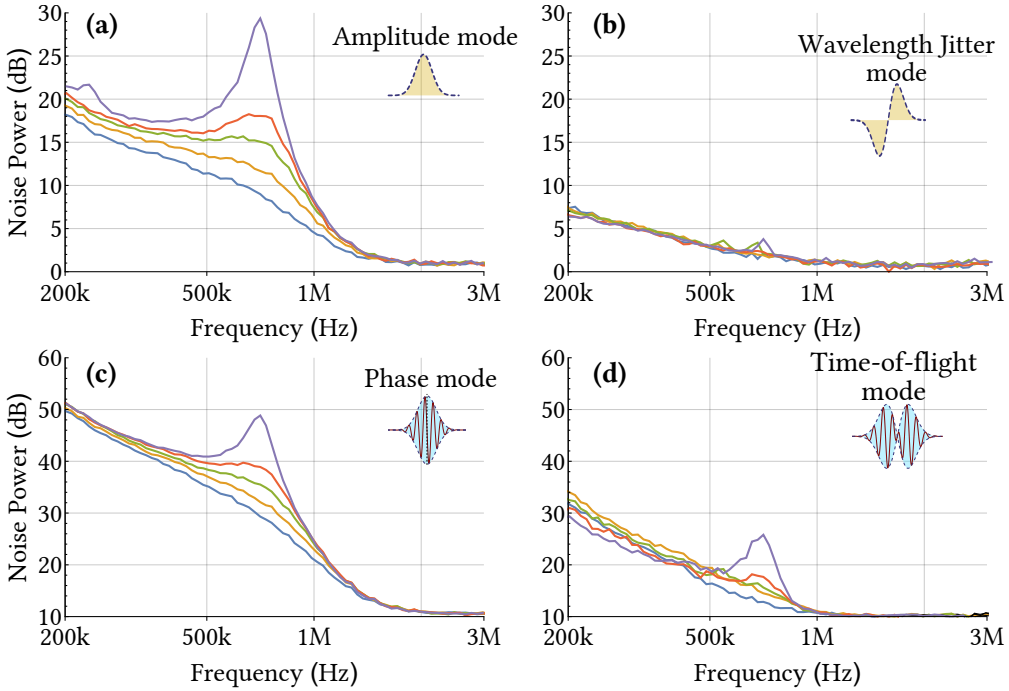

Figure 7.8: Fluctuations of power (a) center wavelength (b) CEO phase (c) and timing jitter (d) for different configurations of the mode-locking mechanism.

7.3.5 Real-time laser dynamics analysis

To conclude, we wish to propose this measurement scheme to resolve the real-time variation of the laser noise. To do so, instead of leaving the laser source free-running, we introduce a perturbation inside the laser cavity and characterize it. Since the measurements in the phase quadrature require to lock an optical cavity, this perturbation needs to be small enough as not to disrupt the cavity's retrocontrol loop.

We decided to adjust the mode-locking mechanism by slowly opening or closing the slit at the output of the laser's cavity. Being a hard-aperture KLM (see section 2.52), doing so either pushes laser operation towards continuous wave generation[5] (slit opened) or towards self Q-switching. In both cases, mode-locking is lost. We propose to dynamically explore the noise characteristics of the laser along this range.

For different opening of the slit, we record the covariance matrices in amplitude and in phase as a function of the analysis frequency. We proceed to eigendecomposition and we project the results in the phase and time-of-flight modes. This ensures that we are tracking the fluctuations in the same mode. The results are shown on figure 7.8.

[5]We note that this configuration results in the least amplitude noise.

We see again that the noise structure is dominated by the fluctuations of phase in every configuration. The parameters that are the most affected by the mode-locking mechanism appear to be the CEO phase and the mean power, both carried by the mean-field mode. In comparison, the fluctuations in timing jitter and center wavelength remains unchanged by the perturbation.

The noise added by the opening of the slit is clearly concentrated in the relaxation oscillations of the system. In amplitude and in phase, the relaxation oscillation peaks is amplified by 20 dB when the slit is opened (*i.e.* close to self Q-switching) whereas it vanishes when the slit is closed (*i.e.* optimal configuration of the system).

This behaviour is observed easily when measuring the power spectrum distribution in amplitude noise using a single detector. However, it is interesting to notice that the phase quadrature is affected by the same amount, and that the fluctuations are concentrated in the global phase of the comb rather than in timing offset.

Because of the way the aperture of the slit affects the laser cavity, the results that we show here is to be expected. Introducing losses in the cavity should not affect the center wavelength nor the repetition rate. This proves however the validity of this method to diagnose the ultrafast source in term of its main parameters.

Rather than measuring the noise matrices over a range of sideband frequencies for different opening of the slit, we also did a dynamical measurement at fixed sideband frequencies. We computed in real-time the covariance matrices while dynamically opening the slit. Note that this was not done for the phase quadrature, since the change in power would most certainly unlock the cavity. The result of the dynamic acquisition on the amplitude quadrature is shown on figure 7.9 for analysis frequencies close to the relaxation oscillation of the system.

We see that the more sensitive parameter to this particular perturbation is the amplitude, while the center wavelength is not affected. This measurement was achieved independently for the four sideband frequencies, such that the timescales may not be compared.

Having access to these fluctuations in real-time opens the possibility to diminish them using a retrocontrol loop. For example, while monitoring the fluctuations in CEO phase noise, it is conceivable to act on an element inside the laser cavity to reduce the noise. Since the obtained decomposition is made in term of uncoupled noise, it should be possible with proper engineering to counter the variation of one parameter independently of the others.

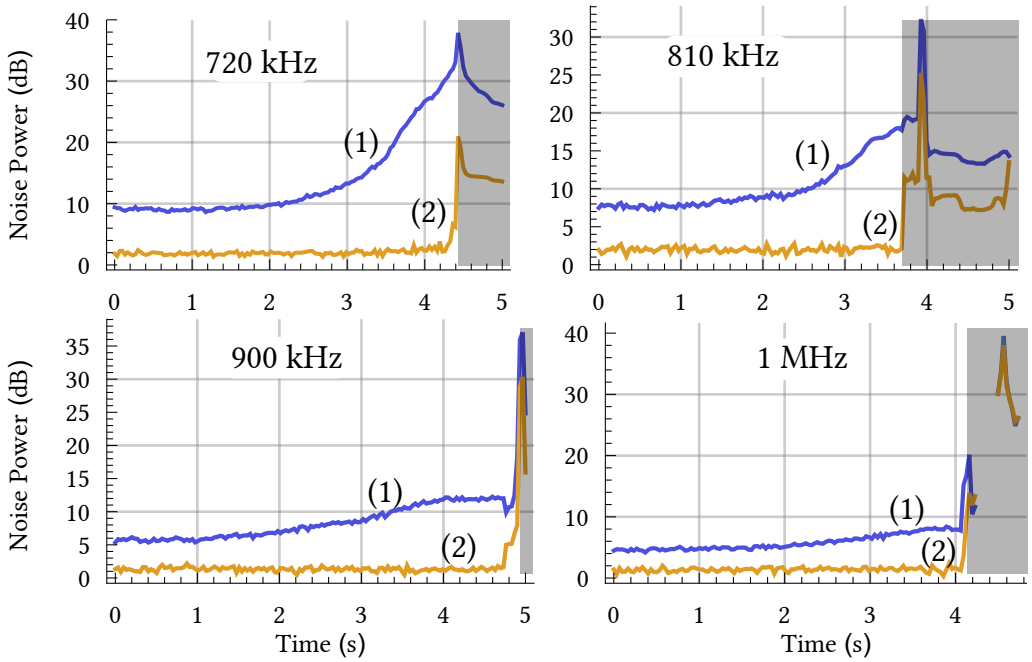

Figure 7.9: Real-time acquisition when the slit at the output of the laser cavity is opened dynamically. This is a dynamic progression between the situations plotted on figure 7.8 at four analysis frequencies close to the relaxation oscillations. The noise are for (1) amplitude and (2) center wavelength jitter. The grayed boxes represent the time at which mode-locking is lost, and the contained data is then not relevant.

Part IV

Going further with quantum frequency combs

8 Multimode squeezed states

(Having spent a day trying in vain to communicate with a NEWFOCUS controller, to the point of building his own communication cable)
"By now, I am firmly convinced that this instrument has become self-aware, and will just refuse to work."

– Jonathan "*Griffin*" Roslund

Contents

8.1 Generating quantum states 190
8.1.1 Creation of squeezed states 190
8.1.2 Parametric down conversion with an optical frequency comb . 191
8.1.3 Objectives and perspectives 192
8.2 Single-pass squeezing 193
8.2.1 Parametric down conversion 193
8.2.2 Eigenmodes of the parametric down conversion 194
8.2.3 Expected efficiency 198
8.3 Second harmonic generation 198
8.3.1 Efficiency 199
8.3.2 The influence of temporal chirp 202
8.4 An ultra-fast squeezer 203
8.4.1 Pump generation 203
8.4.2 Synchronously pumped optical parametric amplifier 204
8.5 Perspectives 205
8.5.1 Quantum enhanced metrology 205
8.5.2 Entanglement 207

In this final part, we overview the future developments of the parameter estimation experiment. It involves the generation of quantum light to perform measurements below the standard quantum limit and the synthesis of a beam entangled in "time".

Toward that aim, we describe the non-linear effects in the femtosecond regime (second harmonic generation and parametric down conversion) that are necessary to generate the quantum resources that are required.

8.1 Generating quantum states

8.1.1 Creation of squeezed states

To generate quantum states with sub-Poisson statistics, several techniques which are all based on non-linear optics can be used. It involves the creation of pairs of photons within a medium which then share complementary information (such as polarization, frequency, etc.).

In our laboratory, generation of quantum states has been achieved within an optical parametric oscillator (OPO) injected by a frequency comb. It consists of a gain medium which presents a $\chi^{(2)}$ non-linearity put in a cavity. Within the crystal, a nonlinear effect converts a pump photon of frequency ω_p and wavevector $\mathbf{k}_p$ into two photons, called signal and idler, whose frequencies and momenta satisfy:

$$\omega_p = \omega_s + \omega_i \tag{8.1}$$

$$\mathbf{k}_p = \mathbf{k}_s + \mathbf{k}_i \tag{8.2}$$

The cut of the crystal is set such that all frequencies propagate with the same velocities, resulting in the maximal gain. In the case were the signal and the idler photons are in the same spatiotemporal mode, the parametric down conversion process is said to be degenerate.

The Hamiltonian of a degenerate parametric down conversion process is written as

$$\boxed{\hat{H}_{PDC} = i g a_p \left(\hat{a}_s^\dagger\right)^2 + \text{h.c.}} \tag{8.3}$$

with $g = \frac{\chi^{(2)}\omega_s}{N_i c}$. To obtain that expression, we considered that the pump is a classical field, and we made the approximation that it is undepleted by the nonlinear process. We also considered the perfect phasematching case $\Delta\mathbf{k} = \mathbf{0}$.

The unitary evolution matrix associated to the Hamiltonian is then given by

$$\hat{U} = \exp\left[-\frac{i}{2}\hat{H}_{PDC}\right] \equiv \exp\left[\frac{1}{2} g a_p \left(\left(\hat{a}_s^\dagger\right)^2 - \hat{a}_s\right)\right] \tag{8.4}$$

which corresponds to the squeezing operator (1.96) with a squeezing parameter $g a_p$. This factor scales with the amplitude of the pump field (*i.e.* the square root of the pump intensity) and with the non-linear susceptibility of the crystal.

It may be shown that this process corresponds to a phase sensitive amplification of the incoming field in the same mode as the signal [Grynberg 10]. More precisely, for an input field $\hat{E}_{in}^{(+)}$ of frequency ω_s and of same polarization as the signal, after propagation

through the crystal, the field $\hat{E}_s^{(+)}$ is characterised by the following quadrature operators:

$$\hat{x}_s = e^{-\gamma \ell_c} \cdot \hat{x}_{in} \tag{8.5}$$

$$\hat{p}_s = e^{+\gamma \ell_c} \cdot \hat{p}_{in} \tag{8.6}$$

where ℓ_c is the length of the crystal and $\gamma = \frac{\chi^{(2)} a_p \omega_s}{N_i c}$ is the gain, with a_p the classical amplitude of the pump and N_i the photons number in the input field. The variances of the quadrature operators are then written as:

$$\left\langle (\delta \hat{x}_s)^2 \right\rangle = e^{-2\gamma \ell_c} \cdot \left\langle (\delta \hat{x}_{in})^2 \right\rangle \tag{8.7}$$

$$\left\langle (\delta \hat{p}_s)^2 \right\rangle = e^{+2\gamma \ell_c} \cdot \left\langle (\delta \hat{p}_{in})^2 \right\rangle \tag{8.8}$$

When the input state is a coherent state or a vacuum state, its variance on both quadrature is equal to unity, and therefore, the amplitude fluctuations of the signal state are found to be below 1. It is said to be *amplitude squeezed*. On the other hand, its phase quadrature has a variance superior to one, and is then said to be *anti-squeezed*.

8.1.2 Parametric down conversion with an optical frequency comb

To introduce the generation of multimode squeezed light, we give a succinct description of the parametric down conversion of an optical frequency comb. A more complete description may be found in [Patera 08] and in [Jiang 12].

For a pump field described by a frequency comb of repetition rate ω_r and carrier-envelope-offset frequency $2\omega_{CE}$, each tooth $\omega_{p,k} = k\,\omega_r + 2\omega_{CE}$ can give rise by parametric down conversion to two frequencies $\omega_{s,n} = n\,\omega_r + \omega_{CE}$ and $\omega_{s,k-n} = (k-n)\,\omega_r + \omega_{CE}$ with $\omega_{s,n} + \omega_{s,k-n} = \omega_{p,k}$. The amplitude of this conversion is dependent on the amplitude a_k of the pump frequency $\omega_{p,k}$. Consequently, a frequency of the signal comb $\omega_{s,n}$ is generated by all the pump frequencies $\omega_{p,k}$ and coupled to all the signal frequencies $\omega_{s,k-n}$ with a strength depending on the amplitude a_k for each k. This is therefore a highly multimode process that results in a highly multimode structure, as shown by figure 8.1.

The interaction Hamiltonian in this case is then written as

$$\hat{H}_{PDC} = ig \sum_{m,n} a_{m+n} \Phi_{m,n} \hat{a}^\dagger_{s,m} \hat{a}^\dagger_{s,n} + \text{h.c.} \tag{8.9}$$

where $\Phi_{m,n}$ denotes the phase mismatch between the interacting waves within the crystal. It can be shown[Eckstein 12] that this decomposition on a very large number of frequency modes may be simplified by diagonalizing the *spectral coupling matrix* or *joint spectral distribution* $\mathbf{L}_{m,n} = a_{m,n}\Phi_{m,n}$. When writing Λ_k the eigenvalues of $\mathbf{L}$ and $\hat{S}_k$

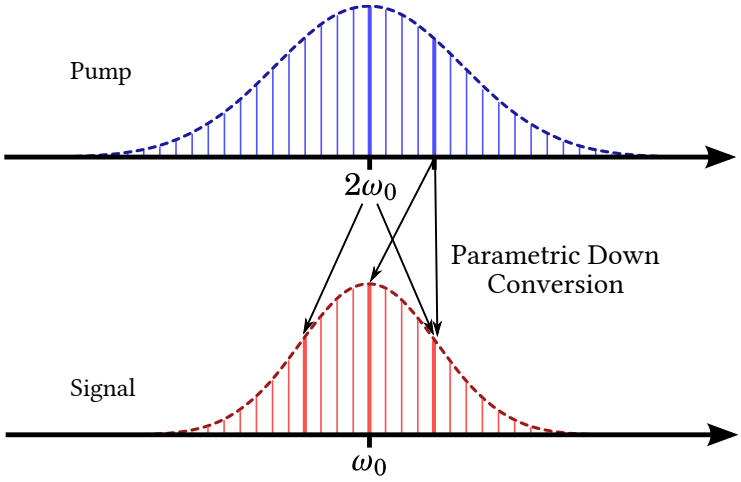

Figure 8.1: Representation of the parametric down conversion process with optical frequency comb. Each tooth of the pump comb can give rise to every tooth of the signal comb. [Figure by Renné Medeiros de Araujo]

the annihilation operators associated to the eigenmodes v_k of $\mathbf{L}$, the Hamiltonian is expressed in the basis of the operators $\{\hat{S}_k\}$ as:

$$\boxed{\hat{H}_{PDC} = ig\sum_k \Lambda_k \left(\hat{S}_k^\dagger\right)^2 + \text{h.c.}} \tag{8.10}$$

This Hamiltonian describes an assembly of independent squeezing operators acting on the modes $\hat{S}_k$ with a squeezing factor $g_k = g\,\Lambda_k$. The modes $\hat{S}_k$ are called the *supermodes* of the system.

In the case we are interested in, it may be shown that Λ_k is real, and when ordered from highest to lowest values, Λ_k is positive for even k and negative for odd k. This means that the even supermodes are squeezed in amplitude, while the odd supermodes are squeezed in phase.

8.1.3 Objectives and perspectives

We aim to generate a number of these quantum supermodes for various applications such as below quantum limit parameter estimation and entanglement. Such resource has already been successfully manufactured by the group [Roslund 13], showing at least a number of 32 supermodes, each individually squeezed, where the lowest order mode is squeezed by 8 dB. This quantum source was also used for the experiment in quantum metrology described in section 5.4.6. See [Cai 15] for the latest development and applications.

As it was referred to earlier, the quantum source consists of a synchronously pumped optical parametric oscillator (SPOPO) which is resonant for the signal field. If we were to generate entanglement between different supermodes, one would have to manufacture two of these multimode quantum beams. Moreover, since it is generated inside of a cavity, the "quantumness" of the state is only observable on an integration time that is limited by the bandwidth of the cavity. In the time domain, this is pictured by the quantum behaviour of a train of pulses that are correlated over the life time of the cavity.

Consequently, observing quantum effects between subsequent pulses is not possible using such squeezer. Having access to the quantum effects in a pulse-by-pulse regime would result in a discrete representation of a continuous variable state, thus leading to interesting perspectives. The parametric down conversion process in single-pass (*i.e.* not in cavity) appears to be well-suited to that particular task.

We propose to utilize such scheme to the generate a signal and idler field with less complexity that an OPO. Since no cavity is present, there is no bandwidth effect, hence every pulse would show quantum properties[Wenger 04]. On the down side, achieving squeezed light generation in a single-pass configuration requires a lot of pump power.

In the following, we give a description of the parametric down conversion process that is oriented toward the main parameters to set and control in order to maximize the amount of squeezing in a single-pass configuration.

8.2 Single-pass squeezing

8.2.1 Parametric down conversion

We begin by showing how to derive (8.9).

We consider the interaction between a pump and a signal field in a non-linear medium with a second order non-linear polarization. Using a classical treatment, it can be shown[1] that the envelope a_s of the signal field satisfies the following propagation equation:

$$\boxed{\frac{\partial a_s}{\partial z}(z,\omega) = \mathscr{E}_{0,p}\frac{\omega_0\chi^{(2)}}{2n_s c}\int_{\mathbb{R}} a_p(z,\omega+\omega')a_s^*(z,\omega')e^{i\Delta k(\omega,\omega')z}\frac{\mathrm{d}\omega'}{\sqrt{2\pi}}} \tag{8.11}$$

where n_s is the index of refraction seen by the signal wave and $\mathscr{E}_{0,p}$ is the field constant of the pump field. Note that even though we considered that the signal and the idler fields are identical, this process may not be regarded as being degenerate since photons are created at different frequencies that satisfy the energy conservation condition (see figure 8.1.

[1] As in the first chapter, we use the paraxial approximation and the slowly-varying envelope approximation.

The quantity $\Delta k(\omega,\omega')$ is the mismatch in wave vector due to the propagation of different polarization in an anisotropic medium. It reads

$$\Delta k(\omega,\omega') = k_p(\omega+\omega') - k_s(\omega') - k_s(\omega) \tag{8.12}$$

In the undepleted pump regime where a_p does not depend on the longitudinal variable, for a real envelope[2] a_s, it is straightforward to obtain the amplitude of the signal field at the output of the crystal. With a crystal length ℓ_c, the signal envelope at the output a_s^{out} is written as a function of the input a_s^{in} as:

$$a_s^{out}(\omega) = \exp[\mathscr{S}_0]\cdot a_s^{in}(\omega) \tag{8.13}$$

where $\mathscr{S}_0$ is given by the following integral:

$$\begin{aligned}\mathscr{S}_0 &= \mathscr{E}_{0,p}\frac{\omega_0\chi^{(2)}\ell_c}{2n_s c}\int_{\mathbb{R}} a_p(\omega+\omega')\,\mathrm{sinc}\left(\frac{\Delta k(\omega,\omega')\ell_c}{2}\right)\frac{\mathrm{d}\omega'}{\sqrt{2\pi}}\\ &\equiv C\int_{\mathbb{R}}\mathrm{L}(\omega,\omega')\frac{\mathrm{d}\omega'}{\sqrt{2\pi}}\end{aligned} \tag{8.14}$$

We wrote the constant factor C that encompasses the medium properties and the indices of refraction seen by the pump and the signal field, and we introduced the joint spectral distribution $\mathrm{L}(\omega,\omega') = a_p(\omega+\omega')\,\mathrm{sinc}\left(\frac{\Delta k(\omega,\omega')\ell_c}{2}\right)$. Using the discrete structure of a frequency comb allows to write the Hamiltonian (8.9).

The squeezing factor is consequently proportional to the eigenvalues Λ_j of L and to the constant C. Note that L is dependent on the amplitude of the pump field, such that the eigenvalues Λ_j are also dependent on the square root of the number of photons in the pump.

8.2.2 Eigenmodes of the parametric down conversion

The multimode structure of the signal field at the output of the crystal is dictated by the eigenmodes of the joint spectral distribution. Using a Gaussian approximation, this diagonalization has an analytical solution[Patera 08] where the eigenvalues have a geometric progression dependent on the properties of the gain medium and the eigenvectors are Hermite-Gauss modes. The spectral width of the first supermode is dependent also upon the properties of the medium and the spectral bandwidth of the pump, while the width of the following modes scales with the square root of the mode order.

We want this squeezing source to be realized from the second harmonic of the laser source described in 3.1.1, which delivers pulses of ~ 20 fs, much shorter in comparison

[2] In the more realistic case were a_s is complex, the calculation links a_s^{out} to its complex conjugate $(a_s^{in})^*$.

to the other laser source that was used to measured the noise matrices of chapter 7 and the below shot noise measurement of section 5.4.6. Whereas the peak power is more important with shorter pulses, the influence of dispersion is also much stronger. Hence, a compromise has to be made between pulse duration and crystal length.

When frequency doubling this source, the maximum achievable bandwidth is on the order of 14 nm. This sets the limit for the bandwidth of the pump to be used in the simulations. The other parameter to be chosen is the crystal type. The nonlinear crystal used in the SPOPO and for second harmonic generation is BIBO (BIB_3O_6), which has a strong nonlinearity but is also quite dispersive.

A very widespread nonlinear crystal in ultrafast optics is Barium Borate, BBO. It has a decent nonlinearity and a very wide phase matching bandwidth, making it ideal for short pulses. We settled to use this crystal for our simulations and experiments.

We set the orientation of the crystal such that phase matching is achieved at the center frequency $\Delta k(\omega_0, \omega_0) = 0$. The phase mismatch between different spectral components of the interacting fields is obtained by Taylor-expanding the pump and signal wavevectors:

$$\Delta k(\Omega, \Omega') = \cancelto{0}{\Delta k_0} + (k'_p - k'_s)(\Omega + \Omega') + \left[\frac{1}{2}k''_p(\Omega + \Omega')^2 - \frac{1}{2}k''_s(\Omega^2 + \Omega'^2)\right] \tag{8.15}$$

where $k'_{s,p}$ and $k''_{s,p}$ correspond to first and second order derivatives with respect to ω taken at the center frequency ω_0. On figure 8.2, we plot the joint spectral distribution matrix and its eigendecomposition for a parametric down conversion in 1 mm of BBO when the pump has a bandwidth of 8 nm FWHM.

The joint spectral distribution corresponds to the product of the Gaussian pump by the phase matching function which results in the curved structure because of the quadratic dispersion in the crystal. It follows that the supermodes have an oscillating behaviour in the spectral wings. From the analytical diagonalization, it can be shown that the width of the first supermode is proportional to the bandwidth of the pump, and inversely proportional to the parametric crystal length, the group velocity mismatch and the dispersion. Choosing the crystal length and the bandwidth of the pump thus allows to taylor the width of the supermodes.

These parameters also affect the eigenspectrum in both its amplitude and its distribution. The configuration that was chosen for this simulation yields a flat distribution of the first four eigenvalues, while the bandwidth of the first supermode is similar to the one of the laser.

This spectral width is important to control in order to access it. To measure the variance in a given mode, one has to perform a projective measurement where the local oscillator is in the same mode. To do so, the local oscillator field needs naturally to have a bandwidth at least equal to the mode that we want to measure. If not, the overlap between the signal and the reconstructed mode will be lower, which, when measuring

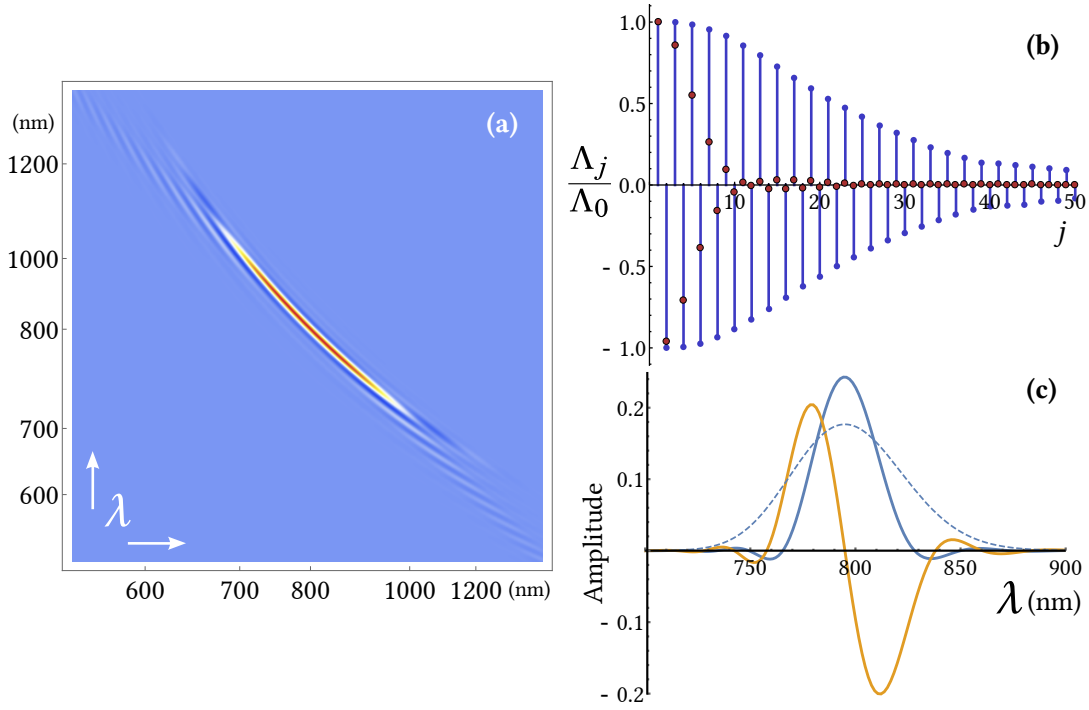

Figure 8.2: Parametric down conversion for 1 mm of BBO and a pump of 8 nm FWHM. (a) Joint spectral distribution. (b) Eigenspectrum of the decomposition and simulated measurement. (c) First two supermodes (plain) and amplitude of the laser's field (dashed).

quantum states, is equivalent to mixing vacuum. This is a source of loss that is very important to control.

Consequently, if one wants to measure every modes that are shown on the eigenspectrum of figure 8.2 using the field from the laser source, the retrieved distribution of squeezing would be very different. A way of predicting this dependency is to use a pragmatic approach based on projective measurements. Consider that we want the measure the noise in a given supermode in a homodyne detection were we are able to shape the local oscillator. In the case were the parameters of the interaction are such that the first supermode is well-approximated by a Gaussian (as it is the case in figure 8.2), it follows that the next supermodes are also approximated by a Hermite-Gaussian basis.

To measure the amount of squeezing in each of these supermodes, we project the multimode vacuum on the mode of the local oscillator that is set by the experimentalist. To construct the projection mode, we measure the first and second moments of this first supermode[3] and build a Hermite-Gauss basis with these parameters. Since the bandwidth of the local oscillator is limited by that of the original field, we multiply the reconstructed

[3]With the SPOPO, this may be done by operating it over threshold such that this mode is non-vacuum.

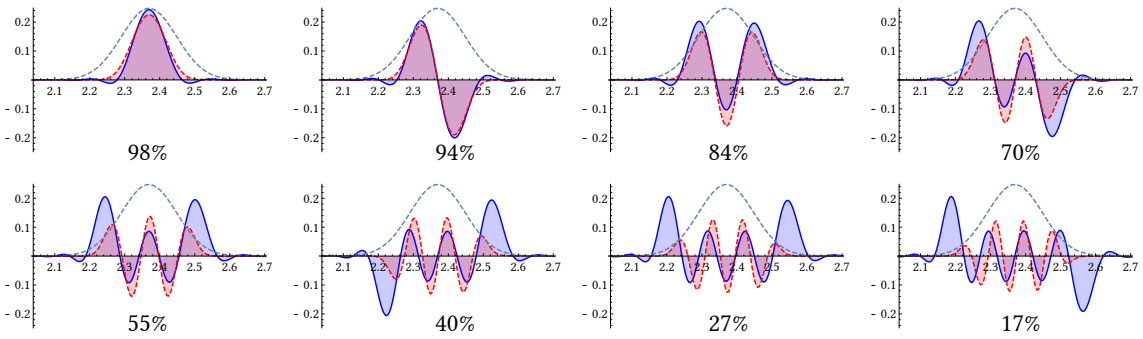

Figure 8.3: Overlap between the first 8 eigenmodes and a reconstructed Hermite-Gaussian basis that has the same moments than the first supermode. This reconstructed basis is also weigthed such that its width may not exceed the maximum possible bandwidth defined by the local oscillator (dashed).

basis by a sharp filter. This allows to simulate that the bandwidth of the local oscillator can be slightly increased with increasing its power and shaping its amplitude.

We then compute the overlap between each modes of this new basis and the eigenmodes computed in 8.2.2, and we use the result to weight the eigenvalues distribution. The result is shown on figure 8.3. This procedure adds a steep cutoff and reduces substantially the number of measurable modes, as shown on 8.2(b). A similar result may be obtained by diagonalizing a subset of the joint spectral distribution matrix. When applied to a simulation of the SPOPO experiment, this method gives a reasonable approximation of the experimental squeezing spectrum [4].

Experimentally, this bandwidth effect is currently limiting the amount of squeezing that is measured in the higher order modes with the SPOPO. Another concomitant effect may be that the pixelization of the search space can only approximate the high frequency variation of the supermodes, and is again equivalent to mixing in vacuum.

For the situation that we study, we do not wish to produce a high number of squeezed modes, in contrast with the SPOPO experiments. However, we are interested in producing squeezed modes that are as close as possible to Hermite-Gauss, as we will explain in section 8.5.1. Computing the overlap between the simulated eigenmodes of the system and the ideal basis is then more adapted to that purpose.

[4] Although the real experimental method to measure the noise in every mode is based on reconstructing the covariance matrix and diagonalizing it. This does not assume any shape of the supermodes, but is still limited by bandwidth and pixelization issues.

8.2.3 Expected efficiency

The previous simulation allows to predict the number of detectable modes and their relative squeezing / anti-squeezing levels. The global efficiency of the process is however not an easy quantity to predict with confidence. Experimental quantities that are hard to evaluate precisely, such as peak power and focussing effects, lead to very different expectations.

Since we already have access to a squeezer in our laboratory, meaningful results can be obtain by doing comparisons. In an OPO, the maximum squeezing is achieved for a pump power at which the cavity is emitting a bright beam of light, similar to a laser. This point is called *threshold* and is dependent in particular on the reflectivity of the OPO cavity. By considering the squeezing factor g_0 of the first supermode, which depends on pump power, one can show that the threshold is reached for:

$$g_{thresh} = \cosh^{-1}\left(\frac{1+r^2}{2r}\right) \tag{8.16}$$

where r is the global reflectivity of the cavity. We calculate the value of this parameter for the experimental settings corresponding to a global reflectivity $r^2 = 70\%$ (finesse of 20). The pump power at threshold is measured to be $P_{thresh} \approx 80$ mW.

In the case of the SOOPO, the squeezing parameter in the n^{th} mode is a function of the eigenvalue g_n. The threshold corresponds in the theory to a singular point where the squeezing parameter goes to infinity. However, when no cavity is considered (*i.e.* in single pass parametric down conversion), the squeezing parameter is directly proportional to this eigenvalue and does not show any singularity. With out experimental parameters, if one were to remove the OPO cavity and measure the squeezing level for the pump power at which threshold is achieved, the expected squeezing level is on the order of 1.5 dB.

This rough estimation allows to infer the maximum amount of squeezing in a single pass configuration for a given pump power. We also note that the squeezing amount scale with the square root of the pump power, and is by far the easiest parameter to adjust in order to increase the squeezing amount.

8.3 Second harmonic generation

In this section, we succinctly present how to create a strong pump for the parametric down conversion process. We derive the governing equations for second harmonic generation in the ultrafast regime and the parameters on which efficiency depends.

8.3.1 Efficiency

With a similar treatment than that done in section (8.2.1) for parametric down conversion, the propagation equation for the signal field[5] within the frequency doubling crystal writes as

$$\boxed{\frac{\partial A_s}{\partial z}(z,\omega) = i\frac{\omega_0\chi^{(2)}}{n_s c}\int_{\mathbb{R}} A_p(z,\omega')A_p(z,\omega-\omega')e^{i\Delta k(\omega,\omega')z}\frac{\mathrm{d}\omega'}{\sqrt{2\pi}}} \tag{8.17}$$

where we considered the center frequency of the signal field as $2\omega_0$, and we write the envelopes $A_i(z,\omega) = \mathscr{E}_{0,i}a_i(z,\omega)$ for a better readability.

In the undepleted pump regime, equation (8.17) may be integrated over the crystal length ℓ_c:

$$A_s^{out}(\omega) = i\frac{\omega_0\chi^{(2)}\ell_c}{n_s c}\int_{\mathbb{R}} A_p(\omega')A_p(\omega-\omega')\,\mathrm{sinc}\left(\frac{\Delta k(\omega,\omega')\ell_c}{2}\right)\frac{\mathrm{d}\omega'}{\sqrt{2\pi}} \tag{8.18}$$

where we consider that the signal field at the input of the crystal has a zero amplitude.

When neglecting the effect of second-order dispersion in the phase-matching function, the second-harmonic field is then written as:

$$A_s^{out}(\omega) = i\Gamma\ell_c F(\omega)\cdot\Phi(\omega) \tag{8.19}$$

where $\Gamma = \frac{\omega_0\chi^{(2)}}{nc}$, $F(\omega) = \int_{\mathbb{R}}\frac{\mathrm{d}\omega'}{\sqrt{2\pi}}A_p(\omega')A_p(\omega-\omega')$ is the self-convolution of the pump field and $\Phi(\omega)$ is the phase-matching function. It reads

$$\Phi(\omega) = \mathrm{sinc}\left(\frac{\Delta k'\ell_c}{2}\right) \tag{8.20}$$

where $\Delta k' = k'_p - k'_s$ is the group velocity mismatch.

In the Gaussian case, the second harmonic of the pump field is another Gaussian of bandwidth $\sqrt{2}\Delta\omega_p$ and center frequency $2\omega_0$ multiplied by the phase matching function which acts as a spectral filter. For a dispersive material, the phase-matching function becomes narrower, hence the second harmonic spectrum is shorter than the limit given by $\sqrt{2}\Delta\omega_p$.

We are interested in the energy W_s contained in the second harmonic field, obtained by integrating the intensity (see (1.41)):

$$W_s^{out} = 2nc\varepsilon_0\int_{\mathbb{R}}\mathrm{d}\omega\left|A_s^{out}(\omega)\right|^2 \tag{8.21}$$

[5]Note that we always consider the pump field as the input of the nonlinear process, being second harmonic generation or parametric down conversion. It does not denotes the same field for both processes.

An exact treatment can be done in the time domain to compute the energy [Weiner 11a]. In the spectral domain, a similar result may be obtained by approximating the phase-matching function by a Gaussian of similar FWHM.

The second harmonic field is then found to be proportional to

$$A_s^{out}(\omega) \propto \frac{\chi^{(2)} W_p \ell_c}{n^{3/2}} \exp\left[-\left(\frac{\omega - 2\omega_0}{2\kappa}\right)^2\right] \tag{8.22}$$

where W_p is the energy in a pump pulse and κ is an effective width defined by

$$\kappa = \sqrt{2}\Delta\omega_p \left[1 + \left(\frac{\Delta k' \ell_c \Delta\omega_p}{\sqrt{2}\xi}\right)^2\right]^{-1/2} \tag{8.23}$$

where $\xi \approx 1.9$ is a numerical factor that approximates the FWHM of the sine cardinal to a Gaussian. For short crystals $\ell_c \to 0$, we find the standard result that the second harmonic field has a width $\sqrt{2}\Delta\omega_p$. A longer crystal then reduces the spectral bandwidth of the second harmonic field.

Hence, the energy in a signal pulse is given by

$$W_s^{out} \propto \frac{d_{eff}^2}{n^3} W_p^2 \ell_c^2 \kappa \tag{8.24}$$

We introduced the effective nonlinear coefficient $d_{eff} = \frac{\chi^{(2)}}{2}$ which is commonly used in the literature to quantify the nonlinearity of a medium [Boyd 03].

The efficiency of the second-harmonic generation process is proportional to:

$$\boxed{\eta_{SHG} \propto \frac{d_{eff}^2}{n^3} W_p \ell_c^2 \kappa} \tag{8.25}$$

It is a standard result that this efficiency is proportional in the CW regime to the pump power, to the square of the crystal length and to the nonlinear coefficient. In the ultrafast regime, however, different cases arise depending on the bandwidth of the pump. We chose to write these conditions as a function of the temporal bandwidth rather than the spectral bandwidth:

- $\left|\Delta k'\right| \ell_c \ll \Delta t_p$: this is the quasi-continuous regime, it corresponds to the situation where the bandwidth of the phase-matching is much broader than the spectrum of the pump. In that case, $\kappa \to \Delta\omega_p$ and the efficiency writes as:

$$\boxed{\eta_{\mathrm{SHG}}^{QCW} \propto \ell_c^2 \frac{W_p}{\Delta t_p}} \tag{8.26}$$

Like the CW case, the efficiency scales with the square of the crystal length and with the energy of the pump. However, because of the pulsed regime, the efficiency is also inversely proportional to the temporal bandwidth Δt_p of the pump.

- $\left|\Delta k'\right| \ell_c \gg \Delta t_p$: the group delay mismatch is much larger than the pulse width, which is equivalent to state that the phase-matching bandwidth is much narrower than the pump spectrum. In this case, $\kappa \to \frac{2\xi}{|\Delta k'| \ell_c}$ which is independent of the bandwidth of the pump. When computing the efficiency in the large group velocity mismatch regime, we obtain:

$$\boxed{\eta_{\text{SHG}}^{GVM} \propto \frac{\ell_c}{|\Delta k'|} W_p} \tag{8.27}$$

In this regime, the second harmonic power scales linearly with the crystal length, and is independent of the pump duration. Efficiency is degraded by the group velocities mismatch. Spectrally, the second harmonic field is filtered by the phase-matching function, which results in the temporal domain in a square pulse shape, with a duration $\left|\Delta k'\right| \ell_c$ independent of the pump pulse duration.

The previous discussion allows to define a characteristic length ℓ_T, called temporal walk-off, as the distance for which the pump and the signal are temporally separated by one unit of bandwidth:

$$\ell_T = \frac{\xi}{\sqrt{\ln 2}} \frac{\Delta t_p}{|\Delta k'|} \tag{8.28}$$

The optimal situation is attained when these two width are matched, meaning $\ell_c \approx \ell_T$. This usually means using a crystal with a broad phase-matching bandwidth compared to the pump field spectrum.

The length ℓ_T gives a limit to the crystal length for temporal effects. A similar derivation may be done in the spatial domain to yield two different boundaries.

The first one arises from focussing effects. When pumped by a Gaussian beam of waist $w_{0,p}$ in the center of the crystal, the transverse mode of the signal beam is also Gaussian with the following properties:

$$w_{0,s} = \frac{w_{0,p}}{\sqrt{2}} \qquad \text{for which} \qquad z_{0,s} = z_{0,p} \tag{8.29}$$

where z_0 is the Rayleigh length of the beam. Defining the depth-of-field, or confocal parameter, b as $b = 2z_0$, it is possible to estimate the optimal crystal length at which efficiency is maximum. The treatment done in [Boyd 68] gives the optimal crystal length $\ell_c \approx 2.84\, b$. This criterion takes into account the fact that the frequency doubling process

is most efficient at the point of focus whereas it is weaker in the other regions of the crystal.

The other criterion to consider is the effect of walk-off. When critical phase-matching is achieved (*i.e.* the cut of the crystal is such that the fundamental and harmonic waves propagate with the same velocities), this poses the problem that the second harmonic energy does not propagate along the wave vector. Hence, the overlap between the two waves is not conserved over the crystal length.

The limit in crystal length ℓ_s (also called aperture length), for a walk-off angle ρ, is defined by the distance for which the second harmonic wave is displaced by one pump beam diameter:

$$\ell_s = \frac{\sqrt{2} w_{0,p}}{\rho} \tag{8.30}$$

giving yet another limit in crystal length to take into account.

One final focussing effect that is worth mentioning is the phase-matching of the different wave vectors of the pump. Indeed, for strong focussing, the edge of the beam propagate with different wavevectors, such that the doubling efficiency is decreased due to phase-matching. This defines the acceptance angle of the crystal.

Obviously, the same considerations need to be applied to parameteric down conversion in order to maximize its efficiency.

8.3.2 The influence of temporal chirp

The previous derivation considered transform-limited pulses. It is important to know the influence of the pump chirp on the second harmonic.

We consider here that the pump field is linearly chirped, *i.e.* it has a quadratic spectral phase ϕ_2 (see section 2.2.2.3) when entering the crystal. As we have seen, such phase expands the pulse length in the temporal domain and decreases the peak power. It should therefore decrease the efficiency of the frequency doubling process.

We add a quadratic spectral phase to the pump field in equation (8.18):

$$A'_p(\omega) = A_p(\omega) \exp\left[i\phi_2 \frac{(\omega-\omega_0)^2}{2} \right] \tag{8.31}$$

It can be shown that the second harmonic field at the output of the crystal thus writes as

$$\left(A_s^{out}\right)'(\omega) = \frac{A_s^{out}(\omega)}{\sqrt{1 - i\phi_2/2\Delta t_p^2}} \exp\left[i\frac{\phi_2}{2} \frac{(\omega-2\omega_0)^2}{2} \right] \tag{8.32}$$

showing that the quadratic phase of the pump is passed to its second harmonic, reduced by a factor 2.

Consequently, the energy in the second harmonic field is found to be:

$$\left(W_s^{out}\right)' = \frac{W_s^{out}}{1+\left(\phi_2/2\Delta t_p^2\right)^2} \equiv \frac{W_s^{out}}{\left(\Delta t_p'/\Delta t_p\right)^2} \tag{8.33}$$

where Δt_p and $\Delta t_p'$ are respectively the temporal width of the transform-limited and the chirped pump pulse, as defined by (2.41). Naturally, we have $\Delta t_p'/\Delta t_p > 1$ whether ϕ_2 is positive or negative.

The efficiency of second harmonic generation is thus degraded with respect to the transform limited case according to

$$\eta_{SHG}' = \frac{\eta_{SHG}}{\left(\Delta t_p'/\Delta t_p\right)^2} \tag{8.34}$$

This shows the necessity to have a transform-limited pump pulse to ensure the best efficiency. More precisely, this same treatment may be used to take into account the dispersion induced by the propagation through the crystal, which can be very dispersive for short pulses. Hence, the optimal situation corresponds to a transform-limited pump pulse in the center of the crystal. Again, the same considerations also apply to parametric down conversion.

8.4 An ultra-fast squeezer

We present in this section the experimental realization of a single-pass squeezer.

8.4.1 Pump generation

We achieved second-harmonic generation in a type-I BBO crystal of 400 µm from transform-limited 20 fs infrared pulses. A prism compressor was used to ensure that the infrared pulses duration was minimal in the frequency doubling crystal. The second harmonic spectral width is on the order of 8 fs in such configuration, which is what is required by the simulation on figure 8.2.

When pumped with an infrared power of ~ 400 mW, we measure an efficiency of ~ 5%, *i.e.* 20 mW of second harmonic power. Such power is not sufficient to efficiently pump the parametric down conversion process. To increase it, one could change the parameters of the frequency doubling , such as focussing and crystal length. However, this would pose other problems such as spatial chirp, poor spatial mode quality and non-gaussian spectrum.

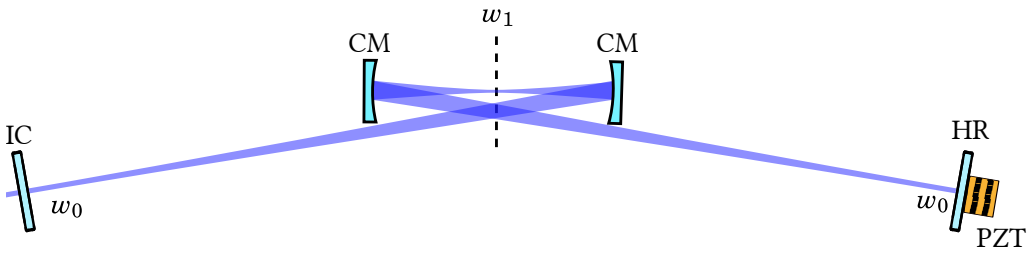

Figure 8.4: Geometry of the SPOPA cavity. The waist at its center is $w_1 = 20$ µm, and the input waist is $w_0 = 180$ µm. IC: input coupler, HR: high reflectivity, CM: curved mirror.

Hence, we chose to place the parametric down conversion crystal in a synchronous cavity resonant for the pump. The resulting scheme can be called a synchronously pumped optical parametric amplifier (SPOPA).

Note that a 8 nm spectrum at 400 nm corresponds to transform-limited 30 fs pulses, which disperse more quickly than in the infrared. The compensation of dispersion of the second harmonic field is therefore very important, especially if it needs to be resonant in a high finesse cavity.

8.4.2 Synchronously pumped optical parametric amplifier

The power circulating inside of a cavity with a high finesse $\mathscr{F}$ is enhanced with respect to the incident beam by a factor of $\mathscr{F}/\pi$. Hence, a cavity of finesse 100 would see its intracavity power enhanced by a factor of ~ 20. Such an enhancement applied to our second harmonic power is more than enough to pump the parametric down conversion process.

During her master thesis internship [Casacio 14], Catxerê Andrade Casacio designed the geometry of a synchronous cavity which provides a waist of ~ 20 µm at its center. It is a linear cavity in a simple layout with one input coupler, one back mirrors and two curved mirrors, as shown on figure 8.4.

Since it is linear, the light travels in both directions inside the cavity, and its length corresponds to half the free spectral range of the laser. The curved mirrors both have a focal length of 50 mm. In order to be a stable resonator, the waist on both the input coupler and the back mirror needs to be of ~ 180 µm.

The cavity was experimentally constructed by Thibaut Michel during his internship. The modematching is achieved using three curved mirrors as to minimize the dispersion on the second harmonic beam. Using an input coupler with a reflectivity of 98%, a finesse of ~ 150 was measured, with a reasonable mode-matching of 90%. The presence of a transverse TEM_{01} mode was originally observed, and it could not be diminished by

aligning the beam to the cavity. It was determined that this transverse mode came from the ellipticity of the beam. Introducing a pinhole to filter it solved the problem.

Using a Pound-Drever-Hall locking scheme were a piezo actuator is modulating the phase of the beam at ~ 800 kHz, a stable lock was obtained with low fluctuations.

As of yet, we could not introduce the parametric down conversion crystal inside of the cavity because of the dispersion. Since the light is going twice through the crystal, taking into account the air, the amount of dispersion for one round-trip with a 1 mm BBO crystal is around 300 fs^2. That amount of phase is enough to double the length of a 30 fs pulse.

Consequently, we acquired chirped mirrors to compensate for the propagation inside the cavity. This would allow to proceed to lock the cavity with a crystal inside.

8.5 Perspectives

Finally, we present the applications to the quantum light that would be generated by the SPOPA. Being a source of multimode squeezed light, it can be applied to quantum metrology to produce below shot-noise sensitivity in parameter estimation. From another perspective, one can consider two of these multimode squeezed beams and use them to entangle quantities that can be linked to the parameters from section 4.2.

8.5.1 Quantum enhanced metrology

We remind from section 4.2.4.2 that a measurement on the detection mode for space-time positioning presents the best sensitivity using classical resources. The sensitivity of this projective measurement is governed by the variance of the signal field in the detection mode. Hence, using squeezed light, the sensitivity is increased beyond the quantum limit, as it was done experimentally in 5.4.6. However, that quantum experiment was a spectral analysis, whereas the space-time positionning experiment can be achieved with a single pulse. The quantum effects would then also be resolvable in a pulse-by-pulse measurement.

By taking into account the variance of the different modes of the signal field, the minimum detectable distance from (4.52) (for a propagation in vacuum) is then written as

$$\left(\delta L\right)_{min} = \frac{c}{2\sqrt{N}} \frac{\sqrt{\omega_0^2 \sigma_{p_0}^2 + \Delta\omega^2 \sigma_{x_1}^2}}{\omega_0^2 + \Delta\omega^2} \tag{8.35}$$

where σ_{p_0} is the noise in the phase mode (in the phase quadrature) and σ_{x_1} the noise in the time-of-flight mode (in the amplitude quadrature). In order for the sensitivity to

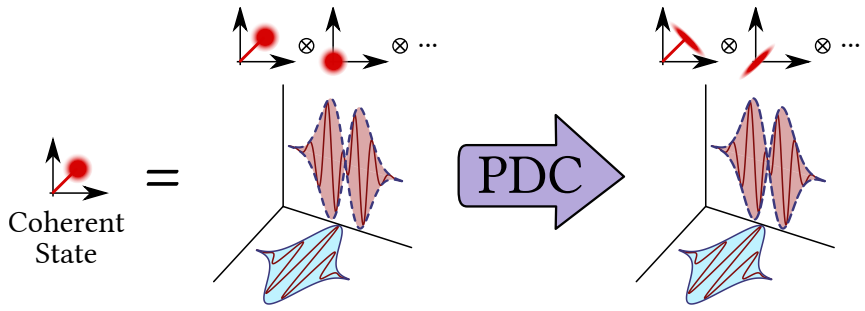

Figure 8.5: Representation of the multimode output of the parametric downconversion process when seeded by a coherent state. The mean-field mode is squeezed on the phase quadrature and the time-of-flight mode is squeezed on the amplitude quadrature.

increase with respect to the standard quantum limit, both these variances need to be smaller than unity.

Remarkably, this is precisely the characteristics of the multimode squeezed light at the output of the parametric down conversion process. Indeed, when the first supermode (corresponding to the mean field mode) is phase squeezed, then the next supermode (corresponding to the time-of-flight mode) is amplitude squeezed. In the case depicted by figure 8.2, the first two eigenvalues have the same absolute value, such that the two first supermodes would show the same reduced variance in orthogonal quadratures, *i.e.* $\sigma_{p_0} \simeq \sigma_{x_1} \equiv \sigma_0$. Hence, the sensitivity reads

$$\boxed{(\delta L)_{SQZ,\min} \simeq \frac{c}{2\sqrt{N}} \frac{1}{\sqrt{\omega_0^2 + \Delta\omega^2}} \cdot \sigma_0^2} \tag{8.36}$$

Therefore, the parametric down conversion scheme outputs directly the necessary resources to perform a below shot-noise measurement of a displacement in space or in time. The important point is that the two first supermodes are squeezed by the same amount while the higher order modes are of no importance. The conditions that are outlined in figure 8.2 appear to be sufficient to generate such quantum state.

We stress that this quantum detection mode is generated directly by the nonlinear process, and does not require the generation of a synthetic beam as it was done in 5.4.6. The parametric down conversion process needs to be seeded since the mean field mode has to be squeezed. A schematic representation is given on figure 8.5.

To produce the squeezed state using the SPOPA, it needs to be seeded in order to produce the beam described by figure 8.5. Note that the signal and idler photons need to be created in the same spatiotemporal mode. To do so, one could use dichroic mirrors to seed the cavity and perform the parametric down conversion in a collinear configuration. This results directly in a squeezed beam, similar to the output of the SPOPO.

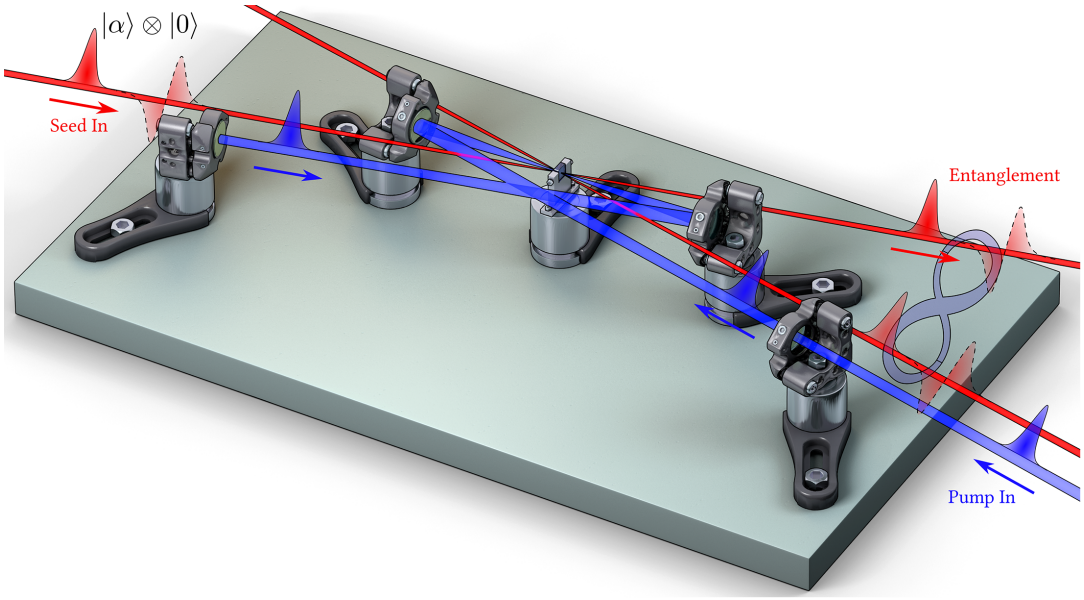

Figure 8.6: Computer graphics representation of the SPOPA. It is seeded by a coherent field in the mean-field mode. In a non-collinear configuration, at the output, there are two entangled beams.

To achieve such scheme, dichroic mirrors of very good quality are required, but this geometry is simple to execute and the down-converted beam is easy to retrieve. The most problematic part would be the dispersion compensation, or more precisely, matching the spectral phase of the seed to the down-converted field.

8.5.2 Entanglement

If two such beams are generated, it is possible to combine them on a beamsplitter to generate entanglement. Entanglement would then be observed between the two mean-field modes and on between the two time-of-flight modes. Since the phase mode is attached respectively to a detection of variation in amplitude and phase on the amplitude and the phase quadrature, the first entangled quantities are amplitude and phase. Similarly, the time-of-flight mode detects a variation of center wavelength and timing jitter, so the entangled quantities are frequency and time.

If the two modes have the same squeezing value, this degeneracy allows to easily change the basis to the detection mode that combines both phase and time-of-flight mode. The entanglement would then be related to this mode which is attached to a measurement of distance. One entangled quantity would therefore by the delay in distance (or in time) while the other quantity is less clearly defined, as it combines energy

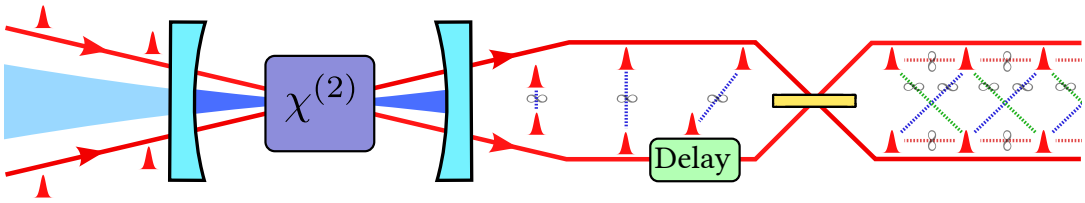

Figure 8.7: Generation of a highly multimode quantum source that is entangled in frequency and multiplexed in time.

and frequency. The study of the properties of such states is among the next objectives of this project.

These entangled beams are generated when seeding the SPOPA in a non-collinear configuration, as depicted be figure 8.6. Because of the small acceptance angle of BBO, this scheme requires tight geometry and small angles which is experimentally challenging. Combining these two beams would then generate squeezing and allow to be applied to quantum metrology.

It is important to stress that this treatment holds for a single pulse, such that these properties may be accessed by resolving the process in the time domain.

Another interesting application of the OPA in the non-collinear configuration is the generation of big states [Yokoyama 13]. It consists of a large number of entangled states (called *cluster states*), which are important resources to continuous variables quantum information. Such highly multimode entangled state can be generated with the SPOPA in non-collinear configuration, as shown by figure 8.7.

After generation of two entangled beams in a non-collinear configuration, one is delayed with respect to the other and the two beams are combined on a beam-splitter. The resulting quantum state is highly multimode and entangled in both frequency and time.

Conclusion and outlooks

In this thesis, we have given a modal description of the field generated by an ultrafast frequency comb. We have explicitly described how this multimode structure is experimentally accessed through the scheme of projective measurement. We have applied this formalism to the extraction of information encoded in a given optical quadrature, as well as to the retrieval of the fluctuations of the laser source.

We have demonstrated that a single parameter information is contained in a single mode of the field, named the detection mode, and we have shown that the best strategy to retrieve it is to use a homodyne detection where the local oscillator is in the detection mode.

We used a spectrally-resolved homodyne detection the set the mode of the local oscillator. It allows to retrieve simultaneously all the information that is contained on a given optical quadrature.

In quantum metrology, we devised an all-optical method to calibrate at the standard quantum limit the phase shift induced by a phase modulating element. The calibration is then utilized to measure the limit in sensitivity of an interferometer, which is found to coincide with the Cramér-Rao bound for Gaussian states. This measurement does not require any knowledge of the physical quantities that define the theoretical limit in sensitivity.

We introduced the detection modes attached to a phase and a time-of-flight measurement. The sensitivity of a measurement on these two modes is found to be in very good agreement with the theory. We constructed the detection mode for a longitudinal displacement, which combines interferometric and time-of-flight measurement, and proved an increase in sensitivity. This allowed to validate the projective measurement protocol applied to space-time positioning.

This protocol could find practical applications. For example, the increase in sensitivity could be used for synchronizing the position between two remote objects in vacuum. The small influence of dispersion allows to use very broadband sources such that the gain in sensitivity would be more important. The modal approach also allow to distinguish between different parameters. As such, this scheme could allow to perform a measurement of longitudinal displacement independently of transverse effect, such as fluctuations in pointing.

We applied this measurement scheme to the dispersive properties of a material. Us-

ing a temporally-resolved homodyne detection, we did extract the same spectrally multimode structure with a continuous rather than pixelized approach, although the measurement is non longer done in real-time. We thus extracted the index dispersion of a medium with a reasonable accuracy. This temporally-resolved measurement could potentially be made real-time by making the delay sweep quicker, and the extraction of timing information could also be improved by using two combs with slightly different repetition rates [Coddington 09].

We also successfully used non-classical light generated by another laser source to enhance the sensitivity in the measurement of a spectral displacement. By introducing squeezed vacuum in the mode attached to the detection of that parameter, we showed an increase in sensitivity due to the reduction in quantum noise in that detection mode.

In our experiments, the limited bandwidth of the laser source made the quantities to be measured extremely small. The enhancement between a standard measurement and one that uses a modal approach was thus also small. It is still remarkable that the enhancement was measurable with precision, proving again the validity of the protocol.

We used the multipixel homodyne detection to measure the spectral fluctuations in amplitude and in phase of the laser source. Using a modal description, we have access in real-time to the dynamics of the collective parameters of a frequency comb. Moreover, this allowed to measure the correlations between the amplitude and the phase noise of an optical frequency comb, bringing interesting perspective on the mode-locking mechanism.

Since it is real-time, we showed that this scheme could potentially be used as an error signal to compensate the fluctuations of the laser source.

Finally, we introduced the theoretical and experimental concepts that are needed to create sources of multimode squeezed light with single-pass parametric down conversion. We presented the development of a synchronously-pumped optical parametric amplifier. Such tool can be used in applications to quantum metrology and fundamental physics with the study of entanglement between a displacement in space and its conjugate variable. With the use of pulsed light, this quantum ressource also presents potential application in continuous variable quantum information with the elaboration of quantum networks.

Appendices

A Medium dispersion

(While explaining a complicated phase-lock loop electrical scheme)
"[...] Then the signal comes into this electrical component" (showing a circle with an R in it) "which is actually me doing the retrocontrol loop by myself. It's the human element !"

– Roman "*Human PID*" Schmeissner

Contents

A.1 Sellmeyer equation 213
A.2 Wave-vector dispersion 214
A.3 Application to delay and dispersion estimation 214

In this appendix, we give useful formula for estimating the dispersion in a medium. It can be a very handy tool in ultrafast optics when building an experiment. It allows to estimate how much delayed a pulse will be with respect to another or the amount of quadratic phase it will acquire. It is also important to estimate the phase-mismatch between the interacting waves in a nonlinear process.

A.1 Sellmeyer equation

For numerical calculations, the main indices of an anisotropic medium may be calculated using Sellmeyer's equation:

$$n_i^2(\lambda) = A_i + \frac{B_i}{\lambda^2 - C_i} - D_i\lambda^2 \qquad i = x, y, z \tag{A.1}$$

where Sellmeyer coefficients A, B, C, D may be found in the literature usually for λ in micrometers.

A.2 Wave-vector dispersion

We expand the wavevector $k(\omega) = \frac{\omega n(\omega)}{c}$ in the spectral domain:

$$k(\omega) \simeq k(\omega_0) + (\omega - \omega_0) \left.\frac{\partial k}{\partial \omega}\right|_{\omega_0} + \frac{(\omega-\omega_0)^2}{2} \left.\frac{\partial^2 k}{\partial \omega^2}\right|_{\omega_0} \tag{A.2}$$

$$\equiv k_0 + \Omega k_0' + \frac{\Omega^2}{2} k_0'' \tag{A.3}$$

Derivative of the index $n(\omega)$ with respect to ω need to be computed. Using Sellmeyer equations, one can compute the derivatives of $n(\lambda)$ with respect to λ. Finally, to deduce each term of (A.2), we use the composition of derivatives $\partial/\partial\omega = \partial\lambda/\partial\omega \times \partial/\partial\lambda$ which then yields

$$\frac{\partial k}{\partial \omega} = \frac{1}{c}\left(n(\omega) + \omega \frac{\partial n(\omega)}{\partial \omega}\right) = \frac{1}{c}\left(n(\lambda) - \lambda \frac{\partial n(\lambda)}{\partial \lambda}\right) \tag{A.4}$$

$$\frac{\partial^2 k}{\partial \omega^2} = \frac{1}{c}\left(2\frac{\partial n(\omega)}{\partial \omega} + \omega \frac{\partial^2 n(\omega)}{\partial \omega^2}\right) = \frac{\lambda^3}{2\pi c^2} \frac{\partial^2 n(\lambda)}{\partial \lambda^2} \tag{A.5}$$

Knowing the main indices of a medium by the Sellmeyer equation (A.1) and the index seen by any propagating wave, we may use relations (A.5) to compute the linear and quadratic dispersion terms.

A.3 Application to delay and dispersion estimation

It is then straightforward to estimate the amount of delay or dispersion that a pulse acquires by propagating through a medium of length L. By expressing λ in mm in Sellmeyer equations and using $c = 299.8$ nm/fs, delay in fs is directly given by[1]

$$\delta\tau = k_0' L \tag{A.6}$$

with k_0' in fs / mm, while the amount of dispersion in fs^2 is given by

$$\phi_2 = k_0'' L \tag{A.7}$$

with k_0'' in fs^2/mm.

On table A.1, we show the index properties of materials that were encountered during this thesis. The knowledge of the properties of glass materials was particularly useful to compensate the amount of dispersion caused by transmissive optics such as lenses and windows, while the properties of air needed to be taken in account for the design of Fabry-Pérot cavities.

[1] Here we consider the delay relative to a path reference in vacuum. We replace vacuum with the medium such that the path traveled is actually $(n(\omega) - 1) \times L$.

Medium	λ_0 (nm)	n_0	k'_0 (fs/mm)	k''_0 (fs^2/mm)
Air	800 nm	$1+3\cdot10^{-4}$	0.9	0.021
	400 nm	$1+3\cdot10^{-4}$	1	0.050
Air (40 mbar)	800 nm	$1+1\cdot10^{-5}$	0.05	0.001
BK7	800 nm	1.51	1760	45
	400 nm	1.53	1950	123
SF10	800 nm	1.71	2510	158
	400 nm	1.78	3350	708
BBO (oo-e)	800 nm	1.66	2284	75
	400 nm	1.66	2481	198
BIBO (ee-o)	800 nm	1.82	2900	166
	400 nm	1.82	3337	480

Table A.1: Table of index properties of some materials that were used in this thesis. For nonlinear crystals, the indices are taken to achieve critical phase-matching.

B Projective measurements by pulse shaping

(Having spent an hour trying to make an expensive Stanford Research Systems PID controller working)
"I'm sure this thing works perfectly – you just need to be an expert in PID theory to precisely set all of the 15 parameters."

– Jonathan "*Labview Guru*" Roslund

Contents

B.1 Pulse shaping the time-of-flight mode 218
B.2 Locking on the time-of-flight mode 219
B.3 Dispersion measurement 221

In this appendix, we review the procedure of projective measurement by pulse shaping, as it was originally intended.

This technique has the main advantage of not requiring a spectrally-resolved detection, thus reducing the complexity of the experiment. Indeed, as it is explained in 5.3, the multipixel detection requires careful alignment and calibration in order to work properly. Moreover, the necessity to demodulate each pixel independently requires low-noise electronics and careful engineering in order to reduce the noise floor of the detection, and particularly cross-talk between each electrical pathway. The way our demodulation was achieved may not be optimal, and the low clearance of 8 dB could certainly be improved.

For quantum experiment, the highest quantity of squeezing where detected using single photodiodes with high quantum efficiency, and the mode projection to measure the variance in a given mode of the squeezed vacuum field is achieved by pulse shaping. The multipixel detection could not measure as much squeezing as the single diode scheme because of the lowest quantum efficiency and the relatively low clearance of the detection scheme.

For our application to quantum metrology, the clearance is not as important, and the clear advantage of single diode scheme is the simplicity of the experimental scheme (moreover, as we develop in 3.3.3 and 5.4.5, a single diode scheme can resolve the spectral structure of the field). However, the drawback that motivated the use of the multipixel detection is the reproducibility of the experiment. Since every mode can be constructed

post-facto with the multipixel detection, a single measurement may be used several times to extract different information.

As we show in this appendix, however, some of the simplest experiment would have been strictly impossible using pulse shaping.

B.1 Pulse shaping the time-of-flight mode

We show the example of pulse shaping the time-of-flight mode, whose expression is given by (4.32).

Shaping this mode is straightforward: a π phase shift is imprinted on the compensation phase 3.5. An quadratic amplitude mask is also applied. The resulting spectrum and the spectral phase measured by spectral interferometry is shown on figure B.1.

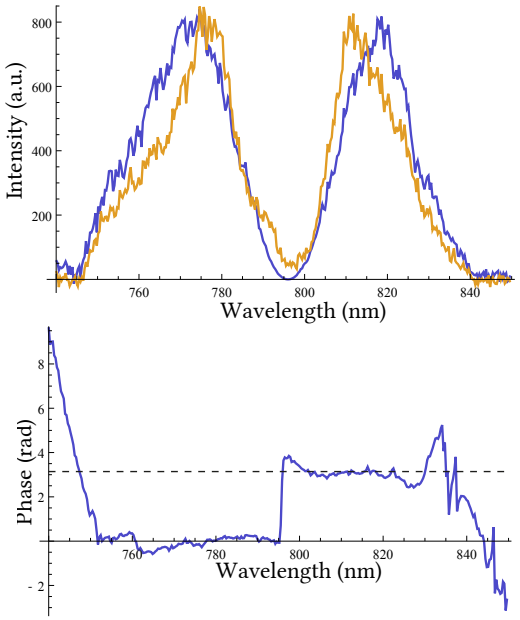

Figure B.1: Top : Spectrum of the time-of-flight mode. The gold trace is the experimental spectrum obtained from the mean-field mode while the blue is measured. Bottom : retrieved spectral phase of the time-of-flight mode by spectral interferometry. It shows a π phase shift at the center wavelength.

The difficulty when trying to pulse shape such a mode is to respect orthogonality. As we develop in appendix C, the modes construction require perfect orthogonality in order for our experiments to succeed. This is experimentally hard to achieve, since the phase shift needs to happen exactly on the center of mass of the mean-field mode.

A solution that we investigated was to dynamically change the wavelength at which the π phase shift occurs while looking at the center of the cross-correlation between the local oscillator and the signal field. Such a cross-correlation measurement is shown on figure B.2. The mode construction is successful when the fringe at time zero is zero, and the symmetry satisfy the theoretical predictions.

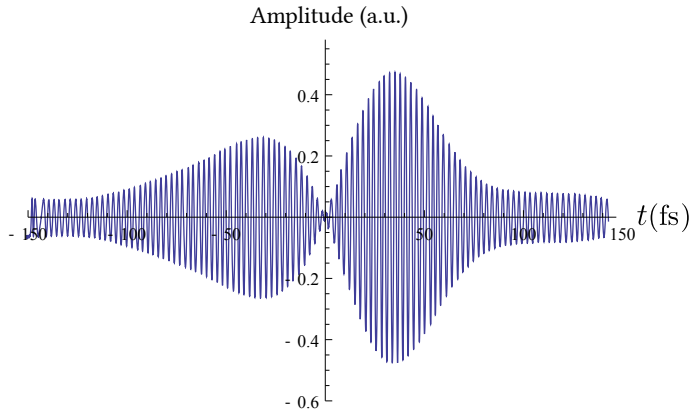

Figure B.2: Crosscorrelation between the signal field and the local oscillator in the time-of-flight mode.

B.2 Locking on the time-of-flight mode

Considering that the time-of-flight mode's construction is successful, to achieve projective measurement on the phase quadrature, one would have to lock the relative phase between the two arms of the interferometer on the phase quadrature. This is usually achieved by locking on the difference of the DC signal from the detectors of the homodyne detection, as shown on figure 5.7. In the case of the phase mode, the lock point is easy to pinpoint since the maximal phase information corresponds to a null DC signal.

In the case of the time-of-flight mode, however, the lock point is not well defined. The first problem to obtain an error signal to lock the delay is that the time-of-flight mode has zero amplitude at its center. There is thus no signal to lock on. It is however not the most fundamental of problems that prevent from locking on such a mode.

We remind that the flip mode (*i.e.* mean field mode with a π phase shift) has the same energy than the mean-field mode, and should therefore be easier to lock on. Since it shows a 80% overlap with the time-of-flight mode, it is possible to use it in projective measurements. Even using this mode, a simple measurement such as the one presented in 5.4.4.1 (comparing the sensitivity of the phase mode to the time-of-flight mode in distance estimation) is very complicated using pulse shaping.

Let us explain how the experiment would work with pulse shaping. Modulating the phase of the field, we use the phase mode to measure the minimum displacement that corresponds to a signal-to-noise of 1. This is achieved by locking on the phase quadrature, which corresponds to the maximal signal that is retrievable. Note that this is a good reference to know whether or not the lock point is effectively on the proper quadrature.

To know the sensitivity of the time-of-flight mode, one would have to use the pulse shaper to put the local oscillator in this mode, and perform the same measurement on the same lock point. However, theoretical simulations show that this lock point does no longer correspond to a maximum of signal.

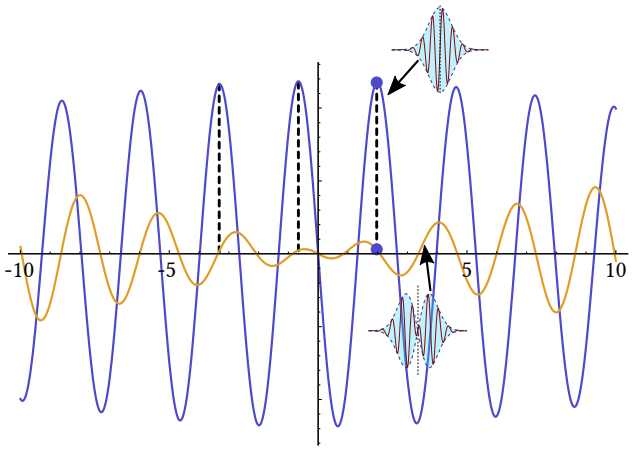

Figure B.3: Crosscorrelation of the high frequency component of the field (*i.e.* the sensitivity to a phase modulation) when the local oscillator is in the phase mode (blue) and the flip mode (gold). In this simulation, the ratio of the two marked point is equal to $\omega_0/\Delta\omega$.

On figure B.3, we show the theoretical cross-correlation between the signal and the local oscillator field for a phase mode and flip mode projection. We marked the maximum of the signal retrieved with a projection on the phase mode. We can see that the corresponding point on the flip mode does not correspond to the maximum signal. There is thus no other way to lock on this mode than to use the DC error signal, which is very small and hard to lock on.

The best option that was devised was to build yet another homodyne detection with the mean-field mode in both arms to generate an error signal. The delay of the other homodyne detection is locked according to this error signal. There was therefore a homodyne detection for locking the delay, and another for measuring the signal. The problem with that scheme is that the path fluctuations are different on both detections, and the measured signal was thus noisier.

B.3 Dispersion measurement

The dispersion experiment outlined in section 5.4.5 aim at measuring the dispersion of a medium by removing the phase mode contribution to the measurement. The original idea behind that experiment made use of pulse shaping, and aimed at measuring the difference between a modulation of distance in air or in vacuum.

Because of a number of complications, we settled for the measurement depicted in 5.4.5. However, a lot of work was put on the original idea, and successful techniques were developed, that we shall expand in this appendix.

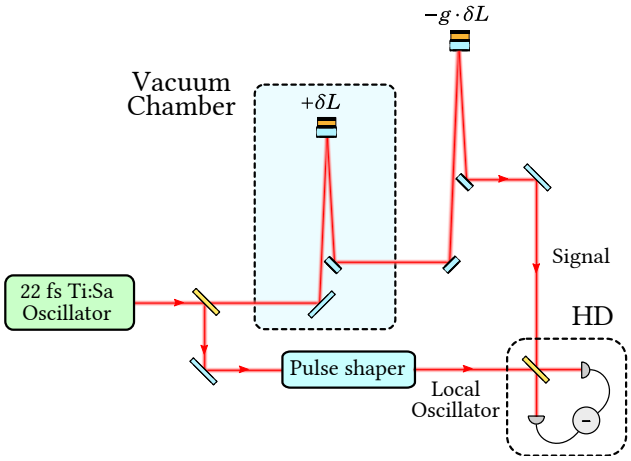

Figure B.4: Scheme to measure the air dispersion. Two piezo actuators modulate the distance δL by an equal amount in vacuum and in air. A variable gain is applied on the second piezo, such that for a specific value, they create a variation of the optical path without any change in distance.

The original scheme is presented on figure B.4. Using a vacuum chamber, a distance δL is modulated in vacuum, while another distance is modulated in air with an opposite phase $-g\cdot\delta L$. A variable gain g may be experimentally tuned.

Written the modulated field and computing the retrieved signal-to-noise ratios in a projective measurement scheme on the phase mode, we have:

$$\Sigma_\varphi(\Omega) = 2\sqrt{N}\,\omega_0\,(1-g\cdot n_0)\,\frac{\delta L}{c} \tag{B.1}$$

whereas on the time-of-flight mode:

$$\Sigma_g(\Omega) = 2\sqrt{N}\,\Delta\omega\,\left[1-g\cdot\left(n_0-\omega_0 n_0'\right)\right]\frac{\delta L}{c} \tag{B.2}$$

where we wrote n_0 and n_0' respectively the index of refraction and the dispersion of air.

We see that, for a specific value of $g = \frac{1}{n_0}$, the projection on the phase mode will be zero, whereas the time-of-flight mode would retrieve the following signal:

$$\Sigma_g(\Omega) = 2\sqrt{N}\,\Delta\omega\,\omega_0 \frac{n_0'}{n_0}\frac{\delta L}{c} \tag{B.3}$$

More specifically, if we scan the gain parameter g continuously and record the variation of (B.1) and (B.3), we would recover linear function that cross zero for two different values of g. The spacing between this value is then found to be proportional to n_0'. In essence, this method is very similar to the one presented in 5.4.5.

Experimentally, we tried to achieve this measurement by pulse shaping. As we developed in B.2, the ability to project on the time-of-flight mode requires to lock the interferometer on another homodyne detection of reference.

To achieve the compensation of the two modulations, we demodulated the signal received by the reference homodyne detection locked on the phase quadrature, thus yielding a signal proportional to (B.1). By setting the electronic demodulation phase on the amplitude quadrature retrieves the difference in the amplitude of the two modulations. The electronic phase quadrature retrieves the sign. These two signals were then used as error signals to lock both the amplitude and the phase of the compensation. One of the actuator was amplitude modulated and the other was phase modulated, such that it is possible to lock the signal (B.1) at zero. Then, ramping a small DC voltage to the amplitude modulation allows to sweep the gain g.

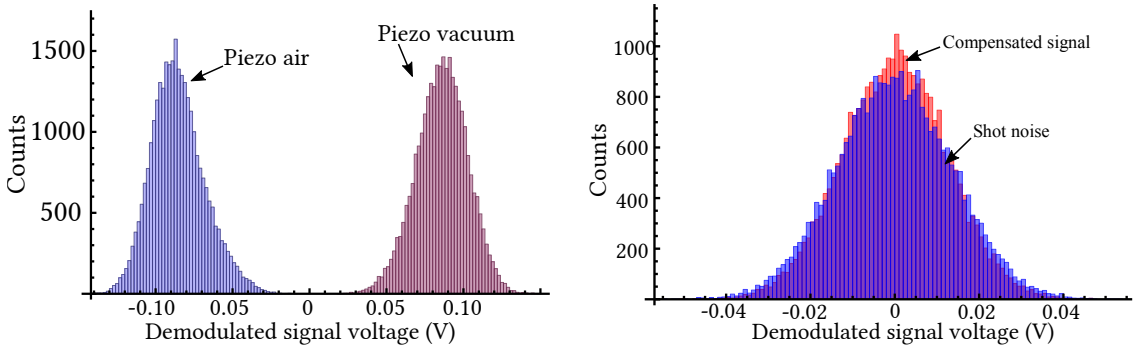

Figure B.5: Histograms of the demodulated signals for the piezo modulations in air and in vacuum. (a) Signals retrieved when both piezos are modulated independently with the same amplitude but with an opposite phase. (b) Same situation, but the two piezos are modulated simultaneously. The variance of the compensated signal is found to be equal to the shot noise.

On figure B.5a, we plotted the histogram of the demodulated signals when the two piezos are modulated independently with the same amplitude but with an opposite phase. On figure B.5b, we recorded another histogram but when both piezos are compensated. By overlaying the signal retrieved when no modulation is achieved, we see that the compensated signal is identical to the shot noise statistics. By locking the two modulations together, we therefore achieved two perfectly balanced modulation, such that the path traveled by the light is not changed. It is then possible to sweep the amplitude of one modulation from both sides of the compensation point, record the signal when projecting on the phase and on the time-of-flight mode, and retrieve the dispersion of air.

Such a measurement would then show that different modes retrieve different parameters in a projective measurement scheme.

Unfortunately, we could not complete this experiment due to the spatial contamination described in 4.3. This contamination was actually discovered while performing this measurement. Indeed, we noticed a very different response of each piezo actuator whether we retrieved the signal-to-noise on the measurement homodyne or on the lock homodyne. This effectively meant that the distance modulation was compensated according to one homodyne, but not to the other. This was explained by the fact that both homodyne were not strictly similar. The reference homodyne did not present a spatial contrast as good as the measurement homodyne. Moreover, the piezo actuators were imaged differently on both beamsplitter, thus recovering a different amount of spatial components.

At this point, we decided to build the multipixel detection described in 5.3 in an effort to distinguish between spatial and temporal modulations. Indeed, a spatial modulation should not be spectrally-dependent. Eventually, we moved towards spatial filtering, as described in 5.1.3.

Nevertheless, this experiment was very successful in the sense that we were able to lock two high frequency modulations in quadrature with no added noise.

C Experimental construction of the detection modes

(Upon noticing the german profanity in my Labview programs) "I think you have a problem."

– Vanessa "*das Heiliges Einhorn*" Chille

In this appendix, we explicit the ways the detection modes for the parameter estimation are constructed.

In section 5.4.2, we introduced the problem of modes construction. Ideally, these should be constructed from the power spectrum of the signal field. When the local oscillator spectrum is similar, the modes can also be constructed from its spectrum. However, when both field are not superimposed, there are extra steps to be added to the modes construction algorithm. We also remind that all the spectra are acquired using demodulated high frequency signals rather than DC signals from the detectors.

We begin by extracting the signal field from the high frequency signal, which we name u_{sig}^{hack}. The local oscillator spectrum is obtained by acquiring the variance of the photocurrents at a quantum limited frequency, such that we measure fluctuations of quantum vacuum. We name the retrieved spectrum u_{LO}^{hack}.

If the two fields showed the same spectral structure, we can reconstruct the homodyne signal by computing the gain. To obtain the multipixel gain (which correspond to Hermite polynomial in the Gaussian case), we need to compute the first moment μ of the signal's spectrum (see section 2.1.3). With the calibration of the multipixel detector, we have a map λ_i shown on figure 5.13b which returns the wavelength of pixel i. By fitting this map to a line, we obtain a continuous function $\mathrm{pix}(\lambda)$ which returns the pixel number of wavelength λ. Knowing the center of mass μ of the spectrum, it is therefore possible to obtain its fractional pixel index $\mathrm{pix}(\mu)$. This part is quite important to the algorithm, since the sensitivity that is measured depends on the spectrum that is being recorded, and not on the full spectrum delivered by the laser.

We can then construct the filter function $f_n(\lambda)$ as

$$\widetilde{f_n}(\lambda) = \big(\lambda - \mu\big)^n \tag{C.1}$$

which are subsequently normalized using $f_n(\lambda) = \frac{\widetilde{f_n}(\lambda)}{\left|\widetilde{f_n}(\lambda)\right|}$.

When we multiply these filters to the signal mode u_{sig}^{hack}, there is no guarantee that the resulting modes are orthogonal, and thus do not form a basis yet. We obtain the proper modes by orthogonalizing each of them to the signal mode. We label these modes u_n^{hack}.

Finally, we need to define new filters from these modes. Indeed, these are defined with respect to the signal field. However, we need to apply these modes to the local oscillator in order to accomplish a projective measurement. The final filters, labeled F_n, are then given by

$$\boxed{F_n(\lambda) = \frac{u_n^{hack}}{u_{LO}^{hack}}} \tag{C.2}$$

where $n = 0$ is the filter to apply to the local oscillator field for a phase detection, $n = 1$ is a time-of-flight measurement, etc... This operation ensure that applying the filter to the acquisition will project on the right mode defined by the signal field. The filters for a given acquisition of the experiment is given on figure 5.12 when a piezoelectric actuator is modulated.

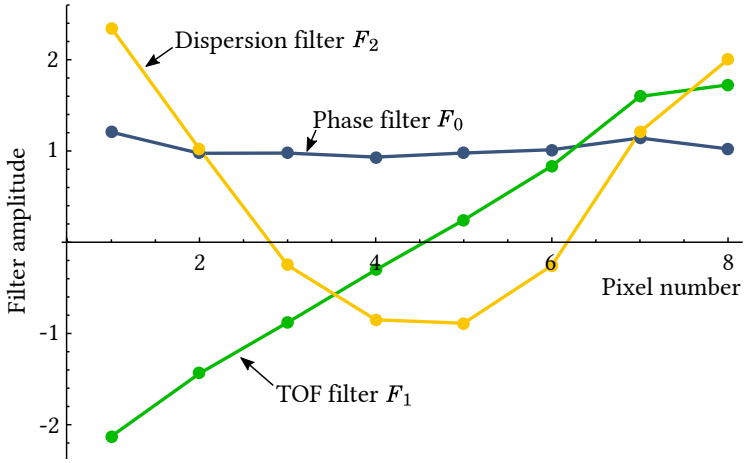

Figure C.1: "Hack" filters obtained by extracting the spectral structure of the field from the measured homodyne signal. Note the difference with the theoretical Hermite polynomial H_n, where for example $H_0 = 1$. This structure in the filters is essential for reproducibility of the experiment.

To accomplish the *post-facto* projective measurement, we then need to apply the filters to the spectrally resolved homodyne acquisition, and compute the signal-to-noise.

D Conjugated variable of space-time position

(About writing a PhD dissertation)
"Stop drinking coffee and start drinking tea. Otherwise, you'll be twitching more and more every passing day."

– Alexandros "*The Greek*" Tavernarakis

In section 8.5, we showed that is it possible to produce quantum states that correspond to the observables defined in 4.2.3. For example, it is possible to introduce squeezing in a detection mode to enhance the sensitivity of the measurement, as it was done in 5.4.6 were we achieved a measurement of a spectral displacement below the standard quantum limit. The same description applies to the measurement of a phase shift, amplitude perturbation and timing jitter.

We also proved that it is possible to squeeze the detection mode for space-time positioning. It is therefore possible to entangle this state to its conjugate quantity. In this appendix, we investigate the physical meaning of the observable that is conjugated to the position in space-time.

The problematic should be posed as follows: consider that we have a source that delivers the beam depicted by figure 8.5, that is squeezed in the detection mode for space-time positioning. If one were to perform a detection of a longitudinal displacement using this mode, the sensitivity would be increased with respect to the standard quantum limit. However, what physical information would be retrieved by a measurement on the orthogonal quadrature ? Since the displacement in space-time is an observable, the orthogonal quadrature should also contain a physical parameter.

D.1 Detection mode for a global displacement

From a classical point of view, the expression of a field that is delayed by a quantity δL is given by:

$$E^{(+)}(\Omega) = \mathscr{E}_0\sqrt{N}\left[v_0(\Omega) + i\,\delta L\left(\frac{\omega_0}{\mathrm{v}_\varphi}\cdot v_0(\Omega) + \frac{\Delta\omega}{\mathrm{v}_g}\cdot v_1(\Omega)\right)\right] \tag{D.1}$$

where v_0 is the mean-field mode and v_1 is the next mode in the Hermite-Gauss basis. The modes $i\cdot v_0$ and $i\cdot v_1$ correspond respectively to the phase mode and to the time-of-flight

mode.

In section 4.2.4.2, we introduced the detection mode $v_{\delta L}$ for measuring δL. It reads:

$$v_{\delta L}(\Omega) = \frac{i}{K_{\delta L}}\left(v_0(\Omega) + \frac{\Delta\omega}{\omega_0}\cdot\frac{\mathrm{v}_\varphi}{\mathrm{v}_g}\cdot v_1(\Omega)\right) \tag{D.2}$$

where $K_{\delta L} = \sqrt{1+\left(\Delta\omega \mathrm{v}_\varphi \Big/ \omega_0 \mathrm{v}_g\right)^2}$ is a normalization factor. The displaced field (D.1) then writes simply as:

$$E^{(+)}(\Omega) = \mathscr{E}_0\sqrt{N}\left[v_0(\Omega) + K_{\delta L}\cdot\frac{\delta L\omega_0}{\mathrm{v}_\varphi}\cdot v_{\delta L}(\Omega)\right] \tag{D.3}$$

We take the case of a displacement in vacuum, such that $\mathrm{v}_\varphi = \mathrm{v}_g = c$. The detection mode then writes as:

$$\boxed{v_{\delta L}(\Omega) = \frac{i}{K_{\delta L}}\left(v_0(\Omega) + \frac{\Delta\omega}{\omega_0}\cdot v_1(\Omega)\right)} \tag{D.4}$$

D.2 Detection mode for a spectral displacement

In section 4.2.2, we derived the detection mode for a spectral displacement. We did not take into account the fact that changing the optical frequency also changes the energy of the field.

Indeed, from the plane-wave expansion (1.16) of the field, we can write:

$$E^{(+)}(t) = \sum_\ell \mathscr{E}_\ell \alpha_\ell u_\ell(t) e^{-i\omega_\ell t} \tag{D.5}$$

We consider a global displacement $\delta\omega$ of the spectrum that affects every frequencies equally. As such, we have

$$E^{(+)}(t) = \sum_\ell \mathscr{E}_\ell \alpha_\ell u_\ell(t) e^{-i\omega_\ell t} e^{-i\delta\omega t} \tag{D.6}$$

The energy of the field is affected by the change in the frequency through $\mathscr{E}_\ell$ (1.17). For a small displacement $\delta\omega$, we have $\mathscr{E}_\ell \to \mathscr{E}_\ell + \frac{\delta\omega}{2\omega_\ell}\cdot\mathscr{E}_\ell$.

The field may then be written as

$$E^{(+)}(t) = \sum_\ell \mathscr{E}_\ell\left(1+\frac{\delta\omega}{2\omega_\ell}\right)\alpha_\ell u_\ell(t) e^{-i\omega_\ell t} e^{-i\delta\omega t} \tag{D.7}$$

We then apply the small bandwidth approximation: $\omega_\ell \approx \omega_0$. Also, since $\omega_0 \gg \Delta\omega$, it is possible to consider that

$$\sqrt{\hbar\omega_\ell}\,\frac{\delta\omega}{2\omega_\ell} = \frac{\delta\omega}{2}\sqrt{\frac{\hbar}{\omega_\ell}} \approx \frac{\delta\omega}{2}\sqrt{\frac{\hbar}{\omega_0}}$$

Consequently, the displacement in energy due to the frequency shift may simply be modeled by a perturbation of the field constant:

$$\boxed{E^{(+)}(t) \simeq \mathscr{E}_0\left(1+\frac{\delta\omega}{2\omega_0}\right)\sum_\ell \alpha_\ell u_\ell(t) e^{-i\omega_0 t} e^{-i\delta\omega t}} \tag{D.8}$$

Finally, the field displaced in frequency and in energy is written from (4.26) by setting $\epsilon = \frac{\delta\omega}{2\omega_0}$. We then obtain

$$\boxed{E_s^{(+)}(\Omega) = \mathscr{E}_0\sqrt{N}\left[u_0(\Omega) + \frac{\delta\omega}{2\omega_0}\left(\cdot v_0(\Omega) + \frac{\omega_0}{\Delta\omega}\cdot v_1(\Omega)\right)\right]} \tag{D.9}$$

The detection mode for $\delta\omega$ is thus given by

$$\boxed{v_{\delta\omega}(\Omega) = \frac{1}{K_{\delta\omega}}\left(v_0(\Omega) + \frac{\omega_0}{\Delta\omega}\cdot v_1(\Omega)\right)} \tag{D.10}$$

with $K_{\delta\omega} = \sqrt{1+\left(\omega_0 \big/ \Delta\omega\right)^2}$.

We can see that this mode is different from (D.10) first by its real amplitude, but also by the weight on the mode v_1. Indeed, a detection of a shift of distance is more easily achieved with large bandwidth, *i.e.* with short pulses for the time-of-flight component. The change in the center of the temporal enveloppe is then easier to detection. The same argument explains why the shift of the carrier is easier to detect with large optical frequencies.

It is also logical that a shift of the spectrum is easier to detect with very small bandwidth, since a small change in the center wavelength results in a large change in the signal at a fixed optical frequency. The fact that the shift in amplitude due to $\delta\omega$ is detected with a sensitivity that scales with $1/\omega_0$ is explained by the fact that, since $\delta\omega$ is small, then the smaller ω_0 is, the easier it is to detect the shift in energy.

One should note that this description is purely theoretical, since it seems hard to find a laser source that could displace the spectrum in such way that the only change in energy comes from a change in photon frequencies. For instance, on figure 5.23, we can see an amplitude variation that is higher than the variation of center wavelength. Although

it may include a contribution from the change in photon frequency, this contribution should be negligible, probably not even detectable.

The most important point is the fact that the mode (D.10) is not the complex conjugate of (D.10). Consequently, it is not possible to perform the quantum derivation from section 4.2.3 when the field is expanded on these modes.

D.3 Conjugated parameter

We propose to write formally the expression of the conjugated parameter. We start by redefining the basis of the field as $\{V_n\}$, where the first mode corresponds to the detection mode:

$$V_0(\Omega) = \frac{1}{\sqrt{1+\left(\Delta\omega \middle/ \omega_0\right)^2}}\left(v_0(\Omega) + \frac{\Delta\omega}{\omega_0} v_1(\Omega)\right) \tag{D.11}$$

We consider that this is the only mode in the basis that is non-vacuum.

In terms of quadratures, the quantum field is written as

$$\hat{E}_s^{(+)}(\Omega) = \mathscr{E}_0\left(\frac{\langle \hat{X}_0 \rangle + i \langle \hat{P}_0 \rangle}{2} V_0(\Omega) + \sum_n \delta\hat{a}_n V_n(\Omega)\right) \tag{D.12}$$

where $\hat{X}$ and $\hat{P}$ are the quadratures of the field in the new basis.

We see that, naturally, the expectation value of the phase quadrature operator is given by

$$\langle \hat{P}_0 \rangle = 2\sqrt{N}\frac{\delta L}{c}\sqrt{\omega_0^2 + \Delta\omega^2} \tag{D.13}$$

We can see that computing the expectation value of the observable $\hat{P}_0' = \frac{c}{2\sqrt{N}\sqrt{\omega_0^2+\Delta\omega^2}}\hat{P}_0$ would yields δL.

However, the meaning of its conjugate variable is more difficult to interpret. It should obviously contain the mean-field, but it should also contain a physical quantity that is detected on the amplitude quadrature with a sensitivity that increases with ω_0 and $\Delta\omega$. This is clearly the contrary of a shift $\delta\omega$ in the center frequency.

Hence, the physical interpretation of that quantity does not seem straightforward and could result from different sources that are not clearly identified.

Bibliography

[Aasi 13] J. Aasi & the LIGO Scientific Collaboration. *Enhanced sensitivity of the LIGO gravitational wave detector by using squeezed states of light.* Nature Photonics, vol. 7, no. 8, pages 613–619, July 2013. Online URL. (Cited on pages 2 and 89.)

[Adesso 14] Gerardo Adesso, Sammy Ragy & AR Lee. *Continuous variable quantum information: Gaussian states and beyond.* Open Systems & Information Dynamics, pages 1–55, 2014. Online URL. (Cited on page 56.)

[Anisimov 10] Petr M. Anisimov, Gretchen M. Raterman, Aravind Chiruvelli, William N. Plick, Sean D. Huver, Hwang Lee & Jonathan P. Dowling. *Quantum Metrology with Two-Mode Squeezed Vacuum: Parity Detection Beats the Heisenberg Limit.* Phys. Rev. Lett., vol. 104, page 103602, Mar 2010. Online URL. (Cited on page 89.)

[Appel 08] Walter Appel. Mathématiques pour la physique, 4^{e} édition. H & K, 2008. (Cited on page 37.)

[Bachor 04] Hans-A Bachor & Timothy C Ralph. A guide to experiments in quantum optics, 2nd, volume 1. 2004. (Cited on page 19.)

[Barnett 02] Stephen M Barnett & Paul M Radmore. Methods in theoretical quantum optics, volume 15. Oxford University Press, 2002. (Cited on page 89.)

[Bartels 04] a Bartels, C W Oates, L Hollberg & S a Diddams. *Stabilization of femtosecond laser frequency combs with subhertz residuallinewidths.* Optics Letters, vol. 29, no. 10, pages 1081–1083, 2004. Online URL. (Cited on page 170.)

[Beck 00] M Beck. *Quantum State Tomography with Array Detectors.* Physical review letters, vol. 84, no. 25, pages 5748–5751, (Cited on page 76.)

[Black 01] Eric D. Black. *An introduction to Pound-Drever-Hall laser frequency stabilization.* American Journal of Pysics, vol. 69, no. 1, page 79, (Cited on page 163.)

[Boyd 68] G. D. Boyd & D.A. Kleinman. *Parametric Interaction of Focused Gaussian Light Beams.* Journal of Applied Physics, vol. 39, no. 8, page 3597, 1968. Online URL. (Cited on page 201.)

[Boyd 03] Robert W Boyd. Nonlinear Optics, volume 5 of *Electronics & Electrical.* Academic Press, 2003. (Cited on pages 110 and 200.)

[Brabec 97] T Brabec & Ferenc Krausz. *Nonlinear Optical Pulse Propagation in the Single-Cycle Regime.* Prl, vol. 78, page 3282, (Cited on page 99.)

[Braunstein 05] SL Braunstein & Peter Van Loock. *Quantum information with continuous variables.* Reviews of Modern Physics, no. April, 2005. Online URL. (Cited on page 25.)

[Briles 10] Travis C Briles, Dylan C Yost, Arman Cingöz, Jun Ye & Thomas R Schibli. *Simple piezoelectric-actuated mirror with 180 kHz servo bandwidth.* Optics express, vol. 18, no. 10, pages 9739–9746, (Cited on page 111.)

[Cai 15] Yin Cai. *Quantum Coherent Control with an Optical Frequency Comb.* PhD thesis, ENS, 2015. (Cited on pages 145 and 192.)

[Casacio 14] C. A. Casacio. Single-pass squeezing with an optical frequency comb. Master's thesis, 2014. (Cited on page 204.)

[Caves 81] Carlton M. Caves. *Quantum-mechanical noise in an interferometer.* Physical Review D, vol. 28, no. 8, (Cited on pages 2 and 89.)

[Chadi 13] a. Chadi, G. Méjean, R. Grilli & D. Romanini. *Note: Simple and compact piezoelectric mirror actuator with 100 kHz bandwidth, using standard components.* Review of Scientific Instruments, vol. 84, no. 5, pages 2013–2015, (Cited on page 111.)

[Chekhovsky 98] Alexander M Chekhovsky, Anatol N Golubev & Michael V Gorbunkov. *Optical pulse distance-multiplying interferometry.* Applied optics, vol. 37, no. 16, pages 3480–3483, (Cited on page 96.)

[Coddington 09] I Coddington, WC Swann, L Nenadovic & NR Newbury. *Rapid and precise absolute distance measurements at long range.* Nature Photonics, vol. 3, no. 6, pages 351–356, (Cited on pages 97 and 210.)

[Cohen 89] Leon Cohen. *Time-Frequency distributions : a review.* Proc. IEEE, vol. 77, no. 7, pages 941–981, (Cited on page 44.)

[Cui 08] M. Cui, R. N. Schouten, N. Bhattacharya & S. a. van den Berg. *Experimental demonstration of distance measurement with a femtosecond frequency comb laser.* Journal of the European Optical Society, vol. 3, pages 1–4, (Cited on page 97.)

[Cui 11] M Cui, M G Zeitouny, N Bhattacharya, S a van den Berg & H P Urbach. *Long distance measurement with femtosecond pulses using a dispersive interferometer.* Optics express, vol. 19, no. 7, pages 6549–6562, (Cited on page 97.)

[Delaubert 06] Vincent Delaubert, N Treps & CC Harb. *Quantum measurements of spatial conjugate variables: displacement and tilt of a Gaussian beam.* Optics letters, vol. 31, no. 10, pages 1537–1539, 2006. Online URL. (Cited on page 104.)

[Delaubert 07] Vincent Delaubert. *Quantum imaging with a small number of transverse modes.* PhD thesis, UPMC & ANU, 2007. (Cited on pages 16, 28 and 102.)

[Eckstein 12] Andreas Eckstein. *Mastering quantum light pulses with nonlinear waveguide interactions.* PhD thesis, Friedrich-Alexander-Universität Erlangen-Nürnberg, 2012. (Cited on page 191.)

[Einstein 35] A Einstein, B Podolsky & N Rosen. *Can quantum-mechanical description of physical reality be considered complete?* Physical review, vol. 47, no. May, pages 777–780, 1935. Online URL. (Cited on page 30.)

[Ferraro 05] Alessandro Ferraro, Stefano Olivares & MGA Paris. *Gaussian states in continuous variable quantum information.* arXiv preprint quant-ph/0503237, 2005. Online URL. (Cited on pages 27 and 29.)

[Furusawa 11] Akira Furusawa & Peter Van Loock. Quantum teleportation and entanglement: a hybrid approach to optical quantum information processing. John Wiley & Sons, 2011. (Cited on page 23.)

[Glauber 63] RJ Glauber. *Coherent and incoherent states of the radiation field.* Physical Review, vol. 49, no. 638, 1963. Online URL. (Cited on page 28.)

[Grynberg 10] Gilbert Grynberg, Alain Aspect & Claude Fabre. Introduction to quantum optics: from the semi-classical approach to quantized light. Cambridge University Press, 2010. (Cited on pages 13, 21 and 190.)

[Haus 90] H. a. Haus & Y. Lai. *Quantum theory of soliton squeezing: a linearized approach.* Journal of the Optical Society of America B, vol. 7, no. 3, page 386, (Cited on pages 170 and 179.)

[Haus 93] HA Haus & Antonio Mecozzi. *Noise of mode-locked lasers.* Quantum Electronics, IEEE Journal of, vol. 2, no. 3, 1993. Online URL. (Cited on page 170.)

[Helbing 02] F W Helbing, G Steinmeyer, U Keller, R S Windeler, J Stenger & H R Telle. *Carrier-envelope offset dynamics of mode-locked lasers.* Optics letters, vol. 27, no. 3, pages 194–196, (Cited on pages 58 and 163.)

[Helstrom 68] Carl W Helstrom. *The minimum variance of estimates in quantum signal detection.* Information Theory, IEEE Transactions on, vol. 14, no. 2, pages 234–242, (Cited on page 86.)

[Ivanov 03] Eugene N. Ivanov, Scott a. Diddams & Leo Hollberg. *Analysis of Noise Mechanisms Limiting the Frequency Stability of Microwave Signals Generated with a Femtosecond Laser.* IEEE Journal on Selected Topics in Quantum Electronics, vol. 9, no. 4, pages 1059–1065, (Cited on page 112.)

[Jacquard 12] C. Jacquard. Réalisation d'une cavité de filtrage pour la métrologie quantique par peigne de fréquence. Master's thesis, 2012. (Cited on page 151.)

[Jeong 14] Hyunseok Jeong, Alessandro Zavatta, Minsu Kang, Seung-Woo Lee, Luca S. Costanzo, Samuele Grandi, Timothy C. Ralph & Marco Bellini. *Generation of hybrid entanglement of light.* Nature Photonics, vol. 8, no. 7, pages 564–569, June 2014. Online URL. (Cited on page 23.)

[Jian 12] Pu Jian, Olivier Pinel, Claude Fabre, Brahim Lamine & Nicolas Treps. *Real-time displacement measurement immune from atmospheric parameters using optical frequency combs.* Opt. Express, vol. 20, no. 24, pages 27133–27146, Nov 2012. Online URL. (Cited on pages 2, 102 and 108.)

[Jian 14] Pu Jian. *Quantum limits in range-finding measurements with optical frequency combs.* PhD thesis, UPMC, 2014. (Cited on pages 56, 63, 87, 89 and 107.)

[Jiang 12] Shifeng Jiang, Nicolas Treps & Claude Fabre. *A time/frequency quantum analysis of the light generated by synchronously pumped optical parametric oscillators.* New Journal of Physics, vol. 14, no. 4, page 043006, April 2012. Online URL. (Cited on page 191.)

[Jones 00] D. J. Jones. *Carrier-Envelope Phase Control of Femtosecond Mode-Locked Lasers and Direct Optical Frequency Synthesis.* Science, vol. 288, no. 5466, pages 635–639, (Cited on page 163.)

[Kim 08] Jungwon Kim, Jonathan a. Cox, Jian Chen & Franz X. Kärtner. *Drift-free femtosecond timing synchronization of remote optical and microwave sources.* Nature Photonics, vol. 2, no. 12, pages 733–736, (Cited on page 97.)

[Kimble 77] HJ Kimble, M Dagenais & L Mandel. *Photon antibunching in resonance fluorescence.* Physical Review Letters, vol. 39, no. 11, pages 691–695, 1977. Online URL. (Cited on page 23.)

[Lamine 08] Brahim Lamine, Claude Fabre & Nicolas Treps. *Quantum improvement of time transfer between remote clocks.* Physical review letters, vol. 101, no. 12, page 123601, (Cited on pages 2 and 96.)

[Lepetit 95] L Lepetit, G Cheriaux & M Joffre. *Linear techniques of phase measurement by femtosecond spectral interferometry for appli-*

cations in spectroscopy. JOSA B, vol. 12, no. 12, pages 2467–2474, (Cited on page 68.)

[Lloyd 99] Seth Lloyd & SL Braunstein. *Quantum computation over continuous variables.* Physical Review Letters, vol. 82, no. 8, pages 1784–1787, 1999. Online URL. (Cited on page 23.)

[Loudon 00] Rodney Loudon. The quantum theory of light. 2000. (Cited on page 22.)

[Martin 09] Michael J Martin, Seth M Foreman, TR Schibli & Jun Ye. *Testing ultrafast mode-locking at microhertz relative optical linewidth.* Optics express, vol. 17, no. 2, pages 558–568, (Cited on page 170.)

[Martinez 84] O.E. Martinez, J.P. Gordon & R.L. Fork. *Negative group-velocity dispersion using refraction.* JOSA A, vol. 1, no. 10, pages 1003–1006, (Cited on page 43.)

[McMullen 77] J D McMullen. *Chirped-pulse compression in strongly dispersive media.* JOSA, vol. 67, no. 11, pages 1575–1578, (Cited on page 43.)

[Medeiros de Araujo 12] Renné Medeiros de Araujo. *Génération et manipulation de peignes de fréquences quantiques multimodes.* PhD thesis, UPMC, 2012. (Cited on page 157.)

[Michelson 94] A.-A. Michelson. *Les méthodes interférentielles en métrologie et l'établissement d'une longueur d'onde comme unité absolue de longueur.* J. Phys. Theor. Appl., vol. 3, no. 1, pages 5–22, (Cited on page 1.)

[Monmayrant 05] Antoine Monmayrant. *Façonnage et caractérisation d'impulsions ultracourtes. Contrôle cohérent de systèmes simples.* PhD thesis, Université Paul Sabatier, 2005. (Cited on pages 63 and 66.)

[Morgner 99] Uwe Morgner, FX Kärtner, Seong-Ho Cho, Yanbei Chen, Hermann A Haus, James G Fujimoto, Erich P Ippen, V Scheuer, Gregor Angelow & Theo Tschudi. *Sub-two-cycle pulses from a Kerr-lens mode-locked Ti: sapphire laser.* Optics Letters, vol. 24, no. 6, pages 411–413, (Cited on page 50.)

[Morin 14] Olivier Morin, Kun Huang, Jianli Liu, Hanna Le Jeannic, Claude Fabre & Julien Laurat. *Remote creation of hybrid entanglement between particle-like and wave-like optical qubits.* Nature Photonics, vol. 8, no. 7, pages 570–574, June 2014. Online URL. (Cited on page 23.)

[Morizur 11] Jean-François. Morizur. *Quantum protocols with transverse spatial modes.* PhD thesis, UPMC & ANU, 2011. (Cited on page 77.)

[Murphy Jr 08] TW Murphy Jr, Eric G Adelberger, JBR Battat, LN Carey, Charles D Hoyle, P LeBlanc, EL Michelsen, K Nordtvedt, AE Orin, Jana D Strasburg*et al. The apache point observatory lunar laser-ranging operation: instrument description and first detections.* Publications of the Astronomical Society of the Pacific, vol. 120, no. 863, pages 20–37, (Cited on page 1.)

[Newbury 07] NR Newbury & WC Swann. *Low-noise fiber-laser frequency combs.* JOSA B, vol. 24, no. 8, pages 1756–1770, 2007. Online URL. (Cited on page 166.)

[Nicolodi 14] Daniele Nicolodi, Bérengère Argence, Wei Zhang, Rodolphe Le Targat, Giorgio Santarelli & Yann Le Coq. *Spectral purity transfer between optical wavelengths at the 10-18 level.* Nature Photonics, vol. 8, no. 3, pages 219–223, January 2014. Online URL. (Cited on page 35.)

[Ourjoumtsev 07] A. Ourjoumtsev. *Etude théorique et expérimentale de superpositions quantiques cohérentes et d'états intriqués nongaussiens de la lumière.* PhD thesis, UPMC, 2007. (Cited on page 26.)

[Paschotta 05] R. Paschotta, a. Schlatter, S.C. Zeller, H.R. Telle & U. Keller. *Optical phase noise and carrier-envelope offset noise of mode-locked lasers.* Applied Physics B, vol. 82, no. 2, pages 265–273, December 2005. Online URL. (Cited on page 2.)

[Patera 08] Giuseppe Patera. *Quantum properties of ultra-short pulses generated by SPOPOs: multi-mode squeezing and entanglement.* PhD thesis, UPMC & Università dell'Insubria, 2008. (Cited on pages 191 and 194.)

[PI 14] PI. *Catalog : piezoelectric actuators.* Physik Instrumente GmbH, 2014. Online URL. (Cited on page 111.)

[Réfrégier 02] P Réfrégier. Théorie du bruit et application en physique. Hermes Science, 2002. (Cited on page 89.)

[Reynaud 92] Serge Reynaud, Antoine Heidmann, Elisabeth Giacobino & Claude Fabre. *Quantum fluctuations in optical systems.* Progress in optics, vol. 30, pages 1–85, (Cited on page 23.)

[Roslund 10] Jonathan Roslund. *Optimal quantum control in the laboratory.* PhD thesis, Princeton, 2010. (Cited on page 63.)

[Roslund 13] Jonathan Roslund, Renné Medeiros de Araújo, Shifeng Jiang, Claude Fabre & Nicolas Treps. *Wavelength-multiplexed quantum networks with ultrafast frequency combs.* Nature Photonics, vol. 8, no. 2, pages 109–112, December 2013. Online URL. (Cited on pages 144 and 192.)

[Roslund 15] Jonathan Roslund, Valérian Thiel, Pu Jian, Claude Fabre & Nicolas Treps. *Sensitivity measurement of a Mach Zehdner interferometer using absolute calibration of a subwavelength displacement.* To be published, (Cited on page 116.)

[Rudolph 06] Wolfgang Rudolph & Jean-Claude Diels. Ultrashort Laser Pulses Phenomena - Second Edition. 2006. (Cited on page 32.)

[Schleich 11] Wolfgang P Schleich. Quantum optics in phase space. John Wiley & Sons, 2011. (Cited on page 26.)

[Schliesser 06] Albert Schliesser, Christoph Gohle, Thomas Udem & TW Hänsch. *Complete characterization of a broadband high-finesse cavity using an optical frequency comb.* Opt. Express, vol. 14, no. 13, pages 1802–1805, 2006. Online URL. (Cited on page 160.)

[Schmeissner 14a] Roman Schmeissner. *Frequency combs at the quantum limit.* PhD thesis, UPMC, 2014. (Cited on pages 58, 162, 165 and 166.)

[Schmeissner 14b] Roman Schmeissner, Jonathan Roslund, Claude Fabre & Nicolas Treps. *Spectral Noise Correlations of an Ultrafast Frequency Comb.* Physical Review Letters, vol. 263906, no. December, pages 1–5, (Cited on pages 169, 173 and 180.)

[Schmeissner 14c] Roman Schmeissner, Valerian Thiel, Clément Jacquard, Claude Fabre & Nicolas Treps. *Analysis and filtering of phase noise in*

an optical frequency comb at the quantum limit to improve timing measurements. Optics letters, vol. 39, no. 12, pages 3603–3606, (Cited on pages 165 and 167.)

[Siegman 86] Anthony E Siegman. Lasers. University Science Books, Mill Valley, CA, 1986. (Cited on pages 14 and 152.)

[Sorokin 00] Evgeni Sorokin, Gabriel Tempea & Thomas Brabec. *Measurement of the root-mean-square width and the root-mean-square chirp in ultrafast optics*. JOSA B, no. January, pages 146–150, 2000. Online URL. (Cited on pages 36 and 38.)

[Spence 91] David E Spence, P Np Kean & Wilson Sibbett. *60-fsec pulse generation from a self-mode-locked Ti: sapphire laser*. Optics letters, vol. 16, no. 1, pages 42–44, (Cited on page 2.)

[Steinlechner 13] Sebastian Steinlechner, Jöran Bauchrowitz, Melanie Meinders, Helge Müller-Ebhardt, Karsten Danzmann & Roman Schnabel. *Quantum-dense metrology*. Nature Photonics, vol. 7, no. 8, pages 626–630, June 2013. Online URL. (Cited on page 94.)

[Swann 06] W C Swann, J J McFerran, I Coddington, N R Newbury, I Hartl, M E Fermann, P S Westbrook, J W Nicholson, K S Feder, C Langrock & M M Fejer. *Fiber-laser frequency combs with subhertz relative linewidths*. Optics letters, vol. 31, no. 20, pages 3046–3048, (Cited on page 170.)

[Thiel 15] Valérian Thiel, Jonathan Roslund, Claude Fabre & Nicolas Treps. *Noise matrices animations*. https://youtu.be/BpIwWnX26A, 2015. Online URL. (Cited on page 182.)

[Trebino 02] Rick Trebino. Frequency-resolved optical gating: the measurement of ultrashort laser pulses. Springer Science, 2002. (Cited on pages 47 and 48.)

[Treps 03] Nicolas Treps, Nicolai Grosse, Warwick P Bowen, Claude Fabre, Hans-A Bachor & Ping Koy Lam. *A quantum laser pointer*. Science (New York, N.Y.), vol. 301, no. 5635, pages 940–3, August 2003. Online URL. (Cited on pages 116 and 155.)

[Treps 05] N. Treps, V. Delaubert, a. Maître, J. Courty & C. Fabre. *Quantum noise in multipixel image processing*. Physical Review A,

vol. 71, no. 1, page 013820, January 2005. Online URL. (Cited on page 28.)

[Udem 02] Th Udem, Ronald Holzwarth & Theodor W Hänsch. *Optical frequency metrology*. Nature, vol. 416, no. 6877, pages 233–237, (Cited on page 2.)

[Verlot 09] P. Verlot, A. Tavernarakis, T. Briant, P.-F. Cohadon & A. Heidmann. *Scheme to Probe Optomechanical Correlations between Two Optical Beams Down to the Quantum Level*. Phys. Rev. Lett., vol. 102, page 103601, Mar 2009. Online URL. (Cited on page 116.)

[Walmsley 96] IA Walmsley & Victor Wong. *Characterization of the electric field of ultrashort optical pulses*. JOSA B, no. November, pages 2453–2463, 1996. Online URL. (Cited on page 45.)

[Weiner 95] AM Weiner. *Femtosecond optical pulse shaping and processing*. Progress in Quantum Electronics, vol. 6727, no. 94, 1995. Online URL. (Cited on page 62.)

[Weiner 00] Andrew M Weiner. *Femtosecond pulse shaping using spatial light modulators*. Review of scientific instruments, vol. 71, no. 5, pages 1929–1960, (Cited on page 43.)

[Weiner 11a] Andrew Weiner. Ultrafast optics, volume 72. John Wiley & Sons, 2011. (Cited on pages 32, 50 and 200.)

[Weiner 11b] Andrew M. Weiner. *Ultrafast optical pulse shaping: A tutorial review*. Optics Communications, vol. 284, no. 15, pages 3669–3692, July 2011. Online URL. (Cited on page 62.)

[Wenger 04] Jérôme Wenger, Rosa Tualle-Brouri & Philippe Grangier. *Non-Gaussian Statistics from Individual Pulses of Squeezed Light*. Physical Review Letters, vol. 92, no. 15, page 153601, April 2004. Online URL. (Cited on page 193.)

[Yariv 67] A Yariv. Quantum electronics, 1967. Wiley, 1967. (Cited on pages 14 and 17.)

[Ye 04] Jun Ye. *Absolute measurement of a long, arbitrary distance to less than an optical fringe*. Optics letters, vol. 29, no. 10, pages 1153–1155, (Cited on page 96.)

[Yokoyama 13] Shota Yokoyama, Ryuji Ukai, Seiji C. Armstrong, Chanond Sornphiphatphong, Toshiyuki Kaji, Shigenari Suzuki, Jun-ichi Yoshikawa, Hidehiro Yonezawa, Nicolas C. Menicucci & Akira Furusawa. *Ultra-large-scale continuous-variable cluster states multiplexed in the time domain.* Nature Photonics, vol. 7, no. 12, pages 982–986, November 2013. Online URL. (Cited on page 208.)